UNIVERSITY OF EXETER

COLLEGE OF ENGINEERING, MATHEMATICS AND PHYSICAL SCIENCES

THESIS FOR THE DEGREE OF DOCTOR OF PHILOSOPHY IN PHYSICS

The vertebral endplate: its structure and function

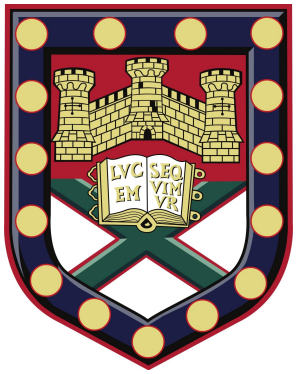

Author:

Fay MANNING

Supervisors:

Prof. Peter WINLOVE

Dr. Jude MEAKIN

Submitted by Fay Manning to the University of Exeter as a thesis for the degree of Doctor of Philosophy in Physics, July 2019

October 27, 2019 (Signature) .....

Abstract

The cause of degenerative changes to the intervertebral disc that can produce back pain are still indefinable. One newer avenue of investigation includes the analysis of vertebral endplates, which lie between vertebral bodies and their adjacent discs. This thesis investigates the structure and function of the vertebral endplate. Multiphoton microscopy was employed as the main imaging method as it has previously shown its ability to differentiate between tissue in osteochondral regions, and its ability to image label free, thick samples reduces sample processing. Animal endplate models were utilised as a healthy model, alongside degenerate human samples from surgery. This thesis aimed to investigate the structure of the vertebral endplate as well as its function.

The structure of the endplate was confirmed to contain three distinct regions; the bony endplate, mineralised cartilage and non-mineralised cartilage. The thickness of the cartilage endplate was shown to be thicker in the cranial endplate ($p = 0.008$), and the mineralised region thicker than the non-mineralised ($p = 0.005$). Additionally, this study confirmed how anchorage of the intervertebral disc is achieved. Microstructurally, annular bundles penetrate through both the mineralised and non-mineralised regions of the cartilage endplate. Within these layers, the bundles sub-divide in a branched structure as an integration mechanism. Energy disperse spectroscopy showed a higher calcium to phosphate ratio in young adult ovine spines ($p<0.05$) compared with mature ovine spines, and age differences in the structure of the bony endplate were also noted. Additionally, Raman spectroscopy on bovine sections showed higher mineralisation in the endplate under the nucleus than annulus using the mineral to matrix ratio (peak ratios of 3.15 and 2.35 respectively). This work highlights the specificity of each of the tissues in the endplate, and how they change based on their location (nucleus/annulus, caudal/cranial) and with age. Degenerative human samples showed higher two photon fluorescence (TPF) signal than the bovine model, and also showed a highly aligned collagen region, parallel to the tidemark which agrees with previous literature.

An important function of the endplate is its role as a nutritional pathway for the diffusion of solutes through the endplate and the convective transport of water. Vessels within the endplate were imaged using multiphoton microscopy. They were measured

to be as small as 5 μm in diameter and within close proximity to the disc (< 70 μm), though never crossing the tide mark. Additionally, the use of a fluorescent tracer confirmed the diffusion from the disc into vessels in the endplate. Through the use of real-time imaging of a fluorescent tracer diffusing from the disc through the endplate, this study showed the tidemark as a barrier, initially holding the tracer up. The study additionally confirmed the presence of small pores in the mineralised cartilage post-tidemark.

Further relating to the function of the endplate, a series of compressive loading experiments were carried out in order to provide novel insight into the micromechanics of the regions of the endplate. The disc displayed the highest amount of micro-strain with measurements reaching as high as - 40 %, though initial strain appears primarily due to fibre realignment. This work highlights the importance of the cartilage components of the endplate in the micromechanics of the disc.

Previously, the vertebral endplate has been underappreciated within the literature and clinical understanding of the its role. This works highlights the intimacy between the intervertebral disc and vertebral endplate, reinforcing the necessity for further investigation of this unique region.

Acknowledgements

Firstly, I would like to offer my special thanks to my supervisors Jude and Peter. Thank you for taking me on for this project, supporting me throughout and allowing me to mould this work into what it is today. Secondly, thank you to Claudio and Jess for teaching me everything I needed to get started on this project, and for being a source of support and guidance throughout. Thank you Ellen for being there for technical help, discussions and rants when needed. Thank you for your general interest in the project and my well being. Thank you to Dave, for saving my skin SO many time with my PC, you truly are a superhero (who deserves some new shoes!).

Thank you to the wider project team at the RD&E, Ipswich and Cambridge, specifically David, Andrew and Tom. Most importantly though, Sheen, thank you for being my buddy through this, for chatting through confusing results, attending conferences with me and just generally being amazing! I would also like to offer my special thanks to to those at the University of Auckland, for welcoming me so amazingly. To Alesha, Tarek, Bella, Hapreet, Vonne, Johnathan, Josh, Meredith, Alex, Ashvin and Neil. Thank you all!

Thank you to the wider bio-phys group for your endless welcome, TV and adventures. From otters (or lack there of) at Ottery, to Mary at lunch, I couldn't have asked for better companions! So thank you to Anna, Michelle, Rikke (and Chris and Alexander!), Bob, Richard and the rest. Mostly though, thank you to Tobi (and Connor), Skye, Michael and Beth. Your constant friendship, support games nights and egg breaks have, at times sabotaged, though mostly helped me through!

Thank you to the gym crew, Adina, Raluca, Chloe and Adam for keeping me STRONK. And a big thank you to my church families, both St Leonard's and West Street, thank you for your encouragement and prayers through thick and thin, especially the Browns, the Hunts and the Taylors.

Lastly, to my Mom, Dad and sister Amy who supported me in this insane endeavor, and to Sam who married me despite this endeavour. I would not be where I am today without you.

Contents

List of Figures

List of Tables

Author's Declaration

The main microscope used in this project was set up by Julian Mojer and maintained by Jessica Mansfield and Chun-Chin Wang. Both the dissection and polarisation microscopes are maintained by Ellen Green. Raman spectroscopy hardware was provided by Nick Stone. Martha Vardaki collected the Renishaw data on bovine endplates and carried out data processing. Ellen Green helped collect WITech measurements on degenerative human samples.

Sally Roberts kindly provided sheep spines from their farm for tissue sections. The human samples acquired in 3.3.4 were obtained for a study of needle damage to the disc by Claudio Vergari, supplied by Daniel Chan and Andrew Clarke at the Peninsula Spine Unit, Royal Devon and Exeter Hospital.

A section of chapter four was part of a collaboration with Auckland University, Chemical and Material Engineering Department, funded by The Society of Back Pain Research. Differential Interface Contrast Microscopes were provided by Ashvin Thambyah with training and guidance provided by Meredith Scholoumn. SEM and EDS data was gathered alongside Nural Haiza Sapiee.

Michelle Bailey provided the custom Matlab script for diffusion fitting in chapter five.

In chapter six, the compression rig was designed and assembled by Jessica Mansfield. The automated rig and custom YATTS software for data analysis was provided by Claudio Vergari.

Abbreviations

LBP	Lower Back Pain
VB	Vertebral Body
IVD	Intervertebral Disc
NP	Nucleus Pulposus
AF	Annulus Fibrosus
EP	Endplate
CEP	Cartilage Endplate
MC	Mineralised Cartilage
non-MC	Non-Mineralised Cartilage
BEP	Bony Endplate
TM	Tidemark
CL	Cement Line
MPT	Multiphoton
SHG	Second Harmonic Generation
TPF	Two Photon Fluorescence
DIC	Differential Interface Contrast
SEM	Scanning Electron Microscopy
EDS	Energy Dispersive Spectroscopy
BMD	Bone Mineral Density
PBS	Phosphate Buffered Saline
MRI	Magnetic Resonance Imaging
YATTS	Yet Another Tissue Tracking Software
MMR	Mineral to Matrix Ratio

1 Introduction

This chapter first presents the context and motivation for the studies conducted within this thesis. The aims then will be discussed and an overview of the thesis chapters will be provided.

1.1 Context and Motivation

Lower back pain (LBP) is an extremely common health problem.[1–3] First incidence of LBP in the UK is between 15.4-36 % per year in a population aged 18-75 years.[4] However, a complete account of the global impact of lower back pain is difficult due to varied methods. For example, different studies have utilised different measurement duration, from point prevalence up to one year.[5–7] Studies have evidenced the influence of age of onset of back pain. Taimela et al., found one-year prevalence as low as 9.7 %, however their population was aged 7-16 years.[8] In comparison, Hestbaek et al., measured one year prevalence in a population aged 30-50 years and showed incidence as high as 56 %.[9] Many incidences of persistent back pain are successfully managed through a combination of conservative measures such as drug intervention, physical therapies and pain management techniques. However, those that fail to respond to these therapies develop pain that is both severe and obstinate. One of the primary causes of this persistent lower back pain is believed to be the degeneration of the intervertebral disc (IVD) which can lead to the compression of spinal nerves and adjacent vertebra.[10] The definition of IVD degeneration fluctuates within the research community as it includes a number of different changes such as annulus tears, disc prolapse and Schmorl's Nodes. Together these three abnormalities provide a strong indication of back pain.[11,12] The current treatment of these cases involves the surgical removal of part of or an entire effected disc. It is estimated that around >35,000 episodes of these surgeries are recorded each year, and this number appears to be on the rise as shown in Fig. 1.1.[13]

It is widely believed that considerable gross changes to the material properties of the discs lead to altered spinal mechanics that can develop in to painful spinal disorders.[14] However, the cause of degenerative changes in the spine are still indefinable. One newer

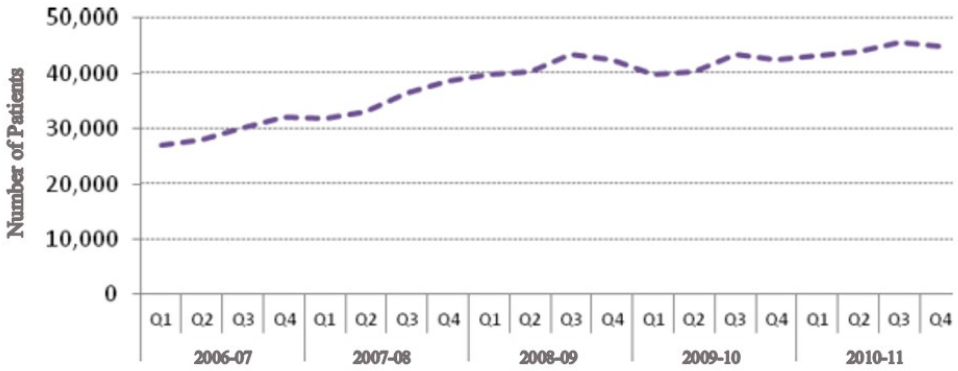

Figure 1.1: *Patients with back pain/ radicular pain - total Finished Consultant Episode (FCE's) with spinal procedures recorded per quarter (April 06-Mar 11), patients with neck pain are excluded*[13]

avenue of investigation includes the analysis of vertebral endplates, which lie between vertebral bodies and their adjacent discs.

Understanding the structure and physiology of the endplate is key, not only in understanding the cause of IVD degeneration, but also in terms of surgical treatment. It has been widely debated as to whether endplates should be left intact or removed during fusion surgeries and methods vary between clinicians. Removing the endplate can be biologically advantageous as it may promote healing through contact with the bleeding bone, however, its mechanical effects are not widely investigated. It has been shown that the removal of the endplates can reduce the in vitro failure load by 33 % ($P < 0.04$), as well as a stiffness decrease ($P = 0.01$), suggesting that the endplates play a vital role in the mechanics of the spine even post-surgery.[15,16] Understanding the structural and mechanical importance of the endplate in the motion segment is therefore key to better understanding how to best support disc implants. Additionally, with the increased focus on regenerative therapies, proposals of nuclear replacements and cell injections are becoming common in the literature.[17–19] However, without the mechanical and nutritional support of a healthy vertebral endplate, the long term viability of such implants is questionable.

1.2 Study Aims

The main aims of the thesis are summarised below.

- to establish a structural understanding of the endplate and its interface with the bone and disc across its surface.
- to establish an understanding of the endplate vasculature, as well as permeability to solutes.
- to determine methods to investigate the mechanical relationship of the bone-endplate-disc interface.

1.3 Thesis Outline

Each results chapter begins with a short introduction and summary of its contents as well as a review of the relevant literature.

- Chapter two consists of a literature review as background to this thesis. Briefly, the physiology of the spine, intervertebral disc and endplates are introduced. Studies pertaining to the structure, vasculature and mechanics of the endplate are critiqued.
- Chapter three focuses on the methodologies utilised within this thesis and the theory that underpins them. First, the imaging set up and image acquisition with the multiphoton microscope are introduced. Then the different animal models are explored and sample preparation described. Lastly, the acquisition of human spine samples from surgical patients is outlined.
- In chapter four, the structure of the vertebral endplate is examined. Firstly using, multiphoton microscopy, second harmonic generation (SHG) and two-photon fluorescence (TPF) signals were utilised to investigate the interaction of mineralised and non-mineralised cartilage at the tidemark. This was supported through the use of Differential interface Contrast Microscopy and Scanning Electron Microscopy (SEM). Additionally, Energy Dispersive Spectroscopy (EDS) and Raman Spectroscopy were utilised to investigate differences in the annular and nuclear regions of the bovine endplate, as well as look at degenerative human samples.
- Chapter five focuses on the endplates role as a nutritional pathway to the intervertebral disc. Here, vessels within the endplate were imaged using multiphoton microscopy both label-free and with the aid of a tracer. Experiments on solute transport and perfusion were also carried out in ovine lumbar spine and bovine tails.

- Chapter six explores imaging of the micromechanics of the cartilage endplate under compression with the multiphoton microscope. The chapter focuses on the problem by loading the endplate while simultaneously imaging. The chapter utilises a custom loading rig and imaging using the multiphoton system.
- Chapter seven summarises and concludes the contents of this thesis as well as giving a brief overview of the potential areas for future development.

2 Background Literature

This chapter provides an overview of the anatomy and physiology of the spine and intervertebral disc, however, the main focus is on the research pertaining to the endplate. The healthy structure and function are discussed as well as changes with aging, degeneration and pathologies.

2.1 The Spine

2.1.1 The Lumbar Spine

The vertebral column is made up of a series of 33 bones called vertebrae. These are grouped into five regions known as cervical, thoracic, lumbar, sacral and coccygeal. The first three regions are known as 'movable' vertebrae whereas the sacral and coccygeal regions are known as 'fixed'.[20] Vertebral bodies are interposed with the soft tissue of the intervertebral disc which allow small movements between vertebra.[21] The lumbar region is made up of the largest of the vertebral bodies[20] and is often referred to as the 'lower back'. This area is of key interest as it is shown to be a common site of intervertebral disc protrusion and other degenerative issues.[22,23]

The lumbar spine is made up of five vertebrae (noted as L1-5 shown in Fig. 2.1).[24] L5 shares a disc with the first of the sacral bones (shown as S1). The vertebrae are made up of two main portions, anterior and posterior. The anterior portion contains; the endplates, vertebral bodies and the anterior and posterior longitudinal ligaments. The posterior portion refers to the neural arch, zygapophyseal joints (facet joints), the bony processes and associated ligaments.[25] The spine can also be thought of as numerous motion segments[21] which are formed of two adjacent vertebrae and the disc found in-between. These are commonly referred to as functional spinal units.[26] Fig. 2.2 illustrates a caudal and transverse view of such a motion segment.

The vertebral bodies are formed of trabecular bone, surrounded with a thin layer of compact bone, apart from at the superior and inferior regions which merge with the

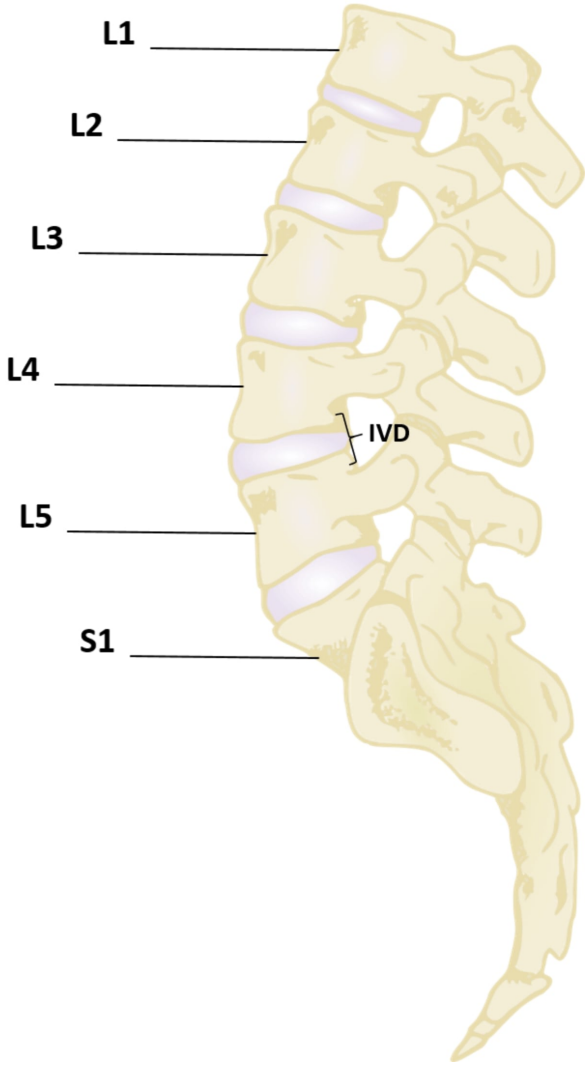

Figure 2.1: *Sketch of the human lumbar spine. It comprises of five lumbar vertebrae (labelled L1 to L5) and one sacral vertebrae (labelled S1) separated by intervertebral discs (IVD).*

vertebral endplate.[20,27,28] During development the growth of bones takes place at the growth plates, which in both long bones and the vertebral bodies occurs either end of the longitudinal direction of growth. In many non-human mammals, the growth plate is delineated from the vertebral body by a cartilagenous layer, distinguishing the plate (Fig. 3.4 A).[29] In the human spine fusion of the growth plate begins at ~ 15 years of age, however, full integration of the plate does not occur until ~ 18 - 25 years of age.[30–32] The literature uses mixed terminology when referring to the transition region from bone to endplate to disc. Some literature refers to the presence of cortical bone, whereas others refer to subchondral bone. Arguably, subchondral bone can be misleading as the term is ambiguous. Madry et al., alone offered over five definitions of 'subchondral'.[33] Even by their own definition (subchondral bone plate and the subarticular spongiosa[33]), subchondral bone is functionally different to that of cortical. This discrepancy in literature definitions is not limited to the bone at either ends of the vertebral bodies; but also extends to the endplate, this will be addressed later.

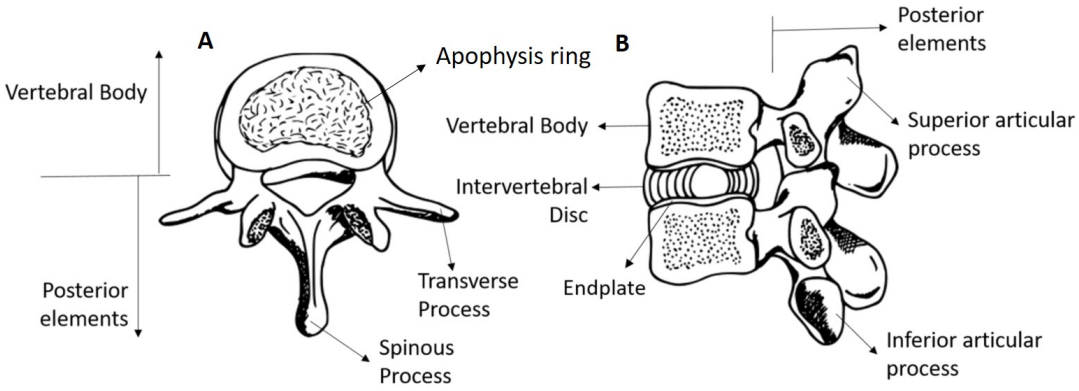

Figure 2.2: *A) Caudal view of The vertebral body and posterior elements B) Transverse cross-section through a motion segment. Schematic adapted from Rodrigues 2015*[34]

2.2 The Intervertebral Disc

The intervertebral disc sits between the vertebrae of the spine, offering flexibility and shock-absorbance to this highly loaded region. The discs are made of two main components, the gelatinous nucleus pulposus and more structured annulus fibrosus (Fig. 2.3).

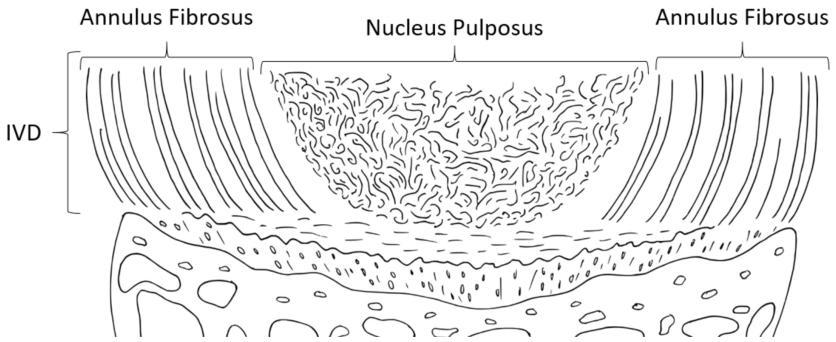

Figure 2.3: *The intervertebral disc. Schematic of the disorganised nucleus pulposus and the highly organised annulus fibrosus that make up the intervertebral disc (IVD).*

2.2.1 Nucleus Pulposus

The nucleus pulposus (NP) is formed of a loose network of collagen fibres within a proteoglycan rich gel.[30,35–41] It is a highly hydrated region with water content as high as 70 - 80 %. Although for many years the structure of the collagen fibres in this region was seen as highly irregular[30,35,42,43] more recent publication have shown a discernible structure- though a highly complex one.[44]

Collagen makes up around 20 % of the dry material of the nucleus, proteoglycans making up 30 - 50 %, with the remaining composition made up of other non-collagenous proteins.[37] Though there are multiple types of collagen present, type II is the most abundant in the nucleus (and commonly found in other load-bearing tissues), it makes up 80 % of the total collagen whilst types V, VI, IX and XII make up the remainder.[37] Elastin is another important component of the extracellular matrix of the disc, aiding its ability to return to its original size after loading. Parallel aligned elastin fibres in the disc nucleus have been shown to both point radially extending from the centre of the nucleus towards the annulus, and vertically between the two endplates.[45] However, at the transitional regions between the nucleus and the annulus it has been shown that the elastin fibres are no longer parallel but rather form a crisscross pattern.[45]

2.2.2 Annulus Fibrosus

Compared to the nucleus, the annulus fibrosus (AF) is highly organised. It forms a fibrocartilage ring around the gel-like nucleus,[37,42,46–49] made of a series of concentric rings (also known lamellae). Each of these is formed of regularly arranged collagen fibre bundles, with elastin running parallel to the fibers.[37,42,46–50] These fibres are connected to the endplate at a 57°angle to the spinal axis. Consecutive layers have alternating direction which generates a cross-ply structure.[37,46–49] The fibres of the annulus display a planar crimped morphology which aids the mechanics of these fibre bundles.[46] In tensile loads the crimps are first straightened, which makes the tissue relatively compliant[46,51] (crimp visible in Fig. 2.4 A). The water content of the annulus (64 - 77 %) is lower than that of the nucleus, however, there is regional variation with the inner layers showing higher hydration levels than the outer layers.[52,53] Like the nucleus, type II collagen is abundant in the annulus, though, it decreases in concentration moving outward from the nucleus, whilst type I increases in concentration.[54]

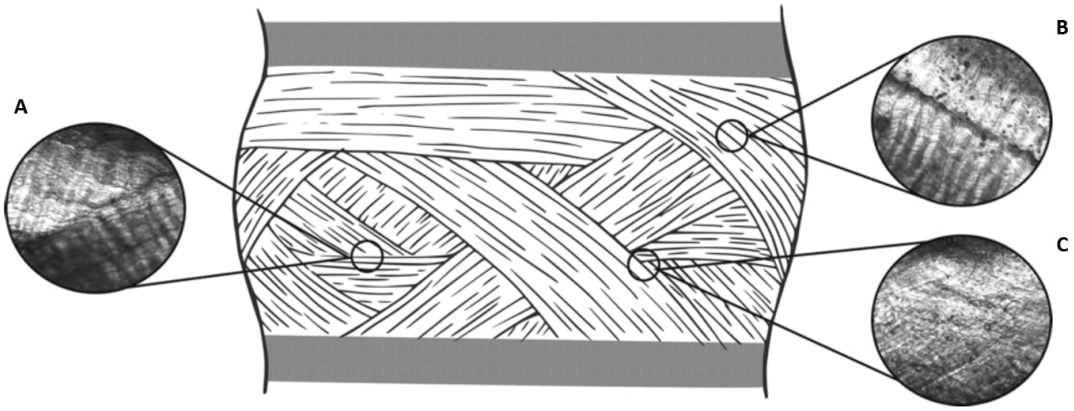

Figure 2.4: *Fibre bundle interactions. Image taken from Vergari et al.,[51] illustrating A) Fibre bundles crossing over one another B) Fibre bundles sitting parallel to one another and C) Fibre bundles interdigitising*.

Although often depicted in the literature as a regular structure of complete rings, the annular fibres show complexities.[48,51] As Fig. 2.4 illustrates, the annulus is discontinuous, with bundles which can either cross over one another (A), run parallel to one another (B) or interact through interdigitation (C).[51] Regions with higher variability in structure and higher interdigitation such as the posteriolateral area, has been shown to be more vulnerable to damage.[37,41,46,49,55–58] In the annulus, elastin fibres are found running parallel to the collagen fibres within the lamellae.[50] Additionally, elastin fibres are found concentrated between the lamellae, which are connected to one another with

cross bridges of dense elastic fibres.[50] The precise role of the connections is debatable, however, it has been suggested that the connections have a stabilising mechanical presence.[50,59]

2.3 The Vertebral Endplate

The vertebral endplate is a discrete entity which forms the transition from the trabecular bone of the vertebral body to the fibres of the intervertebral disc. It is responsible for absorbing and redistributing mechanical forces, anchoring the disc and provides the main nutritional pathway to the avascular disc.

2.3.1 Structure

The literature varies in relation to the nomenclature used in describing the endplate (Fig. 2.5). The endplate comprises of three main components, two that are cartilagenous and one that is bone. The three regions are separated with a tide mark (between the two cartilage regions), and a cement line (between the bone and mineralised cartilage). The cartilagenous endplate is formed of a region of non-mineralised tissue,[60] which if often referred to as 'hyaline cartilage'[61–65] or even just 'cartilage'. The fibres of this region have been shown to be aligned horizontally, parallel to the top of the vertebral body, but they only sit under the inner annulus and nucleus and does not extend to the edge of the vertebral body. In this thesis, this region will be referred to as 'non-mineralised cartilage' (non-MC). The next part of the cartilage endplate is a layer of mineralised cartilage. Due to its high mineral content, it has also been referred to as a 'hyper-mineralised region' since back-scatter SEM shows a strong signal indicating high mineralisation.[66] More commonly this region is referred to as 'calcified cartilage',[60,63,66–69] a term that is borrowed from the description of articular cartilage. The difficulty with this term is that the chemical composition of this region is still not fully understood, and therefore labelling it as 'calcified' cartilage may be misleading. Within this thesis, this region will be refereed to as 'mineralised cartilage' (MC). This region extends further than the non-mineralised cartilage, all the way to the ring apophysis. The non-mineralised cartilage, and mineralised cartilage together will be defined as the cartilage endplate (CEP).

Beyond the cartilage endplate, there is a region called the bony endplate (BEP)[69–72] which has been previously labelled as cortical[11,68,73,74] or subchondral bone.[57,63,75,76]

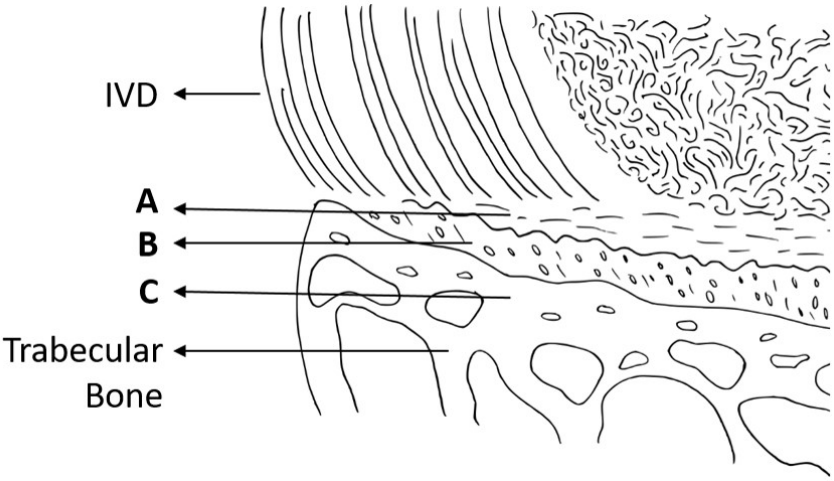

Figure 2.5: *Illustration of the transition from Trabecular bone to the intervertebral disc, with the three regions of the vertebral endplate (A, B and C). A) Non-mineralised cartilage, previously referred to as cartilage and hyaline cartilage. B) Mineralised Cartilage, previously referred to as calcified cartilage and a hyper-mineralised region. C) Bony Endplate, previously referred to as cortical or subchondral bone.*

Again subchondral bone is a term borrowed from articular cartilage which can be misleading about both the structure and function of this region. Similarly, cortical bone has a very defined structure of high density osteons and haversian canals,[77] which does not appear to coincide with what is seen within this region. Due to the potential for structural confusion, this region will be described as the 'bony endplate' within this thesis. The bony endplate has been shown to contain trabeculae like holes containing bone marrow, and have thus been labelled 'marrow contact channels' in relation to their potential role in the nutrition of the disc.[78,79]

2.3.2 Endplate Function

The endplate has three functions in relation to the disc. It plays a role in the mechanics of the motion segment, the anchoring of the annulus and the nutritional supply to the IVD. These three functions will now be discussed.

Mechanics

The structure of the endplate and its interactions with the disc play an important role in the mechanics of the functional spinal unit and thus spine. All aspects of the spinal unit contribute to the deformation and recovery during loading and unloading cycles of

every day events such as standing (~ 1000 N) or light manual work (~ 1500-2000 N).[80] Loading can occur in compression, flexion, extension and torsion (Fig. 2.6). Investigation into the failure mechanisms of the motion segment under tension has been clearly related to the endplate. Rodrigues et al., showed through scanning electron microscopy that the main mechanisms of failure under tension at the endplate exist either along the tidemark (rupture at point of bundle insertion into calcified cartilage) or cement line (rupture at boundary of underlying bone).[81] A paper published later the same year by Balkovek et al., was able to show similar findings, clearly displaying the failure of motion segments at the cartilage and bone interface.[61] This highlights the interface between cartilage and bone as a weakness within the motion segment.[30,82] Although the spine experiences a wide range of different loads including tension and shear, it is likely to experience compression in everyday life. Segment response to compressive loading is complex due to the combination of material properties and complex structure of the segment.[83,84] When the disc is compressed, the annulus bulges outwards[85,86] to contain the essentially incompressible nucleus[85] and the endplate bulges into the vertebral body.[86,87] Uniaxial loading of the motion segment can result in biaxial loading of the endplate, causing higher strain which leads to an increased risk of fracture, a major clinical problem.[27]

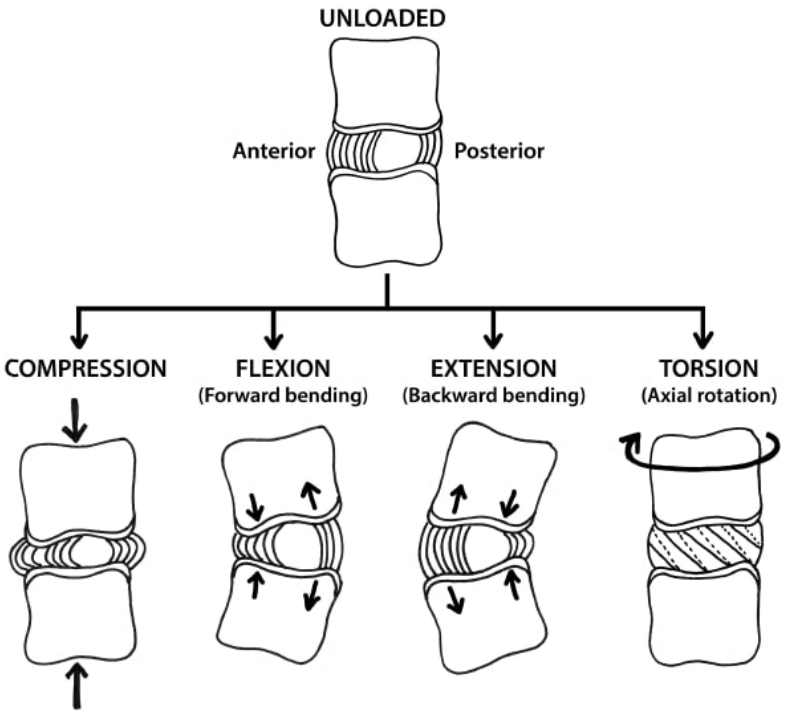

Figure 2.6: *Image taken from Rodrigues 2015[34] illustrating the various models of loading.*

The role of the endplate within compression loading has been widely discussed, but due to the difficulty of direct measurement a range of methods have been used and this complicates the discussion. Some experiments have utilised metal indenters[88,89]) or pressure films below the endplate,[90] however, these methods require dissection of the specimen which may create damage and may not address the interaction of the endplate with the surrounding structures.

Disc Anchoring

As seen above, the disc undergoes a range of loading patterns (Fig. 2.6) which the fibres of the annulus have to withstand. The anchorage of these fibres has been suggested as a weakness in the motion segment. The IVD attaches to the endplate (rather than vertebral bodies) through the lamellae of the inner annulus.[91,92] There is some disagreement in the literature over how far these fibres extend into the endplate structure. Some have observed that annular fibres penetrate directly into the bony endplate,[36,92] whereas others have evidenced that the fibres only extend to the intermediate layer of mineralised cartilage.[93] More recently Rodrigues et al., has suggested using light microscopy and an ovine model that fibres penetrate through the full depth of the cartilaginous endplate, though do not extend far into the bone below.[94] Paietta et al., agreed with this conclusion through the use of second harmonic generation (SHG) and quantitative backscattered scanning electron microscopy (qBSE) on human cadaveric specimens.[66] Although these findings seemed conclusive, later work by Rodrigues et al., again in sheep, showed evidence of bone attachment to the fibres in fibre pull out.[81] This was apparent even after a period of decalcification, suggesting a deeper connection than first assumed, however these 'deeper connections' were not visible under scanning electron microscopy in their study.[81] This deeper connection explains the existence of bone fragments on annular bundles, which have been seen on herniated discs removed during surgery.[63]

It has been suggested that a lack of connection could leave the discs vulnerable, however, Rodrigues et al. further demonstrated what they call 'sub-bundles' or 'leaves'.[94] They proposed that this would increase the anchorage strength of the disc by increasing the area of interface between a bundle and the matrix, which would in turn increase the maximum tensile force required for pullout.[94] Most recently a paper from the same lab as Rodrigues et al., suggested that the anchoring of the disc is aided by the integration of the disc fibres into fibrils that form the osteon network of the bone shown in Fig. 2.7.[95]

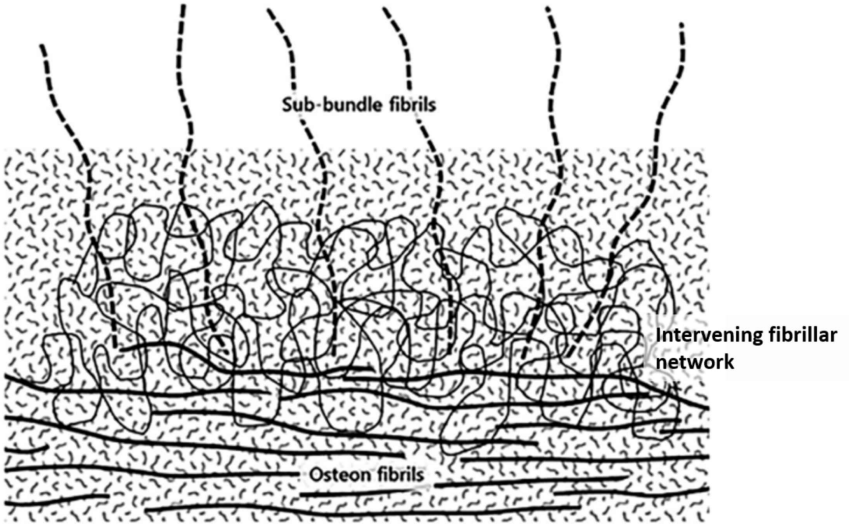

Figure 2.7: *Image taken from Sapiee et al.,*[95] *illustrating suggesting an anchoring mechanisms of disc fibres with osteon fibrils.*

Nutrition

Due to its sparse vascularisation, the diffusion of small solutes through the endplate and the movement of water are key factors in disc nutrition. Hydration varies with loading, if the stress exceeds the osmotic swelling pressure, fluid is expelled.[96] Following this, unloading leads to fluid absorption, returning the IVD to a steady state of hydration explaining the cyclic nature of disc height loss and regain seen diurnally.[96,97] Additionally disc hydration plays a role in redistribution of compressive loads of the spine. Studies have also shown that hydrated discs have a lower stiffness when compared to dehydrated discs.[96,98]

Non-mineralised cartilage has been shown to have a lower hydraulic permeability than the bony endplate,[99] suggesting that it has a role in restricting water transportation through the endplate, which may also help to maintain nucleus fluid pressure. Bony endplate porosity influences both its transport and mechanical role. It has been shown that BEP porosity is highest in the centre, corresponding to the location of the disc nucleus.[100] However, this results in the central region being most vulnerable to fracture when the spine is compressively loaded, particularly with impact. Experimentally, it has been shown that significant predictors of BEP porosity have been shown as BEP thickness, adjacent nucleus pressure and compressive stress of anterior annulus.[100]

Another indicator of the endplates transport role, is the location of marrow contact channels from the underlying bone. Ayotte et al., demonstrated through the use of

fluorescent dye, that during flow in to the IVD, the dye follows the path of the marrow channels into the cartilage within mature sheep endplates.[78] This supports earlier work which suggested that the interaction of these channels which the authors called the 'medullar cavity', with the cartilage endplate facilitated diffusion, and that in calcified degenerative endplates where this interaction was blocked, dye could not penetrate into the disc.[101] Van der Werf later confirmed this through perfusion blocking, using a foil that covers 30% of the disc resulted in a 50% decrease in average perfusion, displaying a weak, but significant relationship between perfused vascular buds and N_2O diffused into the disc ($R_2 = 0.52$, $P = 0.008$).[102]

The movement of small solutes into the disc has been shown to be primarily through diffusion, with the amount of neutrally charged solutes (e.g. glucose) being higher than that of negatively charged solutes (e.g. sulphate ion).[103] Additionally, the molecular weight of solutes effects their transport as shown by the diffusion of fluorescently tagged dextran in bovine tail discs.[104] Following a nonlinear relationship, diffusion coefficients decreased with molecular weight. Diffusion coefficients were also shown to be higher in the nucleus than the annulus, due predominantly to the higher water content in the nucleus which aids diffusion.[104] The permeability of the endplate to solutes is imperative as it has been demonstrated through finite element analysis that when the exchange area of the cartilaginous endplate drops below 40 %, a consequent fall in nutrient concentration will occur. This in turn will initiate cell death, which increases exponentially as exchange area decreases.[105] There is a small amount of diffusion which occurs through the outer annulus, however, experiments in rabbits[106] and dogs[103,107] suggest that the effects of this route do not reach the critical region of the nucleus centre, and this region relies almost completely on the endplate route of transport.[103,106,107]

2.4 Vasculature

The IVD is widely recognised as an one of the largest avascular tissues in the human body.[108,109] As with other avascular tissues, the nutrient concentration of the matrix decreases in relation to the distance from capillaries.[110] For cells to remain viable, a critical level of 0.2 mM glucose and a pH 6.7 must be maintained. As discussed, the primary nutrient transport route of the IVD is that of the vertebral endplate. There is a small amount of diffusion through the outer annulus,[28] however, the inner annulus fibrosus and nucleus pulposus rely almost entirely on nutritional transport through the endplate.[106,107] Additionally, the endplate is key in the removal of metabolic waste

and degraded matrix molecules.[64] This is important as waste products such as lactic acid can alter the cellular environment, by increasing the acidity and decreasing the metabolic activity.[25]

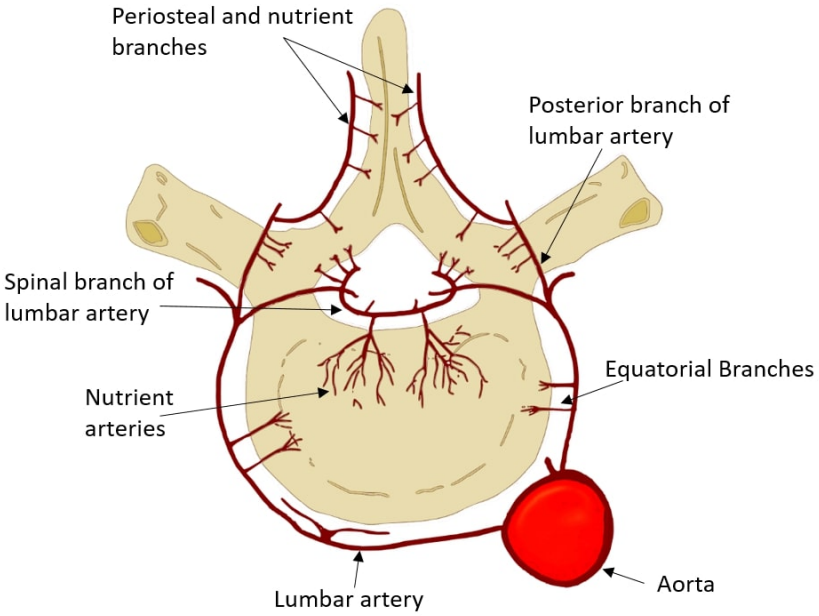

Figure 2.8: *Illustration of the vasculature of the vertebral body. Not to scale.*

The abdominal aorta and the inferior vena cava are the main artery and vein that run parallel to the lumbar spine. The aorta branches into the lumbar artery which inserts into the vertebral body. Equatorial branches and nutritional arteries split off, into the vertebral bone (Fig. 2.8). The capillary network has been suggested to extend all the way to the endplate (though the specific region of endplate is unclear).[111–116]

A venous return/drainage has been suggested by Crock et al., which includes a post-capillary venous network 'on' the vertebral endplate (region specificity is lacking).[116] Additionally, they illustrated large horizontal vessels within the trabecular bone. Detail of the capillary bed within the endplate is severely lacking from the literature. Papers have suggested the occurrence of buds (as shown in Fig. 2.9) or loops, however, these studies are inconclusive.[111,112,115]

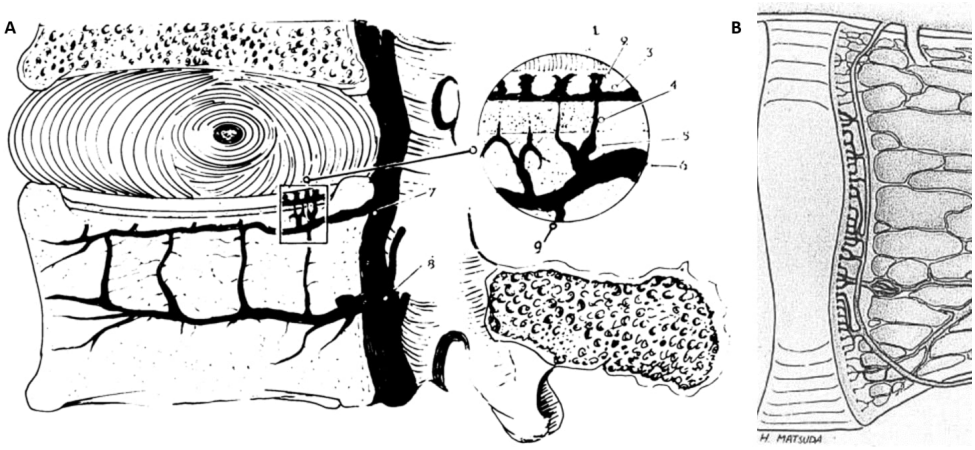

Figure 2.9: *A) Image taken from Crock et al., illustrating the 'post-capillary venous network'.*[116] *B) Image taken from Crock et al., illustrating 'capillary buds' at the vertebral endplate.*[115]

2.5 The Lymph Network

The lymphatic system is a complex maze of capillaries, ducts and nodes which together maintain tissue fluid homeostasis, uptake and transport of lipids as well as immunosurveillance.[117] The system contains channels with blind-ended capillaries which convey interstitial fluid and cellular debris. This system is separate from the surrounding blood vessels.[118] The thoracic duct of the lymphatic system originates a large vessel at level of the second lumbar vertebrae (the Cisterna chyli seen in Fig. 2.10), and ascends into the chest.[119]

Given the proximity of such an important lymphatic to the spine, it is surprising that little research has been completed on the role of the lymphatic system in relation to the intervertebral disc. Early work made use of histological staining to suggest the occurrence of lymph vessels.[120] The study used human specimens of a range of ages (27 week old fetus to 90 years), and showed that lymph vessels were present in the annulus up till the age of 20 years (Fig. 2.11). They were reported as present in the tissue surrounding the annulus in all specimens, although the study only looked at the disc itself, and not the adjacent endplates.[120] A later study by Kashima et al., disagreed with the findings of Rudert et al., despite using a similar method.[121] Positively, they did include the vertebral bodies (and therefore endplates) in their investigation, and concluded that no lymphatics were present in normal spinal vertebrae nor the intervertebral disc of children or adults.[121] They did suggest however, that lymphatics are present in pathological lesions of the spine.

It should be noted that Hsu et al., have discussed how traditional anatomical research methods, e.g. continuous dissection as used in the previous two studies, are difficult due to the complex maze of vessels and ducts.[122] Thus, the role of the lymphatic system in relation to the intervertebral disc is under-researched and inconclusive.

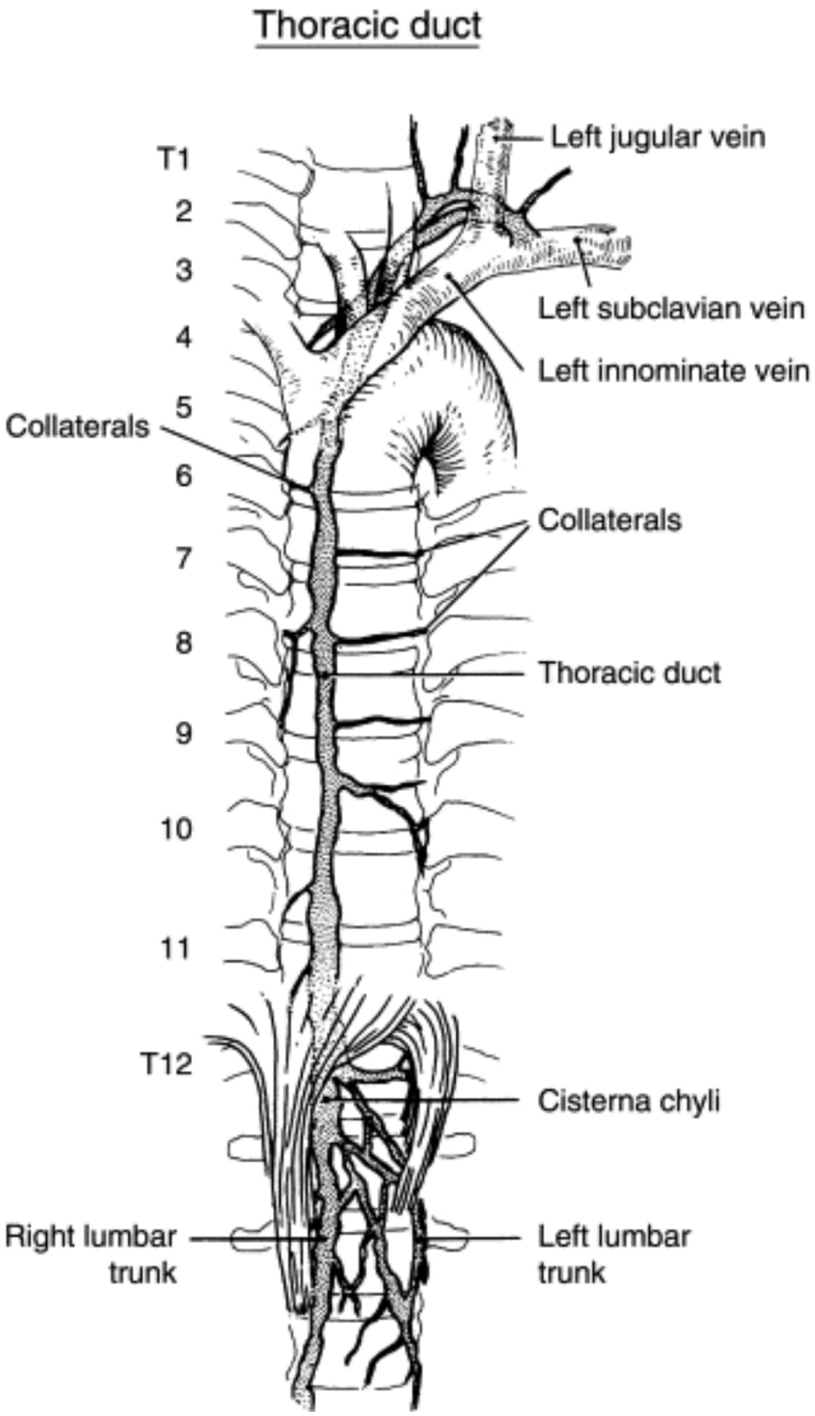

Figure 2.10: *Taken from Pediatric Surgery (Seventh Edition)[119] schematic illustrates the proximity of the Cisterna chyli and the thoracic duct of the lymphatic system to the intervertebral disc and vertebral bodies.*

Figure 2.11: *Taken from Rudert and Tillmann 1993.[120] Lymph vessels marked by dark lead sulphate precipitates (arrows) in a horizontal section of an annulus fibrosus of a 1.5 year old.*

2.6 Aging

With age, the bony endplate has been shown to become more porous and increase in overall permeability.[99] This is supported with other literature from cadavers showing that the small pores in the endplate decreases with age and disc degeneration, as the number of larger holes increases.[123] There is some discussion around how the thickness changes with age, some papers suggest a decrease in endplate thickness within human endplates with age,[99,124] however, Wang et al., suggests that there is no association with endplate BMD nor thickness and age.[125] Rather they showed with cadaveric spines that thickness changes are seen with increased degeneration.[125] The cartilage endplate also has been shown to thin with age,[124] which may reduce its capacity as a 'shock-absorber'.[28] Additionally, porosity and permeability increase steadily with age, in both the cartilage layers[99] which will have an effect on the role of the endplate in the nutrition of the IVD.

2.7 Pathologies

Because the bony endplate region is rich in blood vessels and nerve endings[115,126] the endplate has been implicated in the cause of lower back pain, but research is only recently focusing on this area. Schmorl's nodes (the penetration of disc tissue through the endplate to the vertebral marrow) are the most common of endplate pathologies.

Although first recognised over 150 years ago, the origin of the nodes is still unclear.[127] To complicate the situation, many studies have generalised any visible lesions on the endplate as Schmorl's nodes which may confound a variety of pathologies.

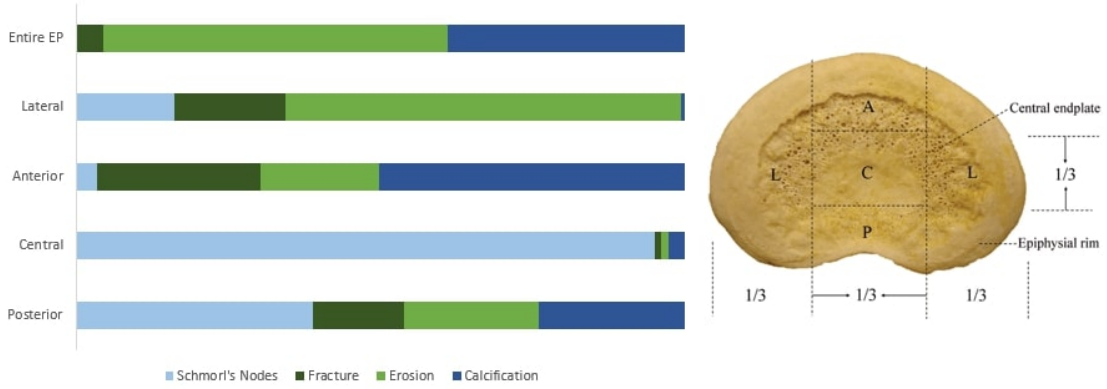

Figure 2.12: *Lesion prevalence (%) grouped by etiology and site. Image on the right indicates the regions of the endplate. Schematic produced with data from Wang, Videman and Battié*[128]

Wang, Videman and Battié began addressing this issue through identifying endplate lesions by spinal level,[128] endplate location and grouped under four etiologies; Schmorl's node, fracture, erosion and calcification.[129–131] Vertebral level (L1-S1), showed no statistical significance in the prevalence of lesions in general ($p = 0.78$), however, different lesion types showed specific distribution patterns. For example, fractures were fairly consistent through the length of the spine whereas erosion seemed to increase towards the caudal end. How these relate to the structural variation in the endplate along the spine is unknown. Similarly, the paper showed the distribution of lesions over the endplate regions (Fig. 2.12). Very little is known about the varying causes of these lesion types, the relation to endplate structure, nor how they relate to LBP and/or disc failure. This suggests the need to investigate variation in endplate structure and function along the spine.

Modic changes are also referenced heavily in the literature in relation to pathologies of endplates and disc degeneration.[75,132–135] One definition describes Modic changes as 'vertebral endplate signal changes' measured with magnetic resonance imaging (MRI).[75] However, MRI scans have shown that Modic changes can affect as much as 75% of the vertebral body.[134] Additionally, considering the reported size of endplates, degenerative changes would unlikely be resolved with such an MRI scan. This suggests that Modic changes are not endplate specific issues, and should not be described as such. This disparity in understanding of the basic structure of the endplate between the clinical and

basic science literature needs to be addressed, and a consensus on the structure and clinical relevance of the endplate attained.

3 Global Methods

This chapter describes the materials and methods that are relevant throughout the thesis. It is split into two main sections of imaging and sample preparation. Firstly, the imaging set up is described and then the two contrast mechanisms, two photon fluorescence (TPF) and second harmonic generation (SHG), are explained. Secondly, animal models of the endplate are explored in relation to the disc and bone, followed by a description of sample acquisition and preparation. Lastly procurement of human samples from surgical patients and sample preparation is described.

3.1 Imaging

The main imaging method utilised in this study to characterise the endplate was multiphoton microscopy. This method offers two main advantages, the first being submicron resolution even in three-dimensional (3D) data sets. Secondly, the reliance on endogenous contrast allows for detailed structural data from intact and unstained samples. Imaging methods such as transmitted light (differential interface contrast or phase contrast) or electron microscopy (scanning (SEM) or transmission (TEM)) require complex sample preparation including fixing and dehydrating, metal surface coating and the production of thin sections. Not only can thin sections limit the imaging for 3D structures in the tissue, but the preparation can produce artifacts when imaged.

3.1.1 Imaging Set-Up

The imaging set up is founded upon a Olympus FluoView microscope which has been converted for multiphoton microscopy. This microscope allows both SHG and TPF imaging in the forwards and back-scattered directions. The Olympus FluoView 300 was utilised as the scanning system with an Olympus IX71 inverted microscope. Scanning and image acquisition were controlled via the FluoView version 5 software. This system has been used in a number of studies previously.[51,136,137]

The laser system is supplied by Coherent and consists of a Mira 900 Ti:sapphire laser pumped by a Verdi (V10) laser (532 nm). The maximum power output of the Mira is 1.5 W with its wavelength tuneable between 690 nm and 990 nm. It has a repetition rate of 76 MHz and pulse width of 200 fs, this is used for both SHG and TPF imaging. The SHG signal was isolated by band pass filters (CG-BG-39-1.00-1 and F10-400-5-QBL, CVI) and focused onto a photomultiplier tube (R3896, Hamamatsu Japan). TPF was also measured in the epi-direction via the same light path with the bandpass filters exchanged to CG-BG-39-1.00-1 and F70-500-3-PFU, CVI.

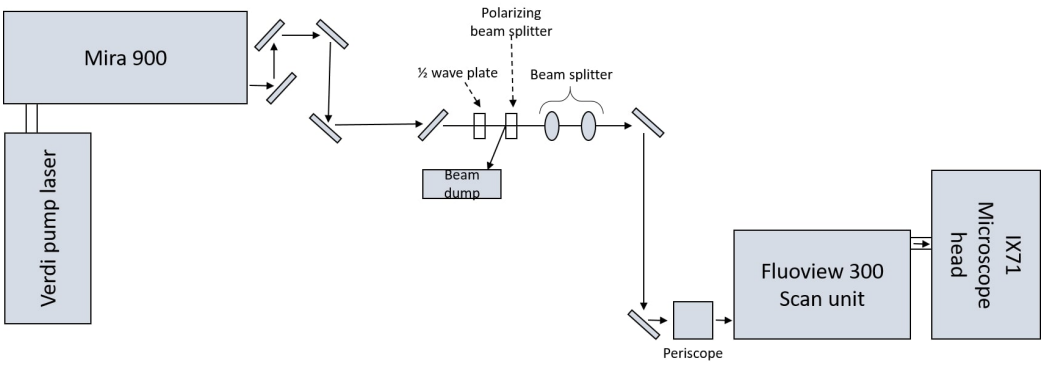

Figure 3.1: *A schematic diagram of the optical table layout.*

3.1.2 Non-Linear Microscopy Theory

Two-Photon Fluorescence

Two Photon Fluorescence (TPF) comprises the simultaneous absorption of two photons ('simultaneous' in this regard is a sole quantum event within the period of ~0.1 fs). The combined photon energy excites an electron to a higher state, the excited electron returns back to its ground state via thermal relaxation, which is followed by the emission of an individual fluorescent photon.[138,139] As illustrated in Fig. 3.2 the exciting photons are usually in the near infra-red and have approximately 50 % of the energy required to raise the electron into its excited electronic state. Because of the nonlinear excitation, the fluorescence is confined to the focal point of the laser beam, and fluorescence power decays as $\frac{1}{z^2}$, where z is the axial distance away from the focus. The benefit of this is lower out of plane photo-bleaching. One of the major advantages of TPF, especially in terms of biological application is the ability to image relatively thick samples due to the reduction in absorption and scattering.[140]

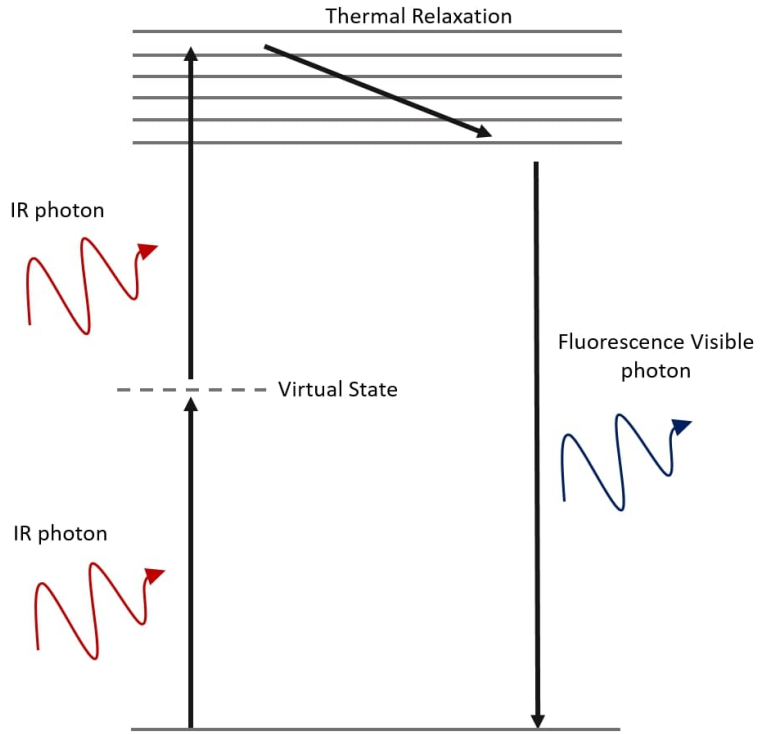

Figure 3.2: *Energy level diagram for TPF where ω is proportional to the photon energy.*

When assessing TPF images formed from biological tissues, it is important to understand which molecules are contributing to the TPF signal as intensity of the signal is dictated by the abundance of endogenous fluorophores. A high number of molecules have been reported as endogenous two-photon fluorophores for example nicotinamide adenine dinucleotide phosphate (NADPH).[141] The endogenous fluorophores expected within the extra cellular matrix are elastin and collagen, with excitation wavelengths of 700-740 and >750 nm respectively. However, in many tissue types, TPF sources are still unidentified. For example, Mansfield et al., noted TPF in mineralised tissues, however, when pure hydroxylapatite, a large component of mineralised tissue, was assessed for a TPF signal no fluorescence was detected.[142]

Second Harmonic Generation

Second Harmonic Generation (SHG), also known as frequency doubling, is a coherent elastic scattering process. It involves two excitation photons being simultaneously absorbed by a medium that is optically non-linear to produce a SHG photon that has a wavelength precisely half of the excitation wavelength (Fig. 3.3).

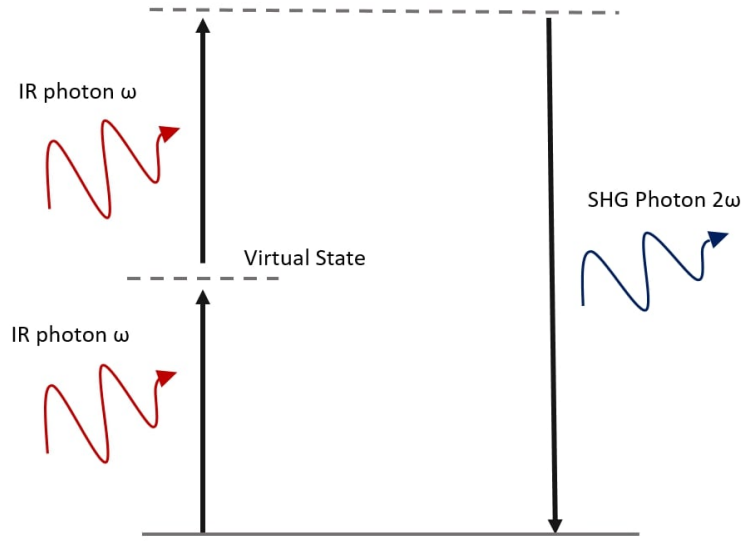

Figure 3.3: *Energy level diagram for SHG where ω is proportional to the photon energy.*

Because SHG is a symmetry breaking process it is emitted only by non-symmetric structures. Within a biological context there are multiple structures which are known as sources of SHG (Table. 3.1). Collagen, the most abundant structural protein in the body, is one of the largest contributors to the SHG signal within this project.[143] Some research has investigated whether the intensity of the SHG signal, determines the type of collagen (type I, II or III), however, the results indicated that the intensity was more reliant on the the degree of order and alignment.[144]

Table 3.1: *Biological sources of SHG reported in the literature.*

Source of SHG	Location
Fibrillar collagen[145]	Extracellular matrix
Tubulin[146]	Cytoskeleton
Microtubules[147]	Cytoskeleton
Actin/Myosin[148,149]	Muscle Fibres

The intensity of the second harmonic signal produced from a collagen sample is dependent on the orientation and polarisation state of the laser excitation light with respect to the fibre axis.[150] The SHG intensity will be highest when the collagen fibre and imaging plane are aligned, and lowest when they are perpendicular. This is exploited in polarisation SHG to reveal detail of intrafibrillar organisation.[143,151,152]

Paietta et al., seems to be the only paper using multiphoton microscopy to look at vertebral endplates, however, they only applied SHG to the imaging of the soft, cartilage tissue.[66] Mansfield and Winlove applied the combined techniques to investigate fibre

organisation at the tidemark and cement line in equine metacarpophalangeal joint.[136] By combining the techniques, a greater visualisation of these transitional tissues was obtainable than when utilised on their own. The application of multiphoton microscopy to the endplate will allow a greater understanding of the structure, the integration of multiple tissue types and hopefully this will lead to a better understanding of failure mechanisms.

3.2 Samples

3.2.1 Animal Models

The feasibility of utilising healthy human tissue for experimentation is limited, not only by strict ethical guidelines but also the availability of sufficient and appropriate tissue. Animal models have been used widely in spinal investigations.[29] No one animal model is classified as the 'gold standard' as varying differences between species and breed make certain models more appropriate in certain situations.[153] Models are invariably assessed by different criteria, for example in regards to the intervertebral disc, parameters such as water or proteoglycan content are important, whereas in the vertebral body, bone density is a major concern. In regards to the vertebral endplate, due to its relationship and proximity to both the disc and bone, the model has to be a compromise of attributes. Another important consideration is whether the model is being used as a 'healthy' representation, or that of degeneration. Degeneration models can fall into two categories of 'induced' or 'spontaneous'[153] which will dictate the animal model used. Further we can subdivide again into structural or mechanical groups which will play a part in the decision on the model.

Animal Models of the Intervertebral Disc

In selecting an animal model, a number of factors have been discussed including, disc size, loading, water and proteoglycan content as well as notochordal cell depletion, which occurs in human discs, though not all mammals.[154] Table 3.4 is an overview of the discussed disc attributes across both species and age.

i. Disc Size

Animal models in the disc literature range from small rodents, through to large mammals. Animals as small as mice, rats and rabbits are advantageous as they provide possibilities for genetic knockout/mutation, technological investigations and surgical interventions such as tail amputations.[154] However, one of the acknowledged contributors to disc degeneration, is the reliance of this avascular tissue on diffusion for its nutrition supply, which is proportional to the size of discs.[155] This questions the clinical relevance of small animal models, and begs investigation of disc height, width and size of the nucleus pulposus. In a paper discussing this O'Connel et al.,[155] compared eight different animals to the human disc by normalising to the disc lateral width. This allowed for comparison of the whole disc and nucleus height, anterior-posterior (AP) width and area. The results indicated surprisingly that the mouse and rat lumbar, and mouse tail discs were the closest representation of the human lumbar intervertebral disc geometry.[155] However, rates of diffusion are dependent upon absolute dimension, as well as cellular density which arguably plays a more important role than disc size alone[107] as cellular density will effect the nutritional demand.[156]

ii. Disc Loading/Mechanics

Spines endure different loading patterns in bipeds compared to quadrupeds. Some bipedal models have been used in the past, such as primates,[157] or even genetically engineered bipedal mice and rats,[158] however, these models raise complex ethical issues. The most commonly utilised models within the research are that of quadrupeds such as dogs, cows and sheep. Additionally, several models utilise the tail vertebrae of certain animals as an accessible and cheap alternative to whole spines. Again, compared to bipedal, tail discs will undergo different loading patterns. However, it has been noted that a model should not be disregarded solely on the bases of quadruped or tail as a high amount of disc loading comes from the associated muscles and ligaments.[159] This suggests that the loading experienced by IVD's in large quadruped animal spines and tails could be comparable in loading to that experienced in the upright stance of humans.[29]

iii. Notochordal Cell Depletion

During the development of the spine, intervertebral discs are formed through the accumulation of the mesenchyme around the notochord and subsequent segmentation.[29] In human spines, notochordal cells are present in utero, however, after birth they rapidly reduce with none remaining in the nucleus by early adulthood.[29] The source of nucleus cells in the mature disc is unclear and suggestions include the inner annulus or even the

cartilage endplates.[160,161] This is contrary to that of the a number of species whose notochordal cells remain present in the nucleus throughout adulthood. Notochordal cell persistence is an important factor in the suitability of a model, as they have a great effect on the viability of the disc.[154] The literature has attested to their role in proteoglycan metabolism,[162,163] hyaluronan production,[164] and they may play a part in progenitor cell function.[29] A few species, such as sheep, goats[165] and some breed of dogs (known as chondrodystrophoid (CD) dogs)[166] are among those who lose their notochordal cells from the nucleus post birth, and are thus predisposed to disc degeneration in later life. It is supposed that some species can have an induced reduction in their notochordal cells through intervention,[167,168] and their studies have highlighted apoptotic processes as key in the reduction of notochordal cells.[169]

iv. Water and Proteoglycan Content of the IVD

As with several other factors, not only species, but disc level and age of animal come into play when addressing water and proteoglycan content. Most species display higher levels of both water and proteoglycans in the nucleus than the annulus. However, when it comes to aging, human discs display a complex pattern of increasing proteoglycan content in the nucleus until age ~ 25-40 yrs, and then a decrease.[170] Bovine tail displays a similar increase in proteoglycan content, but do not achieve as great a level as humans, with a 24-48 month old caudal bovine discs showing similar proteoglycan content to that of 40-60 yr old human discs.[170,171] Similarly, a 4 year old ovine disc shows comparable proteoglycan content to that of a 60-80 yr old human disc.[170,172] Water content of human disc also declines with age, a drop from ~ 77 ± 4 % to 69 ± 2 % and 89 ± 2 % to 75 ± 2 % in the annulus and nucleus respectively[170] (Table. 3.2). This makes human adult disc comparison with animal models difficult as animals such as the rabbit (at 13 weeks) have a lower water content of the annulus (63.6 v 69 % in humans), and higher in the nucleus (81.6 v 75 %). The bovine tail appears to be the more comparable where we see a decrease in the annulus water content from 73 ± 7 % to 67 ± 2 % between 8 - 20 months and 20 - 48 months, not only following the same pattern as seen in humans but reflecting similar values.

Table 3.2: *Reported variations in intervertebral disc physiology between species and with age.*

Species	Posture	Disc Height (mm)	Age	Region	Notochordal Presence	Water Content (%)	Proteoglycan Content (mg/g dry weight)
Human (lumbar)	Bipedal	11.3 ± 0.3	0-2 yr	Anterior AF	Present [38, 173]	77 ± 4 [170]	117 ± 57
				Posterior AF		78 ± 5 [170]	149 ± 66 [170]
				NP		89 ± 2 [170]	458 ± 130 [170]
			2 - 5 yr	Anterior AF	Present [38, 173]	70 ± 3 [170]	90 ± 31 [170]
				Posterior AF		74 ± 3 [170]	128 ± 24 [170]
				NP		87 ± 1 [170]	659 ± 85 [170]
			5 - 15 yr	Anterior AF	Present to ~ 10 years [38, 173]	69 ± 3 [170]	82 ± 19 [170]
				Posterior AF		72 ± 2 [170]	126 ± 26 [170]
				NP		86 ± 1 [170]	632 ± 119 [170]
		11.3 ± 0.3 [155]	25 - 40 yr	Anterior AF	Absent [38, 173]	66 ± 3 [170]	103 ± 33 [170]
				Posterior AF		69 ± 2 [170]	174 ± 34 [170]
				NP		82 ± 2 [170]	695 ± 221 [170]
			40 - 60 yr	Anterior AF	Absent [38, 173]	68 ± 3 [170]	121 ± 36 [170]
				Posterior AF		72 ± 2 [170]	164 ± 67 [170]
				NP		77 ± 3[170]	356 ± 140 [170]
			60 - 80 yr	Anterior AF	Absent [38, 173]	69 ± 2[170]	84 ± 48 [170]
				Posterior AF		73 ± 2 [170]	100 ± 49 [170]
				NP		75 ± 2 [170]	188 ± 117 [170]
Rabbit (mid-thoracic and lumbar)	Quadruped	1.42 ± 0.39 [155]	4 wk	AF	Present [173, 174]	NA	100 [175]
				NP		NA	300 [175]
			13 wk	AF	Present [173, 174]	63.6 ± 2 [176]	NA
				NP		81.6 ± 2 [176]	NA
Pig (lumbar)	Quadruped		12-18 mo	AF	Present	64 ± 3 [177]	NA

Table continued on next page. AF = Annulus Fibrosis, NP = Nuceus Pulposis, NA= Not available

Species	Posture	Disc Height (mm)	Age	Region	Notochordal Presence	Water Content (%)	Proteoglycan Content (mg/g dry weight)
Pig (tail)	Tail		6 mo	NP	Present	85 ± 5 [177]	NA
				AF		70 ± 5 [178]	NA
Greyhound (lumbar: non-chondrodystrophoid)	Quadruped		0-10 mo	NP		90 [178]	NA
				AF		NA	40 [175, 179]
				NP		NA	119 [175, 179]
			11 - 20 mo	AF		NA	40 [175, 179]
				NP		NA	97 [175, 179]
			21 - 60 mo	AF	Present ~ 5 years [71, 173, 180]	NA	40 [175, 179]
				NP		NA	124 [175, 179]
			90 - 100 mo	AF		NA	40 [175, 179]
				NP		NA	97 [175, 179]
			>100 mo	AF		NA	40 [175, 179]
				NP		NA	54[175, 179]
Beagle (lumbar: chondrodystrophoid)	Quadruped		0-10 mo	AF	Present 6 months [154, 173, 180]	NA	30 [175, 179]
				NP		NA	78 [175, 179]
			11-20 mo	AF	Absent [154, 173, 180]	NA	43 [175, 179]
				NP		NA	94 [175, 179]
			21 - 30 mo	AF	Absent [154, 173, 180]	NA	63 [175, 179]
				NP		NA	94 [175, 179]
			> 31 mo	AF	Absent [154, 173, 180]	NA	63 [175, 179]
				NP		NA	74 [175, 179]
Bovine (tail)	Tail	6.90 ± 0.35 [155]	NA	AF		NA	78 [175, 179]
				NP		NA	341 [175, 179]
			8 - 20 mo	AF	Present 12 months [173, 181]	73 ± 7	88 ± 47 [171]
				NP		77 ± 6	243 ± 171 [171]
			24 - 48 mo	AF	Absent	67 ± 2	98 ± 37 [171]

Table continued on next page. AF = Annulus Fibrosis, NP = Nuceus Pulposis, NA= Not available

Species	Posture	Disc Height (mm)	Age	Region	Notochordal Presence	Water Content (%)	Proteoglycan Content (mg/g dry weight)
Sheep (lumbar)	Quadruped	3.93 ± 0.07 [155]		NP		77 ± 2	166 ± 50 [171]
			9 mo	NP	Absent	86 ±4	321 ± 21 [182]
			9 - 12 mo	Outer AF	Absent	74 ± 6	NA
			4 yr	AF	Absent	NA	65.6 ± 3 [172]
				NP		NA	138 ± 9 [172]

AF = Annulus Fibrosis, NP = Nuceus Pulposis, NA= Not available

Animal Models of the Vertebral Body

Like the intervertebral disc, the vertebral body has a number of different aspects that can be similar or dissimilar between different species. The bodies are made up of trabecular bone, surrounded by an outer cortical shell (except under the disc/endplate). When assessing model suitability, it is important to consider the physical properties, such as those presented in Table 3.3, however, we must also consider the development of the spine and less well documented properties such as the curvature. As with the disc, study purpose is important in assessing the appropriateness of each measure in relation to the project. For example, studies on bone plugs integration will have different requirements to a fracture risk study.

Comparison of animal models is presented first in regards to the composition (mineral density), fracture stress (a crude indicator of mechanical properties) and geometry (height). Secondly, the mechanisms of growth and ossification are compared and finally, the shape of the surface zone, and thickness of the endplate.

i. Height, BMD and Fracture Stress

Table 3.3 summarises three of the main parameters to be considered in research using animal models for the human vertebral bone. Vertebral body height helps to describe the size of vertebrae as well as its shape when documented across the width of the bone. In the central region of mature adult spines, vertebrae measure 24.5 ± 0.6 mm.[183] Pig vertebrae are similar in size (23.4 ± 0.5 mm[183]) whereas cow and sheep vertebrae are larger.[184] These are important to consider as we know cervical human vertebrae are smaller than those in the lumbar regions, which suggests why porcine spines is a commonly used model for the cervical spine in studies.[185] Human bone mineral density is significantly lower than seen in the quadruped animals, and this is also reflected in the fracture stress, which poses a particular problem if the model is aiming to mimic aged or pathogenic bone. For example osteoporosis sees an increase of bone fragility which is reflected in a decreased bone mineral density (BMD) and bone mechanical properties.[186]

Table 3.3: *Reported variations in vertebral body physiology between species and with ages.*

Species	Maturity	Region	Vertebral Body height (mm)	Bone Mineral Density (g/cm^3)	Fracture Stress (mean (range) N/mm^2)
Human (Lumbar)	Adult			0.172 ± 0.005 [187]	1.21 (0.08 - 2.40) [188]
	Mature Adult	Anterior	27.8 ± 1.5 [183]	0.10 ± 0.01 [187]	
		Central	24.8 ± 0.6 [183]		
		Posterior	28.2 ± 2.0 [183]		
Bovine (Spine)	Immature	Whole Body		3.40 ± 0.164 [189]	5.67 (1.98 - 9.28) [188]
Bovine (Tail)	Adult	A/P Average	38.4 ± 3.05 [184]		
Porcine (Lumbar)	Immature	Anterior	24.3 ± 0.5 [183]		2.4 (1.70 - 3.76) [188]
		Central	23.4 ± 0.5 [183]		
		Posterior	24.2 ± 0.6 [183]		
	Adult	A/P Average	37.1 ± 5.2 [184]	1.00 ± 0.044 [189]	
Ovine (Lumbar)	Adult	A/P Average	36.5 ± 1.6 [184]		13.22 (3.30 - 15.79) [188]
	Mature Adult	Anterior	39.4 ± 2.0 [190]		
Cervidae/Deer (Lumbar)	Adult	Whole Body		1.237 ± 0.275 [191]	
		Ventral	40.5 ± 3.8 [191]		
		Dorsal	43.4 ± 2.0 [191]		

A/P Average = Combined anterior and posterior average, NA= Not available

ii. Growth and Ossification

As previously mentioned, in the majority of mammalian vertebrae, the growth plate is delineated from the vertebral body by cartilage (Fig. 3.4 A). Integration of the human growth plate occurs between ~ 18 - 25 years of age (Fig. 3.4 B),[29–32] however, in many mammals, this epiphysis remains throughout life, effectively within the vertebrae. This highlights a major difference between human and animal models (including sheep and cow), the lack of an apophysis ring (rather than epiphyseal, as it infers that the ring makes no independent contribution to vertebral growth[192]) at the outer rim of the vertebral body (Fig. 2.3). This is significant as it is reported that the outer annulus fibres anchor into this apophysis and therefor it plays a role in the mechanics and stability of the motion segment as a unit.[192] This does not rule out such animal models, however, care must be taken when applying findings to the human spine.

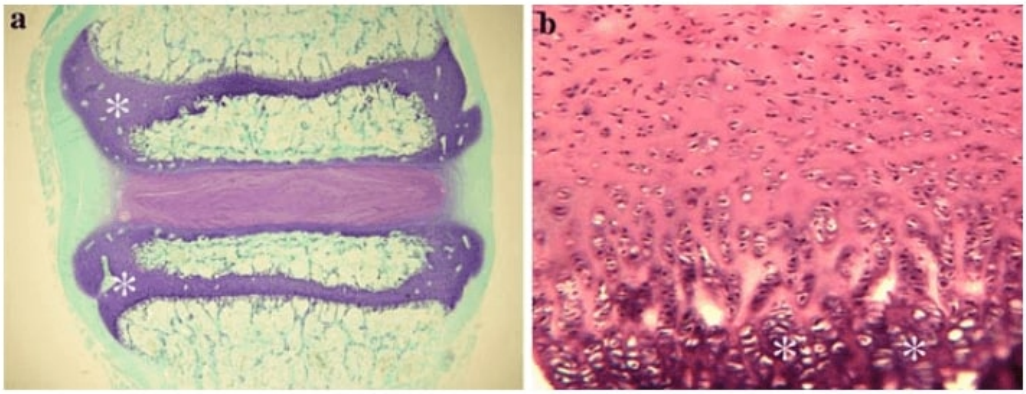

Figure 3.4: *Growth plate locations in sheep and human. A) Growth plates (asterisks) occur within the vertebral bodies of many species, above image is from a sheep. B) Human growth plates, are restricted to the base of the cartilage endplate (CEP), interfacing between the disc and vertebral. Image taken from Alini et al.,*[29]

iii. Curvature/Convexity

The shape of the caudal and cranial regions of the vertebrae influence how the endplate sits, and differences in this have been noted, though not well documented. As is obvious from Fig. 3.4 A, the sheep vertebrae and endplates are relatively flat, though slightly convex centrally. Bovine tail endplate shape varies, but mostly protrudes in a convex manner towards the centre of the disc, whereas the human lumbar vertebra curves inwards after the apophyseal ring, in a concave manner. The cranial human endplates have been reported to have a greater degree of concavity, however, the spinal level is shown to effect this.[128] The complexity of these shape variations suggests that loading mechanisms could be responsible. Though this has not been investigated in the

literature explicitly, it is acknowledged that altered endplate shape will effect the overall loading of the motion segment.

iv. Endplate Size and Thickness

Large quadrupeds have been shown to have a constant endplate diameter throughout the spine, whereas the vertebral endplates in humans gradually increase in anterior-posterior diameter from the cervical to lumbar region.[128,190] However, within the lumbar spine itself a very small amount of variation is seen, with anterior-posterior diameter ranging from 33.8 - 36.2 mm.[128]

Considering the extensive use of animal models within endplate investigations, there is very little information on the thickness. Comparably, the thickness of the human endplate is relatively well documented,[128,193–195] however, the endplate thickness is often calculated from the concavity of vertebral bodies measured by radiography techniques.[195,196] This means that these papers often do not differentiate between the regions of the endplate, except in some cases where the BEP is classified as the 'cortical shell'.[193,194] Overall, the human endplates are suggested to be 1.5 ± 0.8 mm thick in the lumbar spine, though cranial endplates (in relation to the disc) are shown to be ticker.[128,195]

Animal Models: Conclusion

For this study a model that provided a possibility for a range was ages was necessary, however, preliminary investigations in a less appropriate model can be valuable. There is no single animal model that is perfect for the human lumbar endplates. From the reviewed models, the ovine and bovine were selected for this study. The ovine is the preferred model, as it shows similarities with the human in term of biochemical composition, water content and the lack of notochordal cells in maturation. Additionally, it has been reported to have a hypermineralised cartilage region indicative of the mineralised endplate. The bovine tail was selected as an additional model, as the low cost and easy availability would allow for high sample numbers and trial experiments as well as perfusion experiments which are not viable with the sheep model.

3.2.2 Animal Sample Acquisition

Various abattoirs and farms were used to acquire the animal models for this study. Bovine tails were purchased from Gages Farm Abbatoir Newton Abbot, on the day of slaughter. Immature sheep spines came from Darts Farm Topsham, frozen, after having their soft

tissue removed for meat sale. Mature sheep spines proved much harder to come by, not only due to the lower demand for hogget or mutton, but also due to food standard regulations. The Food Standards agency, in a bid to decrease the risk of bovine spongiform encephalopathy (BSE) reaching humans, requires the removal of specified risk material. In sheep vertebral columns are cut through the middle and the spinal cord removed against BSE transmission. This process incurs damage to vital tissue for experimentation. One such spine was acquired from a local mutton farm. This spine was therefore only utilised in methodological development. This meant reliance upon the death of birthing ewes, either acquired post natural death from S. Roberts, Oswestry, or post slaughter from Gages Farm Abbatoir. The spines of natural death had a lot more blood clotting due to them not being butchered right away, additionally they had to be frozen for storage and transport to the lab. The details are shown in Table. 3.4.

Table 3.4: *Animal models, their ages and locations of origins.*

Animal Model	Age (yrs)	Number	Acquired from
Bovine Tail	<1	10	Gages Farm Abattoir
Ovine Lumbar	<1	2	Darts Farm
Ovine Lumbar	~2	1	Gages Farm Abattoir
Ovine Lumbar	4	1	S. Roberts
Ovine Lumbar	7	1	S. Roberts

3.3 Dissection

3.3.1 Bovine Tail

Tails were obtained fresh, on the day of slaughter. The first step was to remove the skin and hair, this was done using a scalpel incision down the length of the tail. The skin was then peeled away by separating it from the connective tissue with a series of slices. Once the skin was removed, the fat, muscle and connective tissues remained. These were also removed with a scalpel and extra care was taken in the region of the disc in order to prevent damage (Fig. 3.5).

Motion segments were then separated from one another by cutting through the vertebral bodies roughly 1 cm from the endplate in the mid-transverse plane with a hack saw, leaving sections containing vertebrae-disc-vertebrae. For most experiments flat cross-sections were required, therefore these motion segments were sliced sagittally with a hack saw (Fig. 3.7).

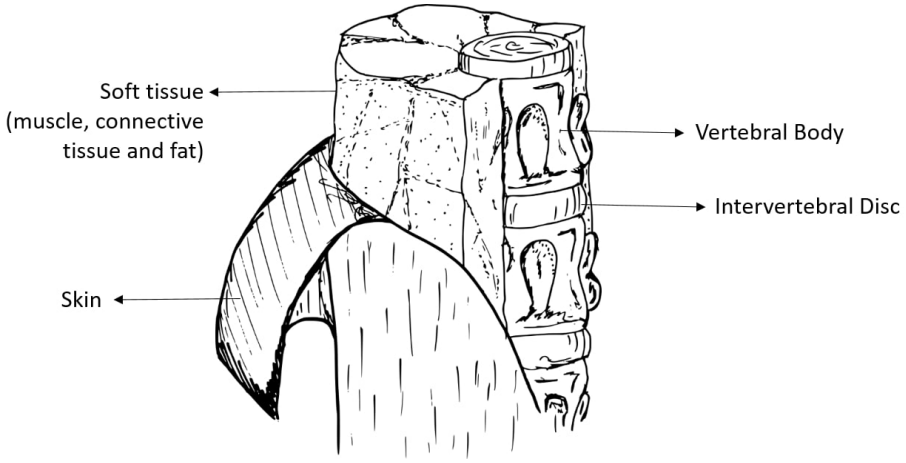

Figure 3.5: *Schematic of a cow tail, showing the initial stages of dissection. Firstly skinning, then soft tissue removal to expose the discs and vertebral bodies.*

3.3.2 Sheep Spine

The sheep spine was obtained frozen, with most of the soft tissue removed. However, in all cases the pelvis and sacrum were still attached and required separation from the spine. Once separated from the pelvis, the spine was cut into motion segments in a similar manner to the bovine tail. One thing to note was that compared to the bovine tail, the sheep vertebrae contained much more blood (see Fig. 3.7).

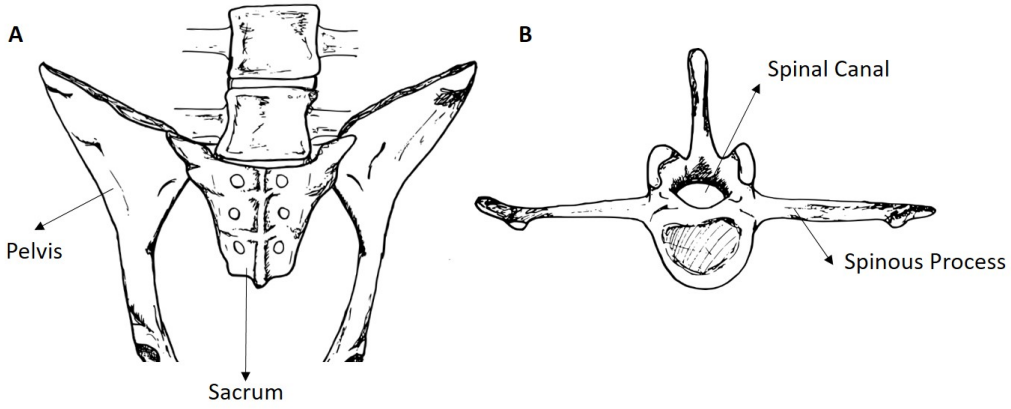

Figure 3.6: *Schematic of A) the Lumbar/sacral junction of the sheep spines received from the butchers. B) Example of a ovine lumbar vertebrae showing the spinal canal and spinous processes.*

3.3.3 Preparation for imaging

Both ovine and bovine motion segments were sectioned sagittally to produce cross-sectional views by using a hack-saw. In order to create a flat surface to enable imaging,

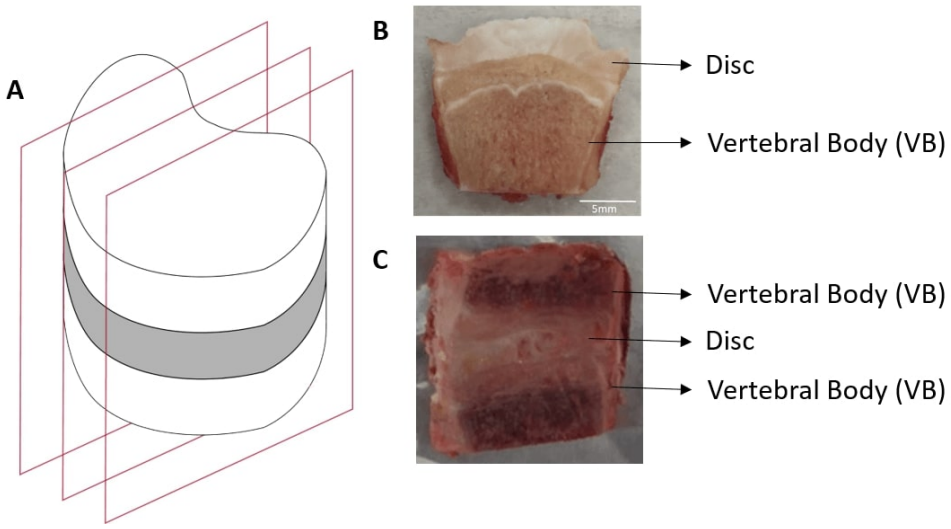

Figure 3.7: *Cross-sectional sample preparation. A) Schematic of sagittal slices through a motion segment. B) Cross-section showing a bovine slice excised at the disc. C) Cross-section of ovine motion segment.*

these cross-sections were frozen onto stubs using Optimal Cutting Temperature compound (OCT, AGR1180, Agar Scientific) and frozen at -20 °C. The samples was then covered in the compound and completely frozen until solid. Sagittaly, they were progressively flattened using a hardened steel knife within a cryo-microtome (Bright Instruments, OTF 5000). In order to remove excess OCT, samples were washed in phosphate buffer saline (PBS, 0.1M, pH 7.4, Sigma-Aldrich).

3.3.4 Human Tissue

Human samples were collected from spinal surgeries carried out at Peninsula Spine Unit, Princess Elizabeth Orthopaedic Centre, Royal Devon and Exeter Hospital. Disc sections were removed from patients during discectomy procedures and frozen immediately at the RD&E tissue bank, Exeter. Samples were acquired by Claudio Vergari from the tissue bank for another study.[51] Patient gender, age, severity of degeneration and clinical notes are displayed in Table 3.5.

Mineralised regions of tissue were removed from the discs for use in this project (the rest of the tissue was utilised by the other study). Samples were therefore non-uniform and non-region specific. They displayed a white-ish bumpy surface that felt hard, and a softer underside (Fig. 3.8A). Samples were cut vertically using a razor blade and places on their side in order to create a cross-section including both the soft and hard tissue.

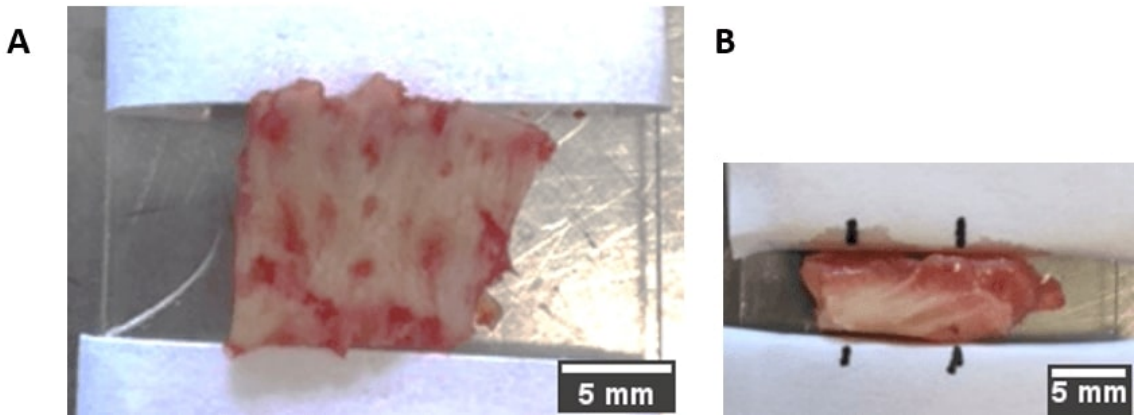

Figure 3.8: *Degenerative Human sample. A) Image of the top side of a human samples showing the 'white-ish' hard surface. B) A sagittally cut slice of a human sample, showing two imaging points (noted by vertical black lines) in regions of differing tissue colouring.*

Samples were kept hydrated with PBS (0.1M, pH 7.4, Sigma-Aldrich) soaked tissue and placed in a petri dish for imaging.

Table 3.5: *Human Sample Descriptors*

	Sex	Age (yrs)	Severity*	Clinical Notes
1	Female	66	Moderate	Foraminal disc bulge
2	Female	53	High	Spondylolisthesis
3	Female	37	High	Spondylolytic spondylosistisis
4	Male	54	High	Lytic spondylosistisis
5	Male	78	High	Widespread degenerative changes
* Severity graded as: moderate or high.				

4 Endplate Structural Study

4.1 Introduction

Structural understanding of the vertebral endplate has developed over the years from the view that it is a nondescript 'plate',[20] to a plate which consists of regions of bone and cartilage.[62] Many studies have been limited to light microscopy[30,93,197,198] and/or polarised light microscopy,[35,92,198] although more recently some investigation using electron microscopy has allowed fibril level investigation.[66,81,94,95,198,199] As mentioned previously (2.3), the structure of the endplate described in the literature is confused by differing nomenclature, however, it is primarily described as being made up of three main components, two that are cartilagenous and one that is bone. The two cartilagenous regions are the non-mineralised cartilage (non-MC)[61–65] and the mineralised cartilage (MC).[60,63,66–69] The cartilage tissues are separated by a tidemark (TM), and the bony endplate (BEP) is separated from the MC by a cement line (CL).[69–72]

Clinically, the vertebral endplates are poorly understood, not only in their role in implant stability,[200] but also in regards to pathologies. Modic changes are often described in clinical literature as endplate changes.[75,132,134] However, Modic changes can effect as much as 75% of the vertebral body, suggesting these are not endplate specific issues. This disparity in the understanding of the basic structure of the endplate between the clinical and basic science literature needs to be addressed, and a consensus on the structure of the endplate attained.

This chapter reports studies that utilised multiphoton microscopy, second harmonic generation (SHG) and two-photon fluorescence (TPF) to image the microstructure of the endplate. This was supported by Differential Interface Contrast Microscopy (DIC), Scanning Electron Microscopy (SEM) as well as spectroscopic methods to investigate the structure and biochemistry of the endplate.

4.2 Methods

4.2.1 Multiphoton Cross-sectional Study

Sample Preparation and Imaging protocol

Bovine tail samples were utilised for this section of the study. Samples were prepared by standard preparation procedures described in Chapter 3.3.1. Samples were then placed on microscope slides with a cover-slip to reduce the dehydration of the sample and to allow for easy region of interest (ROI) marking. For this purpose white labels with five measured lines were attached to the cover slip to indicate the imaging lines (Fig. 4.1). A 10x air objective (Olympus UplanSApo 10x/0.40) was used to image a reference line parallel to the edge of the label (blue line in Fig. 4.1). Maps were then taken perpendicular to the edge of the label at each ROI (green lines in Fig. 4.1). Each image acquired partially overlapped with the previous image to enable reconstruction of the maps later.

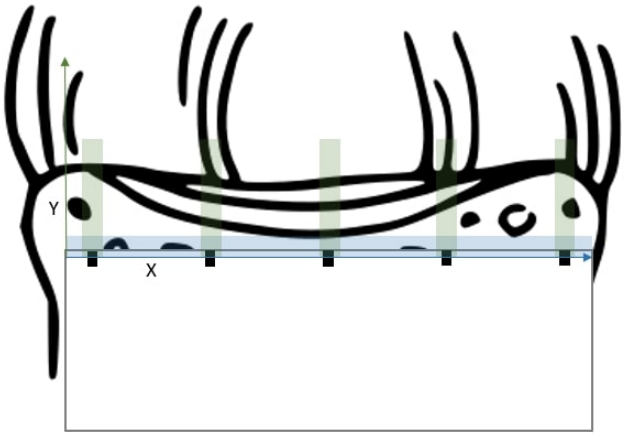

Figure 4.1: *Schematic of cross-sectional samples with a white label indicating the 5 marked ROI. Maps were then taken perpendicular to the edge of the label at each ROI (green lines). Not drawn to scale.*

Decalcification Protocol

Following traditional histological preparation, some samples were fixed and demineralised. Motion segments were cut sagitally into ~1 cm sections and placed into 4 % paraformaldehyde solution for 5 - 7 days (PFA Solution, Thermo Scientific, 4 % in PBS formalin, CAS 30525-89-4). Samples were then decalcified in 10 % formic acid for 7 - 14 days, until soft enough to slice with a scalpel blade. Sample slices were then fixed

to metal stubs with Optimal Cutting Temperature compound (OCT) and frozen at -20°C. Progressively more OCT was added to the sample, then frozen until the samples were covered in the compound and completely frozen. Sagittal sections were then cut, with a disposable blade (Feather ®, S35, VWR™) to create 20 μm slices using the cryo-microtome (Bright OTF5000). Every third consecutive slice was saved for imaging. Slices were stored in phosphate buffered saline (PBS, 0.1M, pH 7.4, Sigma-Aldrich) and frozen before imaging. For imaging, samples were defrosted and mounted onto microscope slides. The sample was kept hydrated with PBS, and a cover slip was placed over them which was held in place by water tension. Due to the use of the cover slip, the 25x water immersion objective lens could be utilised (Olympus, XYPLN 25x/1.05).

4.2.2 Raman Microscopy

Bovine Sample Preparation and Marking

Cow tails were obtained from a local abattoir and frozen intact at -2°C. Once frozen, functional units (half vertebra, disc, half vertebra) were cut using an oscillating saw (Makita TM3000C/2). Thick slices (about 5 mm) were then cut longitudinally, parallel to the mid-sagittal plane. The slices were frozen in phosphate-buffered solution (PBS), and the surface was pared using a cryo-microtome (Bright Instruments, OTF 5000) to obtain the smooth flat surface necessary for measurements and to remove tissue which may have been damaged by the saw. Samples were then transferred to microscope slides. PBS was applied to maintain the hydration of the samples between measurements.

In order to compare similar regions of the same sample in multiphoton imaging and Raman microscopy, areas were marked with white sticky labels. The white label was marked with a dot, which appeared black under the multiphoton compared to the fluorescence of the label. The same dot was visible under the white light microscope of the Raman set up (Fig. 4.2). The measurement order was randomised to reduce the effect of time/dehydration on the results.

Bovine Raman Microscopy Measurements

A Renishaw inVia spectrometer was employed (Renishaw plc, New Mills, Wotton-under-Edge, Gloucestershire, GL12 8JR), with a near-infrared diode excitation laser at 785 nm. The system is equipped with reflected white light imaging and generates 300 mW of power. The laser light is initially focused through the microscope lens (×50 long working

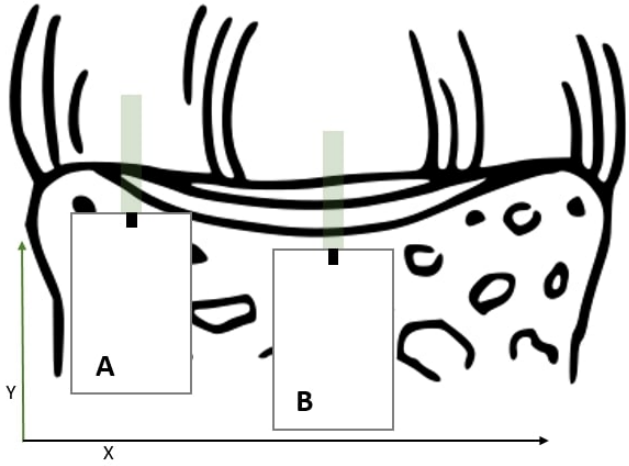

Figure 4.2: *Schematic of cross-sectional samples with a white label indicating A) marking for area under the annulus B) marking for area under the nucleus. Green lines indicate images maps taken in the Y direction.*

objective) onto the sample on a motorized XYZ stage. The Raman back-scattered light is collected through the collection optics and focused onto the grating, and Rayleigh light is rejected. A dispersion grating then splits the beam into its constituent wavelengths which are directed onto a CCD detector (deep depletion CCD, 1024 × 256 pixels). For the point measurements recorded in this study, we used a 600 l/cm grating which was centred at 1300 cm^{-1} for the fingerprint region (spectral range: 36 – 2327 cm^{-1}) and 2700 cm^{-1} for the high wavenumber region (spectral range: 1741 – 3497 cm^{-1}). The exposure time was 2 accumulations of 3 seconds and the cosmic ray removal option of the software (Wire) was applied. External standards (Si, NeAr) were measured in calibration routines prior to each set of measurements in order to ensure reproducibility and comparability between the samples.

Spectra were obtained from bone to disc along a line perpendicular to the tidemark in spatial steps of 50 μm in bone and disc and 10 μm in the endplate region. Single Raman spectra were plotted using Origin software[201] (OriginLab, Northampton, MA, USA). For data pre-processing, the spectra were loaded into Matlab R2018b (The Mathworks Inc., Natick, Massachussetts, USA) and were subjected to baseline correction using asymmetric least squares smoothing.[202]

4.3 Scanning Electron Micrsocopy and Energy Dispersive X-ray Spectroscopy

4.3.1 Ovine Sample Preparation

Two motion segments were used from ovine lumbar spines, one from a young adult (1-4 years) and one from a mature adult (4 years +). Motion segments were prepared as seen in 3.3.2 and 4.2.1, then sectioned into four central regions as shown in Fig. 4.3. Prior to sectioning samples were placed in hexane and agitated for 24 hours on a wobble plate to remove fat. In order to remove the proteoglycans, samples were placed in an enzyme/buffer solution for 3 days (Sodium acetate 0.1 mol, Sodium chloride 0.1 mol, adjusted to pH 5 by adding Acetic Acid at 37 °C, containing bovine testicular hyaluronidase 1.25 mg/ml, Sigma Type I-S, 400– 1000 units mg). Samples were kept in an incubator at 37 °C and the solution changed every 12 hours.

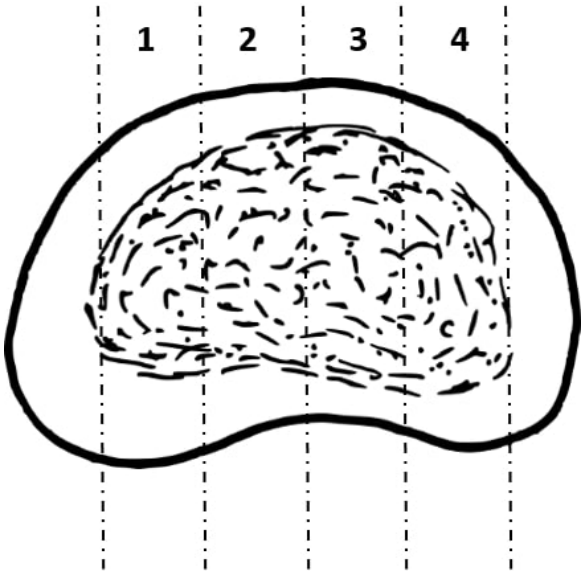

Figure 4.3: *Caudal view of the motion segment showing the where the four central regions were cut from. Outer most regions were discarded.*

Samples were then washed in PBS and the surface ground using descending grit size sandpaper to produce a smooth imaging surface. For ease of grinding, samples were kept as motion segment cross-sections until smooth, then cut through the centre of the discs, separating the caudal and cranial endplate. This was in order to fit onto the stubs required for the Scanning Electron Microscopy (SEM). This resulted in a total of 8 samples of each age (n=16). Prior to critical point drying, samples were dehydrated by exposure to increasing concentrations of ethanol (50 %, 60 %, 75 %, 90 %, 100 %) each for

30-45 minutes. Critical point drying (CPD) was then carried out to reduce tissue destruction under the vacuum conditions of the SEM chamber. Samples were then attached to stubs using carbon tape and sputter coated (Quorum Q150R S) with a double-coating of platinum under vacuum.

4.3.2 SEM and EDS Protocol

SEM is routinely employed o image nano-scaled structures such as the fibril of the intervertebral disc. SEM uses a focused beam of high-energy electrons to 'scan' the surface of the sample. This reacts with the sample to release energy energy from the surface in different forms. These forms include secondary electrons (illustrating the topography of the surface), backscattered electrons (atomic composition) and x-rays (elemental composition).[203,204]

Samples were imaged with a Philips XL30S FEG Field Emission Gun SEM under high vacuum. Images were taken in the backscatter mode in order to visualise mineralisation as grey scale changes. Gross regional images as well as magnified regions of interest were obtained at 3-4 locations across the disc; inner and outer anterior, mid-disc and posterior. Energy dispersive X-ray spectroscopic (EDS) line plots were also run in each region, measuring the weight percentage of calcium (Ca) and phosphate (P) from the disc to the bone.

4.4 Differential Interface Contrast (DIC) Optical Microscopy

DIC employs advanced optical principles to enhance the contrast of structural interfaces without the need for staining. A key feature is its directional sensitivity, which makes it ideal for studying anisotropic structures such as the intervertebral disc.[205,206]

Ovine sample preparation followed the same process as 4.3.1 up to and including the immersion in the enzyme buffer solution. Sample slices were then sagittaly sectioned with a sledge microtome (Leica SM2000 R) to create 20 μm slices. Every third consecutive slice was used for imaging. Slices were kept hydrated in PBS at <5°C until imaging.

Gross image maps of all samples were taken at low magnification (4x) on a DIC microscope (Nikon Eclipse 80i DIC). Regions of particular interest were returned to and viewed with 10x, 20x and 40x objectives.

4.5 Degenerative Human Samples

4.5.1 Human Sample Preparation

Mineralised regions of disc tissue removed during surgery were stored at - 80 °C . Samples were cut vertically with a razor blade from the 'mineralised' to the sorft tissue to create a cross-section. This was then secured to a metal stub using OCT, and progressively covered with the medium and frozen until covered. This was then sliced using disposable blades on the cryo-microtome (Bright Instruments, OTF 5000). For co-registration of multiple images using the WITech instrument, samples were sectioned to between 20 - 30 μm. These were placed on microscope slides with PBS and a cover slip.

4.5.2 Multiphoton Imaging Protocol

Images were taken with a 10x objective (Olympus UplanSApo 10x/0.40) and a a 25x water immersion lens (Olympus, XLPLN 25XSVMP2 M25 x 0.75W) on the multiphoton system described in Chapter 3.

4.5.3 Human Raman Microscopy Measurements

Raman spectra and Raman maps were collected in a backscattered geometry using a WITec confocal Raman microscope, model Alpha 300R, (WITec Inc, Ulm, Germany), equipped with a thermoelectrically cooled CCD detector, a Nd:YAG 532 nm excitation laser and a 20·x 0.4 NA objective (Zeiss, EC EpiPlan), for back-scattered light collection. The spectrometer grating used was 600 g mm-1, BLZ = 500 nm. Raman spectra were typically recorded using an exposure time of 1.0 s and 50 accumulations with an average laser power of between 7 and 10 mW at sample. This was a different system than previously employed for the bovine samples due to collaboration with a different colleague as well as the decision to employ a shorter excitation wavelength to yield a stronger Raman signal.

Analysis was performed using Witec Project 4.0 software and fluorescent background was removed using the background subtraction 'shape function'.

4.6 Image Manipulation

4.6.1 False Colouring of Multiphoton Images

Images acquired with the multiphoton microscope contained both the SHG and TPF channels in the form of two single channel grey images. In order to view both channels simultaneously, false colouring was required. This was performed using the FIJI version of ImageJ (Fiji is just ImageJ (http://fiji.sc/)). In order to maintain the information of the grey scale image, lookup tables (LUT) were utilised. An LUT is a predefined table of grey values with matching red, green and blue values so that shadows of grey are displayed as colorized pixels. This ensures that differences in color in the false coloured image reflect differences in intensity. The colours green (SHG) and blue (TPF) were selected based on the use in previous literature examining the tidemark of the metacarpophalangeal joint using similar methods.[136] In order to view both channels in the same image, a composite image was created. When creating composite images, original LUTs and display ranges are preserved, ensuring no loss of detail from the original grey scale images. Once images were scaled appropriately, FIJI also could be used to measure regions of interest. In some cases, a map of a region was taken using a number of overlapping snapshots. These images were initially processed in FIJI to add the false colour, then they were built into a continuous map in GNU Image Manipulation Program (GIMP, 2.8.18).

4.6.2 Directionality

To parametise the change in organisation of the disc collagen fibres, Fourier transform image analysis techniques available in the Fiji version of ImageJ®were used. A region of interest was selected and the directionality plugin was applied.[207] This calculated the weighted sum of the Fourier components at each angle of the Fourier transformed image. A Gaussian peak was fitted to the histograms of the components as a function of angle. In addition to primary direction, the visibility (peak height – background) gives an indication of the degree of organisation, along with the width of the peak. A indiscernible broad peak indicates a lower order, a highly visible sharp peak indicates a higher order.

4.7 Statistics

Statistics were run in SPSS (IBM SPSS Statistics 25). Data were first checked for parametricity through homogeneity of variance (using a Levene's test), for normal distribution and independence. If the data met these assumptions, parametric tests were utilised, if an assumption was not met, a non-parametric equivalent was utilised.

4.8 Results

This section first compares the gross structure of the endplates in the bovine tail, ovine spine and degenerate human samples. Then the tide mark is focused upon in the animal models, followed by fibre connectivity and the BEP. Penultimately the micro-structure of the degenerate human samples is compared to the animal models, before results of biochemical studies are presented.

4.8.1 Gross Endplate Structure

Bovine Tail

Bovine tails were obtained from animals entering the food chain, and thus are <1 year of age at slaughter. This is evident from the visible growth plate within the vertebral bodies (Fig. 4.4).

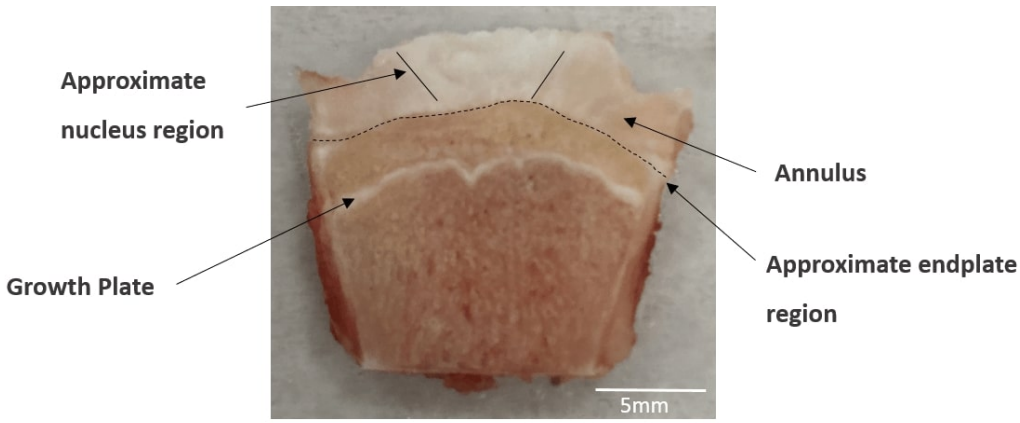

Figure 4.4: *Image of sectioned bovine tail motion segment. The approximate annulus, nucleus and endplate regions are indicated, as well as the growth plate.*

Multiphoton microscopy provides an in-depth view of the gross structure of the endplate (Fig. 4.5). The trabecular bone and BEP can be visualised and by combining SHG and TPF the distinction of the mineralised and non-MC is visible. The osteocytes of the bony region are not obvious, but the lacunae of the chondrocytes give the cartilage regions a distinguishable 'dimpled' appearance that also helps differentiate the cartilage from the disc and bone. Fig. 4.5 was taken from the annular region, hence it shows aligned fibres. In the inner annular regions the tidemark is clearly visible and its irregular contours are noteworthy.

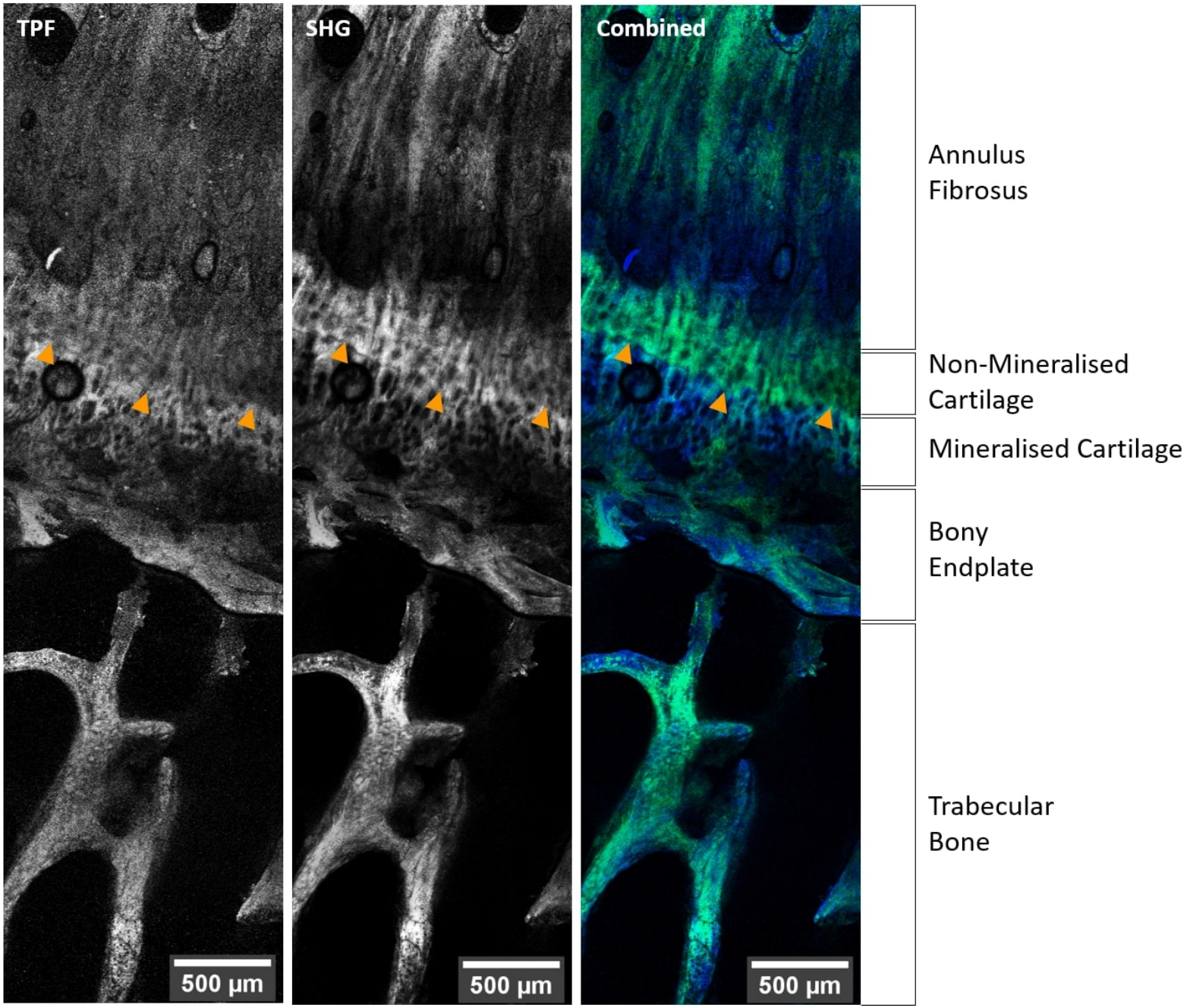

Figure 4.5: *Example multiphoton image of the transition from the trabecular bone, to the disc in the bovine tail inner annulus. Note that all three regions of the endplate are present: BEP, mineralised and non-MC. In the composite image, SHG is false coloured green, and TPF in blue. The tidemark is indicated with orange arrow heads.*

Ovine Lumbar Spine

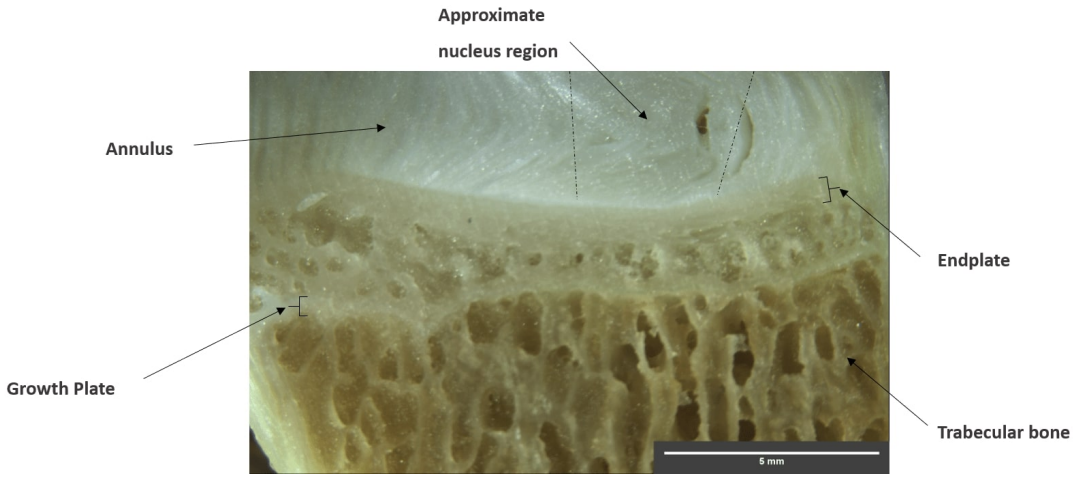

Figure 4.6: *Dissection microscope image of a sectioned ovine lumbar motion segment. The approximate annulus, nucleus and endplate regions are indicated, as well as the growth plate.*

Dissection microscope images of ovine smaples showed growth plates still present despite the spines being > 1 year, however, detail of the endplate was not visible other than a delineation between the bone and the disc (Fig. 4.6). In multiphoton images of ovine samples, the tidemark is not always as clear as in the bovine, due to a higher SHG signal in the mineralised regions indicting a lower level of mineralisation (Fig. 4.7). Osteons in the bony region are evident, and shows the interdigitisation of the MC with the BEP. Under the annulus, the SHG from the non-MC is disrupted by the strong signal from the highly aligned annulus, however, the disorganisation of the nucleus allows for clearer identification (Fig. 4.7).

Even though samples required demineralisation for DIC microscopy the mineralised tissues, such as the trabecular bone and BEP, are still clearly distinguished from the soft tissues. As Fig.4.8 shows, the trabecular bone is easily identified by its large trabecular holes that are filled with round fat calls. The BEP is denser than the trabecular bone, though still containing some marrow channels. The cement line delineates the BEP from the MC. The lamella layering of bone is also visible. The bony regions show many small dark dots which are the lacunae of osteocytes, whereas the cartilage regions show larger lacunae from chondrocytes.

In Fig. 4.8, the tidemark is not obvious. There is a slight lightening of the image colour, however, the contrast and magnification does not allow for easy distinction between the two cartilage types. The image is taken from the nuclear region and a lack of obvious fibres or integration of the disc to the non-MC is to be noted.

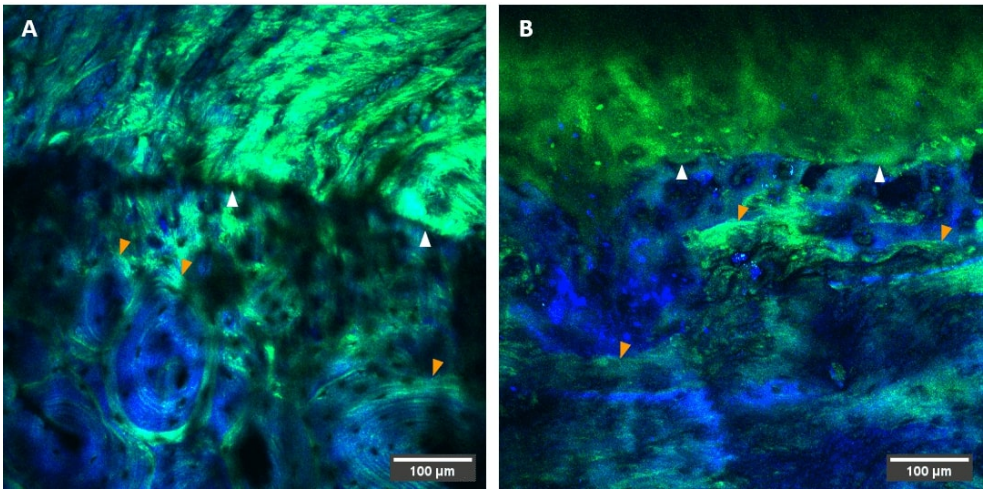

Figure 4.7: *Multiphoton images of the endplate region in 4 year old sheep in two regions A) Inner annulus B) Nucleus. White arrowheads indicate the tidemark, whilst orange arrow heads indicate the cement line.*

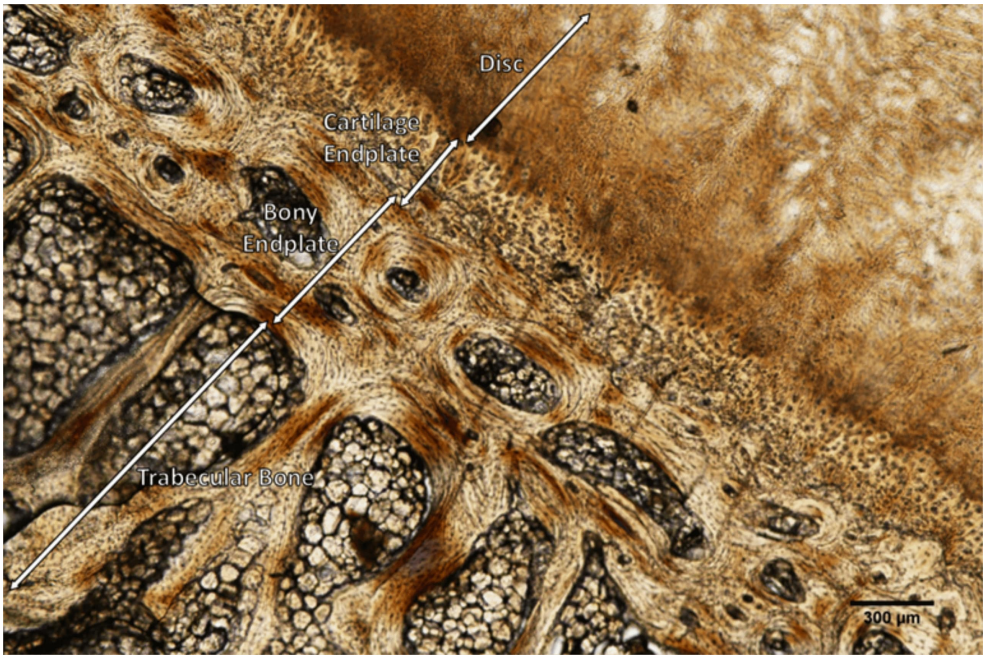

Figure 4.8: *DIC image of a 20 µm demineralised section of a mature ovine endplate. Highlighted are the trabecular bone, BEP, cartilage endplate (the mineralised/non-mineralised distinction is not visible) and the disc (nucleus).*

4.8.2 Age Differences in the Ovine Endplate

DIC

In the macroscopic view, differences between maturity (young adult 1-4 years, mature 4 years +) are obvious in the BEP. Fig. 4.9 shows that in the young adult ovine spine, this region is populated largely by osteons, punctuated with vessels. This region is distinct from the large trabecular spaces filled with fatty marrow tissue (dark circles) as it is denser and lacking in trabeculae. The osteons additionally form an undulating cement line that distinguished the BEP from the MC.

Conversely, in the mature adult, the presence of osteons is markedly lower, and the existence of small trabecular like holes containing fat cells are more prolific (Fig. 4.10). The distinction between the trabecular bone and BEP is less clear and it appears as though the trabecular bone has extended, getting progressively more dense. Similarly, the cement line between the bone and cartilage is harder to distinguish in the mature animal, although it is slightly more visible in the annular region. The annular and nuclear BEP show a similar thickness in the mature samples, though the small trabecular holes of the endplate appear slightly larger under the annulus (Fig. 4.10).

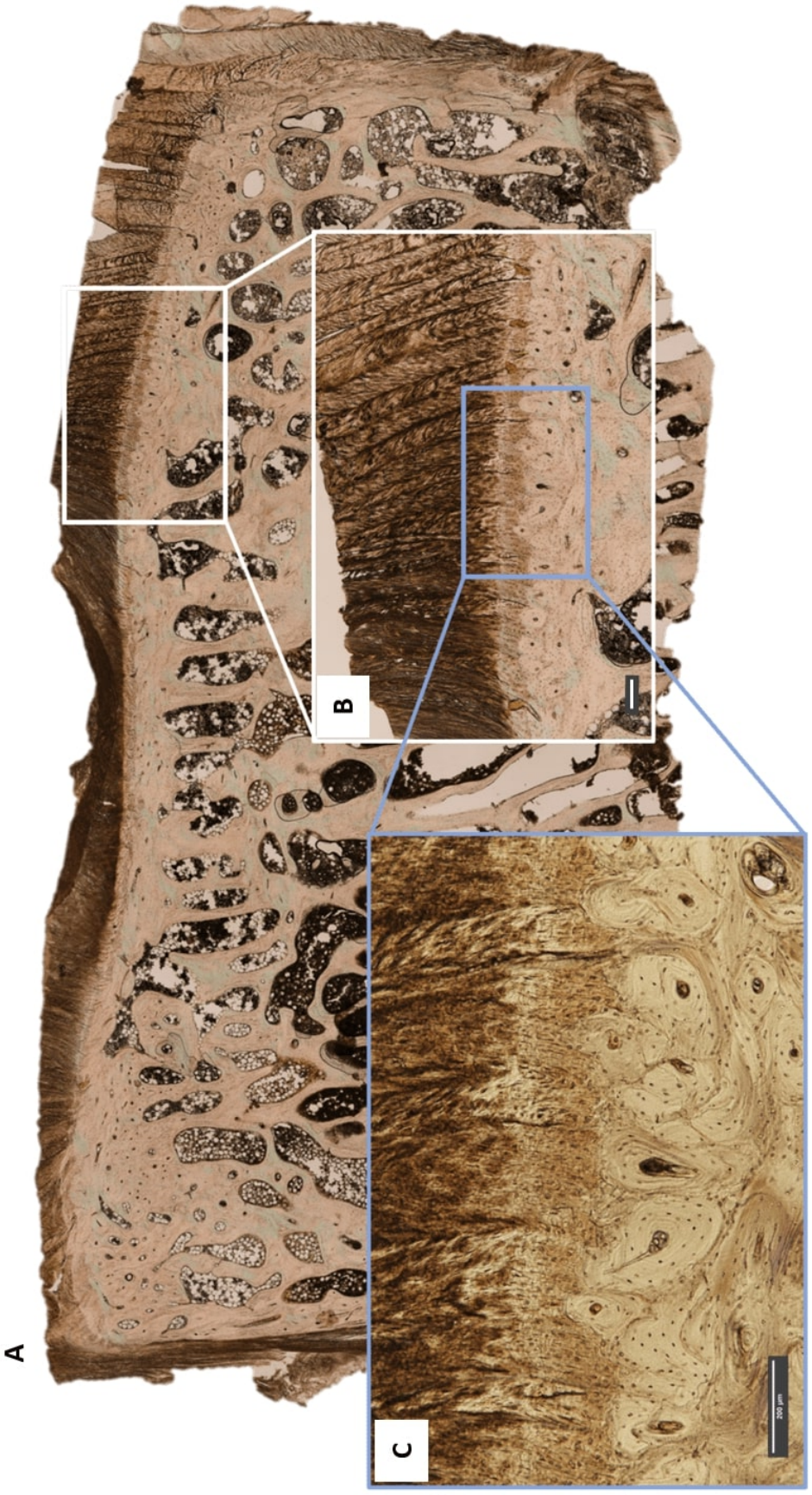

Figure 4.9: *A) Low magnification DIC map of whole motion section of young adult ovine spine. B and C) Increasing magnification of the BEP under the annulus at a point of high osteon density. Scale bar = 200 µm*

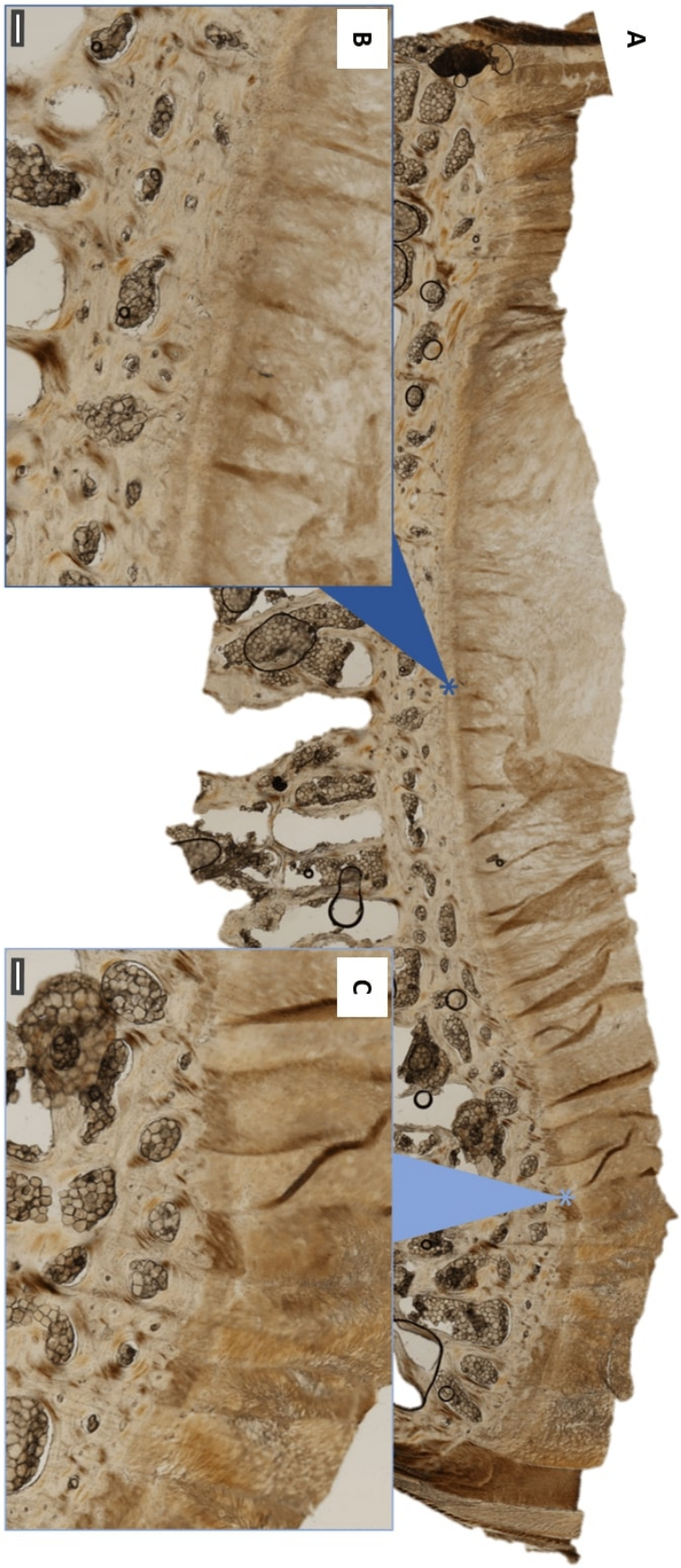

Figure 4.10: *A) Low magnification DIC map of whole motion section of mature ovine spine. B) Magnification of the BEP (BEP) under the nucleus. C) Magnification of the BEP under the annulus. Scale bar = 200 µm*

SEM and EDS

Scanning electron microscopy is able to show both the tidemark and cement line as shown in Fig. 4.11. However, due to the charging of the sample, which appears as areas of white intensity, they are not always clear (charging occurs when there is no conducting path for electrons to flow, if the electrons remain on the sample, it will repel electrons from the incoming beam). The SEM images allow a qualitative assessment at the differences between young adult and mature adult endplates. As shown in Fig. 4.11, within the mature adult, the cranial region of MC appears much thicker than the caudal region, with a higher cellular density (dark dots indicate lacunae of chondrocytes). Conversely the caudal endplate appears to have a higher cellular density post-TM in the non-MC region, as well as having a greater distance between the TM and the closest marrow channel. The young adult displays an opposite trend with the MC of the caudal endplate appearing slightly thicker. Compared to the mature, both the TM and CL were much harder to distinguish on the young adult, and it is interesting to note that there are no marrow channels present in the young adult images (at this magnification and ROI), indicating a thicker layer of dense bone between the CL and marrow than in the mature adult endplates.

Quantitatively, Energy dispersive x-ray spectroscopy (EDS) can compare the mineralisation of the regions by analysing the Calcium to Phosphate ratio (Ca/P ratio). Measurements at three regions, two in the annulus (Anterior-AF and Posterior-AF) and one centrally in the mid-nucleus (Mid-NP), were compared between the mature and young adult. Fig. 4.12 illustrates that the young adult had a higher Ca/P ratio than the mature adult, $t(498) = -7.8$, $p = < 0.001$. There is a significant effect of location on the Ca/P ratio, $F(2,497) = 35.8$, $p < 0.001$. As homogeneity of variance could not be assumed, Games-Howell post-hoc test was used and showed significant difference between mid and anterior ($p < 0.001$), mid and posterior ($p < 0.001$), but no difference between posterior and anterior ($p = 0.980$).

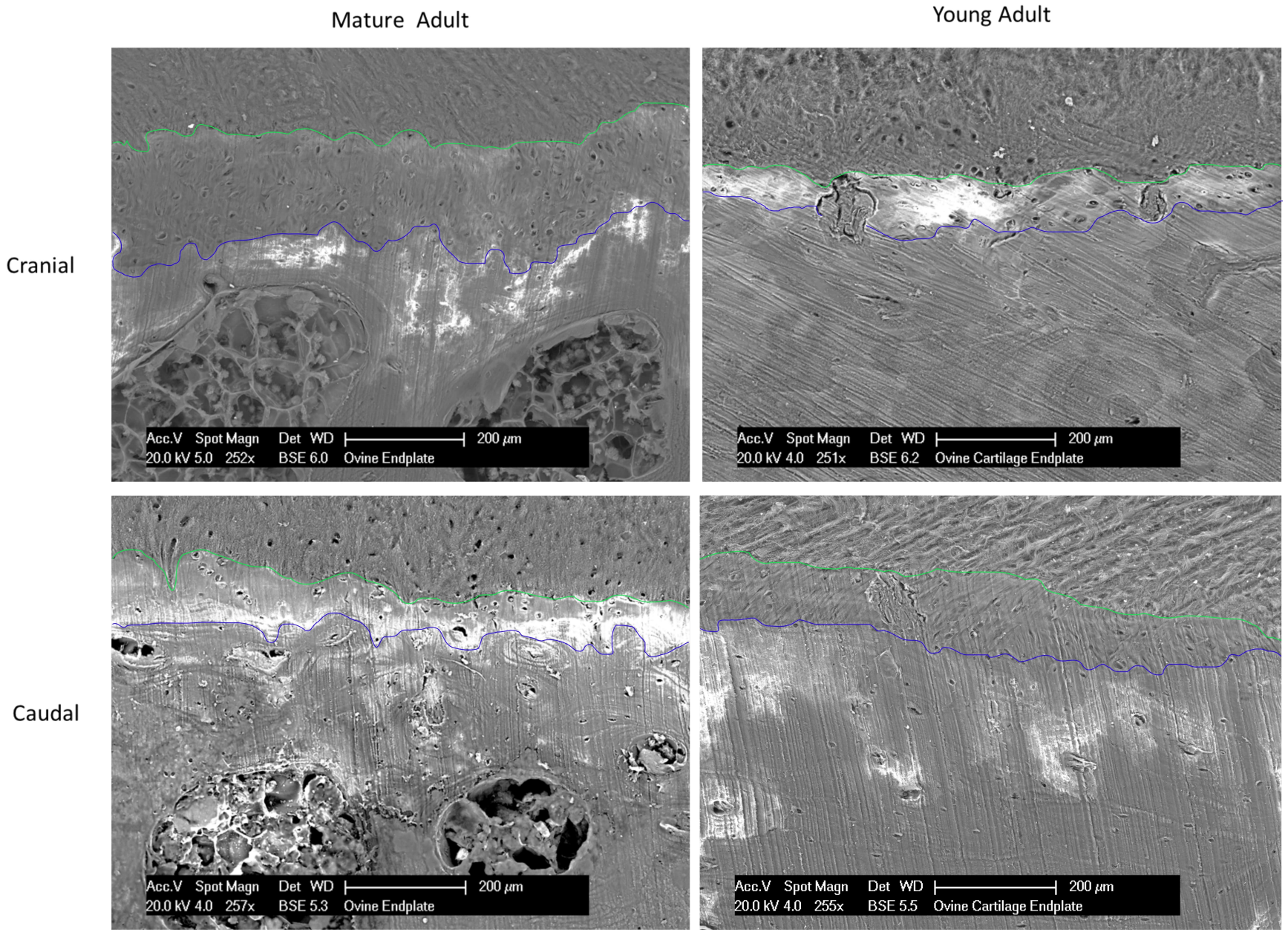

Figure 4.11: *Scanning electron images of caudal and cranial endplate regions in both mature and young adult ovine spines. The green line indicates the tidemark, and the blue the cement line.*

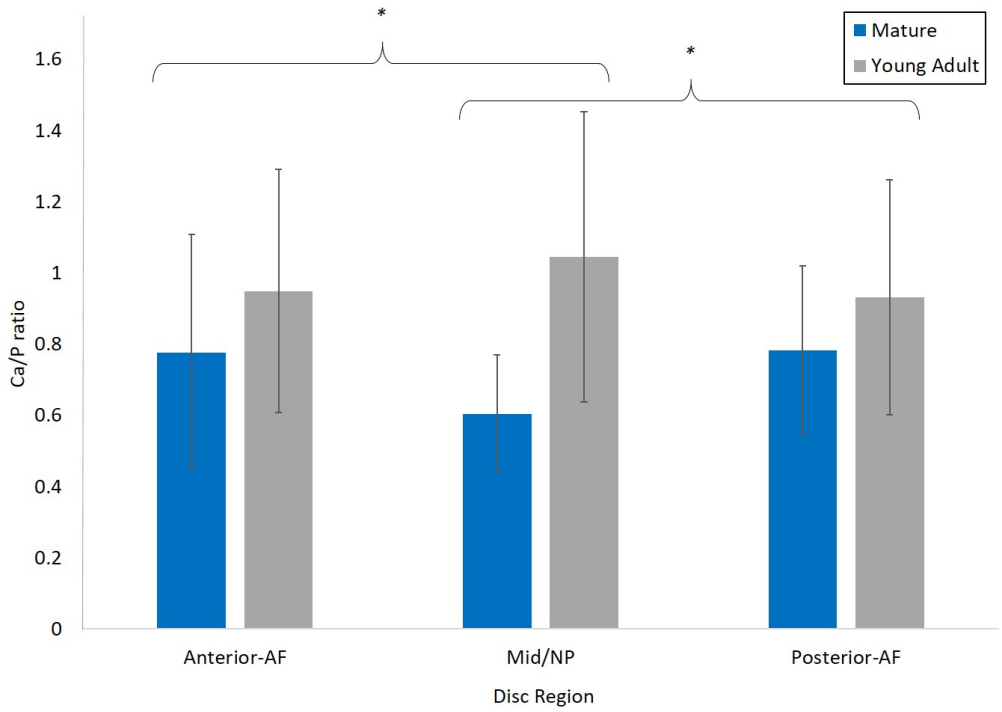

Figure 4.12: *Calcium to phosphate (Ca/P) ratio as calculated from EDS spectral analysis at the anterior annulus fibrosus (AF), mid/nucleus pulposus (NP) region, and the posterior AF. The Ca/P ratio was shown to be significantly higher different between the anterior and mid, and posterior and mid. * $p < 0.001$.*

4.8.3 The Tidemark in Ovine and Bovine Endplates

The tidemark delineates the mineralised from the non-MC within the endplate. Using DIC microscopy, the tidemark appears as a dark line (Fig. 4.13). Multiple tidemarks have been imaged in the annular regions of ovine sections (indicated by the bracket in Fig. 4.13), however, as Fig. 4.14 shows, even at high magnification little detail is revealed, making the quantification of this phenomenon difficult. However, as seen in 4.8.1 multiphoton microscopy can differentiate between the two cartilage types. Fig. 4.15 shows that the tidemark is clearly defined, mainly by a change in intensity of the SHG and TPF signals. This was demonstrated further in Fig. 4.16 where it was shown that the TPF intensity is higher in the MC, and lower in the non-mineralised, though the source of the TPF in the mineralised tissue is still unknown.[142] Conversely, the SHG showed an opposite relationship, with a higher intensity in the non-MC. Both SHG and TPF showed a steep drop and recovery of signal at the tidemark, this was evident in both the image (B) and the intensity profiles (C) of Fig. 4.16.

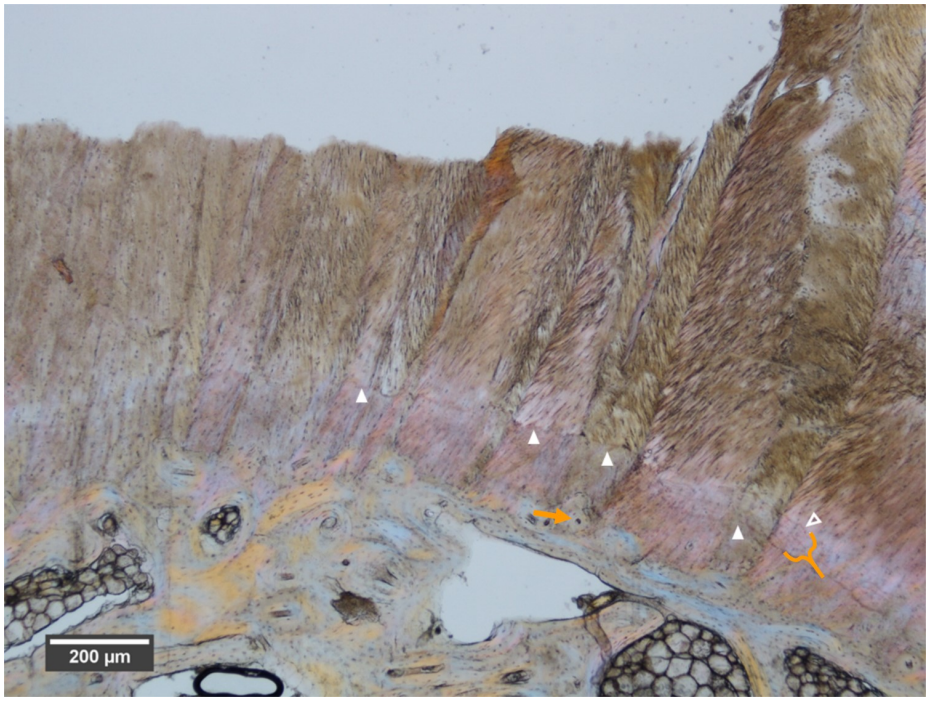

Figure 4.13: *DIC image of mature ovine annulus section. Filled arrow heads indicate the most prominent tidemark (TM). Orange brackets indicate multiple tidemarks with the furthest indicated with an unfilled arrow head. Orange arrow indicates an osteon at the edge of the BEP.*

Using this identification of the two regions, their thickness in ovine samples was measured. Samples were measured in the mid to inner annulus regions, as the deliniation of the tidemark was clearest. Measurements were taken from the tidemark to the ce-

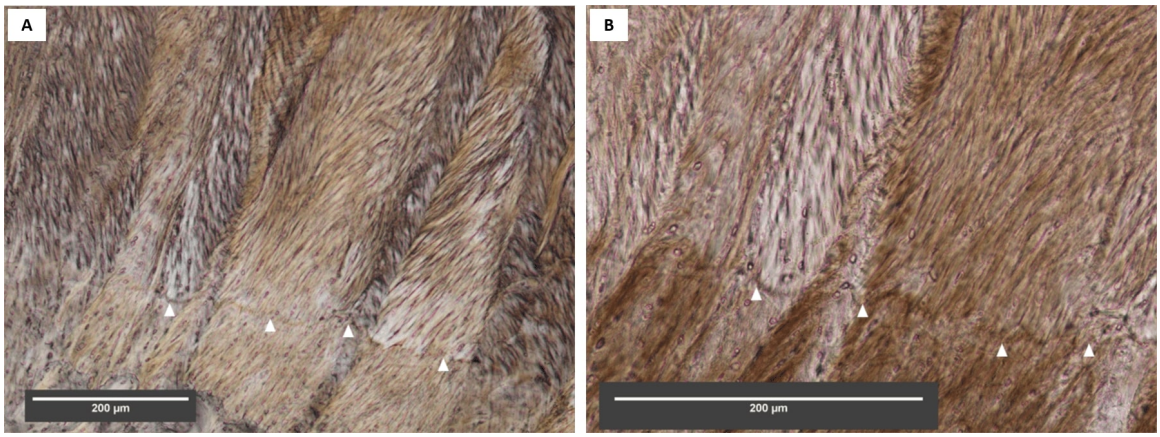

Figure 4.14: *DIC images of mature ovine annulus section. A and B) Increasing magnifications of the TM (indicated with filled arrows) taken with DIC microscopy.*

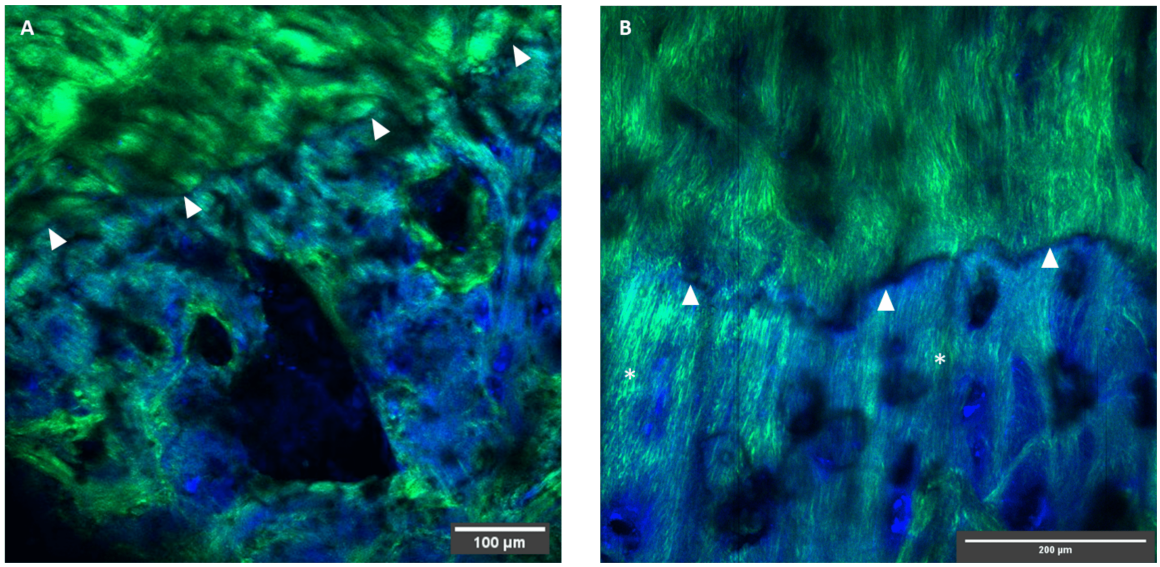

Figure 4.15: *Multiphoton images of bovine tail endplate, annulus. A and B) Composite SHG (green) and TPF (blue) images of the tidemark (TM) at two regions of the endplate. A) Outer annulus B) Inner annulus. TM indicated with a filled arrowhead.*

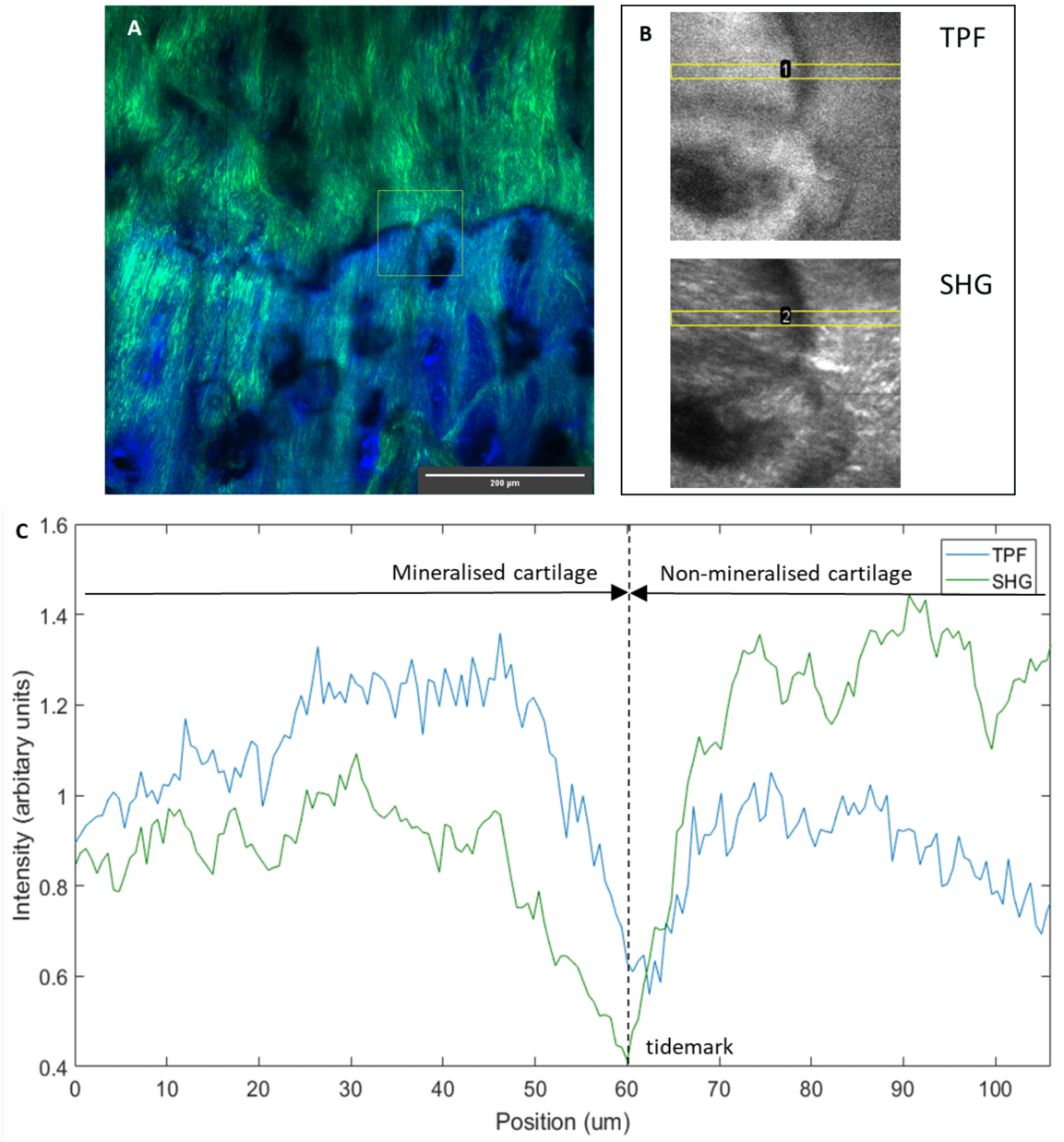

Figure 4.16: *Decrease in signal intensity at the tidemark. A) Composite TPF (blue) and SHG (green) multiphoton image of the tidemark. Yellow box indicates ROI used to analyse intensity change across the tidemark (TM). B) Separated TPF and SHG images taken from (A), rotated 90 °right with yellow boxes indicating the ROI used to plot intensity profiles across the TM. C) Plot profile of the intensities of TPF (blue) and SHG (green) across the tidemark. Note that TPF has a higher intensity prior to the tidemark, and SHG post-tidemark.*

ment line in FIJI. There was a significant effect of endplate location (caudal/cranial) on the endplate thickness after controlling for CEP region (MC/non-MC) with an ANCOVA, $F(2,91) = 7.42$, $p = 0.008$. Additionally, CEP region also affected the thickness when controlling for endplate location, $F(2,91) = 8.20$, $p = 0.005$.

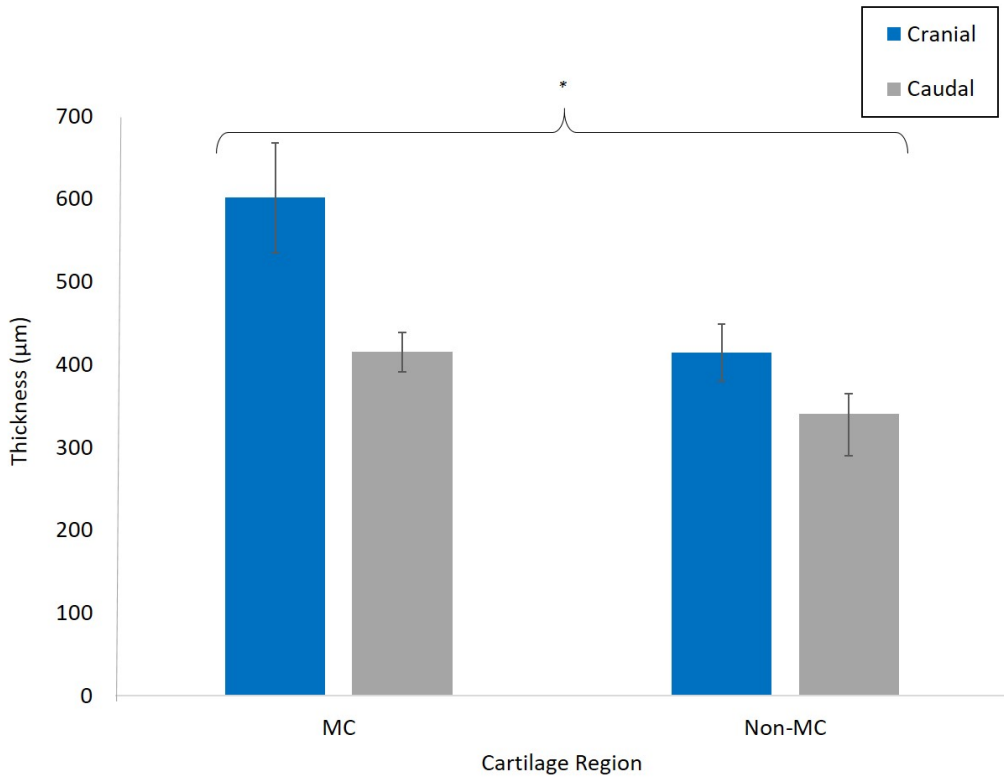

Figure 4.17: *Thickness of the MC, and non-MC at endplate of the mid to inner annulus of ovine lumbar endplates. Tissue thickness was significantly effected by both endplate location ($p = 0.008$) and CEP region ($p = 0.005$).*

4.8.4 Fibre Connectivity Between the Disc and Endplate

As previously discussed (chapter 2.3.2), it is presumed that the endplate provides mechanical coupling between the disc and vertebra, an important aspect of this is providing anchorage for the fibrous protein of the disc. In this section we discuss the organisation of the collagen and elastin in the endplate.

The annulus fibrosus is easy to image as it gives a strong SHG signal as shown in Fig. 4.18. It is more difficult to visualise the disc fibres and non-MC as the former passes into the latter and they have similar SHG intensities. As Fig. 4.19 demonstrates, the contrast between the annulus and MC is much easier to see.

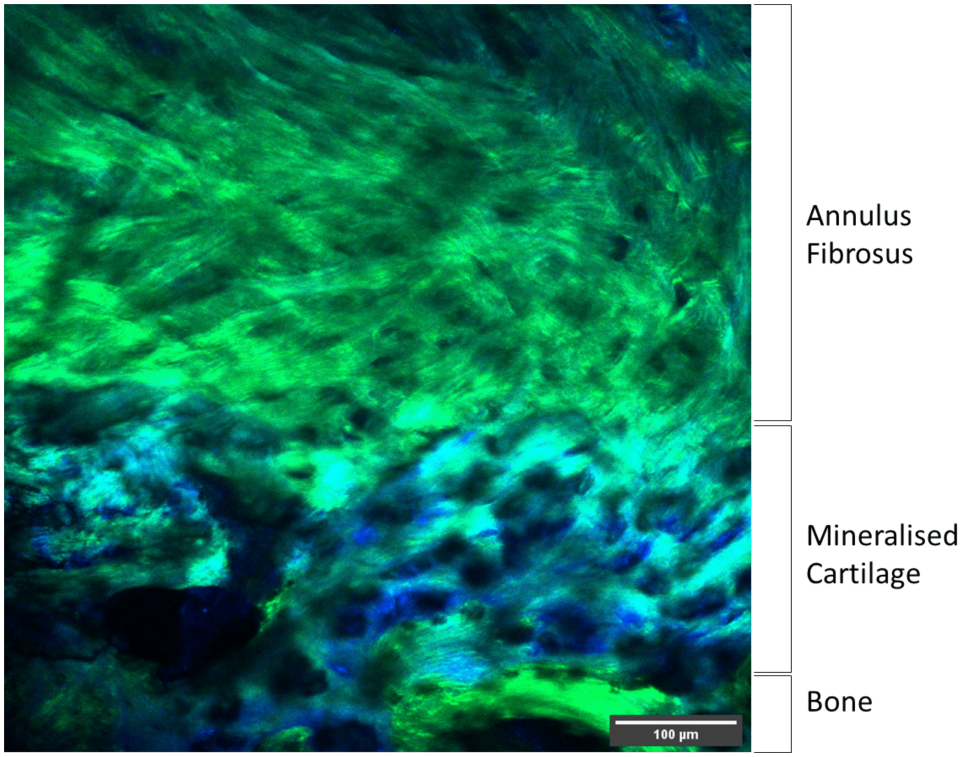

Figure 4.18: *Composite SHG (green) and TPF (blue) multiphoton image of the ovine annulus integration into the MC at low magnification.*

Sub-Bundling

Fig. 4.19 A shows the annular fibres anchoring into the MC, though some of the fibres continue within this mineralised region (highlighted with a white *) suggesting a deeper connection of the tissue. Fig. 4.19 B confirms this continuation of the fibres through the MC, and reinforces the suggestion of primary annular bundles (PAB) splitting into smaller bundles (sub-bundles, SB).[34,94] This is reinforced further with Fig. 4.20 which shows sub-bundles of disc fibres extending from the edge of the PAB and interlacing with the surrounding matrix. In some regions however, the fibres appear to stop fairly abruptly at the cement line which they approach in a perpendicular direction (Fig. 4.21). This suggests a sudden end with little anchorage at the bone.

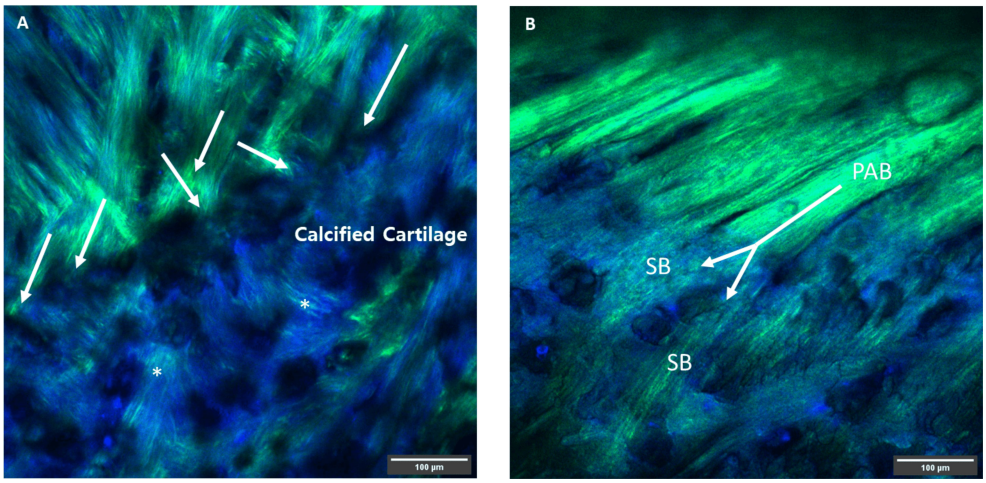

Figure 4.19: *Multiphoton image of the annulus, MC and bone. Composite SHG (green) and TPF (blue) multiphoton image of ovine tissue showing A) Insertion of annulus fibres into the MC with fibre continuation highlighted with an (*). B) Evidence of primary annulus bundles (PAB) splitting into sub-bundles (SB) as they insert into the MC.*

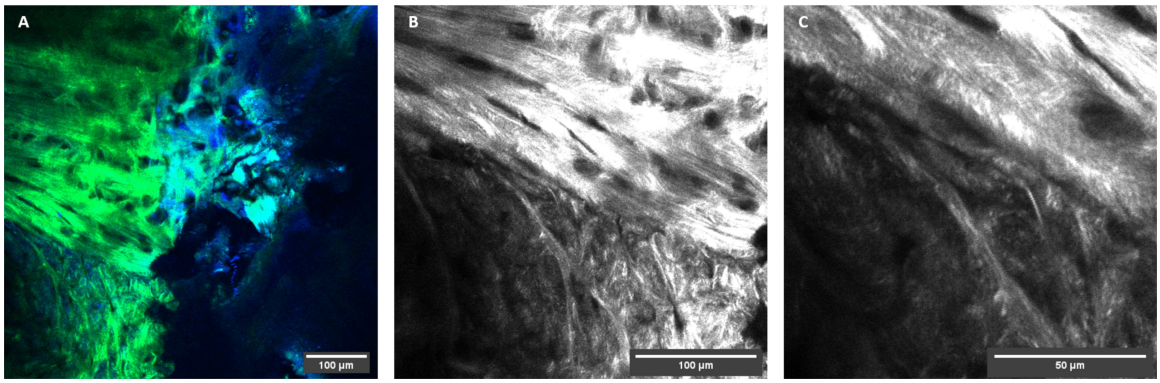

Figure 4.20: *Multiphoton images of calcified ovine section showing anchoring of fibres below the annulus. A) Composite SHG (green) and TPF (blue) image B and C) SHG images magnifying the sub-bundling of the primary annular bundle.*

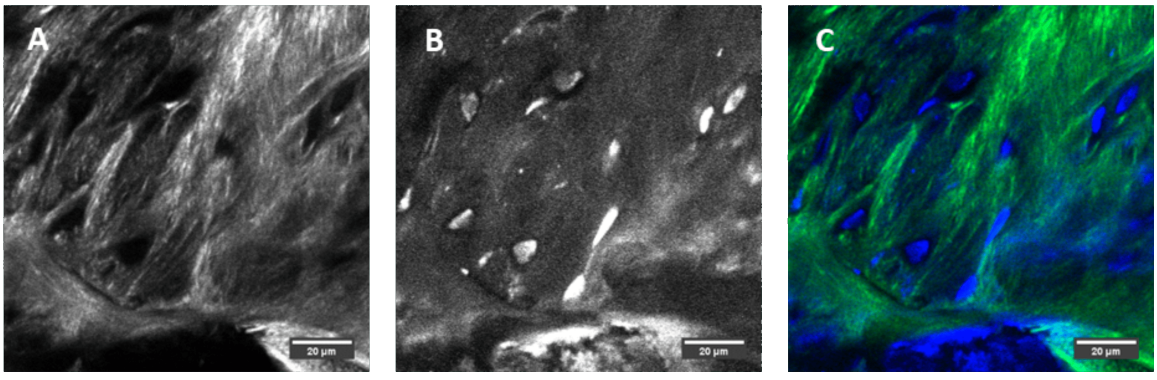

Figure 4.21: *Multiphoton images of decalcified ovine section showing anchoring of fibres below the annulus. A) SHG image. B) TPF image. C) Composite SHG (green) and TPF (blue) image.*

Fibre Integration

Fourier transform analysis was used to measure the predominant collagen fibre angle and degree of order of specific regions using FIJI (see methods 4.6.2). Fig. 4.22 shows the progressive interaction of annular disc fibres with the cartilage endplate. Regions of disc (ROI 4), disc and cartilage integration (ROI 2,3 and 6), and cartilage (ROI 1 and 5) were measured. At this magnification, the disc is highly ordered (black line), but as the fibres insert into the cartilage they loose a predominant angle, and become less ordered (aqua and purple lines). In the cartilage regions the fibres show no predominant angle at this magnification (red and green line).

At a higher magnification, Fig. 4.23 shows a representative Fourier transform in which the disc still appears to have the highest order, and shows an alignment from 30-80 °. The decrease in order from disc to endplate was a trend seen among all samples analysed. ROI 1 and 2 show low order with no clear angle preference (range between 24 and 96 °). They appear rather similar, however, ROI 3 does have a slightly higher peak, suggesting a slightly increased order of tissue.

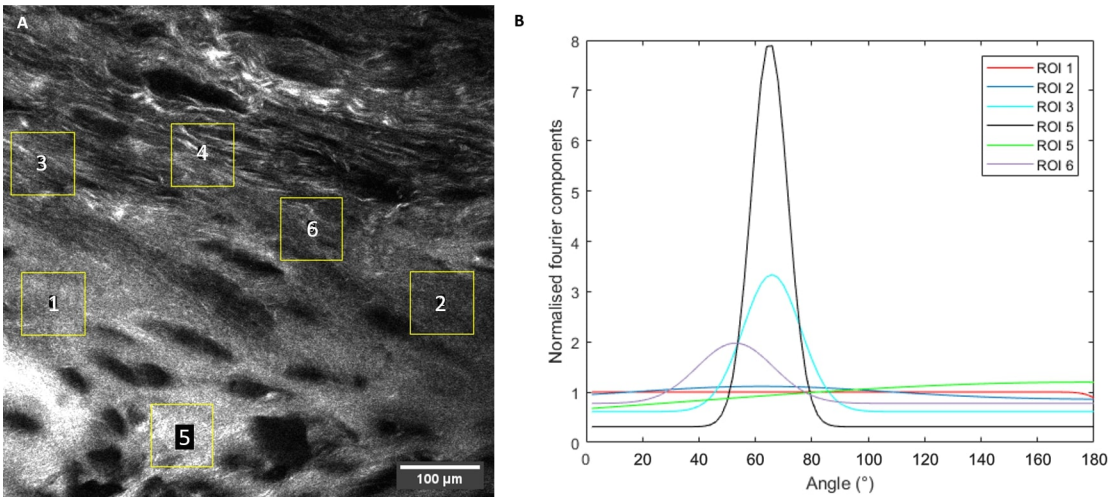

Figure 4.22: *Fourier transform of five regions of interest. A) SHG image of disc fibre integration with cartilage matrix in the ovine endplate. Six regions of interest with differing fibre organisations highlighted with yellow boxes and numbered. B) Histograms of directionality from SHG image (A) of six regions of interest. The values on the y axis are normalised so that the average value of the Fourier components is equal to 1.*

Comparing the fibre alignment above the cement line (ROI 1) and below the cement line (ROI 2), Fig. 4.24 demonstrates that both regions are relatively organised, however, it was not possible to obtain a signal from the central region of the image, as the SHG was not bright enough, suggesting that these fibres are perpendicular to the imaging plane.

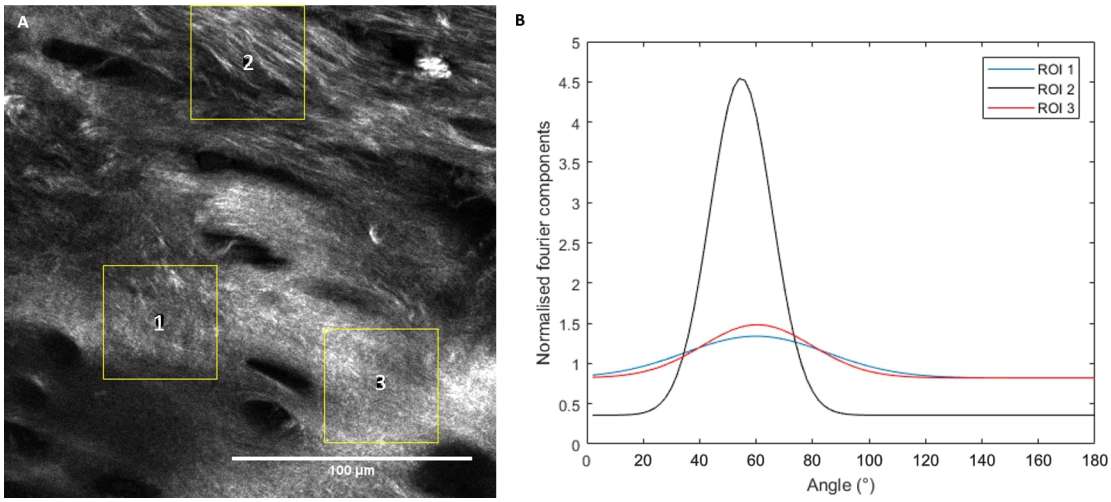

Figure 4.23: *Fourier transform of three regions of interest. A) Zoomed SHG view of the ovine disc fibre integration with cartilage matrix. Three regions of interest with differing fibre organisations highlighted with yellow boxes and numbered. B) Histograms of directionality from SHG image (A) of three regions of interest. The values on the y axis are normalised so that the average value of the Fourier components is equal to 1.*

This should be further investigated with polarisation sensitive SHG, as the transition from type II collagen in the disc to type I in the bone is of interest. The integration with the bone, is visualised in Fig. 4.25. The fibres extending from the bottom left cross the cement line and show integration with the fibres forming the round shape of the osteon.

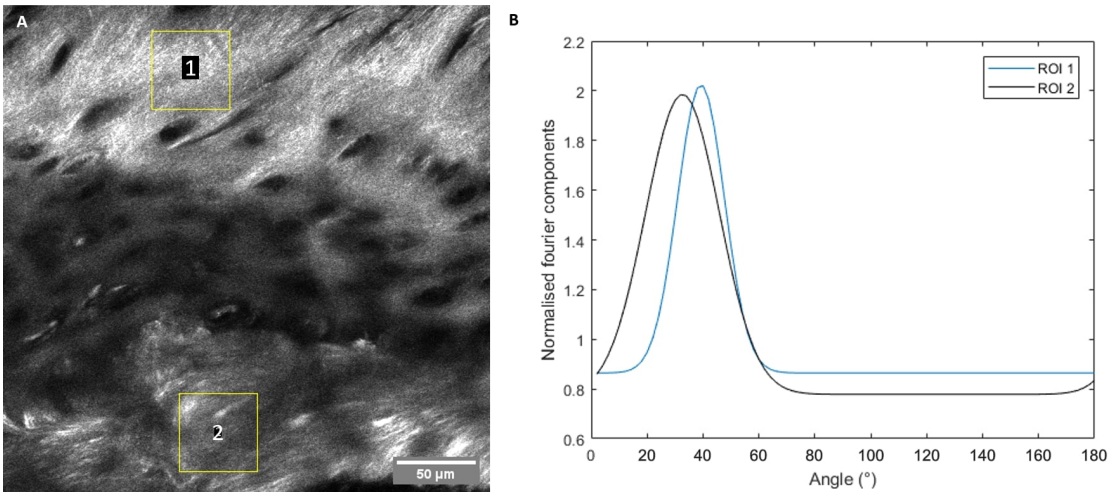

Figure 4.24: *Fourier transform of two regions of interest. A) SHG image of the ovine cement line. Two regions of interest, one post and one prior the cement line. ROI highlighted with yellow boxes and numbered. B) Histograms of directionality from SHG image (A) of two regions of interest. The values on the y axis are normalised so that the average value of the Fourier components is equal to 1.*

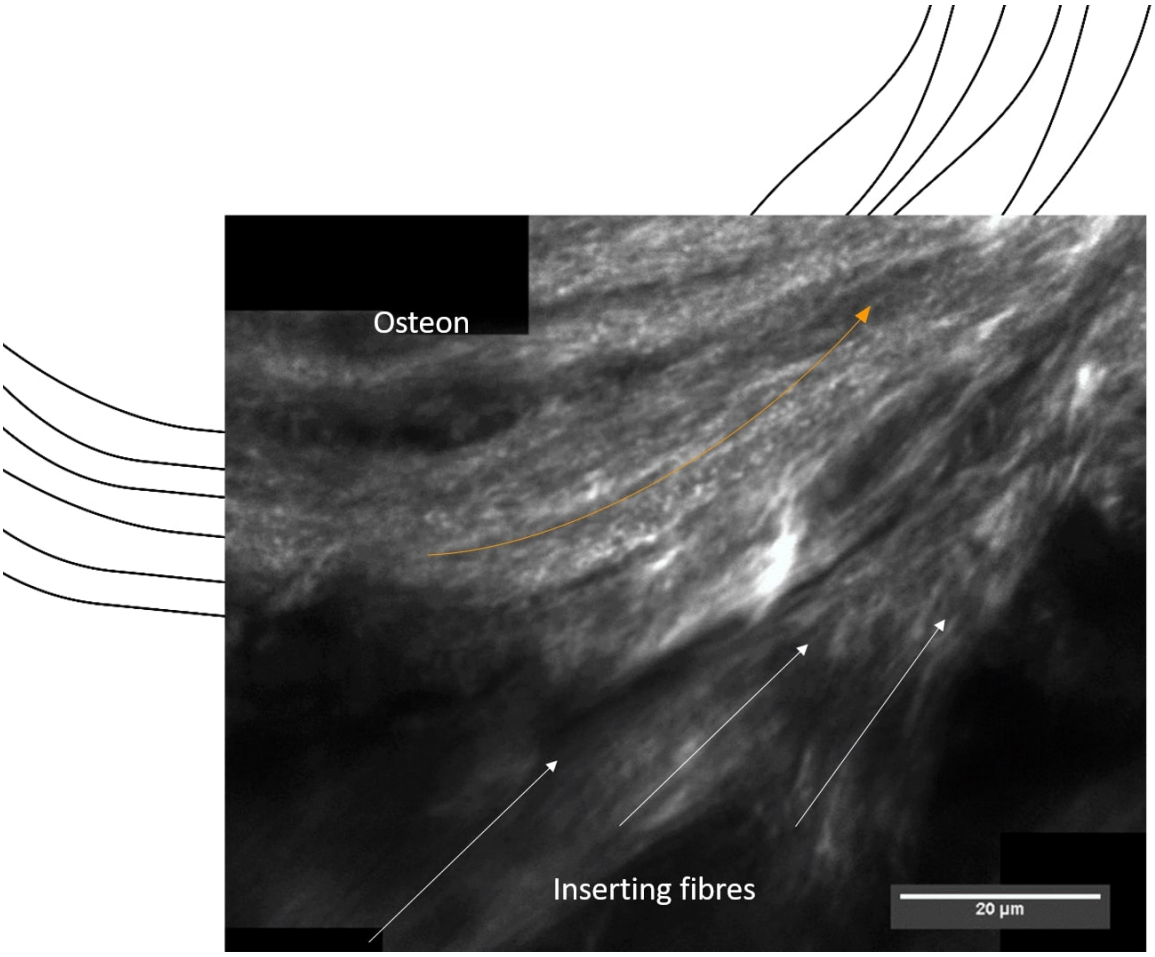

Figure 4.25: *SHG image of disc fibre integration (white arrows) with osteonal fibres (orange arrow).*

Elastin in the Endplate

Elastin was visualised in the cartilage regions of the endplate. Fig. 4.26 shows a number of instances where elastin like fibres were present (indicated by green arrows). These fibres are evident in the TPF images but not the SHG images and therefore cannot be collagen fibres. They appear as thin, bright TPF lines and were most commonly seen in images of the cartilage/TM regions, however, were not imaged frequently enough to quantify their abundance. Fig. 4.27 also shows elastin fibres (green arrowheads), however, this time in the nucleus, in contrast to the cartilage endplate these appear much shorter, less aligned and less uniform. Considering the collagen fibres of nucleus form a loose network compared to that of the highly aligned and organised annulus, the elastin fibres following a similar pattern corresponds. This also raises the question of the role of the elastin fibres in the mechanics of the disc and endplate, or whether the endplate merely tethers the disc network.

The diameter of these fibres is difficult to measure, however, taking an intensity profile across a fibre can distinguish it from the background and give an estimation of the size. Fig. 4.28 shows the intensity profile across an elastin fibre in the non-MC, and in the nuclues of the IVD. The peak of the intensity profile indicates the elastin fibre, however, the high background signal makes defining the exact size difficult. Fig. 4.28 A suggests a thickness size of 0.6 - 1.2 μm depending on which points are included either side the peak. Similarly Fig. 4.28 B, suggests between 1.2 - 1.8 μm. This is consistent with the diameter of single fibres in disc and cartilage.

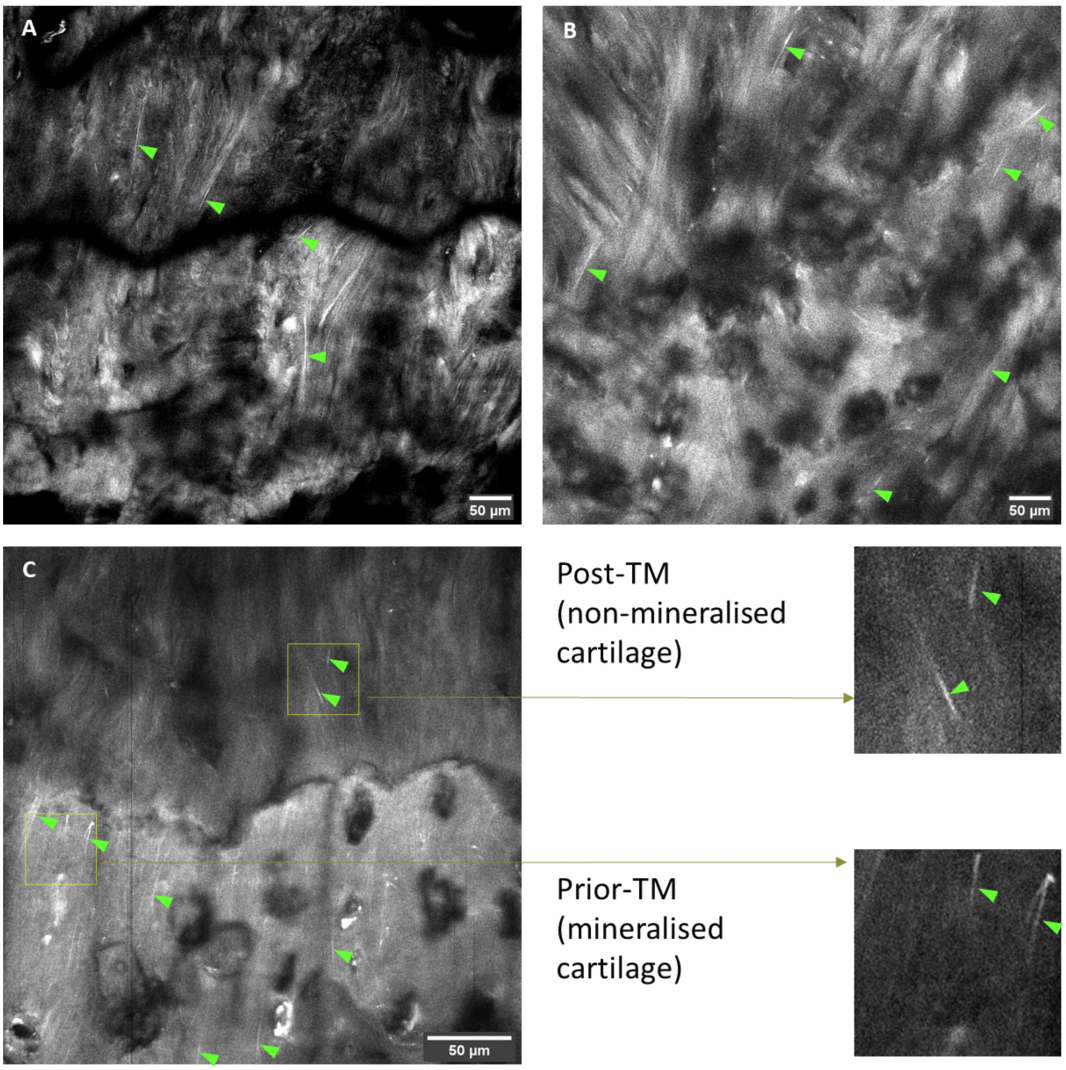

Figure 4.26: *TPF images of Elastin fibres at the tidemark. A, B and C) TPF images that show evidence of elastin fibres (indicated by green arrowheads). C) Displays two regions of interest indicated by yellow boxes and magnified views of these regions.*

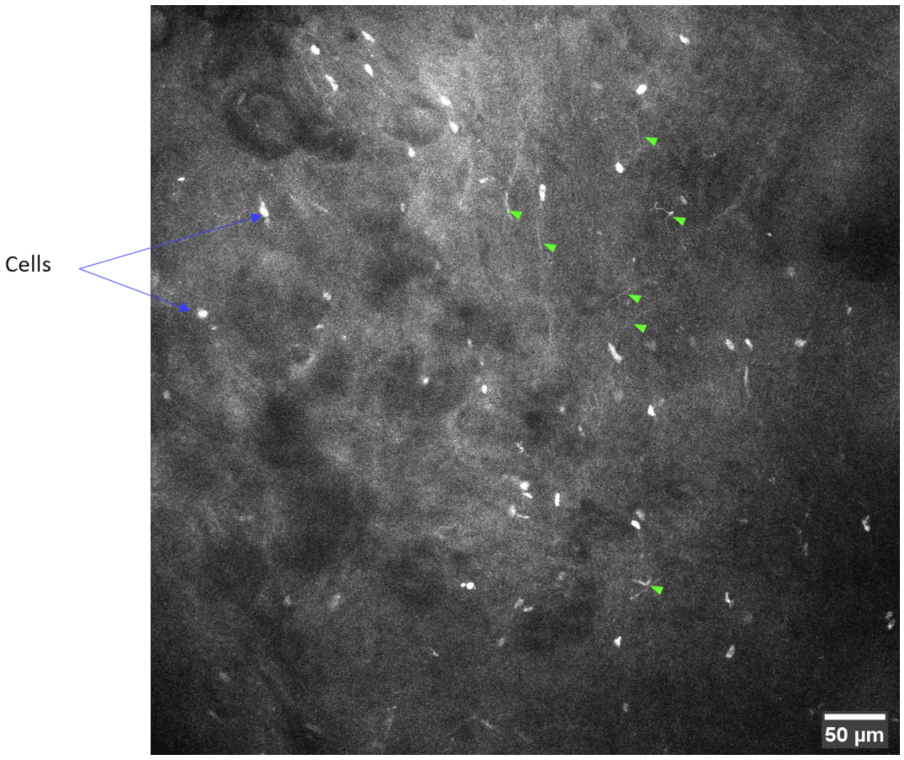

Figure 4.27: *Visibility of short elastin fibres in the nucleus with TPF. Blue arrows indicate autofluorescence from cells, green arrow heads indicate some elastin fibres.*

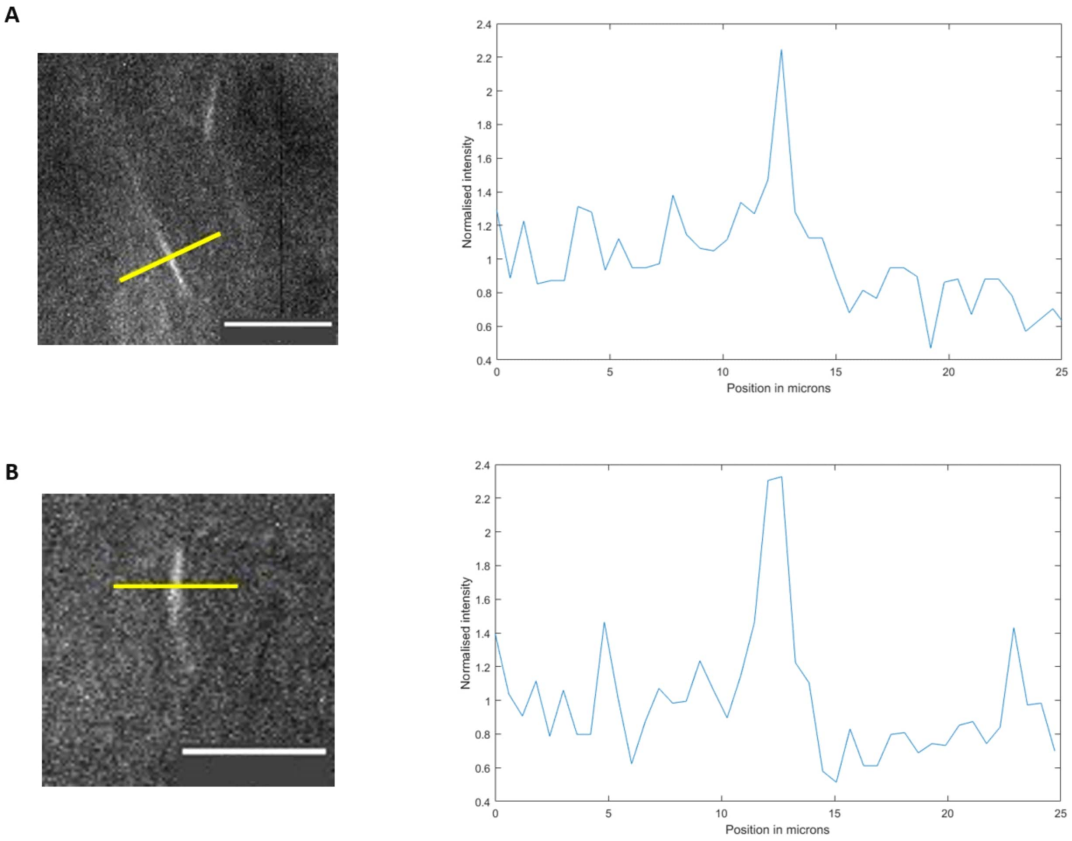

Figure 4.28: *Elastin fibre thickness. A) TPF image of an elastin fibre from the non-MC region with ROI in yellow. Intensity of the line plot indicates a thickness of 0.6 - 1.2 µm. B) TPF image of an elastin fibre from the IVD nucleus with ROI in yellow. Intensity of the line plot indicates a thickness of 1.2 - 1.8 µm.*

4.8.5 Bovine Biochemical Composition

Characteristic Raman spectra of the bovine bone, endplate (cartilage endplate) and disc are shown in Fig. 4.29, all spectra have common bands due to collagen and proteoglycans. The bone is notably different from the other two regions, especially due to the intense phosphate peaks, whilst the disc and endplate have similar peaks and related intensities.

A list of the bands observed in the average spectra of Fig. 4.29, together with their assignments to vibrational modes are shown in Table. 4.1. The assignments have been derived from literature on cartilage and bone as no studies currently exist on the endplate region. Bands such as amide III at 1245 and 1270 cm^{-1} are peaks which can be de-convoluted from the broad amide III peak and are characteristic of the triple helix of collagen.

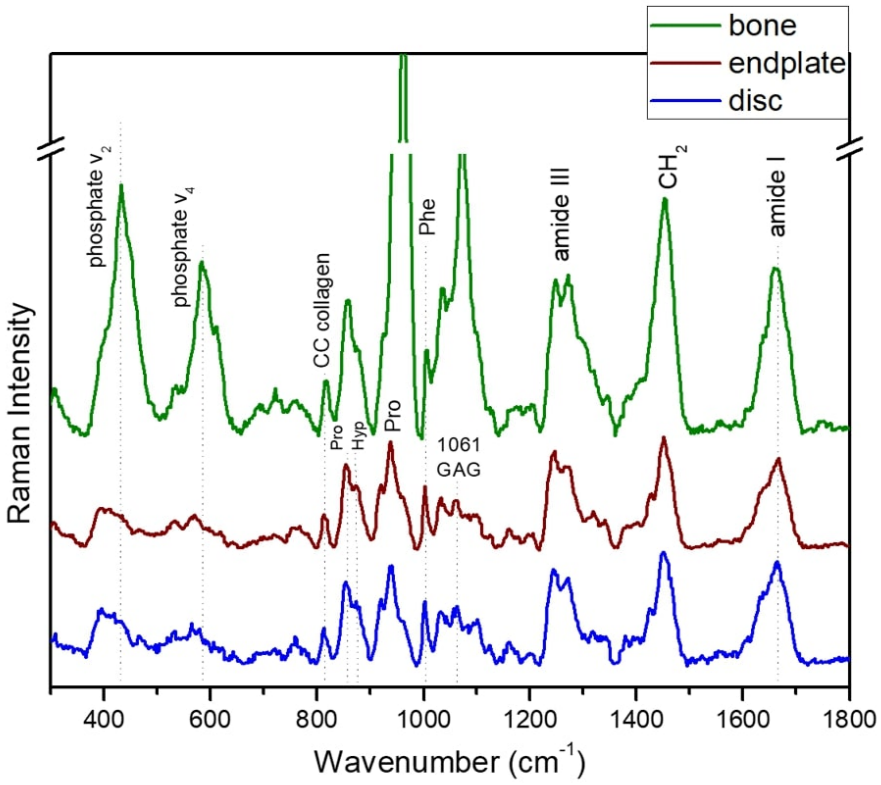

Figure 4.29: *Example Raman spectra, characteristic of bovine bone, endplate (cartilage) and disc (annulus). Intensities of the endplate and disc (annulus) have been normalized to the phenylalanine band (1003 cm^{-1}). The spectral offset has been adjusted for clarity. Peak attributions can be seen in Table. 4.1.*

Table 4.1: *Raman shifts (cm^{-1}) and assignments of the bands observed in a characteristic Raman spectrum of bovine endplate[201,208–211] (the assignments were derived from cartilage and joint tissues research papers as there are currently none specifically for endplate).*

Raman shift (cm^{-1})	**Assignment**
813	C-C of polypeptide collagen backbone
854	(C-C) stretch of proline ring
873	(C-C) stretch of hydroxyproline ring
919	(C-C) stretch of proline ring
938	(C—C) deformation, aggrecan/ (C—O—C) stretch, GAG/ collagen, ν C-C (protein backbone proline)
1003	phenylalanine (C—C) symmetric ring stretch
1033	phenylalanine (C—C) symmetric ring stretch
1061	SO-3 symmetric stretch; GAG
1172	ω CH2 proline
1205	(C—C6H5) stretch; phenyalanine, tryptophan, hydroxyproline, tyrosine
1245	(C-N) amide III
1270	(C—N) stretch alpha-helix; amide III
1318	(CH3, CH2) proline,
1340	glycosaminoglycans, δ C-H (CH2)
1426	glycosaminoglycans, vs COO-
1450	(C—H) bend; protein CH2,CH3 scissor
1553	ν C=C aromatic ring (Trp, Tyr)
1667	ν (C=C) and (C = O) stretch alpha-helix; Amide I

Spectral Ratios

In order to compare the spectral bands between the endplate regions under annulus and nucleus, it was necessary to quantify the height of the specific spectral bands. More specifically, spectral ratios were employed in order to compare normalized values as in previous studies.[212] This is essential as the absolute values of spectral bands can be affected by scattering cross-section, sampling volume, orientation, absorption and instrument settings in each measurement.[213]

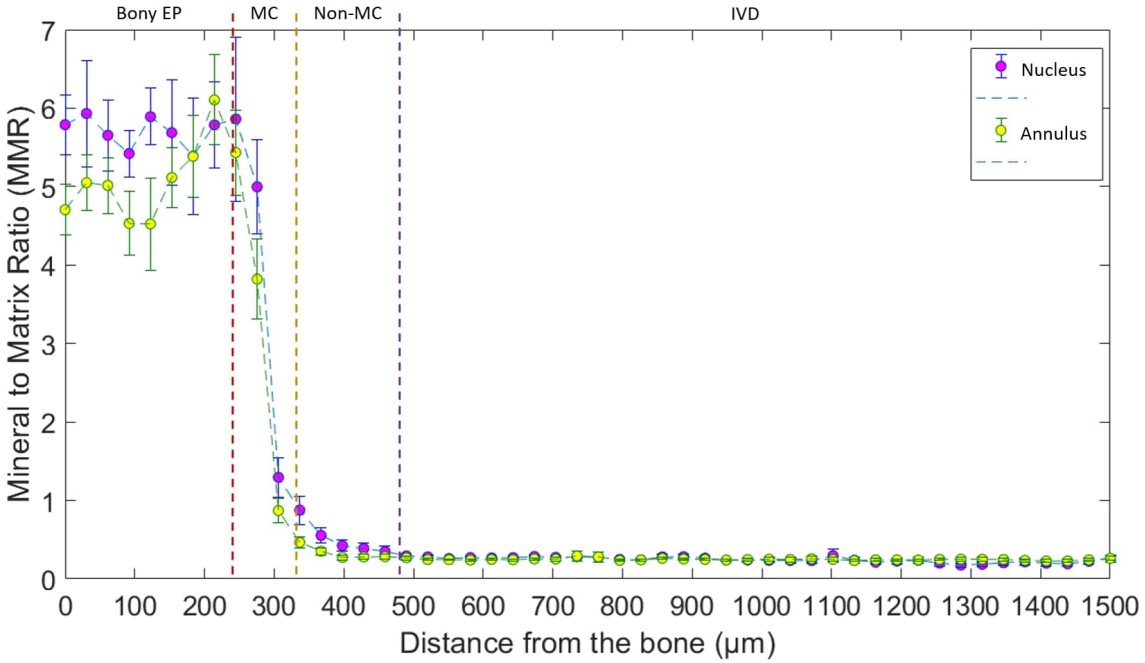

Figure 4.30: *Mineral to Matrix Ratio [959 cm^{-1}/(855 cm^{-1} + 877 cm^{-1} + 922 cm^{-1})] of 8 bovine samples as a function of the sample depth in the transition from BEP to the annulus (green/yellow plots) and the nucleus (blue/pink plots). Error bars show standard deviation.*

The following ratios were investigated:

- Mineral to Matrix Ratio (MMR) [959 cm^{-1}/(855 cm^{-1} + 877 cm^{-1} + 922 cm^{-1})] describes the mineral aspect of the bone composition (Fig. 4.30). The primary phosphate vibration (v1) at 959 cm^{-1} is normalized to the amount of collagen matrix (855 cm^{-1} (proline), 877 cm^{-1} (hydroxyproline) and 922 cm^{-1} (proline) of collagen), with the collagen peaks employed to be independent of collagen cross-linking modifications.[212,214–216]

  Table. 4.2 demonstrates a higher MMR under the nucleus than the annulus in the BEP. Fig. 4.30 shows a steep decline from the MC that continues through the

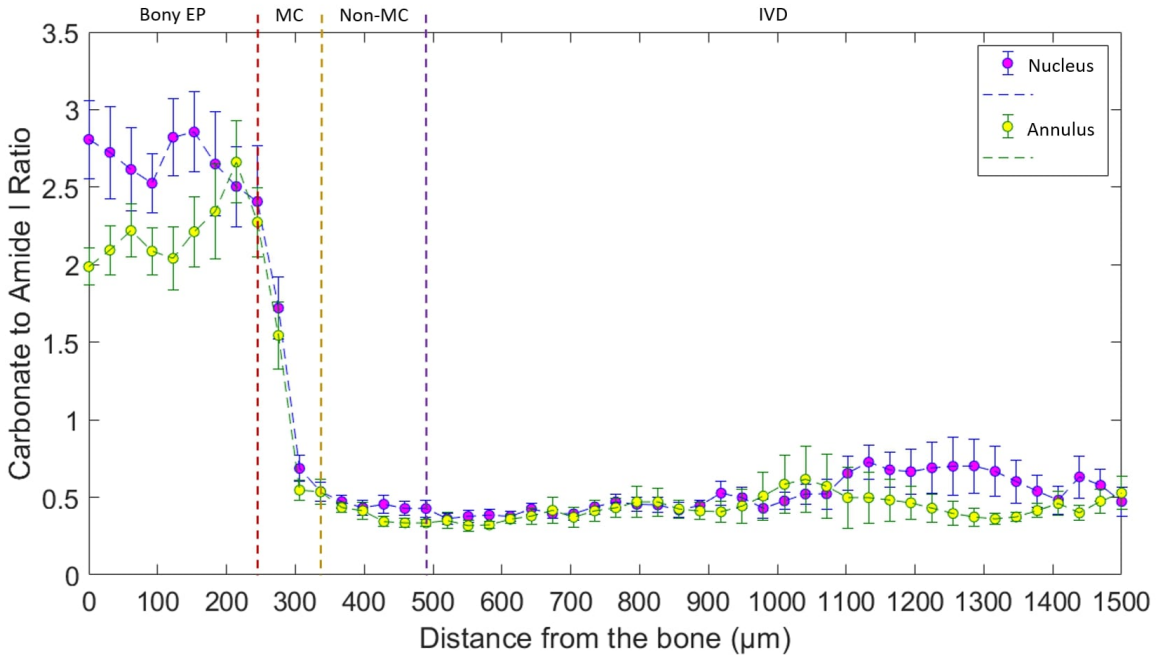

Figure 4.31: *Carbonate to Amide I ratio [1074 cm^{-1}/ 1665 cm^{-1}] of 8 bovine samples as a function of the sample depth in the transition from BEP to the annulus (green/yellow plots) and the nucleus (blue/pink plots). Error bars show standard deviation.*

non-mineralised, but remains marginally higher under the nucleus. There is no mineral present in the non-MC or disc which makes the MMR not applicable to this region.

- Carbonate to Amide I ratio [1074 cm^{-1}/ 1665 cm^{-1}] is another measure of mineral bone component over organic matrix which may indicate bone remodelling.[212,217] Table. 4.2 shows carbonate to amide I ratio is higher under the nucleus, however, starts to drop before reaching the MC. Decrease continues in the MC (Fig. 4.31), but is not as steep a drop as seen in MMR (Fig. 4.30). Again, because of the lack of mineral in the IVD and non-MC this ratio does not apply to these regions.

- Carbonate to Phosphate Ratio (CPR) [1074 cm^{-1}/ 959 cm^{-1}] describes the content of carbonate over the phosphate ions in the molecule of bioapatite in bone. As CPR is an indication of ionic substitution into the phosphate positions within the apatite lattice,[212] it is also related to the architecture of bone and the mineral crystallinity.[218] The measure of CPR should be disregarded in relation to the IVD and non-MC as the carbonate and chondroitin sulphate peaks are too close to differentiate here. The higher the CPR, the more carbonate present in the tissue.

The CPR is very similar under the annulus and nucleus in the bone and MC. In the non-MC it is shown to be slightly higher under the annulus (Fig. 4.32).

- Phosphate to Amide I ratio [959 cm^{-1}/ 1665 cm^{-1}] is another indicator of the mineral content in the bone, normalized to the matrix content.[216] The higher the phosphate to amide 1 ratio, the more phosphate present in the tissue, indicates a higher level of mineralisation.

  The ratio is higher under the nucleus than the annulus in the BEP and MC (Fig. 4.33, Table 4.2). The lack of mineral in the non-MC and IVD explains the low ratio under both the annulus and nucleus.

- Water content [30 cm^{-1}] normalized to the CH spectral band [2853 cm^{-1}/ 2945 cm^{-1}] indicates the hydration of the sample. Water content is higher under the nucleus in the BEP, however, the standard deviations indicate great sample variability. The annulus shows much lower water content, but has very small standard deviations in the BEP. The results in the non-MC show a slight rise in the water content,but again with very high variation between the samples.

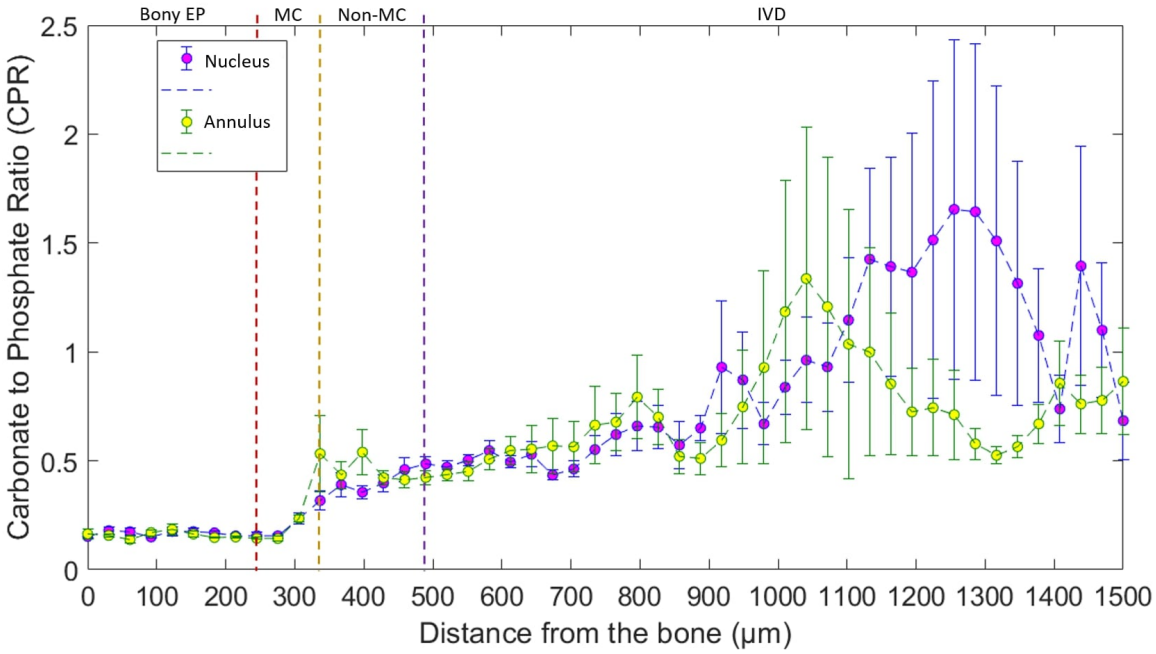

Figure 4.32: *Carbonate to Phosphate Ratio (CPR) [1074 cm^{-1}/ 959 cm^{-1}] of 8 bovine samples as a function of the sample depth in the transition from BEP to the annulus (green/yellow plots) and the nucleus (blue/pink plots). Error bars show standard deviation.*

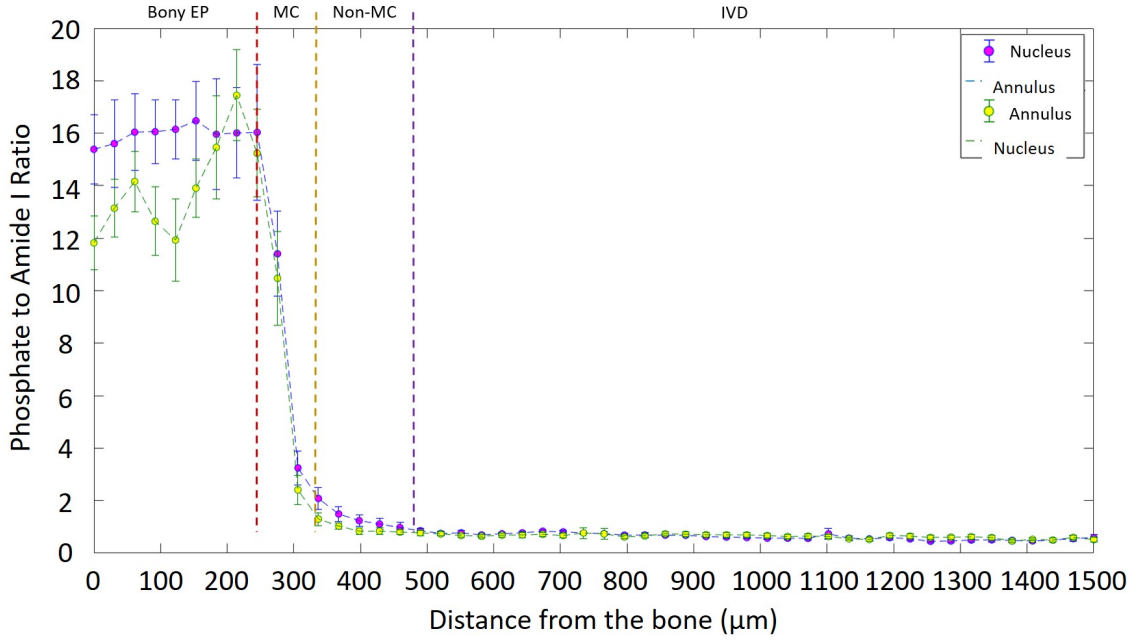

Figure 4.33: *Phosphate to Amide I ratio [959 cm^{-1}/ 1665 cm^{-1}] of 8 bovine samples as a function of the sample depth in the transition from BEP to the annulus (green/yellow plots) and the nucleus (blue/pink plots). Error bars show standard deviation.*

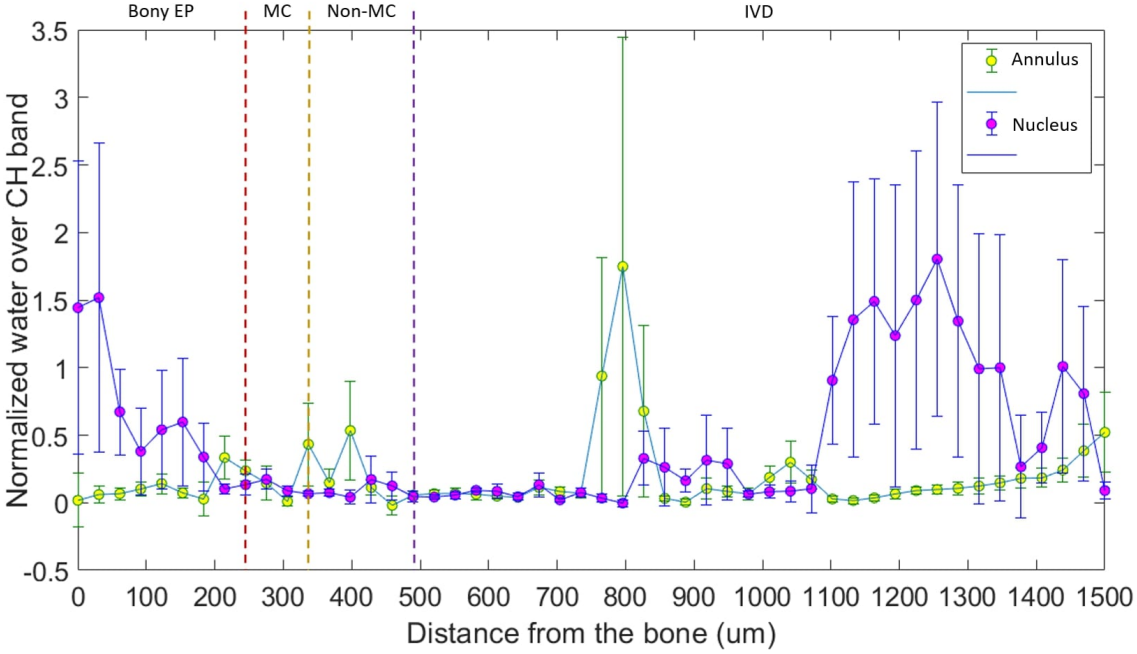

Figure 4.34: *Water content normalised to the CH spectral band [2853 cm^{-1}/ 2945 cm^{-1}] of 8 bovine samples as a function of the sample depth in the transition from BEP to the annulus (green/yellow plots) and the nucleus (blue/pink plots). Error bars show standard deviation.*

Table 4.2: *Average peak height ratio values for bone endplate (Bony EP), MC (MC), non-MC (non-MC) and intervertebral disc (IVD) under the nucleus and under the annulus. (grey values are calculated on overlapping bands so might not be as accurate)*

Peak Ratio	Bony EP		MC		Non-MC		IVD	
	Nucleus	Annulus	Nucleus	Annulus	Nucleus	Annulus	Nucleus	Annulus
MMR	5.71	5.1	3.15	2.35	N/A	N/A	N/A	N/A
Normalised CS	N/A	N/A	1.16	1.07	0.71	0.67	1.05	0.89
Carbonate to Amide I	2.66	2.21	1.2	1.05	N/A	N/A	N/A	N/A
Phosphate to Amide I	15.97	13.97	7.33	6.44	N/A	N/A	N/A	NA

4.8.6 Degenerate Human Tissue

The human samples utilised in this study were excised during surgery to replace degenerate intervertebral discs. The human samples showed wide variability at both the macro and micro level making generalisation difficult. Although the sample sites were not classified by the surgeon, they were classified post-hoc as annulus or nucleus depending on the collagen orientation in the soft tissue.

Fig 4.35 shows a representative image of a 20 μm slice of a human sample with a dissection microscope. Because these samples were also used for bio-chemical analysis, they were not fixed and tended to roll in on themselves as thin sections, causing artefacts (Fig. 4.35 A). It was not possible to distinguish the different regions of the endplate, even to ascertain whether there was any MC or BEP at all. Some contrast in the images seemed to indicate a tidemark and cement line, but this could also be due to the sample topography (Fig. 4.35 B).

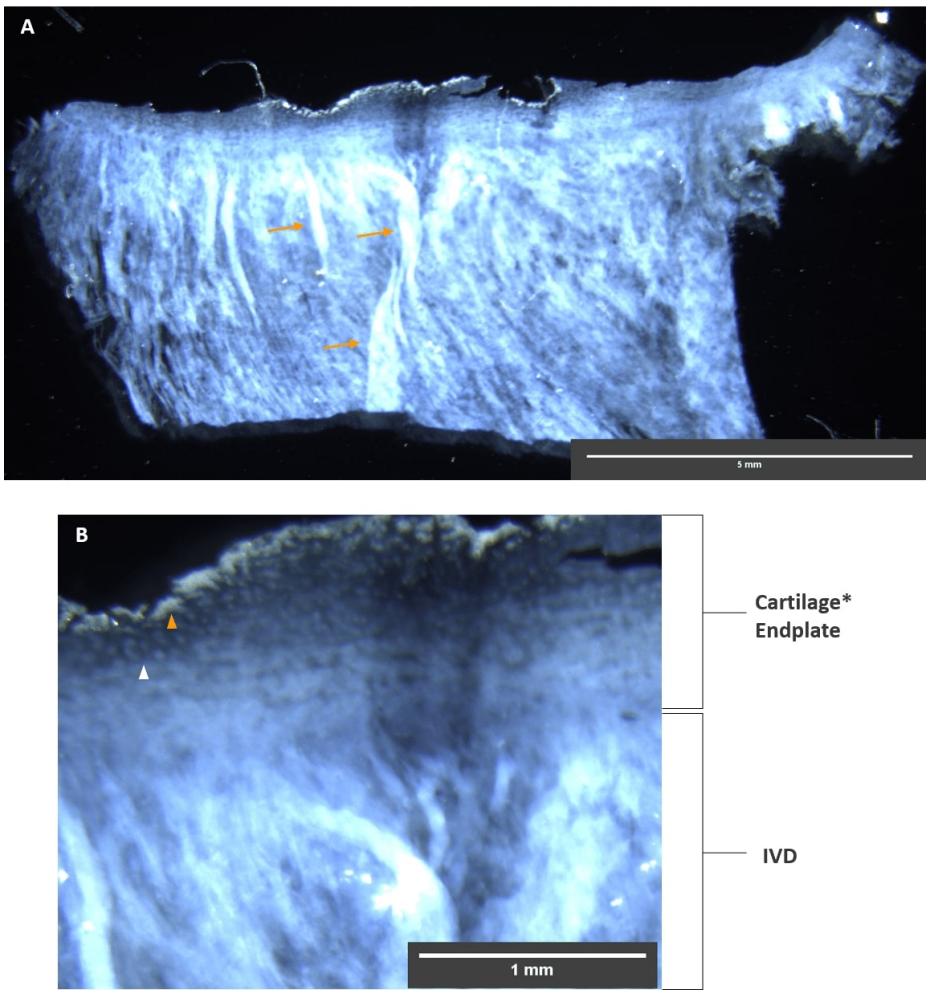

Figure 4.35: *Low resolution dissection microscope images of a Human specimen (Female, 53 years with high levels of degeneration). A) shows the whole sample. Orange arrows indicate where the section has folded in on itself creating artefacts in the image. B) Focused on the top edge of the sample shows a cartilage region, whether it is mineralised or non-mineralised is not known(*). However, a possible tidemark is indicated with a white arrow head, and cement line with an orange arrow head.*

Multiphoton images of the human samples also showed no clear tidemark. The specimen in Fig. 4.36 does show a slight decrease of TPF and increase of SHG moving from the disc upwards, however, there is no clear delineation. Additionally, the disc, especially in the mid-left of the image shows a high TPF signal, suggesting that the soft tissues are also giving high TPF signal. This may arise from the formation of fluorescent cross-links in the collagen or other processes associated with aging and warrants further investigation. The high TPF signal was seen across the human samples, however, their structure differed. Fig. 4.37 doesn't show an obvious tidemark, however, there is an obvious change in fibre direction as indicated by the white arrows.

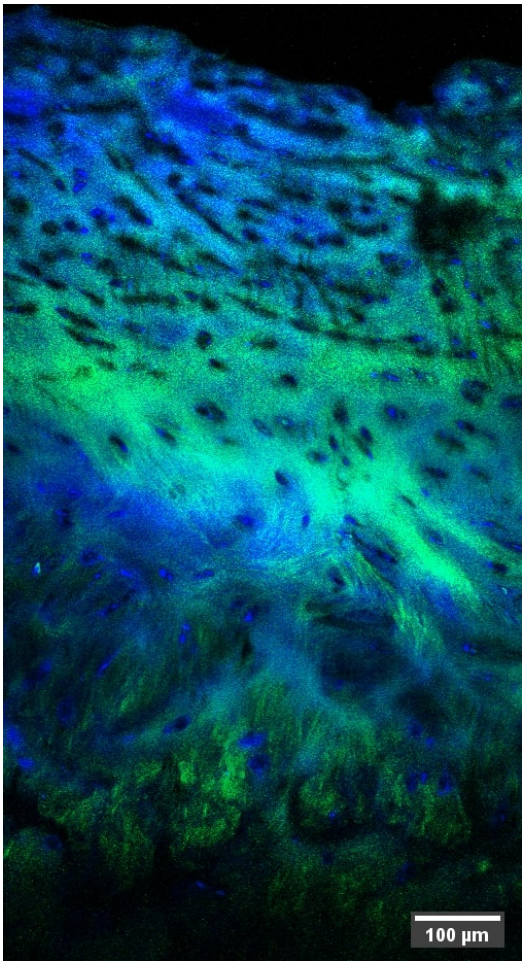

Figure 4.36: *Multiphoton image of the same sample as shown in Fig. 4.35, orientation is the same with the cartilage at the top of the image, and the disc below. SHG = green, TPF = blue.*

Fig. 4.38 A, shows the higher auto fluorescence was seen within the human tissue. Additionally cells are more clearly outlined and there appears to be a separation of some mineralised tissue from the non-mineralised. The delineation of the endplate from the disc is also much more uniform compared to the bovine. In Fig. 4.38 B, the samples show a highly aligned region of cartilage under the disc which is not apparent in bovine

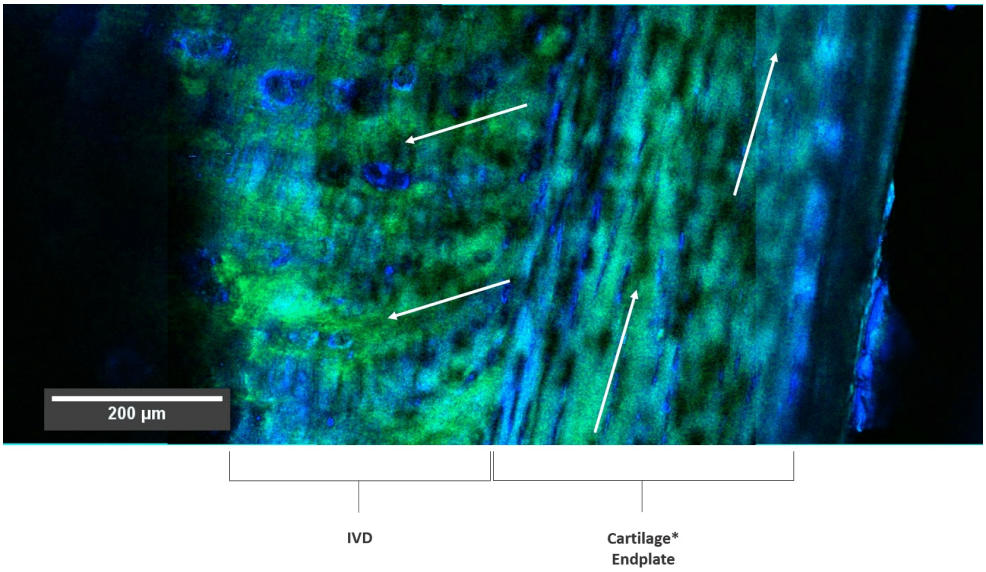

Figure 4.37: *Multiphoton image of another human sample (Male, 54 with high levels of degeneration). The right hand side of the image shows a cartilage region (* unknown if mineralised, or non-mineralised), and the IVD to the left. White arrows indicate the predominant tissue direction. SHG = green, TPF = blue.*

samples. It additionally appears that the fibres of the disc curve, and change direction to join the cartilage, which was not seen in the bovine. There is no visible TM in the human sample, though it is obvious in the bovine (Fig. 4.38 C).

The nuclear region, again shows the cells are much clearer in the human than bovine. The dark parallel lines on the cartilage of the human samples are artefacts from the cutting process and do not pertain to the structural study of the endplate (Fig. 4.39 A). Fig. 4.39 B, shows there is little to no SHG signal beyond the aligned cartilage region. This is very different to the bovine where we see an increase in the SHG signal from the collagenous disc fibres. The TPF signal past the cartilage indicated that there is tissue present, just not that which produces a SHG signal. Additionally, the closer to the disc, the lower the intensity of the SHG signal. This is the opposite to the bovine in which we see the clear jump at the tidemark junction between the mineralised and non-MC. This may be indicative of degenerative structural changes in the collagen that weakened the SHG, as when viewed under polarised light (no images collected) collagen still appeared present.

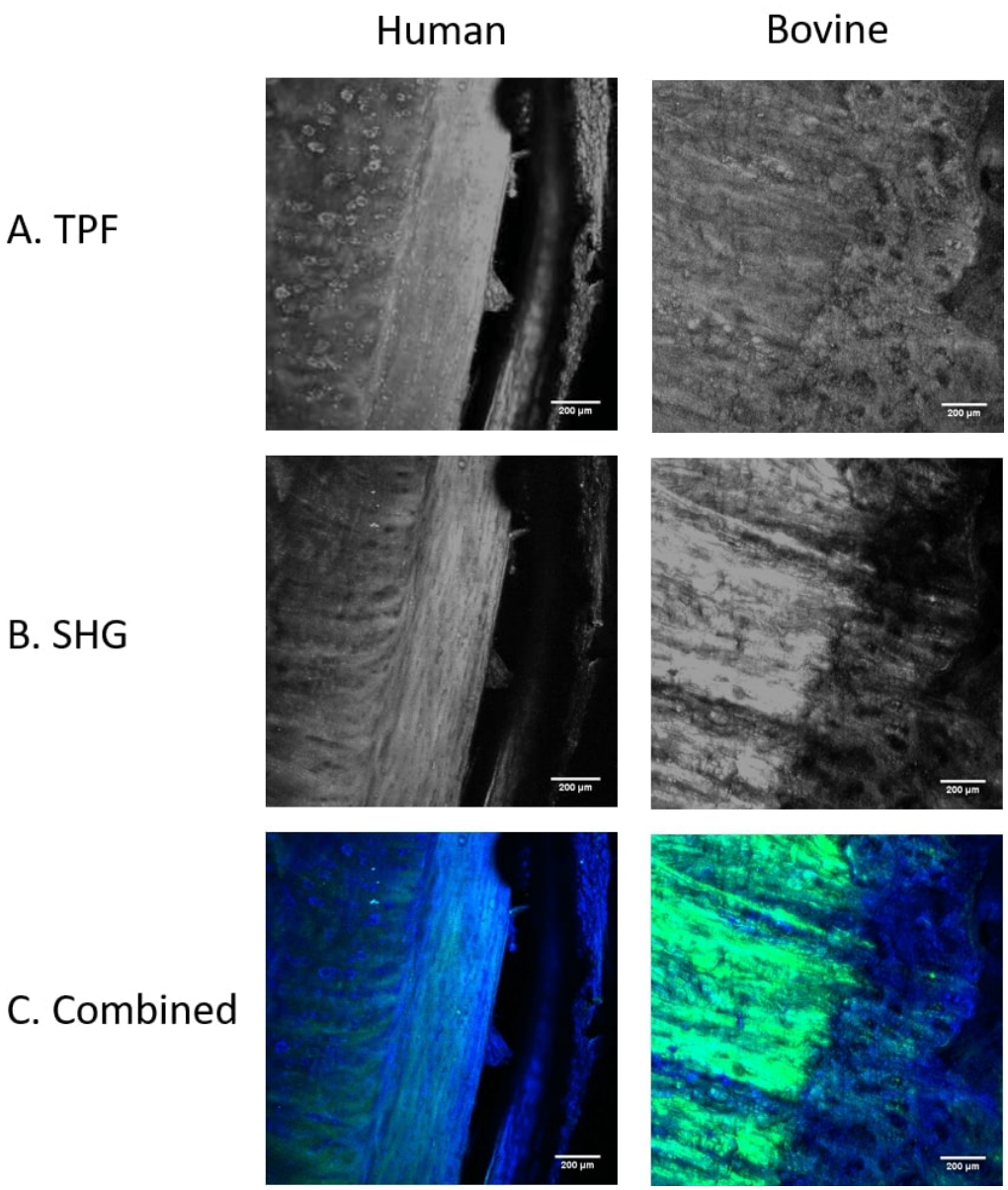

Figure 4.38: *Comparison of multiphoton images of annular region of endplate in human (Male, 54 with high levels of degeneration) and bovine. A) TPF signal only. B) SHG Signal only. C) TPF (blue) and SHG (green) composite.*

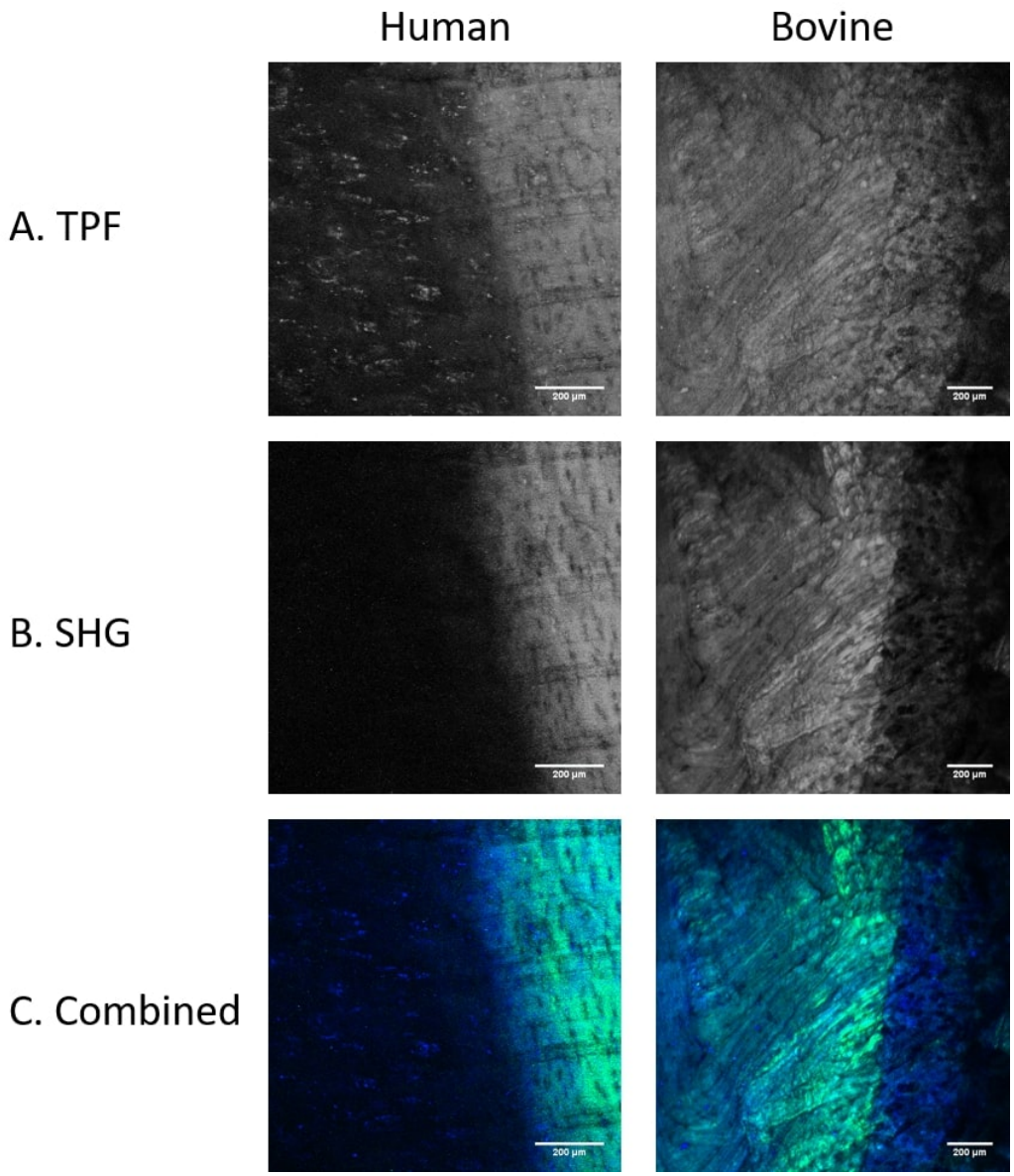

Figure 4.39: *Comparison of multiphoton images of nuclear region of endplate in human (Female, 37 with high levels of degeneration) and bovine. A) TPF signal only. B) SHG Signal only. C) TPF (blue) and SHG (green) composite.*

Human Raman Microscopy

Spectra of the degenerate human samples showed small amounts of phosphate at the very edge of the sample. Characteristic spectra were taken from three regions, these are shown in Fig. 4.40 as dark, transition and light. The dark region in the white light image indicates an intense phosphate peak compared to the other two, though they all have spectra in common due to proteoglycans and collagen (Fig. 4.41).

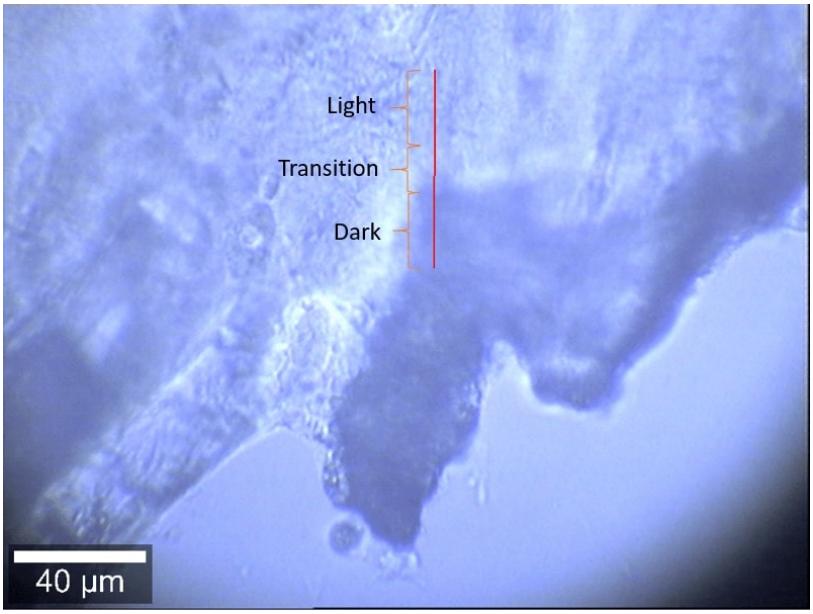

Figure 4.40: *White Light image of human sample indicating the three regions of interest, dark, transition and light.*

Comparing the degenerate human and bovine tissues (Fig. 4.41), the dark region of the human (green line) is more similar to the MC of the bovine (red) than the bone (green). The human light region also appears similar to the disc in the bovine, with similar peaks being displayed. This suggests that the human sample contains a thin layer of MC, and the amount of phosphate progressively drops as it transitions to disc tissue.

Raman intensity maps for peaks of interest are shown in Fig. 4.42. The phosphate appears to be in small clusters, and the intensity of these clusters reduce the further into the non-MC (Fig. 4.42 A). The phosphate clusters almost correlate to the dark regions in the amide III map (Fig. 4.42 B), however, further analysis would be required to confirm this.

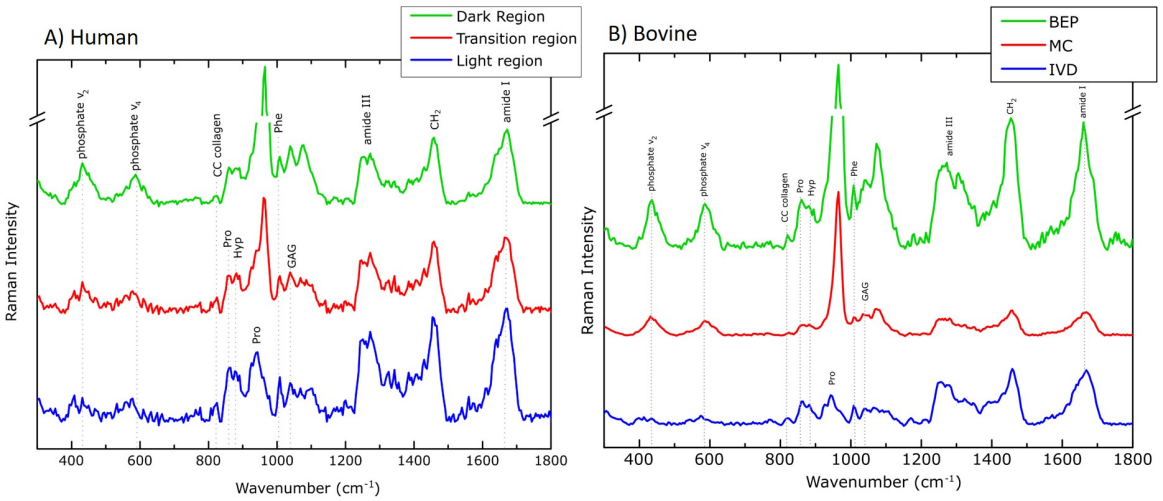

Figure 4.41: *Comparison of degenerate human and bovine spectra. A) Example point spectra from each of the three regions shown in Fig. 4.40. B) Representative bovine spectra of the BEP, MC and disc. The spectral offset has been adjusted for clarity. Peak attributions can be seen earlier in Table 4.1.*

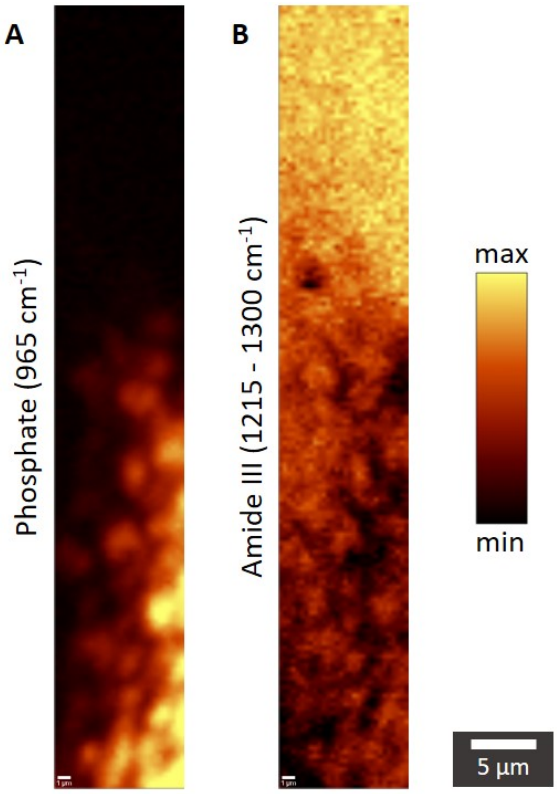

Figure 4.42: *Phosphate and amide III intensity maps of the region indicated with the red line in Fig. 4.40 at higher magnification (10 x 60 µm). A) Intensity map of phosphate [959 cm^{-1}]. B) Intensity peak of amide III [1215 cm^{-1} - 1300 cm^{-1}].*

4.9 Discussion

This study distinguished three regions of the endplate:

1. The Bony Endplate - a dense region of bone between the trabeculae of the vertebrae and the cartilage regions of the endplate.

2. Mineralised Cartilage - separated from the BEP by a cement line, this region is as its name indicates, is formed of a MC

3. Non-Mineralised Cartilage - separated from the MC with a tide mark, this region contains little to no mineral and its fibres align parallel to the tidemark.

First the general structure is discussed followed by focus on each specific zone.

4.10 Endplate Structure of the Bovine and Ovine Models

Sheep lumbar spines and cows tails have distinct growth plates and the endplate follows the contours of the growth region, resulting in a flat and convex endplate respectively (Fig. 4.4 and 4.8.1). This study did not have access to any intact human spinal units, however, the literature indicates the human endplate is usually concave, sitting within the apophysis ring.[192] Although it should be noted that the ratio of height at the centre of the vertebral body compared to the posterior changes with aging, degeneration or disease.[219,220]

Another difference between the animals was the visibility of the tidemark. Bovine samples showed the most clear distinction between mineralised and non-MC (Fig. 4.5). Ovine samples also showed the tidemark, however, they displayed a higher SHG signal in both the disc and MC, making a clear distinction more difficult. Therefore the bovine tail was utilised to analyse the tidemark, whereas the high SHG signal of the ovine made analysis of the soft tissues easier and was therefore used predominantly when relating to the disc and its anchorage to the vertebrae. The amount of SHG signal produced is dependent on the orientation and polarisation of the incident laser light with respect to the fibre axis. Maximum SHG signal is detected when the light is polarised along the fibre axis.[149,150,152] Therefore the difference in signal between the ovine and bovine samples may indicate variation is fibre axis, causing a change in the SHG. Further investigation using polarisation dependence SHG such as utilised by Yasui et al.,[150] is imperative in

understanding the differences between these two models, and how it relates to the endplate structure and function.

4.11 Age Differences

4.11.1 DIC

Within the adult ovine spine samples age played a role in the observed structure. DIC optical microscopy showed an abundance of osteons in the young adult spine (1-4 years, Fig. 4.10) that were not present in the mature adult spines (4+ years, Fig. 4.9), yet did show a number of larger trabecular like holes. The young adult spines were all above 1 year meaning they had all reached maturation. Similar findings have been shown with aging in the illiac crest, femur and tibia.[221–223] The 'trabecularisation of the endocortical surface' due to increased remodelling sees an increase in the porosity of cortical bone and a reduction of osteons, which contain the bones' blood supply.[224,225] An increase in remodelling would explain the reported increase in porosity of the endplate with age, and the decrease in trabecular thickness.[99] The decrease in osteons containing blood vessels within the haversian canals, may also relate to the reduction of blood supply to the disc with age.[30,120]

4.11.2 SEM and EDS Imaging

In agreement with the preceding discussion, SEM images suggest an increase in the porosity of the endplate with age through the occurrence of more marrow channels, and fewer osteons in the mature adult spine (Fig. 4.11). Although the tidemark and cement line were visible in some images, they were not always obvious, making the quantification of these observations difficult. However, EDS allowed the calculation of the Ca/P ratio. Due to the homogeneity of samples, it was difficult to compare different regions of the endplate in the Ca/P ratio, however, the young adult samples showed a statistically higher Ca/P ratio in all three regions measured (anterior-AF, mid-NP and posterior-AF, Fig. 4.12). However, this result should be considered with caution, as the Ca/P ratio of bone is estimated to be 1.6 due to the ratio of calcium to phosphate in predominant mineral hydroxyapatite ($Ca_5(PO_4)_3(OH)$). None of the averages measured in this study were much higher than 1. The levels recorded are much more akin to mono-calcium phosphate (0.5) and di-calcium phosphate (1.0).[226] Lower levels of Ca/P have been associated with bone loss,[227] however, such low levels would not be expected in healthy

animal samples. More likely, the method of sample preparation limited this study. In order to use the samples for DIC after using them for SEM (could not be done before as demineralisation is required for DIC), samples were not embedded, limiting the amount of polishing possible. Backscatter SEM and EDS require highly flat surfaces for the best results, which by looking at the SEM images in Fig. 4.11 is obvious was not the case with the samples in this study. Another possibility is that the presence of fat, marrow and collagen may have obscured the experimental measurements.[228,229] Samples were subjected to a hexane wash and hyaluronidase treatment to remove the fat and other components, however, possibly due to the thickness of the samples, the fat cells were still obvious in the marrow channels. This may have increased the charging. If these difficulties can be overcome, it would be interesting in future work to be able relate the changes in mineral with the changes observed in the porosity of the endplate, as these both would effect the mechanical function of this region.

4.12 The Cartilage Endplate

4.12.1 The Tidemark

The tidemark was most clearly visualised by a change in SHG to TPF ratio detected with the multiphoton system (Fig. 4.16). Research by Mansfield et al., was able to identify the tide mark of articular cartilage using similar imaging techniques.[136] In agreement with this study, Mansfield also showed a similar drop in intensity of both SHG and TPF, as well as the change in SHG/TPF ratio, with TPF being higher below the tidemark, and SHG higher above.[142]

The source of a higher intensity of TPF in the MC still remains unknown. Previous work has tested pure hydroxylapaptite for a TPF signal, however, it was not found to fluoresce.[142] Suggested explanations for the increased fluorescence below the tidemark include the presence of an additional fluorophore in the MC, which is not present in the non-MC. Another explanation is that the same fluorophores are present in both the mineralised and non-MC, however, the concentration is greater in the MC. More work is needed to determine the reason for increased fluorescence within the MC.

4.12.2 Elastin

One contributor to the TPF signal is elastin. The elastin fibres in Fig. 4.26 and 4.27 were identified as they were visible in the TPF, but not SHG meaning they could not be collagen.[230] Additionally, they had a similar appearance to elastin fibres shown in the cartilage endplate and intervertebral disc with immunostaining[50] and articular cartilage with TPF.[142,230] The majority of the fibres within the cartilage endplate appear to be relatively short (although this could have been due to them continuing out of the imaging plane), straight and aligned perpendicular to the tide mark, parallel to the collagen fibres (Fig. 4.26. This agrees with the previous immunostaining of the endplate, however, the abundance of elastin in this study appears much lower than previously reported.[50] This is most likely due to the background fluorescence of the matrix. Thicker fibres appear brighter and stand out against the background, these have been shown to measure between 0.6 - 1.2 μm, which is similar to that seen in articular cartilage.[142,230] One study reported fibres appearing to have single pixel diameter and below a certain size the fibres probably will not be visible against the background fluorescence of the extra-cellular matrix.[142,230]

Compared to the elastin in the cartilage endplate, the fibres seen in the nucleus appear much shorter, less aligned, and often curved. This suggests that unlike in the cartilage, these fibres are not under tension. Elastin was only visualised in the bovine tail, but the greater TPF background in the human could have been restricting the visibility of these small fibres. The coexistence of collagen and elastin fibres networks influence the mechanical properties of a tissue.[231] Therefore, the role of the elastin network within the endplate is paramount to understanding the biomechanical environment of the disc, and spinal functional unit. In order to investigate elastin further, it may be worth using an elastin specific stain such as Van-Gieson or Picrosirius Red that will increase the TPF signal intensity higher than that of the background.[232]

4.12.3 Cartilage Endplate Geometry

The distinction of the tidemark and cement line within bovine tail samples allowed the measurement of the thickness of the MC at the inner annulus. However, the lack of distinction between the disc and non-MC made the measurement of the non-MC more difficult. Both cartilage types were thicker in the cranial endplates compared to the caudal at the inner annulus, though the change in thickness was not measured across the

endplate. Surprisingly little work has previously been done on the thickness of the individual cartilage regions. Nosikova et al., showed a thinning of the MC with age (22 v 45 year old human), however, their method of backscatter mode SEM did not allow the measurement of the thickness of the non-mineralised region, nor did they compare the caudal and cranial endplates.[198] Van der Houwen et al., however, did compare the caudal to cranial and found a similar pattern of the cranial endplates being thicker (note in their paper, labelled the endplate inferior and superior in relation to the vertebrae, rather than disc).[195] They did not differentiate which regions of the endplate they were measuring, however, their measurements of thickness are close to those of the combined mineralised and non-MC regions in this study (cranial ~ 1000 μm, caudal ~ 700 μm). The reason for the asymmetry between adjacent endplates is currently unexplained, as functionally the endplates have the same mechanical requirements which suggests this may be a result of differing development, though this is unsubstantiated at this time. Research has indicated that fracture occurrence is disproportionate between endplates, with the caudal plates showing higher incidences.[233] However, this is most likely a result of the thinner endplate rather than an explanation for the morphological differences.

4.13 Fibre Anchoring

SHG enabled the visualisation of the collagen fibres anchoring the annulus to the endplate. Due to the high SHG signal coming from both the disc and non-MC, it was hard to visualise the fibres continuing through to the MC (Fig. 4.18), however, distinct annular bundles were seen inserting into the MC, meaning they had to pass through the non-MC (Fig. 4.19). At initial insertion of the annular bundles into the MC, they are seen to split from the primary annular bundle (PAB) into sub-bundles (Fig. 4.19 and 4.25). This concurs with previous research by Rodrigues et al., who imaged the sub-bundling of the annulus with SEM in mature ovine specimen.[94] They suggested that this is a mechanism to increase the strength of the anchoring of the disc within the endplate, and Junhui et al., came to a similar conclusion from work on human cadaver samples.[94,234] It is important to note that neither of these papers distinguished between the two cartilage regions, rather referred to the 'cartilage endplate' as a single entity. Additionally, both papers note the abrupt end of the fibres at the cement line (start of the bone), as Fig. 4.21 appears to show, however, Fig. 4.25 seems to suggest a fibril level integration of sub-bundles with the osteon matrix. This is in agreement with recent evidence from

Sapiee et al., who suggested intermingling and blending of the fibrils across the CEP-BEP junction.[95]

As previously stated, within the nucleus, the individual collagen fibres cannot always be resolved, however, Fourier transform image analysis was able to reveal the collagen fibril organisation.[136] The annulus bundles are both highly aligned and ordered, however, as the fibres insert into the cartilage matrix, they loose both directionality and order (Fig 4.22 and 4.23). The bone beyond the cement line, shows a highly ordered and directional matrix, similar to that seen in the annulus (Fig. 4.24). This disorganisation of the fibres may actually provide structural integrity of the anchoring of the disc and help to offer resistance to both annular pull-out and shear strain.[95] Fig. 4.43 from Sappiee et al., illustrates this hypothess by showing the integration between the fibrils in the annular sub-bundles with fibril osteons being facilitated with an intervening irregular fibrillar network.[95] This also supports the finding of Fig. 4.25, that there is a level of integration with the osteon fibril, and that not all fibres end abruptly as previously proposed by Rodrigues et al., and Junhui et al.[94,234]

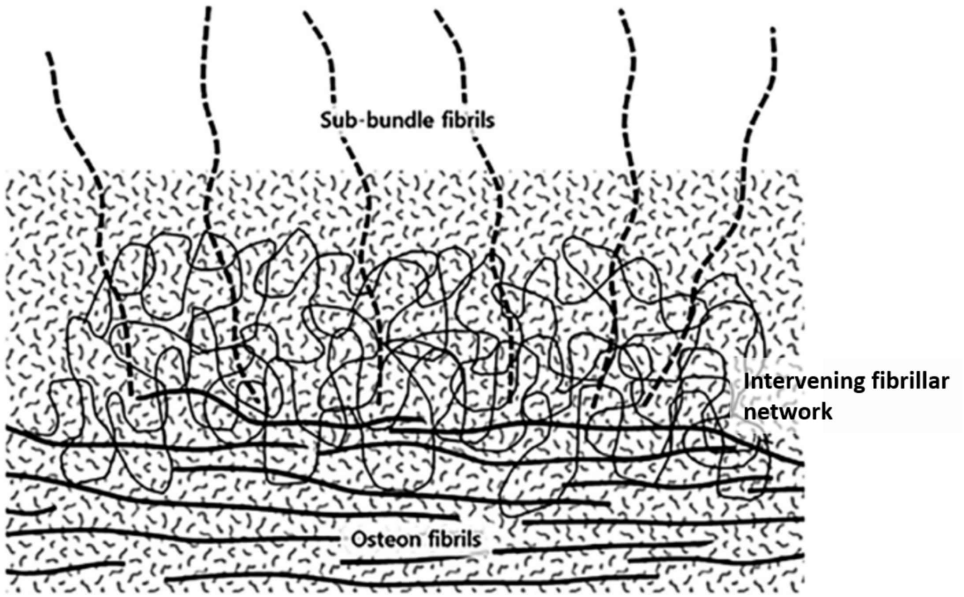

Figure 4.43: *Image taken from Sapiee et al., showing the integration of fibrils in the annular sub-bundles with fibril osteons, supported by an intervening irregular fibrillar network*[95]

This integration across the cement line, not only explains the existence of bone fragments on annular bundles which have ruptured,[63] but also challenges the suggestion that the CEP and BEP are not well integrated.[235] A number of papers support the finding of CEP/BEP integration, noting a 'tight-bonding' between the two endplate regions,[56]

but the cement line has been shown to be the point of failure when discs rupture. Under tension the CEP is stripped from the BEP,[61,81] suggesting that though a higher level of integration exists than first expected, the cement line is still the weakest point in the endplate.

4.14 Bovine Bio-chemistry

The assignments of the Raman shift bands were derived from papers pertaining to cartilage and joint tissues (Table. 4.1) as Raman microscopy has not been utilised in the endplate before. The BEP, also shows similar patterns to the subchondral bone in the rabbit cartilage. Additionally, in agreement with previous work, the phosphate contribution in the Raman spectra of the bone beneath the cartilage was obviously stronger than all the other contributions (Fig. 4.29).[236–238]

The Mineral to Matrix Ratio (MMR) (959/856 + 877 + 921 cm^{-1}) corresponds to the relative ratio of the mineral (hydroxyapatite) over the matrix component of the bone (predominantly collagen type I). As the MMR ratio indicates the level of mineralization in the bone tissue,[239] high values were reasonably observed in the BEP but not in the disc area (Fig. 4.30). This is because the phosphate ($\nu_1 PO_4^{3-}$) band which is representative to the mineral part is diminishing through the transition from the bone to the disc in relation to the matrix component (collagen prolines). It should be noted here that the matrix component is independent of the collagen type (I or II), as the proline content,[240] and therefore the Raman bands in the two molecules, are extremely similar. Still focusing on the mineral aspect of the tissue, the Carbonate to Phosphate Ratio (CPR) solely refers to the hydroxyapatite bone analogue as a marker for the carbonate substitution in its lattice.[212] As the band intensity in the spectral range 1120-1280 cm^{-1} is the contribution of a number of Raman peaks,[241] the carbonate band (1076 cm^{-1}) partially overlaps with the OSO_{3-} symmetric stretch of chondroitin sulphate (1064 cm^{-1}),[208] which is located in the disc instead of the cortical bone. In Fig. 4.12, we can observe that the subchondral bone shows higher levels of carbonate substitution in closer proximity to the endplate, whereas the CPR values in the disc area corresponds in reality to chondroitin sulphate. The mineralization level can also be assessed by the phosphate to amides ratio (Fig. 4.33) which follows the same trend as the MMR values, indicating higher levels in the endplate area compared to the disc.

Interestingly, both the MMR and phosphate to amide I ratios indicated a higher level of mineralisation under the nucleus than under the annulus. Little is understood of

the mineral content of the endplates, however, some studies have reported on the bone mineral density (BMD), which is suggested to be highest in the peripheral region of the human endplate.[242] Although BMD is not a measure of mineral content, it has been reported that in the spine, bone mineral content is responsible for 86.2% of variations in BMD.[243] Therefore, it is likely that the higher mineral content reported under the nucleus in this study is a characteristic of the bovine model, and would not be seen in human endplate. However, as stated earlier, this is the first study that has applied spectroscopic measures to the endplate, and therefore further investigation is required in order to validate these results.

4.15 Degenerate Human Tissue

One of the main differences seen between the healthy bovine model and the degenerate human samples was that the human samples displayed no obvious tidemark. This however could be due to a number of reasons:

1) Literature reports a higher auto-fluorescence signal with age.[244–246] This was evident in the human samples in this study, as compared to the bovine, the background fluorescence in the disc increased as well as the chondrocyte lacunae becoming more distinguished (Fig. 4.36 and 4.37). This made the identification of the tidemark by means of the change in SHG to TPF ratio difficult.

2) There is no non-MC present. It has been reported that with age the non-MC becomes progressively ossified.[62] If this is the case, then we would not expect a tidemark, as there would be no non-MC to delineate. However, the microscopy discussed below rules out this suggestion.

3) There is no MC on these samples. During the process of removing discs in surgery, clinicians first cut out the disc, inadvertently removing some of the endplate (such as the samples received). They then scrape away the endplates to expose the bleeding cancellous bone which promotes the integration of implants.[15] This suggests that during the initial disc removal only sections of the non-MC are removed with the disc.

4) Samples were taken from unknown regions of the disc (see methods in chapter 3.3.4). These samples were acquired from excised discs in a tissue bank, meaning their origin location was unknown. Studies have reported that at the outer regions of the annulus (though within the ring apophysis), only the MC is present, meaning no tidemark.[62,247]

The annulus fibre bundle arrangement also shows differences to the bovine and ovine samples. Fig 4.36 B shows the fibre bundles curving as the integrate into the region of cartilage that is aligned horizontally to what would be the tidemark. This highly aligned region of cartilage has previously been reported by Paietta et al., in human cadaver samples, and they also showed the annulus fibres present in the first 500 pixels post tidemark (no scale provided), showed a similar orientation to the fibres present in the cartilage. This suggests that the annulus fibres re-orientate to integrate with the horizontal cartilage fibres.

4.15.1 Degenerate Human Tissue Raman Microscopy

Raman microscopy of the degenerative samples confirms the presence of non-MC (red peak in Fig. 4.41 as the spectra obtained show similar peaks to cartilage reported in the literature.[201,248] Additionally, the presence of a mineralised region is seen with an indicative intense phosphate peak,[236–238] though this region is only ~ 60μm in width from the sample edge. The bovine MC endplate was measured to be between 400 - 600 μm in thickness earlier in the study at the inner annulus. The difference in thickness measured here may be due to animal differences, however, it is more likely due to either surgical procedure (point 3 above) or location (point 4 above).

The representative spectra for the bovine and degenerative human samples (Fig. 4.41) show similarities due to the presence of collagen and proteoglycans. The phosphate peaks appear higher than all others in the BEP of the bovine, however, it appears that the 'dark' region of the human sample is more comparable to the MC in the bovine. Maps of the degenerative human samples showed clusters of phosphate at the transition region. Using light microscopy combined with histological stains (hematoxylin and eosin (H&E) and Masson's trichrome) Junhui et al., also reported mineralised 'dots' at the transition region of cadaveric human samples (Fig. 4.44 B). They showed calcium deposits between fibre bundles, and proposed that this increased the strength of integration between the disc and cartilage endplate (Fig. 4.44).[234] Combined with the earlier understanding of fibre anchorage, and the present discussion of mineral deposits increasing the strength of anchorage, it is possible that the tidemark is not as weak a point as literature has led to believe.

This work requires further attention, not only as to the differences in healthy and degenerative tissue, but also to the possibility of regional variation such as was seen in the bovine samples.

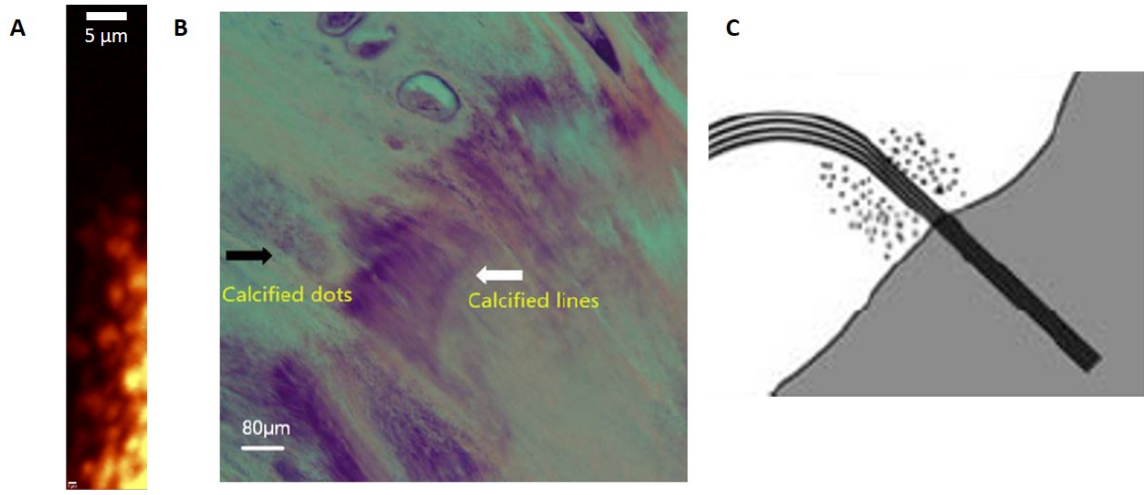

Figure 4.44: *A) Phosphate intensity map showing clusters of mineralisation (Fig. 4.42). B) Image taken from Junhui et al., showing 'calcified dots' in human sample.[234] C) Schematic taken from Junhui et al., illustrating the suggested role of the mineral in fibre anchoring.[234]*

4.16 Conclusion

In this chapter the aim was to establish a structural understanding of the endplate and its interface with the bone and disc across its surface. Some of the main structural findings are summarised in Fig. 4.45.

The structure of the vertebral endplate was examined primarily using multiphoton microscopy, contrasting second harmonic generation (SHG) and two-photon fluorescence (TPF) signals. This method was able to differentiate between the mineralised and non-mineralised cartilage of the endplate in the ovine and bovine samples (Fig. 4.45 B), confirming the three distinct regions of the endplate: the bony endplate, mineralised cartilage and non-mineralised cartilage. Bovine samples showed thicker cranial endplates, with the mineralised cartilage being thicker than the non-mineralised suggesting an explanation for higher fracture rates noted in caudal endplates.[233] Differential Interface Contrast microscopy (DIC) confirmed age differences in the ovine bony endplate with young adult spines displaying high numbers of osteons which were not present in the mature adults endplates (Fig. 4.45 A). Additionally, Energy Dispersive Spectroscopy (EDS) showed a difference in the biochemistry of the endplate with age. The results showed a higher Ca/P ratio in young adult ovine spines. Raman microscopy on bovine sections showed differences in the chemical profile of the endplate under the annulus compared to the nucleus. This work highlights the specificity of each of the tissues in the endplate, and how they change based on their location (nucleus/annulus, caudal/cranial) and with age.

SHG in ovine sections was able to show the integration of disc fibres with the cartilage matrix, through sub-bundling, and the merging of fibre networks resulting in disorganisation, which provides structural integrity of the anchoring of the disc and help to offer resistance to both annular pull-out and shear strain[95] (Fig. 4.45 C). Additionally, integration with osteon fibres has been shown, highlighting the intimacy of the connection between the disc, endplate and vertebral body. Further, spectroscopic work in degenerative human samples suggested the presence of mineral clusters at the tidemark which may help strengthen anchorage of the disc.

This chapter has reported the methods and results of studies utilising multiphoton microscopy, second harmonic generation (SHG) and two-photon fluorescence (TPF) to image the microstructure of the endplate. This was supported by Differential Interface Contrast Microscopy (DIC), Scanning Electron Microscopy (SEM) as well as spectroscopic methods to investigate the structure and biochemistry of the endplate. The structure of the endplate is relevant to its function. In the following two chapters the function of the endplate will be investigated in terms of its role as a nutritional pathway, and its mechanics.

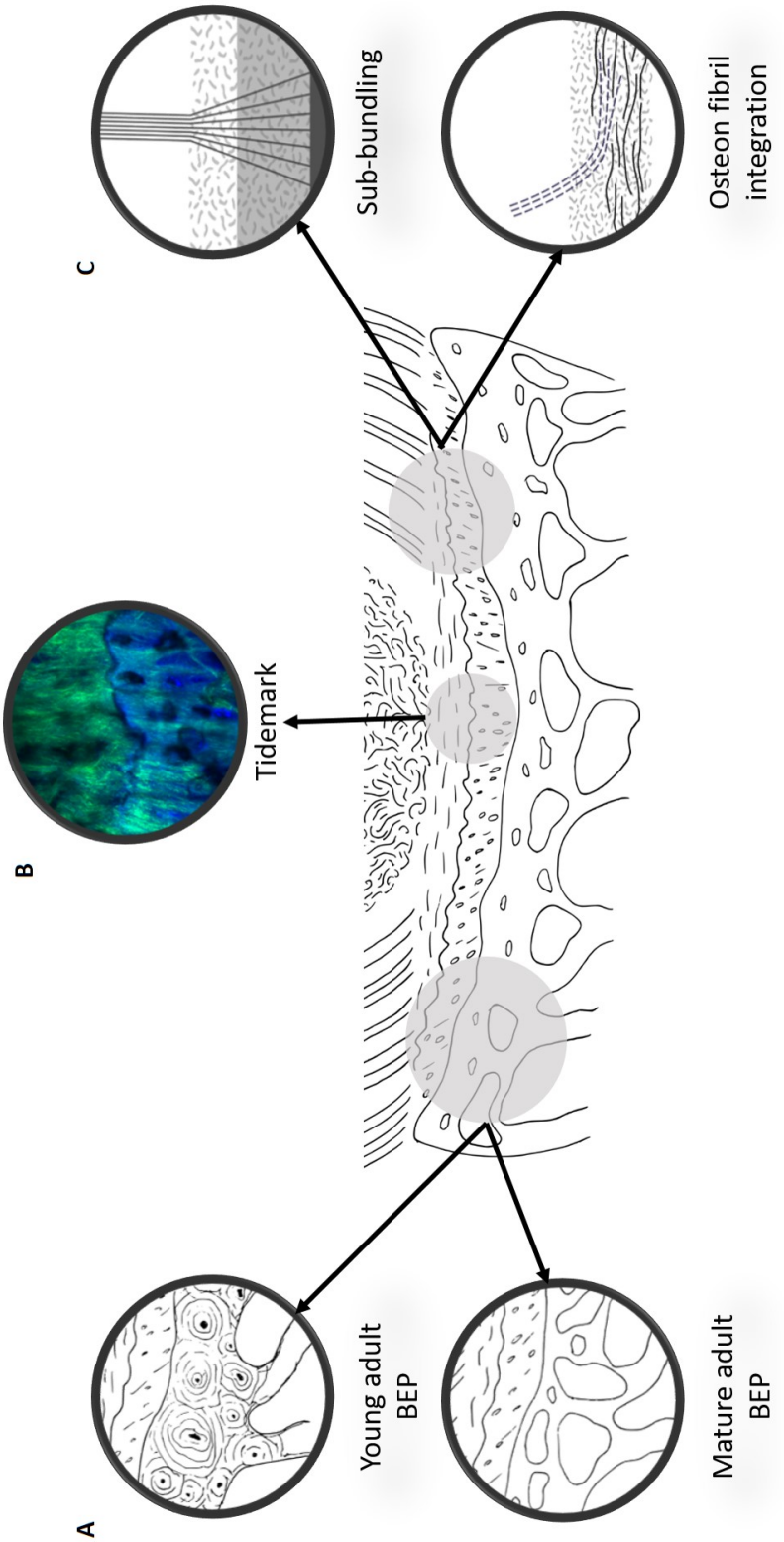

Figure 4.45: *Schematic representing some of the main structural findings from chapter four.*

5 The Endplate as a Nutritional Pathway

5.1 Introduction

As discussed previously in chapter 2.4 the avascular intervertebral disc relies primarily on the endplate as a means of nutrient delivery as well as waste removal.[64,106,107] This chapter first presents the previous literature on the nutritional role of the endplate and the various methods previously utilised. This will provide context and motivation for the studies conducted within this section. The study methods and results will then be described followed by a discussion of the results in relation to previous literature.

5.1.1 The Endplates Nutritional Role

A simple but effective method to investigate the role of the endplate in the nutrition of the disc is that of blocking the predicted path. By either partially or fully restricting the flow through the endplate, its role can be investigated.[249] Not only does this shed light on the role of the endplate in disc degeneration as it calcifies with age,[101,250] it also relates to the surgical practice of vertebral augmentation in which a 'cement' is injected into the vertebral body.[251,252] Studies using a cementing method of augmentation have produced mixed results. Kang et al., cemented the disc of immature pigs bilaterally (both caudal and cranial endplates), and after three months found them to have 'severe intervertebral disc degeneration' and described 'diseased nutritional diffusion patterns'.[253] A similar study on adult dogs concluded that endplate cementing caused no 'discernible degeneration' visually nor with an ELISA[249](Enzyme-linked immunosorbent assay, a technique designed for detecting and quantifying substances such as peptides, proteins, antibodies and hormones). However, their study only blocked the cranial endplate (unilateral) in the majority of its animals. When the histology was examined 'marked changes' were noted closer to the cemented endplate compared with closer to the open endplate. There were only results for one dog with both endplates blocked and again histologically this showed gross changes compared to control.[249]

Krebs et al., study was more thorough, investigating augmentation bilaterally, unilaterally and distally (one away from the cemented disc) in 12 mature sheep.[254] They showed that even with an 80 % filling no statistically significant degeneration was seen, yet there was a trend of increased degeneration between 6 and 12 month time points. This trend was also observed in a rat tail 'vascular isolation' experiment, which indicated that a single vertebral isolation induce a disc degeneration, with some small trend for recovery.[255] However, their study indicated that a bilateral isolation did not show any spontaneous regeneration post degeneration.[255]

The occlusion/augmentation method indicates that there is some form of relationship between the blocking of the endplate and disc degeneration. However, due to its indiscriminate nature- there is little control over where/what the cement is filling and it can leak into the spinal cavity causing complications- it essentially adds little to the fundamental understanding of the endplate as a nutritional pathway.

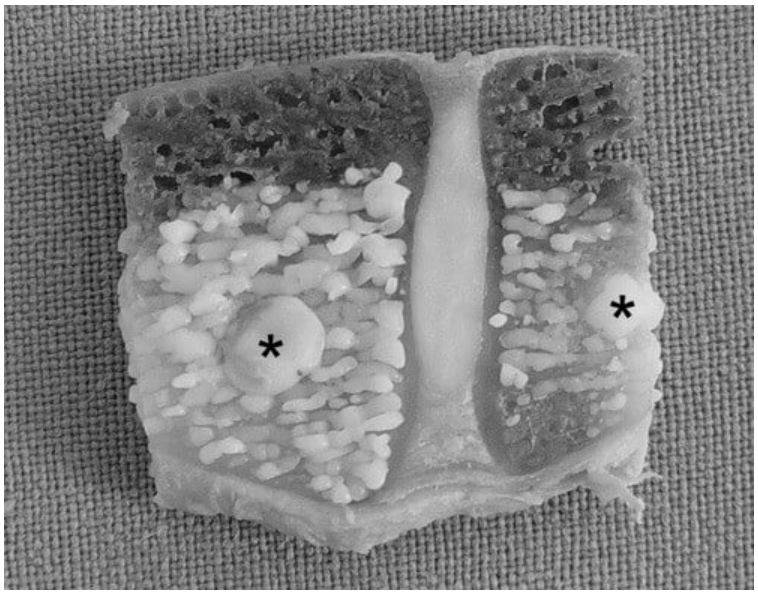

Figure 5.1: *Image taken from Krebs et al.[254] Photograph of a sagittal section through an intervertebral disc specimen with the two adjacent vertebrae. Both the vertebrae are augmented with PMMA and approximately 80 % of the length of the endplates are in contact with cement. The asterix indicate the injection holes.*

Laffosse et al.,[256] took a more conservative approach, aiming to investigate the importance of 'marrow contact channels' in relation to endplate permeability using micro-CT. Utilising an immature pig model they found that, as expected, there is a greater percentage of openings under the nucleus than annulus (31.4 ± 17.4 %). Additionally, they reported a correlation between effective permeability and marrow contact channel surface area.[256] Benneker et al., also investigated 'endplate openings' and though there

were no measurements of permeability, they found a significant positive correlation between openings and degeneration grade in 39 MRI scans of human lumbar discs.[123] The study also found a correlation between opening density and age, although this was not as strong as with degeneration.

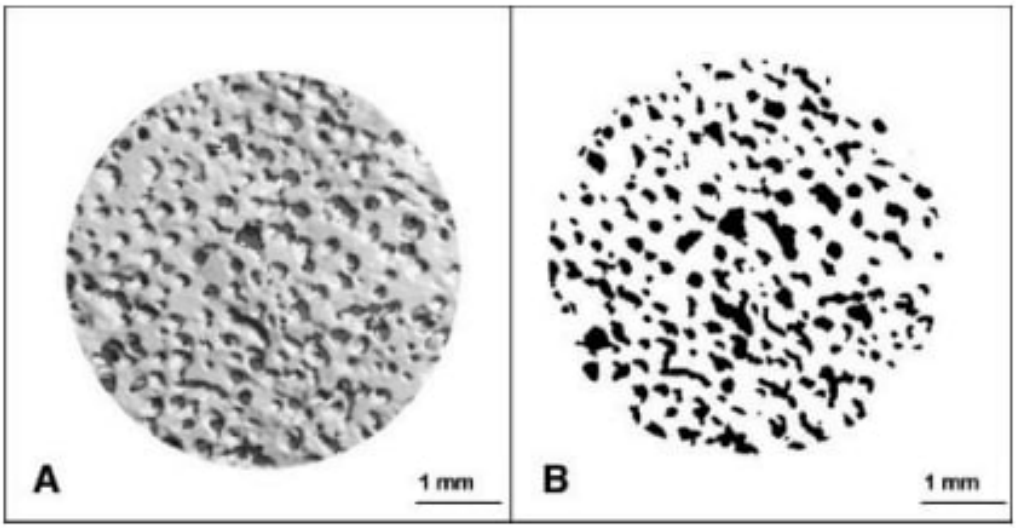

Figure 5.2: *Taken from Laffosse et al., 2010.[256] 2D image of the entire disc VEP interface in gray-scale mode (A) and after conversion into a binary 2D image (B) where capillary buds in contact with the CEP are visualized in black.*

The literature on 'endplate openings' or 'marrow contact channels' is hard to follow due to a variety of terms used. Recently Cao[257] has shown a 'canal network' within the vertebral endplate using propagation phase contrast synchrotron microtomography. They relate these to the nutrition canals talked about in previous literature,[258] and show a width range of 10-80 μm. What is unclear from these studies, is how the 'canals' relate to the vascular network originating in the bone. As Fig. 5.2 shows the openings can vary in shape and size, and therefore cannot be directly related to vasculature without further investigation into the capillaries of the endplate.

To address this question of delivery of nutrients to the disc, Ayotte et al.,[78] and Van der Werf et al.,[102] both used the diffusion of fluorescent markers to investigate how the channels interact with the disc. Ayotte et al., demonstrated with procion red that 'flow in' from the bone to the disc followed the marrow contact channels until the bone-cartilage interface/tidemark and then dispersed into the cartilage following conventional diffusion of solutes.[78] On the contrary, Van der Werf et al.,[102] showed dye filled vascular buds in sheep endplate, similar to those which Oki et al.,[111] described in rabbits which

appeared to be in the cartilage endplate adjacent to the disc. Thus, the direct route of nutritional supply to the disc is not clear from such studies.

5.1.2 Capillaries of the Endplate

The vasculature of the vertebrae and endplate is discussed in part in chapter 2.4. As shown in Fig. 5.3 A, Crock and Goldwaeer have suggested a vascular network comprising of large horizontal vessels within the trabecular bone which extend into the 'endplate' (region specificity is lacking).[115] Oki et al., used scanning electron microscopy to visualise the vascular network, which had been infused with resin, in the endplates from five rabbits.[111] They showed that the blood vessels extend from the subchondral bone to the 'vertebral endplate', where the arteriolar coil to form micro-vessel loops, known as the vascular bud. Oki et al., investigated rabbit endplates[111] and the size of their capillary network closely resembled the 'canal size' imaged in rats in the study by Cao et al.,[257] ranging from 10-100 μm in diameter. This is the only paper to have provided such detailed description of the vascular network in the endplate, due to the destructive methods, it is still difficult to accurately relate the vessels to the surrounding endplate tissues as the definition of 'vertebral endplate' varies in the literature as previously discussed. This is the only paper to have described vascular loops. Other studies have alluded to the presence of such loops, as a continuous network is necessary for the vasculature to be physiologically viable, however, little evidence has been provided.

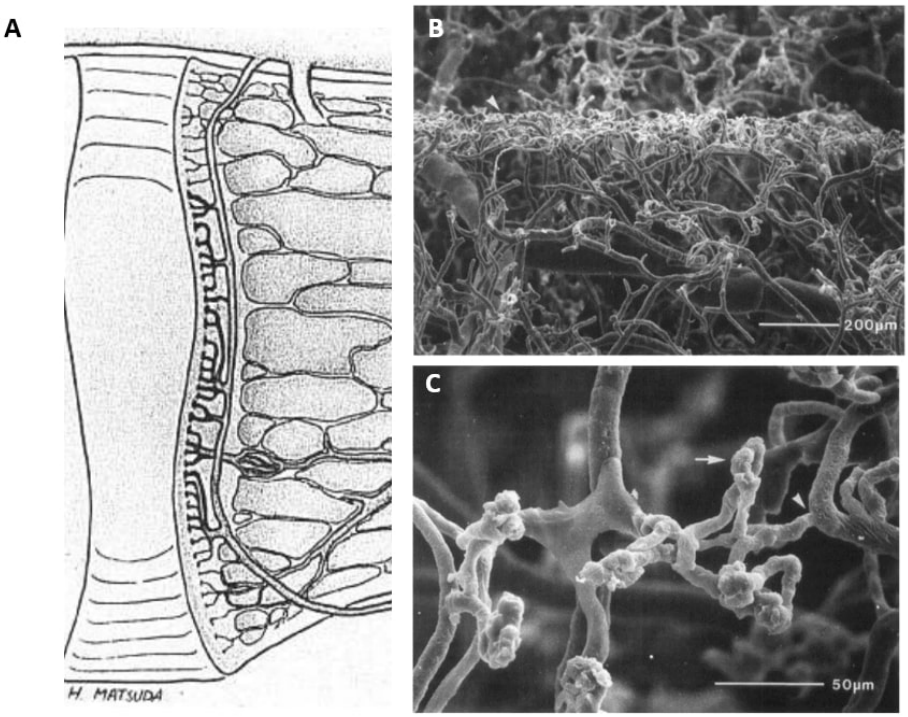

Figure 5.3: *A) Image taken from Crock and Goldwasser[115] et al., illustrating the capillary 'endings' in flat buds. B and C) Images taken from Oki et al.,[111] of the resin cast of the vasculature in a rabit endplate B) Arrowhead points to C) Arrow points to the capillary 'loop' and arrow head points to the branching of the vessel*

5.1.3 'Flow Out of the Disc'

As previously mentioned not only is the endplate structure related to the nutrient delivery, but also affects the removal of metabolic waste and loss of degraded matrix.[64] Despite this important functional role of the endplate, little attention has been paid to the 'flow out'. The aforementioned study by Ayotte et al.,[78] measured the resistance ratio between flow in/flow out. They demonstrated a direction-dependent resistance, where there was shown greater inhibition to flow out than flow in. They suggested that during flow out the fluid is constrained by the cartilage overlaying the 'marrow contact channels' resulting in high drag forces (Fig. 5.4).

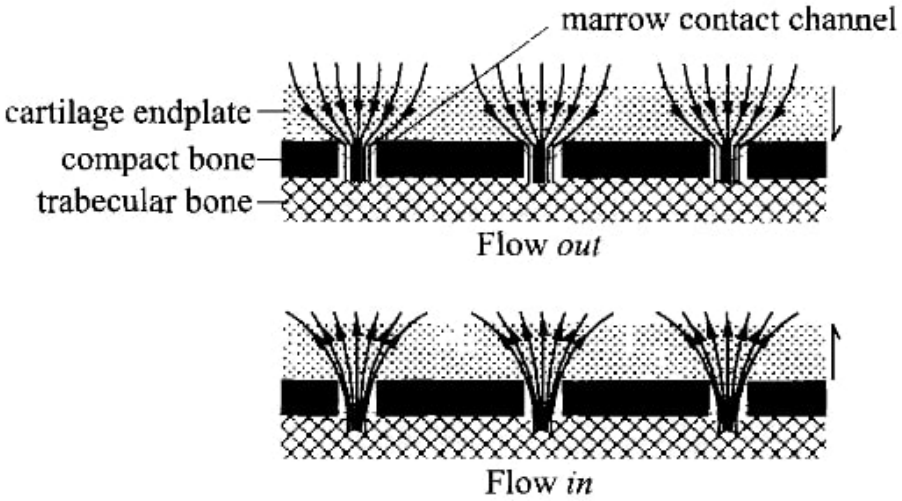

Figure 5.4: *Taken from Ayotte et al.,.[78] Schematic illustrating the direction-dependent flow caused by the cartilage overlaying the marrow contact channels.*

The paper related their findings to the water transport necessity to 'to ensure that all of the fluid lost during daily loading is recovered during rest', however, given the size of waste components such as lactate (89 g/mol), they are more likely to travel via diffusion than convection.[259] Given the importance of waste removal (increased acidity, cellular apoptosis and ultimately disc degeneration[64]) it is surprising that this topic has not gained more interest. It reinforces the necessity to understand the endplates role, as if structural changes to the endplate (due to aging or disease) effects the removal of waste, it too will contribute to disc degeneration.

This chapter utilised multiphoton microscopy, contrasting second harmonic generation (SHG) and two-photon fluorescence (TPF) to investigate the role of the endplate as a nutritional pathway to the intervertebral disc. Tracers such as Fluorescein, labeled

Albumin and Evans Blue aided in visualising the micro-circulation and diffusion rates through the endplate.

5.2 Methods

5.2.1 Label Free Imaging

Lumbar vertebra from five year old sheep were collected from the abattoir and frozen intact at -25 °C until use. Samples were prepared to provide sagittal cross-sections of the bone-disc-bone following previously discussed methods (3.3.1). In order to clear the marrow channels and vasculature of clotted blood, samples were placed in distilled water for 2 hours. This breaks down the cell by osmotic mechanisms. Samples were then rinsed in phosphate buffed saline (PBS) to remove the debris. Superior endplates were then excised using a scalpel to cut through the disc. The superior endplate sections were then frozen in optimal cutting temperature compound gel (OCT gel) and cryo-microtomed using previously discussed methods (3.3.3) to create a flat imaging surface. Samples were then placed on a microscope slide, with a cover slip. The objective used for imaging was a 25x water immersion lens (Olympus, XLPLN 25XSVMP2 M25 x 0.75W). Utilising the SHG and TPF signal, the tidemark was located on the sample and followed along the length of the sample whilst imaging anything that appeared vessel-like in shape.

5.2.2 Small Molecule Diffusion

Cross-sectional slice

Samples followed the same preparation as 5.2.1. a fluorescein solution of 0.1 % concentration (Fluorescein 95 %, Sigma-Aldrich, CAS 2321-07-5) was placed in a Petri dish, with the superior endplate section suspended above. Only the disc touched the liquid (Fig. 5.5). The samples were left for 20 minutes to allow for perfusion of the disc and endplate, though not the complete saturation of the sample. After exposure to the dye the samples were patted dry with tissue paper, to remove surface liquid and prevent contamination of other areas of the sample, then transferred to a clean Petri dish for imaging.

Trephine Core

Lumbar motion segments were severed with a scalpel through the disc. Regions of interest of 5mm diameter were removed using a surgical grade trephine (5 mm diameter). The cores were then exposed to 0.1 % fluorescein as shown in Fig. 5.6. Samples were

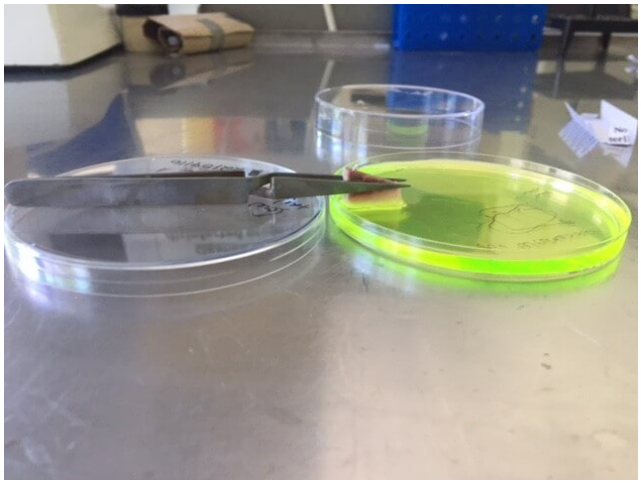

Figure 5.5: *Schematic of experimental setup for sample perfusion with 0.1% fluorescein.*

then frozen and encased with OCT gel, and ground in the frontal plane using the cryo-microtome to produce a flat imaging surface. The samples were then a half cylinder shape. To avoid having to grind the curved back, a sample holder was 3D printed with a curved groove thus enabling a still, flat imaging surface (Fig. 5.6). Ultimately this set up was ineffective as sectioning a core added no benefit, and slowed down the preparation process. Additionally suspending the samples in the dye proved trickier than the flat samples, due to the curved edges. This method was not pursued further.

Motion Segment

Rather than pre-section the disc into segments, it was decided that whole vertebrae should be exposed the dye therefore maintaining more of the in vivo structure. Bovine tail, rather than Ovine lumbar, was used. The tail had visibly less blood clotted in the marrow spaces, and therefore it was assumed that this would lead to both a clearer path of the dye (blocked by less debris), and clearer images (less nucleic material to create auto fluorescence). Therefore bovine tail motion segments were stripped of soft tissue and excised by a central cut through the disc. These exposed discs were then placed into the dye, and refrigerated at 5 °C for varying durations (30 min, 1 hour, 24 hours, 3 days). After the allotted time had passed, the samples were removed from the dye, patted dry to remove any excess/surface dye and then immediately frozen to prevent any continued perfusion. To prepare for imaging, samples were cut in the sagittal plane into thin cross-sections and cryo-microtomed to form a flat imaging surface. The sample was kept frozen during all preparation so that minimal dye movement occurred during preparation. The sample had to be thawed for ~ 15 mins before being imaged, meaning

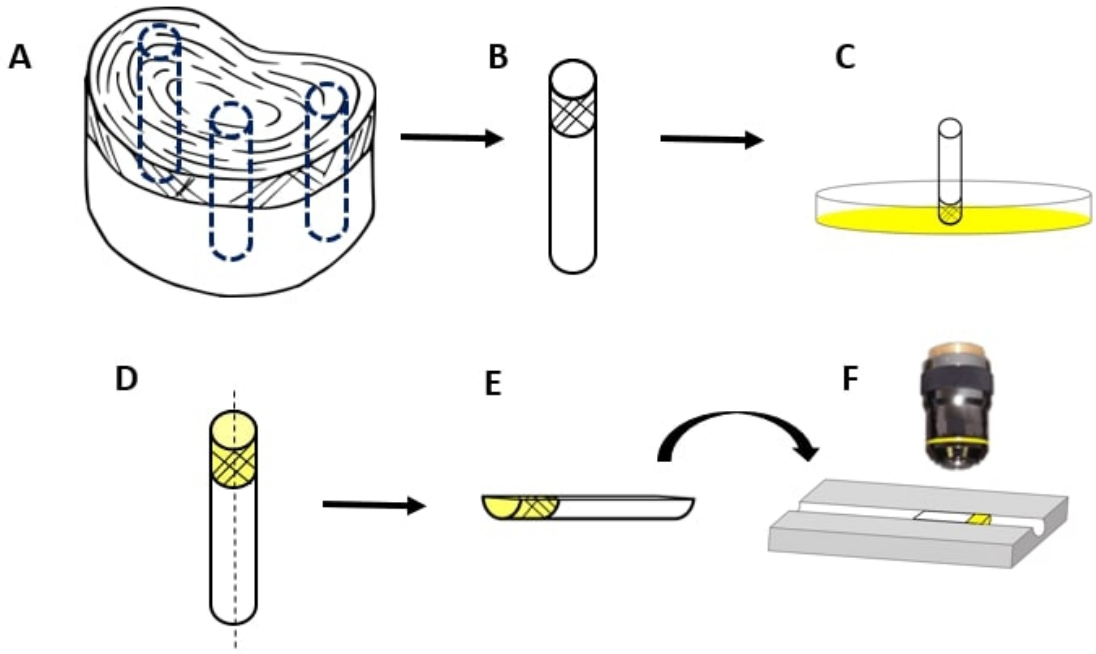

Figure 5.6: *Process of preparing trephine core samples for imaging. A: Core taken from vertebrae and disc segment. B- Trephine core schematic. C- Core placed disc first into 0.1% fluorescein. D- Core sectioned in two. E- Result of flattening the core. D- Flattened core in 3D printed holder, providing a flat imaging surface.*

there may have been some diffusion of the dye during the capture protocol. The capture protocol could range in time from 30 - 90 mins depending on the quality of the sample flatness. Additionally to avoid distortion of the image by the adhesion of the dye to a cover slip, a 10x air objective (Olympus, UPlanSApo 10x/0.40) was utilised.

5.2.3 Large Molecule Diffusion

Fluorescein is a relatively small molecule (332.31 g/mol), and as such diffuses easily where larger molecules may be restricted. To investigate this, a 0.05 % concentration of labelled albumin was used (Albumin–fluorescein isothiocyanate conjugate, Sigma-Aldrich, 66,000 g/mol), this concentration gave a good signal when a droplet was imaged on a microscope slide and did not saturate the detector. A one hour exposure time was initially chosen as with free fluorescein 30 minutes was sufficient to reach the tidemark and allow pooling of the dye in the available spaces of the cartilage. It is expected that a larger molecule would take longer, therefore the time was doubled. However, after 1 hour no dye was detected, the same with 4 hours. It was decided to leave the sample for a longer period to ensure dye movement, and was therefore left for 16 hours.

5.2.4 Real-Time Visualisation of Solute Uptake

In order to image the diffusion of fluorescein in real-time from the disc into the endplate, a set up was required that both fitted under the microscope and restricted the dye to a one way diffusion. The microscope stage already had an attachment which could hold a Petri dish, for this reason the Petri dish was used as the base and 3D printed resin walls were used to form a well to contain the sample and dye. The walls were then adhered to the Petri dish with vacuum grease (Dow Corning® high-vacuum silicone grease). A number of methods to secure the sample, and to prevent dye from going around or under the sample, were trialed. Neither vacuum grease alone (Fig. 5.7), wax, nor a border of blue tack prevented the dye from going under the sample, however, placing the sample on top of a section of blue tack (Blu Tack, Bostic 30813254), with only the disc in contact with the dye, proved viable.

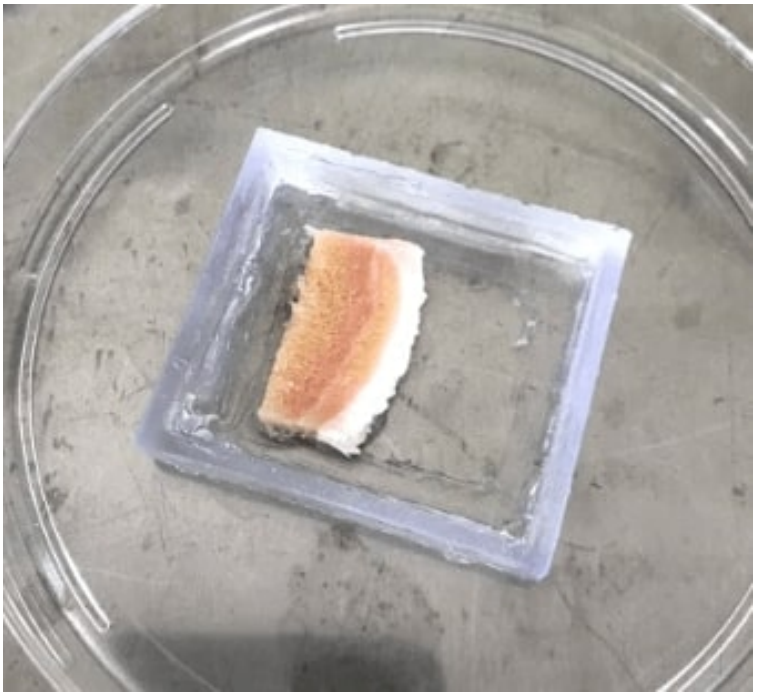

Figure 5.7: *3D printed resin walls secured to a Petri dish with vacuum grease. Sample is affixed and surrounded with vacuum grease, but this still allowed the dye underneath the sample.*

The 10x air objective (Olympus, UPlanSApo 10x/0.40) was used to avoid the need for a cover slip during this experiment. Once the sample was under the microscope, the objective was focused over the disc/cartilage endplate junction. This was identified from the visibility of both disc fibres and dimpled cartilage structure in the SHG and TPF. FluoroView version 5 software was used to set up an imaging sequence that took an image every 45 seconds. Image acquisition took 11 seconds meaning a duration of 34 seconds

between each acquisition. The experiment was then left to run for 120 minutes, or until the tidemark was crossed.

5.2.5 Bovine Tail Perfusion

In order to investigate the relation of the micro-circulation of the endplate to the wider vasculature of the spine, bovine tails were perfused with a tracer. The tail was utilised as a model as it could be attained within a short period of slaughter with the skin intact. Once the main artery and vein were canulated it formed a relatively closed system of circulation.

Preparation Procedure

At the time of slaughter, tails were excised and, whilst still warm, cannulated then flushed through. The main artery (median caudal) was partially dissected away from the surrounding tissue, in order to insert a cannula (Simms Portex). The cannula fitted snugly in the vessel, however, it was secured with surgical suture thread to prevent it from slipping out. Following the same process the median caudal vein was cannulated (Fig. 5.8). A syringe was then attached to the cannulated artery in order to flush the system with a PBS and Heparin solution. This process was done to prevent the clotting of the blood within the vasculature, therefore the tail was flushed until the fluid flow out of the venous cannula was clear. Once this process was complete the tail, with cannulas still attached, was transported in an insulated container to the laboratory.

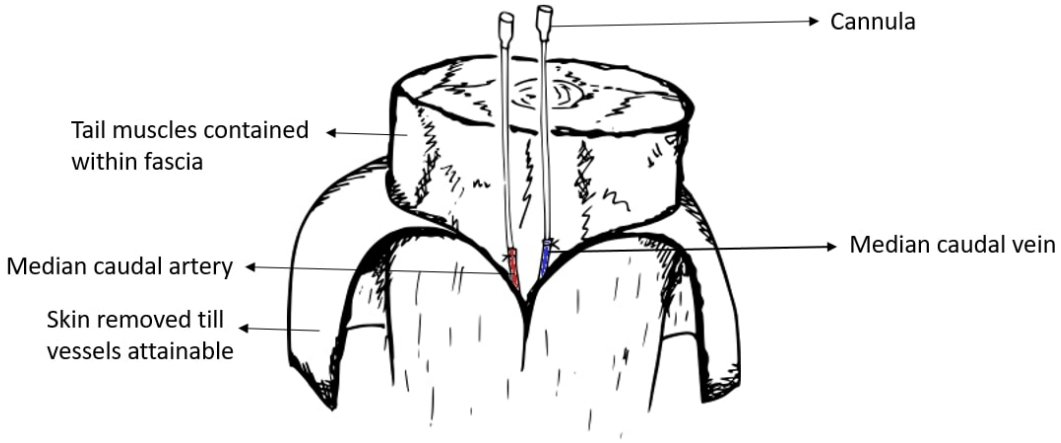

Figure 5.8: *Schematic of a bovine tail with the skin removed enough to expose the median caudal vein and artery which were then cannulated and secured with surgical thread.*

Once in the laboratory the tail was transferred to a dissection area and again a syringe was attached to the artery and flushed with PBS to check for clots or remaining blood as well as assessing whether the connections were still secure post travel. Following this a pre-prepared solution of dye (Evans Blue, 0.01 % concentration, Sigma-Aldrich) was slowly pushed through the tail via the cannulated artery. This process was stopped when the vasculature in the visible soft tissue appeared blue.

Imaging with Dissection Microscope

Imaging over wide fields was undertaken with a Leica dissection microscope fitted with a Mako camera (WILD M10 G231C IRC PoE). It allows for observation of a sample, using light reflected from the surface of an object rather than transmitted. Samples were viewed in two ways; First, caudally in the transverse plane. A vertebral segment was removed by slicing through the adjacent discs, the superior disc was used as the region of interest. Images were taken of the disc over a range of magnifications, and then removed carefully. Secondly, sagittal cross-sections of the disc-endplate-vertebral interface were cut with a hack saw, following previously mentioned protocol (3.3.1) for cutting and grinding. The sample was kept frozen throughout this process so to avoid the movement of the dye.

Imaging with Multiphoton Microscope

The sagittal cross-sections imaged under the dissection microscope were then imaged under the multiphoton following standard protocols (3.1.1). The Evans Blue dye was visible in the TPF channel.

5.2.6 Image Analysis

Image Manipulation

Acquired images contained both the SHG and TPF channels. These were separated from one another false coloured and a composite image created using the FIJI version of ImageJ®(Fiji is just ImageJ, http://fiji.sc/). Once images were scaled appropriately, FIJI also could be used to measure regions of interest. In some cases, a map of a region was taken using a number of overlapping snapshots. These images were initially processed

in FIJI to apply the false colour, then they were built into a continuous map in GNU Image Manipulation Program (GIMP, 2.8.18).

FIJI also allowed the measurement of the intensity of pixels, which indicate the intensity of the signal detected from TPF and/or SHG. The intensity values are in the format of a 'byte image' which labels each pixel with an 8-bit integer giving a range of possible values from 0 to 255. Additionally, the green and blue (RGB) intensity of a coloured image can be profiled, indicating the contribution of each channel. With false coloured SHG and TPF images, this can show the intensities of each.

Diffusion Modelling

Fick's first law (5.1) governs the motion of diffusing molecules in the steady state, where concentration is constant in time. Where X is the distance in cm, t is the time in seconds and D is the diffusion coefficient.

$$D = \frac{x^2}{2t} \tag{5.1}$$

A script written by Michelle Bailey in Matlab 2014b (The MathWorks, Inc., Natick MA), was utilised in this study for fitting some experimental diffusion data. The script was originally written to assess diffusion through a gel, but was applied in this study to the diffusion through the endplate. It utilises Fick's second law (5.2) where C is the concentration.

$$\frac{\partial C}{\partial t} = -D\frac{\partial^2 C}{\partial X^2} \tag{5.2}$$

The boundary conditions were set as follows:

$t = 0 : x > 0, C = 0$

$t \geq 0 : at\, x = 0, C = C_0$

where C_0 is constant. Applying these boundary conditions and solving Fick's second law (5.2) in one dimension gives:

$$C = \frac{1}{2} C_0 erfc\left(\frac{x}{2\sqrt{Dt}}\right) \tag{5.3}$$

Fitting this equation to data for concentration as a function of either position or time allows the diffusion coeffcient, D to be determined.

5.3 Results

5.3.1 Vessels of the Endplate

Label Free Imaging

Fig. 5.9 shows a vessel visible within the MC matrix. It sits close to the tidemark between the mineralised and non-MC. The highly aligned fibres of the annulus are clearly shown on the left hand side of the image; it is assumed that the fibres have penetrated the cartilage layer as there is evidence of sub-bundling (see split arrow) which occures post insertion into the non-MC (discussed in 4.13).

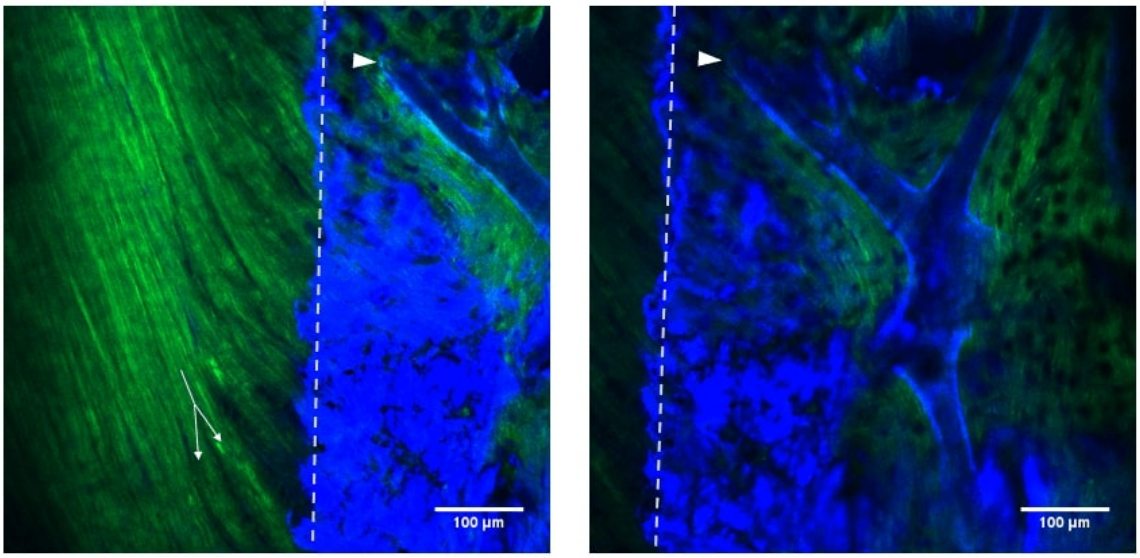

Figure 5.9: *Multiphoton image of vessel within the endplate. Green SHG, Blue TPF false coloured and over-laid. Left image shows clearly with directional annulus fibres. Right image shows more of the cartilage in which the vessel sits.*

The vessel visible in Fig. 5.9 is a branch connected to a larger vessel, with other branches. The branches range in width from 35-38 μm compared with the trunk which is 127.2 μm across, measured in FIJI (5.2.6). The only visible 'end' of a branch (labelled with white arrowhead) is thinner than the body of the vessel (28.9 v 38.4 μm), however, very few of these 'ends' were imaged, the majority of vessels imaged continued out of the focal plane or were cut by the sample preparation.

Fig. 5.10 Shows a map built up of multiple composite SHG and TPF images to visualise a larger region of tissue. It appears to show a vessel making direct contact with the disc. However, it is hard to assess whether this image is taken at the tidemark region as the

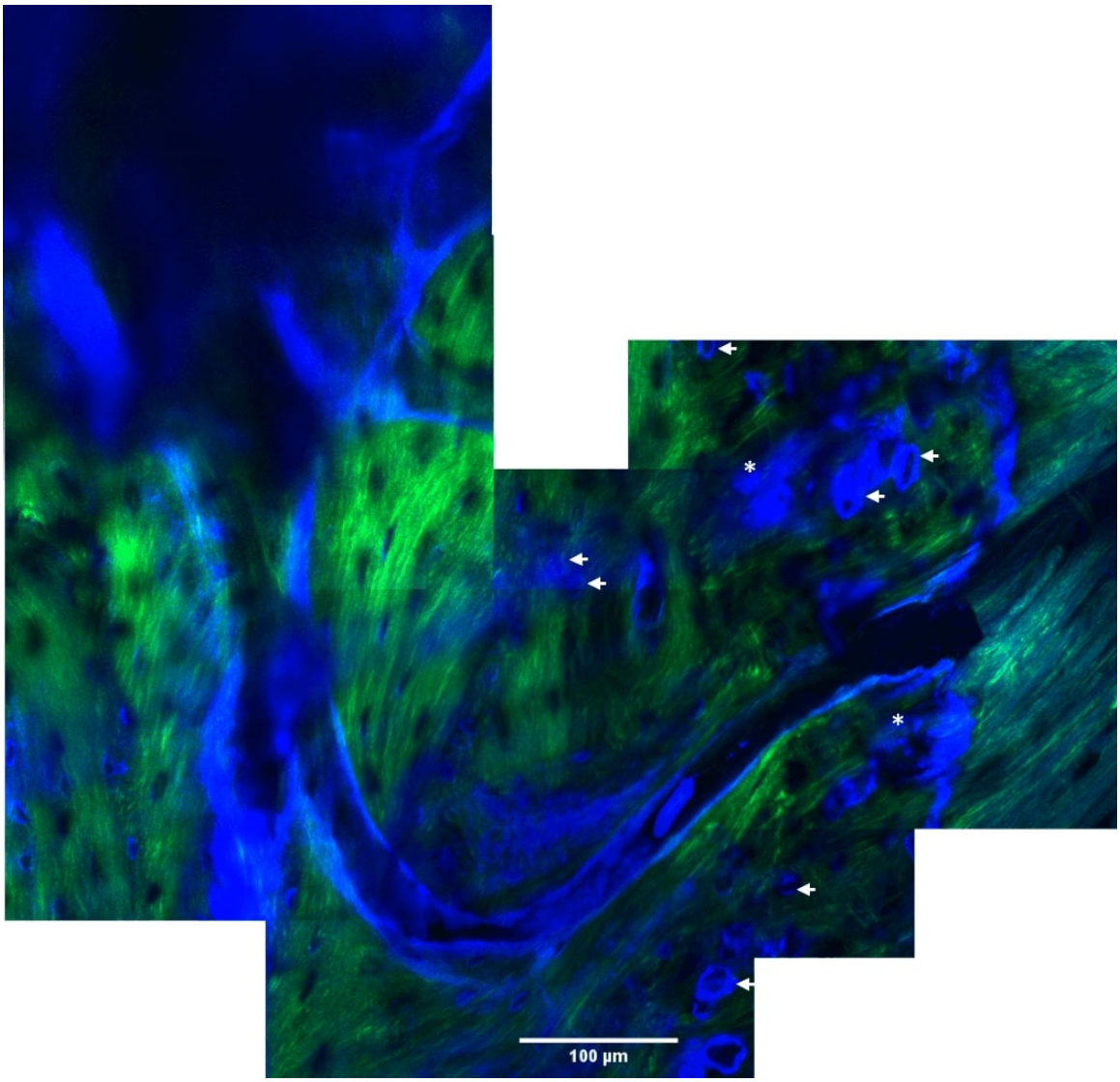

Figure 5.10: *Multiphoton image map created in GIMP of vessel within the endplate. Green SHG, Blue TPF false coloured and over-laid. The disc is shown on the right hand side. White arrows indicate possible transverse vessels. Asterix denotes region of undefinable high TPF.*

disc is less visible than previous images. The high TPF signal along a relatively vertical line does, however, indicate mineral suggesting that this is the MC. Further changing position in a z-stack through the sample, D-F of Fig. 5.11 indicate that this vessel does not stop at the tide mark but rather continues into the non-MC/disc. There appears to be a gap in the disc fibres as if there was something in between the bundles.

Around one third of images gave the suggestion of smaller diameter vessels. For example, Fig. 5.12 A shows a larger vessel (45.1 ± 9.4 μm, mean and SD diameter measured in FIJI) splitting into two forks (left fork: 19.4 ± 3.0 μm, right fork: 26.2 ± 1.6 μm). The left fork then appears to meet another vessel which, as it carries on towards the TM, reduces in size. The filled arrow heads indicate this smaller vessel which is 11.9 ± 1.7 μm in diameter. At this magnification the vessel walls are not clear, so to confirm its identity, images were acquired at a higher magnification. When magnified and grey scale inverted (Fig. 5.12 B) the vessel appears slightly more distinct. Fig. 5.12 C illustrates the vessel path that can be deduced from A and B, however, due to the loss of focus, a full network of the vessels inter-connectivity is not possible. Fig. 5.12 A also demonstrates the difficulty in identifying vessels. The unfilled arrow heads indicate two lines which look similar in appearance to the vessel walls, however, no inter-connectivity is apparent. Further, the arrows in Fig. 5.10 and 5.12 indicate possible transverse vessels that have been cut during preparation. These transverse vessels, ranging in diameter from 5 - 23 μm, are seen more frequently closer to the tide mark. High TPF signal such as that indicated with an asterisk in Fig. 5.10 can make visualisation of these vessels difficult.

Figure 5.11: *TPF image, focused at the 'end' of the vessel(see white box on top left green/blue image), moving through focal points from A-F at a step size of 10 µm.*

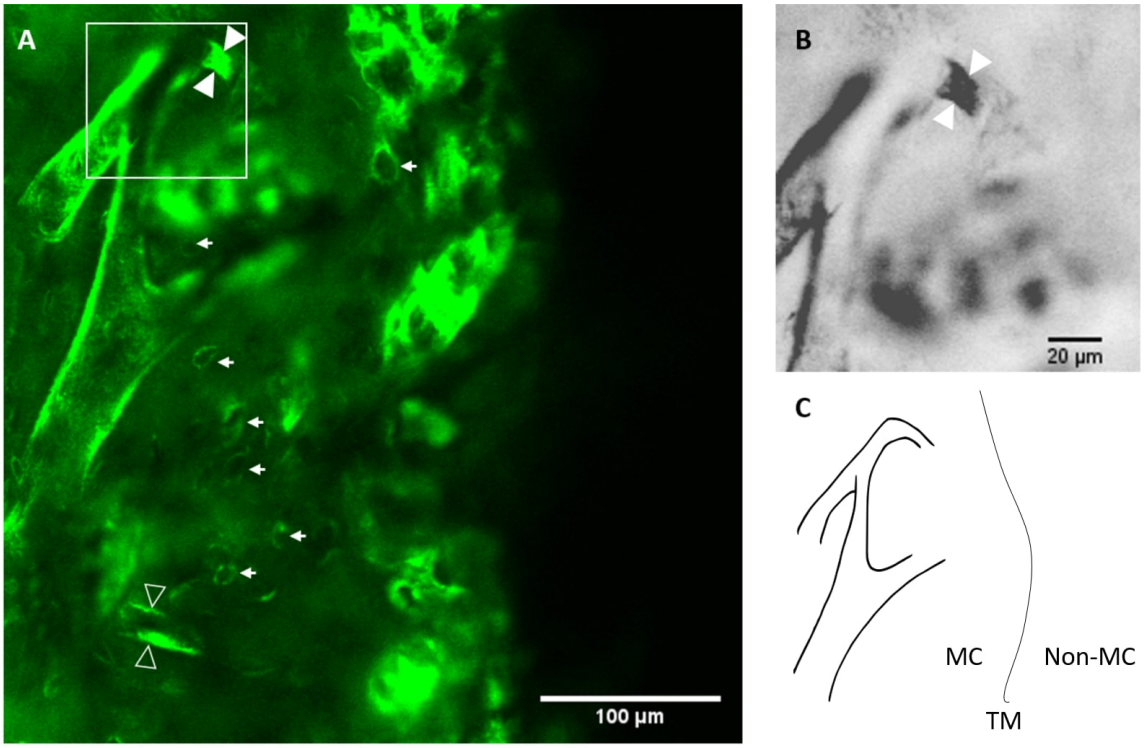

Figure 5.12: *A) TPF image of branching vessel. Filled arrow heads indicate branching of potential smaller vessel. Unfilled arrowheads indicate other potential vessels. White arrows indicate possible transverse vessels cut in the frontal plane. B) Magnified view of branching to a potential smaller vessel. Image has been converted to gray scale and inverted. C) A schematic suggesting the vessel layout in relation to the MC (MC), tidemark (TM) and non-MC (non-MC).*

Diffusion into Vessels

Fig. 5.13 shows results from an experiment in which the fluorescein tracer was introduced from the bone. It shows vessels extending from marrow channels within the bone and form an interconnected network. Additionally, the tracer has entered the disc on the right hand side. Saturating the disc with tracer allowed vessels to be imaged at high magnification. In Fig. 5.14 tracer has entered distinct channels, indicated with white arrow head. However, there is also evidence of the tracer permeating the surrounding tissue (noted in Fig. 5.14B with *).

Some vessels display confusing structures, however, with the 2D nature of the images and the lack of visualisation of the smaller vessels it is hard to interpret their structure (Fig. 5.15). A single image showing vessels can have multiple interpretations of the structure, vessels could be interconnected (Fig. 5.15B) or they could be two distinct vessels in close proximity which continue out of the focal plane (Fig. 5.15C).

Fig. 5.17 is one of few examples of diffusion of fluorescein from the disc through the cartilage into a vessel. The distance between the end of the vessel and the start of the saturated soft tissue (most obvious in the SHG as a slightly darker line) is between 37 - 50 μm. It is important to note that though a vessel lumen is visible in the SHG image there is no other obvious path/structure that the fluorescein is following.

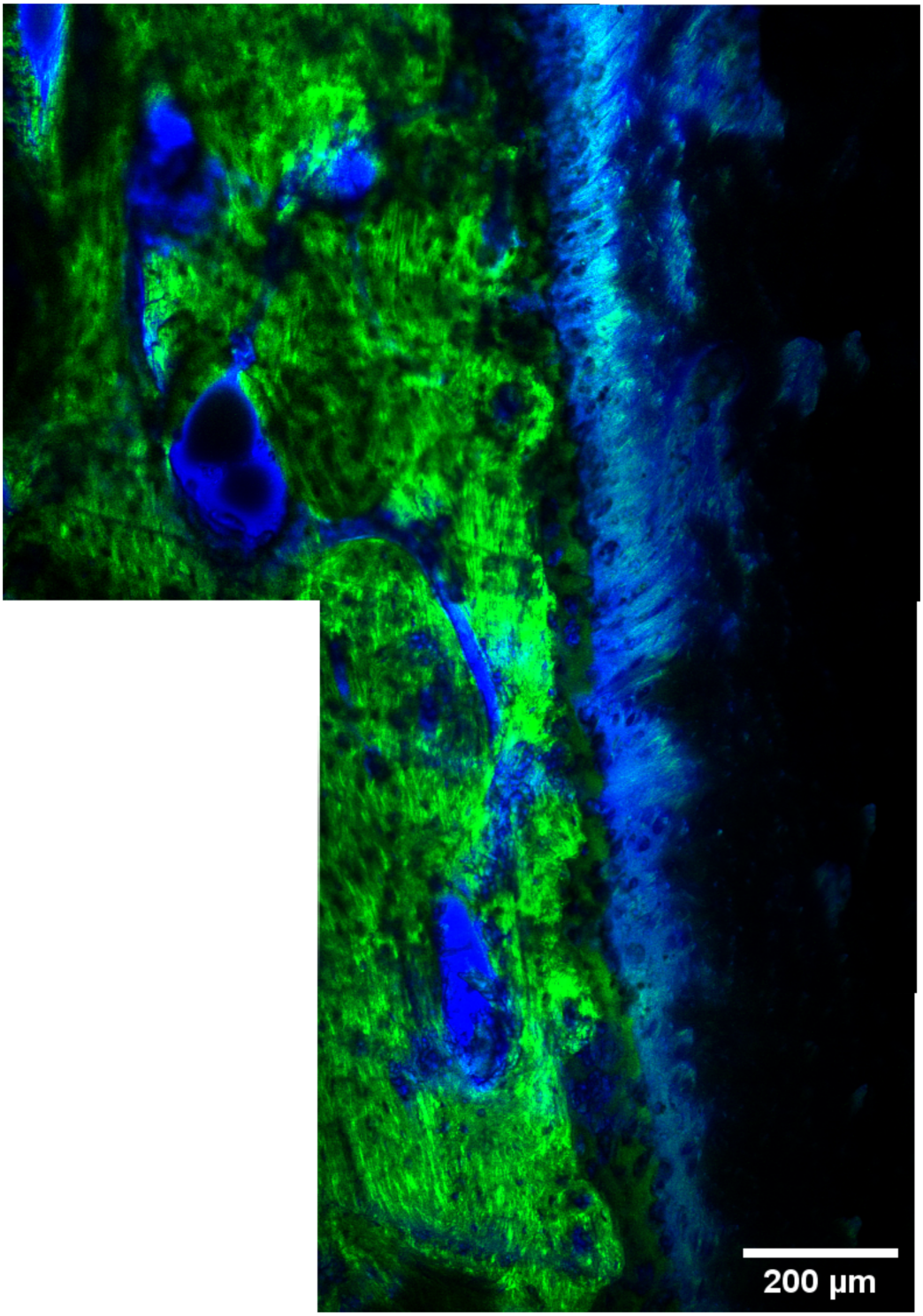

Figure 5.13: *Composite SHG (green) and TPF (blue) images, fluorescein detected with TPF. Map built in GIMP of region from the disc (right hand side) to bone (left hand side) after exposure to fluorescein from the bone side for 1 hour.*

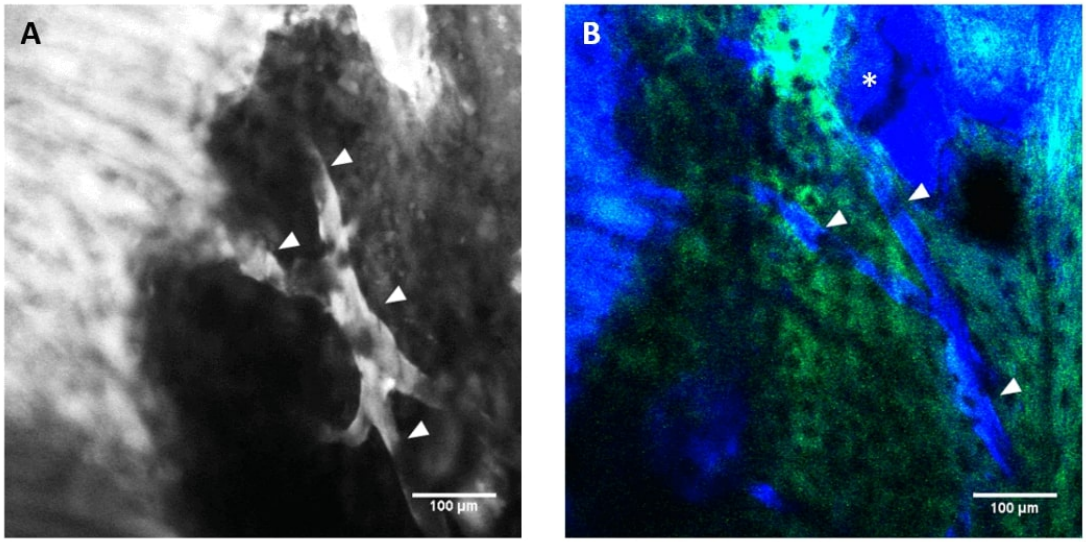

Figure 5.14: *A- TPF image of saturated disc and filled vessels. B- Composite SHG (green) and TPF (blue) images, of a different area of disc and more vessels. Fluorescein detected with TPF. White arrow heads indicate possible transverse vessels. * indicates tracer in surrounding tissue.*

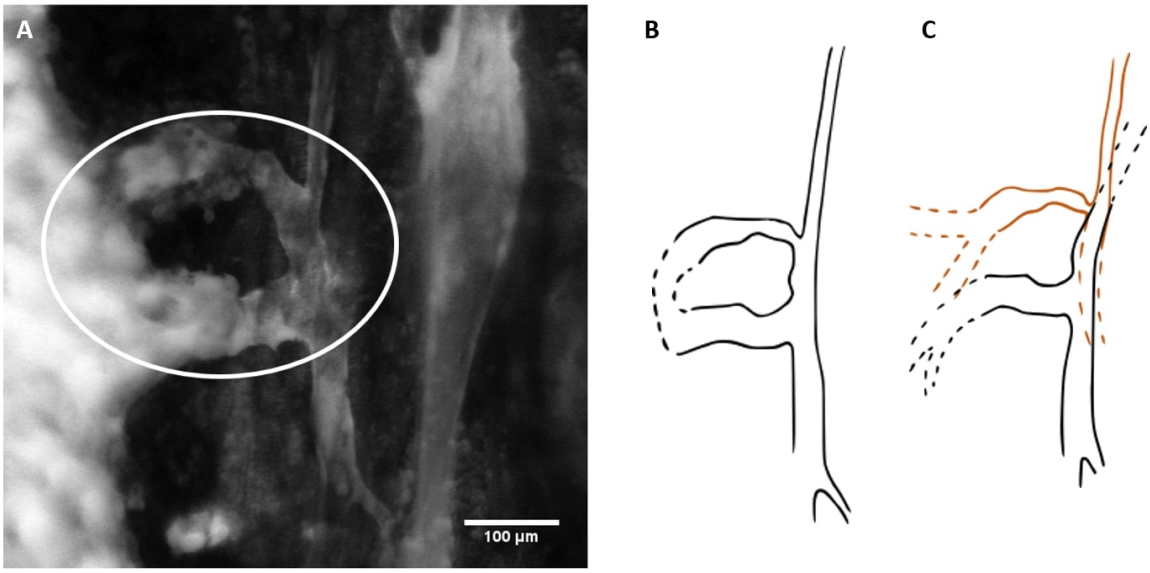

Figure 5.15: *A) TPF image of saturated disc and filled vessels. White circle indicates appearance of a loop. B) Schematic of an interpretation of the vessel structure from A. C) Schematic of an alternative interpretation of the vessels structure in A. Red colour used to emphasise separate vessels.*

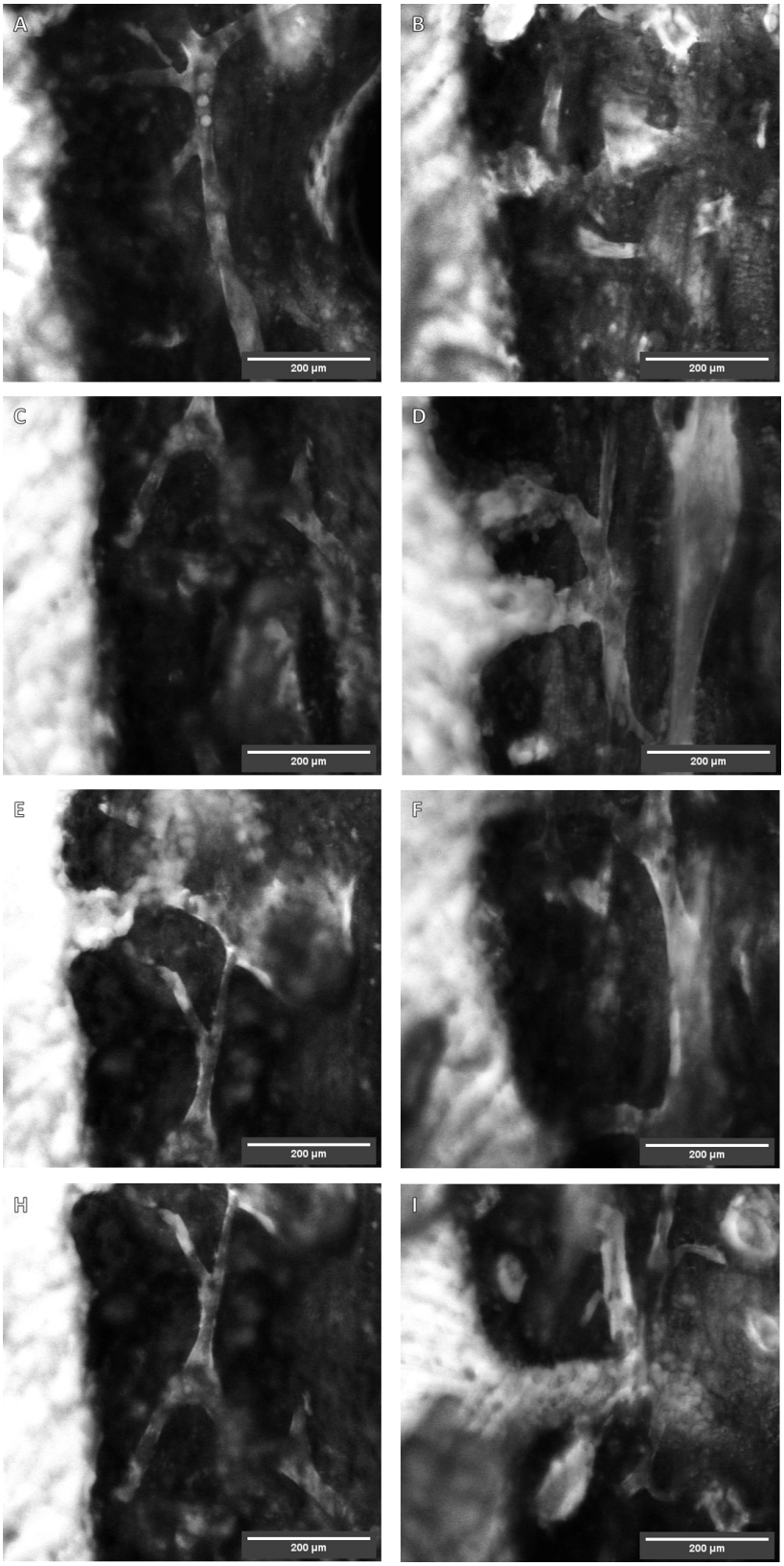

Figure 5.16: *TPF images of saturated disc and filled vessels showing the range of shapes and structures seen in several samples*

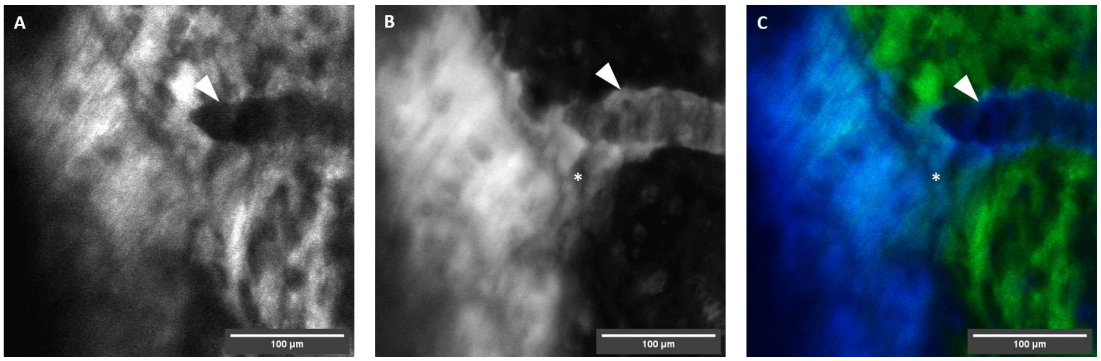

Figure 5.17: *A) SHG image showing a lack of signal where a vessel is, and surrounding cartilage and disc (left) B) TPF image of the vessel, and the fluorescein diffusing across from the disc into the vessel. C) Composite SHG (green) and TPF (blue) of A and B.*

5.3.2 Small Molecule Diffusion

In samples that had been exposed to the fluorescein for 30 minutes and viewed in cross-section, movement of the fluorescein appears to be limited at the tidemark, indicated by the white line (Fig. 5.18). However, there is patchy TPF signal in the cartilage and bone regions indicating the dye accumulating in certain spaces (denoted with *). There does not appear an obvious route that the dye has taken, however, the 'marrow contact channel' network is extensive and could provide out-of-plane pathways.

Fig. 5.19 shows more clearly the dye (blue) in the available spaces. There is a significant region just below the tidemark which contains no tracer and large regions of dye further down. Time case studies showed progressive filling of these spaces (Fig. 5.20). At 60 minutes exposure (B) there seems a much more consistent filling of the available spaces, but again, no clear route of travel is visible. After 24 hours (C) the cartilage endplate becomes completely saturated with the dye.

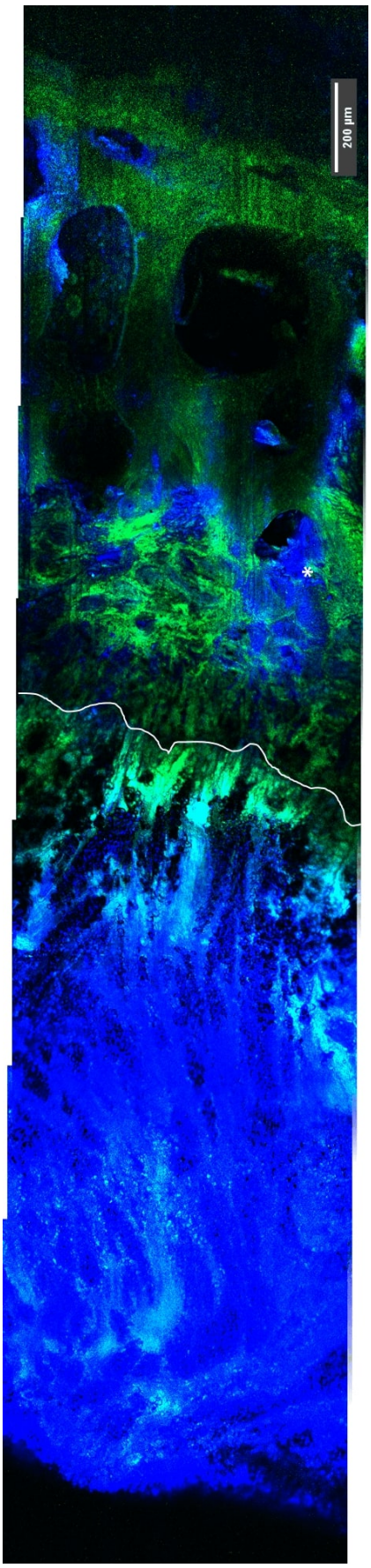

Figure 5.18: *Composite SHG (green) and TPF (blue) cross-sectional map of sample dipped in 0.01 % fluorescein for 30 minutes. The dye is detected as TPF. White line indicates the tide mark and asterisk indicates dye gathered in available spaces.*

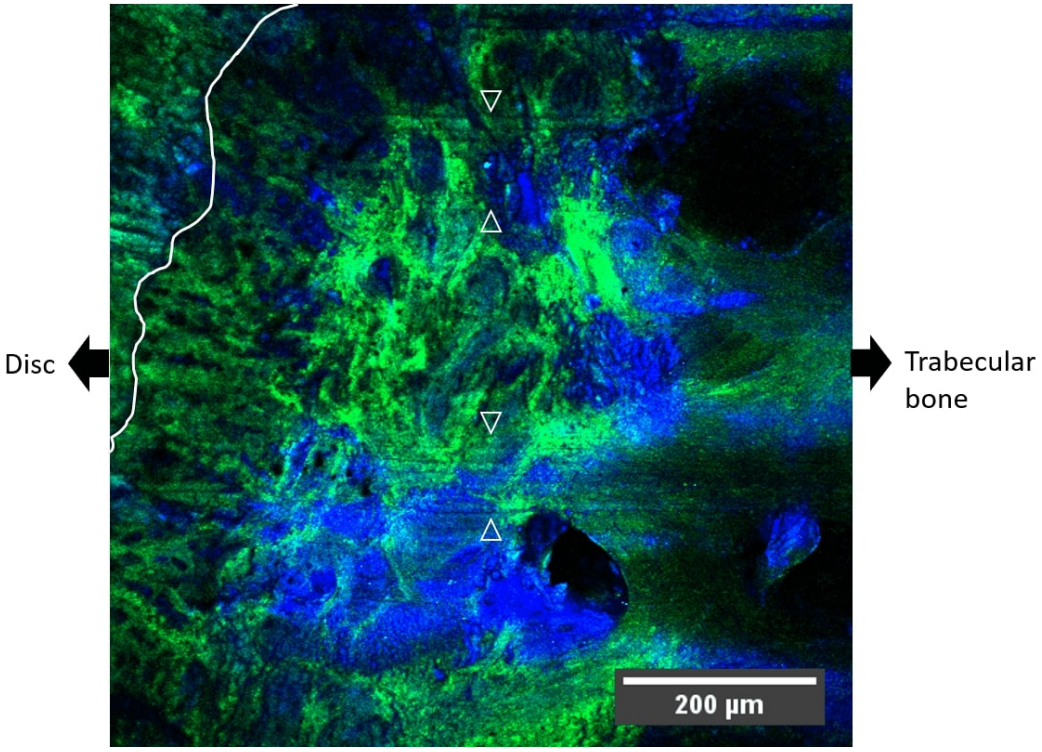

Figure 5.19: *High magnification view of the fluorescein (detected with TPF, shown in blue) filling the available spaces. White line indicates the tide mark, with the disc to the left of the image, and trabecular bone to the right. Arrow heads indicate horizontal artifacts created with the microtome blade during preparation.*

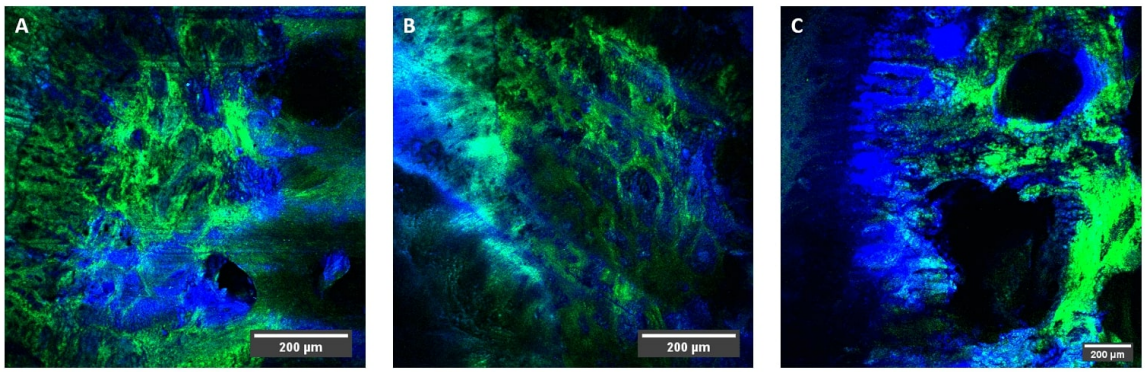

Figure 5.20: *Composite SHG (green) and TPF (blue) images, fluorescein detected with TPF. A- Image of region close to the tide mark after exposure to fluorescein for 30 minutes. B- Image of region close to the tide mark after exposure to fluorescein for 60 minutes. C- Image of region close to the tide mark after exposure to fluorescein for 16 hours.*

In order to quantify uptake, profiles of pixel intensity across the image were taken in FIJI (Fig. 5.21). The intensity was taken from a central line drawn from the start of the image up to the tide mark (tidemark indicated by the white line in Fig. 5.19). The intensity values are in the format of a 'byte image' which labels each pixel with an 8-bit integer giving a range of possible values from 0 to 255. This showed saturation of the disc tissue, but the intensity fell rapidly with depth into the endplate.

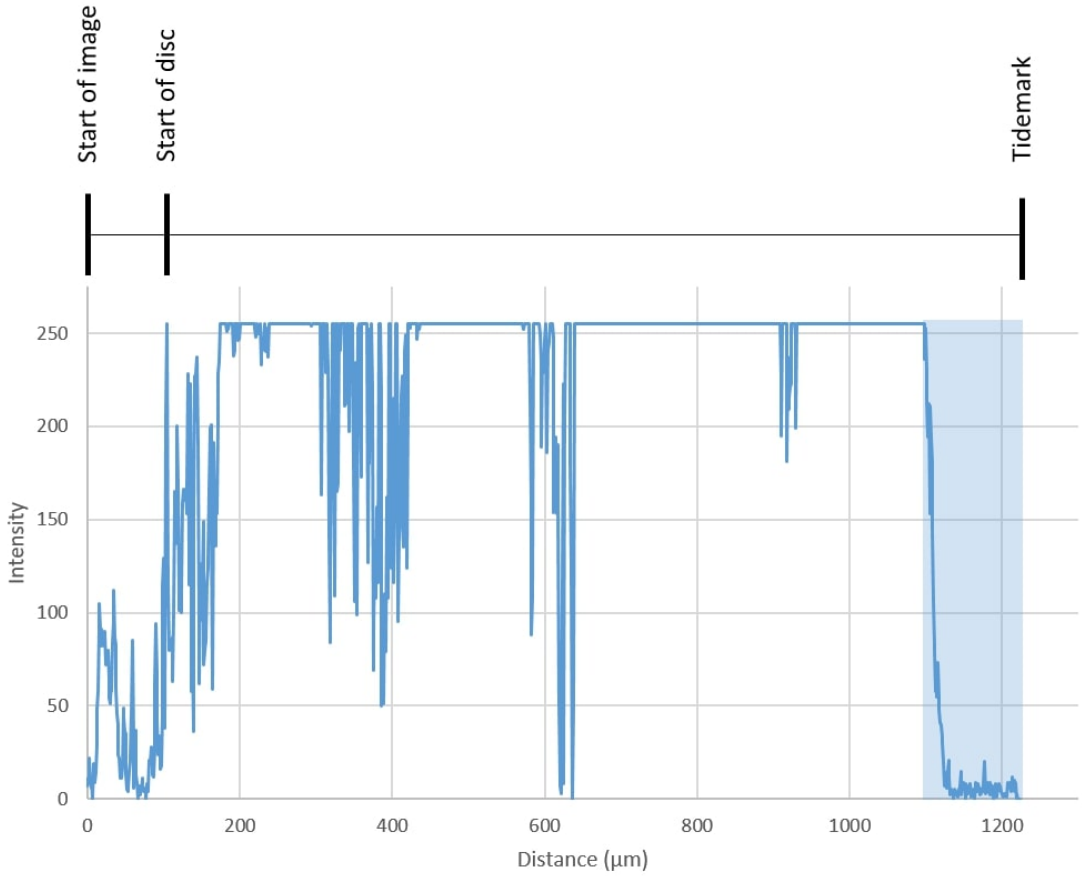

Figure 5.21: *TPF pixel intensity measured in FIJI plotted against distance in µm from the start of Fig. 5.18 to the tidemark (white line). The blue highlighted region was fitted to the diffusion equation, shown in Fig. 5.22.*

Regions showing a smooth distribution of data (highlighted in blue in Fig. 5.21) were fitted to the diffusion equation (5.3) using a custom matlab code. The fit is shown in Fig. 5.22 and gives a diffusion coefficient of D = 5.76 x 10^{-9} cm^2s^{-1}. This fit assumes that the saturation of the disc occurs at time 0, as there is a concentration gradient in the endplate.

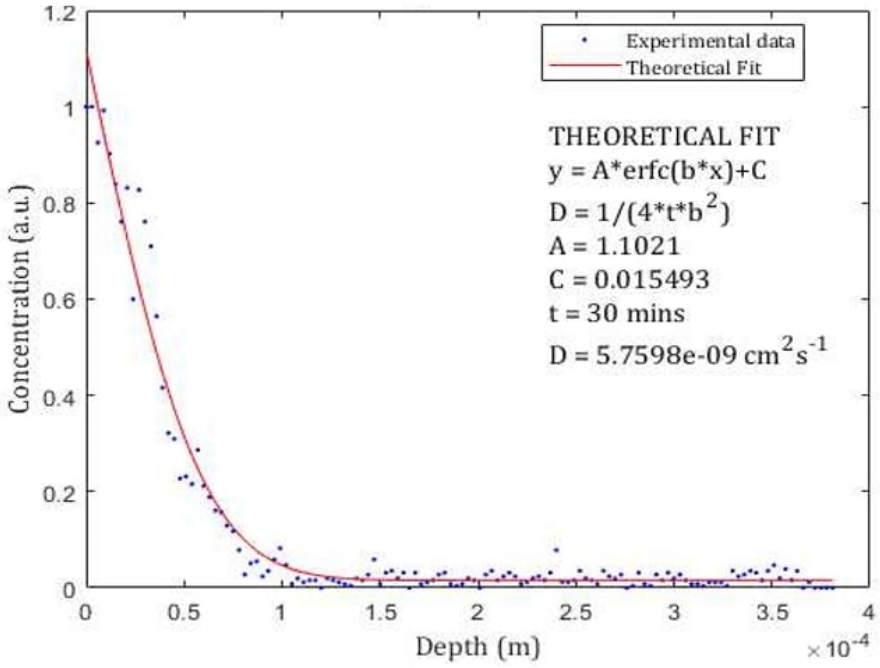

Figure 5.22: *Theoretical fit of the experimental data from the highlighted blue section from Fig. 5.21.*

Exposure for three days still showed a highly saturated disc region, though most strikingly different was the pooling of the dye in the trabecular holes around what are most likely lipocytes (Fig. 5.23).

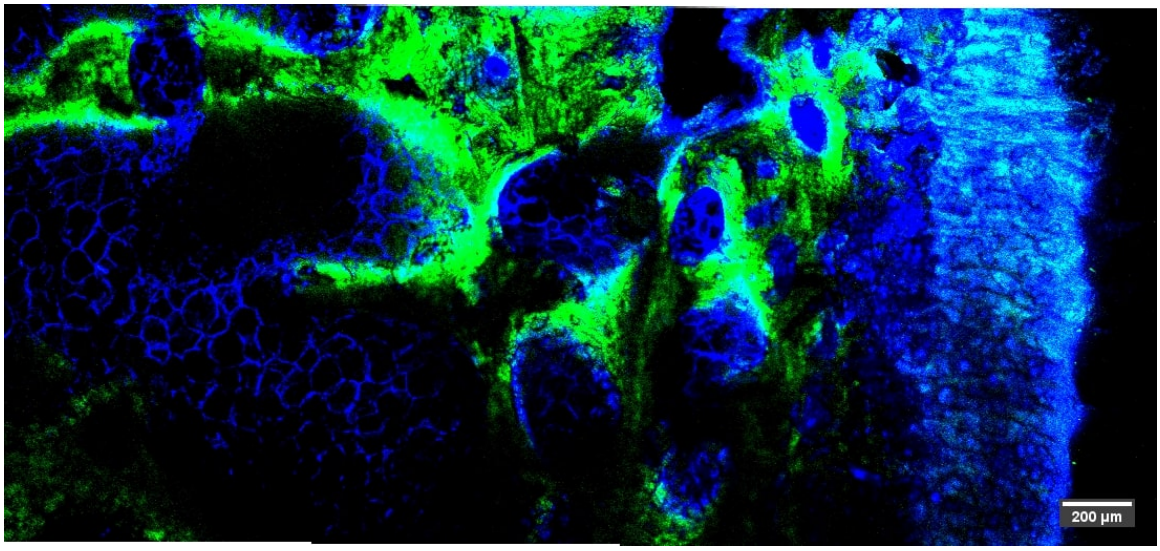

Figure 5.23: *Composite SHG (green) and TPF (blue) images, fluorescein detected with TPF. Image of region from the disc (right hand side) to bone (left hand side) after exposure to fluorescein for 3 days.*

5.3.3 Large Molecule Diffusion

Fig. 5.24 shows two regions which have markedly higher intensities than the other regions (patch 1 and 2 shown in Fig. 5.25). Measured from the start of the disc on the left side of the image, the initial ~ 1500 μm of disc is much brighter than the rest of the image, suggesting the signal is from the Albumin tracer. However, due to the heterogeneity of the tissue, and the consistent lack of obvious concentration gradients in samples imaged the diffusion of albumin was not quantifiable. The second higher intensity region (patch 2) appears to be within the MC, before the tidemark. This patch of brightness does not seem to be due to any tracer as it comes after a section of lower intensity. Additionally, this higher intensity region is also seen in the SHG channel, suggesting that this is auto fluorescence of the tissue rather than the presence of the tracer. Thus it can be assumed the brighter region of the disc is due to the labelled albumin, and that in 16 hours it has only managed to travel a very short distance through the disc, not even reaching the tide mark.

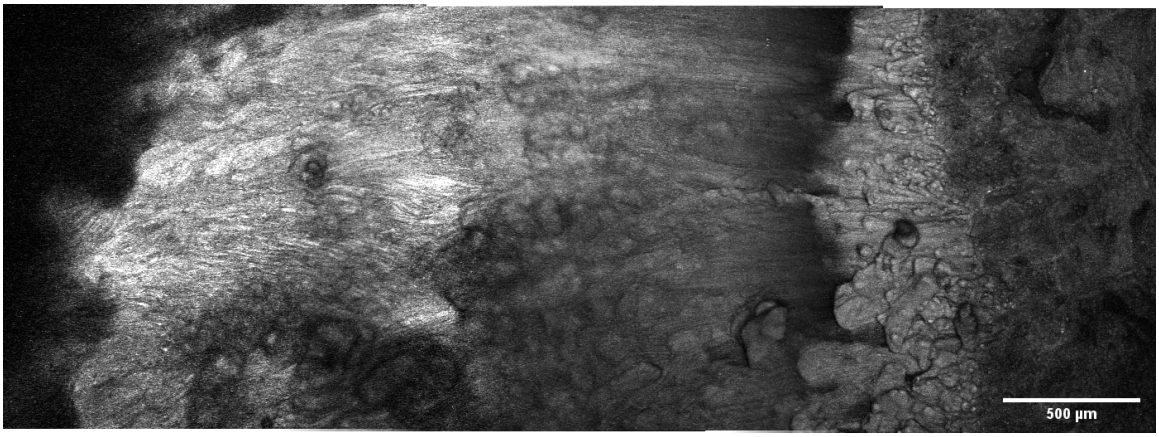

Figure 5.24: *TPF map built in GIMP of cross-section of disc/bone interface after 16 hour exposure to Albumin.*

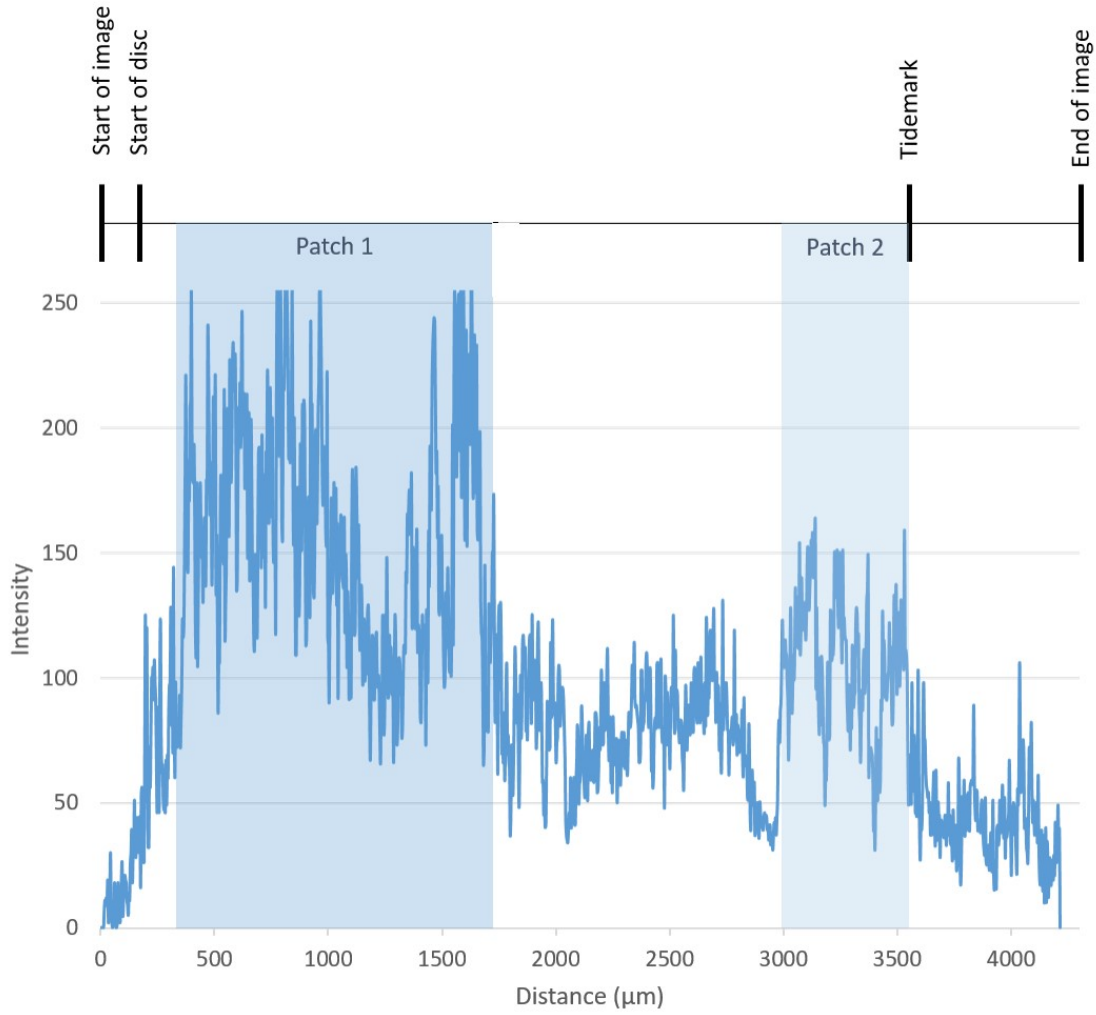

Figure 5.25: *TPF pixel intensity measured in FIJI plotted against distance in µm from the start of Fig. 5.24 to the end.*

5.3.4 Real-time Tracer Uptake

Cross-sectional slices were imaged over time to visualise the movement of fluorescein through the disc, endplate and bone (See methods: 5.2.4). The aim was to produce one-way diffusion such as shown in Fig. 5.26 A and B. However, some experiments showed evidence of the tracer entering through channels at the side of the sample as seen in Fig. 5.26 C. Although this was not the aim of the experiments, it is interesting to note that the disc became saturated much faster.

These studies showed that, as in the previous diffusion experiments the tide mark was providing a barrier (Fig. 5.27). The fluorescein is slightly visible at 6 minutes, and much more so at 7 mins. Once it has reached the tidemark it quickly builds up in intensity. Beyond the tide mark, from 9 mins the tracer spread along an irregular front, forming patches of high intensity ranging in size range from 5 - 18 μm in diameter. However, due to their hazy edges and change over image slices they were difficult to measure accurately. The diffusion coefficient from the sample shown in Fig. 5.27 from the surface touching the dye up until the tidemark, was D = 3.9 x 10^{-7} cm^2s^{-1} calculated using Fick's first law (Eq. 5.1).

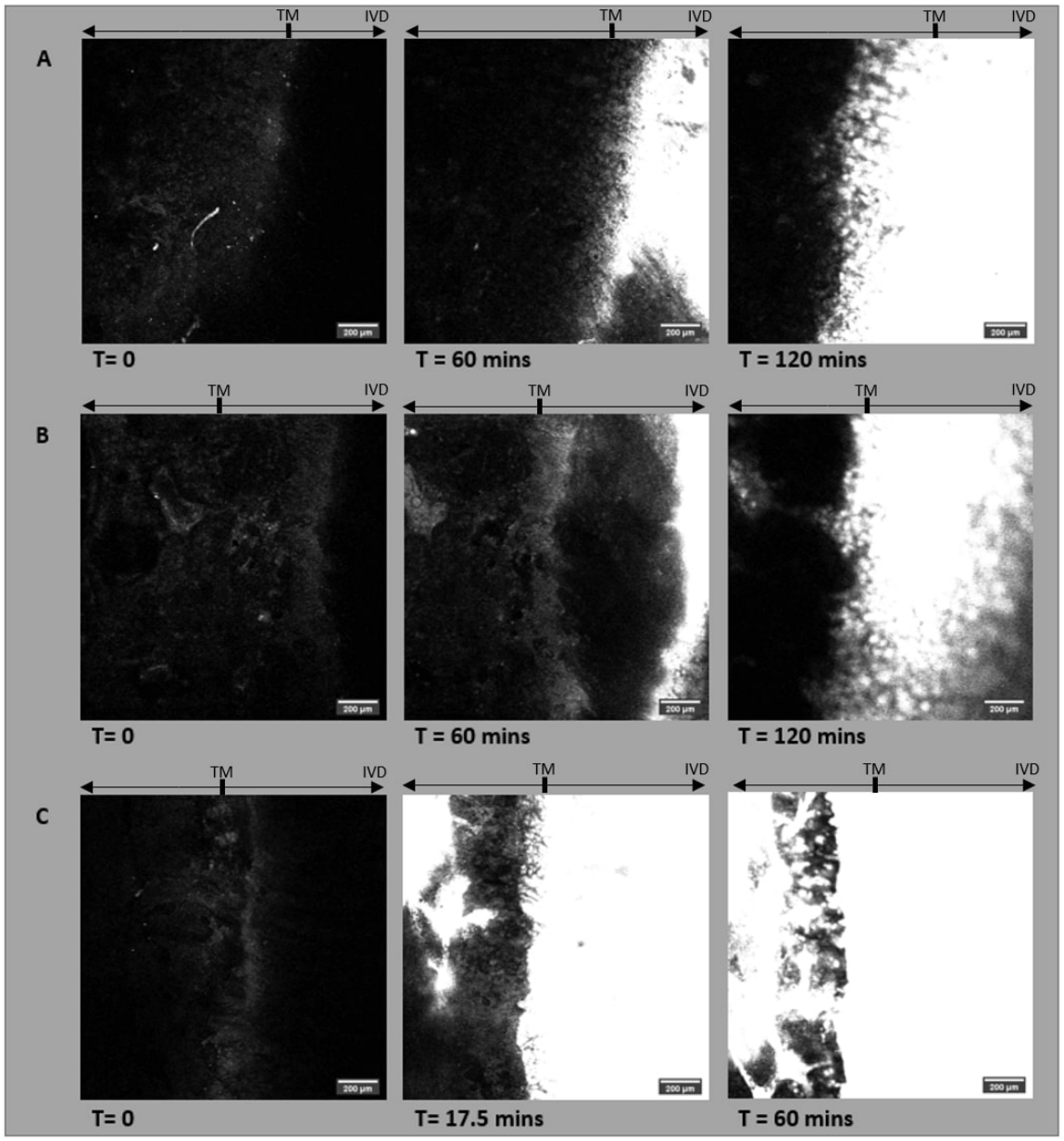

Figure 5.26: *TPF images extracted from stacks of images taken at 30 second time intervals while the disc was exposed to fluorescein. The disc (labeled IVD) was exposed to fluorescein from the right hand side of the frame. The tide mark is indicated above each image (TM). A) Sample shown at 0, 60 and 120 minute time points. B) Another samples shown at 0, 60 and 120 minute time points. C) A sample with dye entering through a side channel. Shown at time points 0, 17.5 and 60 minutes.*

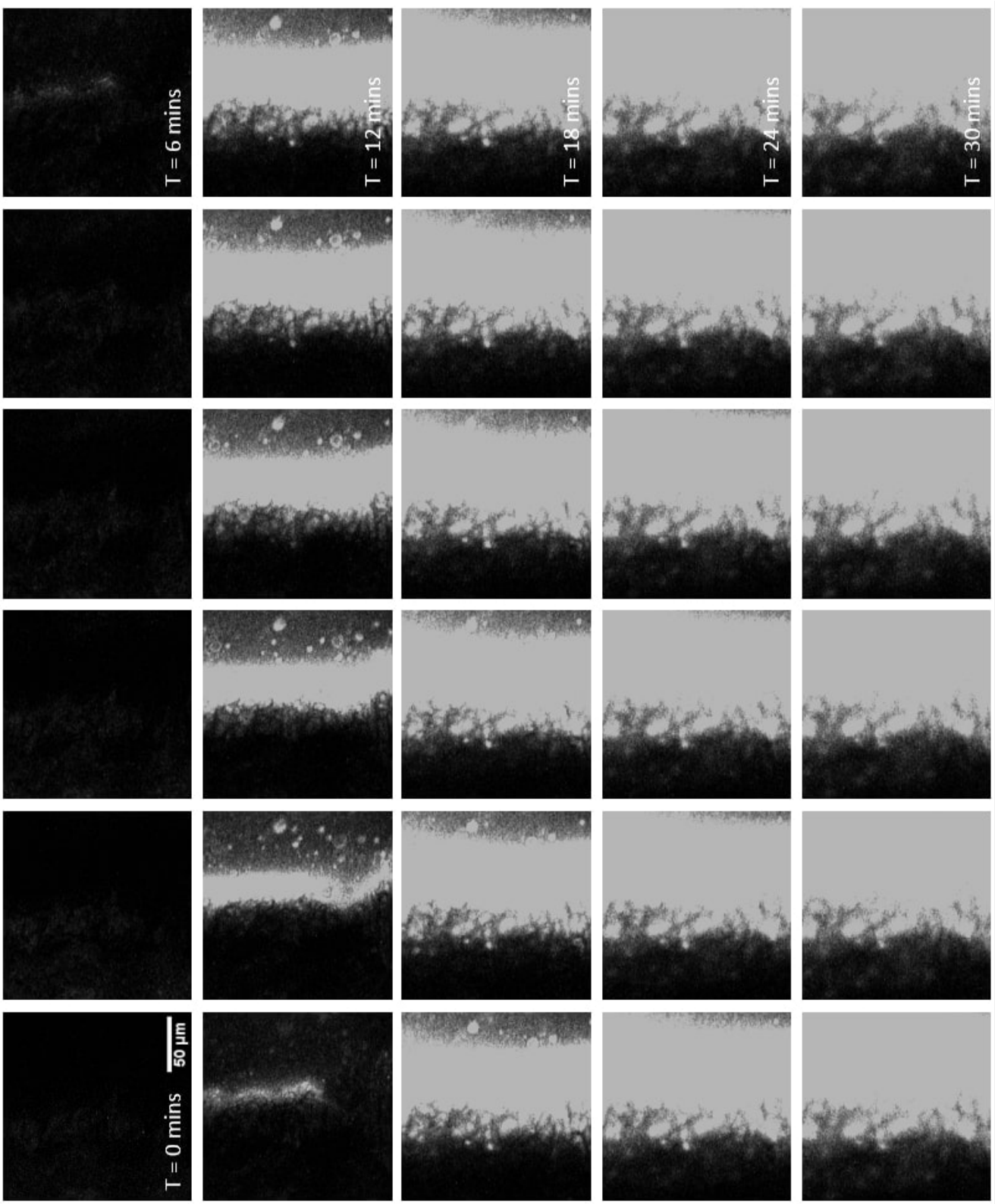

Figure 5.27: *TPF images extracted and magnified (300 %), from stacks of images taken at 1 minute time intervals. Disc was exposed to fluorescein from the right hand side of the frame. Read left to right, top to bottom.*

5.3.5 Perfusion of the Bovine Tail

Fig. 5.28 B and C show that the microcirculation of the skin was well perfused with the Evans blue, whereas the avascular tendons remained white indicating that the Evans Blue had not diffused out of the vessels at a timescale of 60 mins perfusion. When the musculature was removed, vessels close to the disc tissue were evident in the region between the two vertebrae (Fig. 5.29 A). When the soft tissue was removed to expose the disc, it was predominantly white as expected, however, as the unfilled arrow head in Fig. 5.29 B indicated, some dye has diffused out of the vasculature and into the annulus fibrosus. In cranial transverse sections, the dye has penetrated a number of layers of the outer annulus (Fig. 5.30).

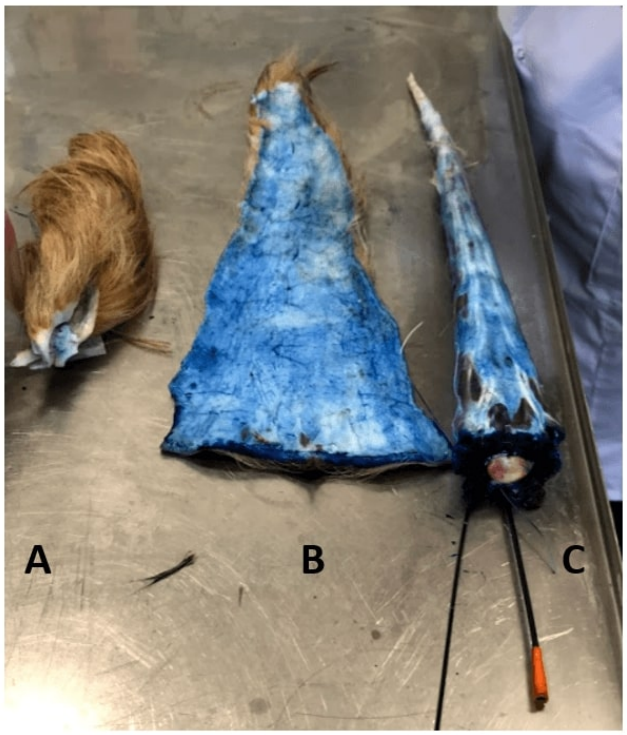

Figure 5.28: *Photograph of A) End of bovine tail removed with skin intact B) Skin removed, blue colour shows that the vasculature has been perfused with the Evans Blue C) the perfused tail, skinned with canular still inserted. Blue of the fascia and darkness of the muscle due to the Evans Blue dye.*

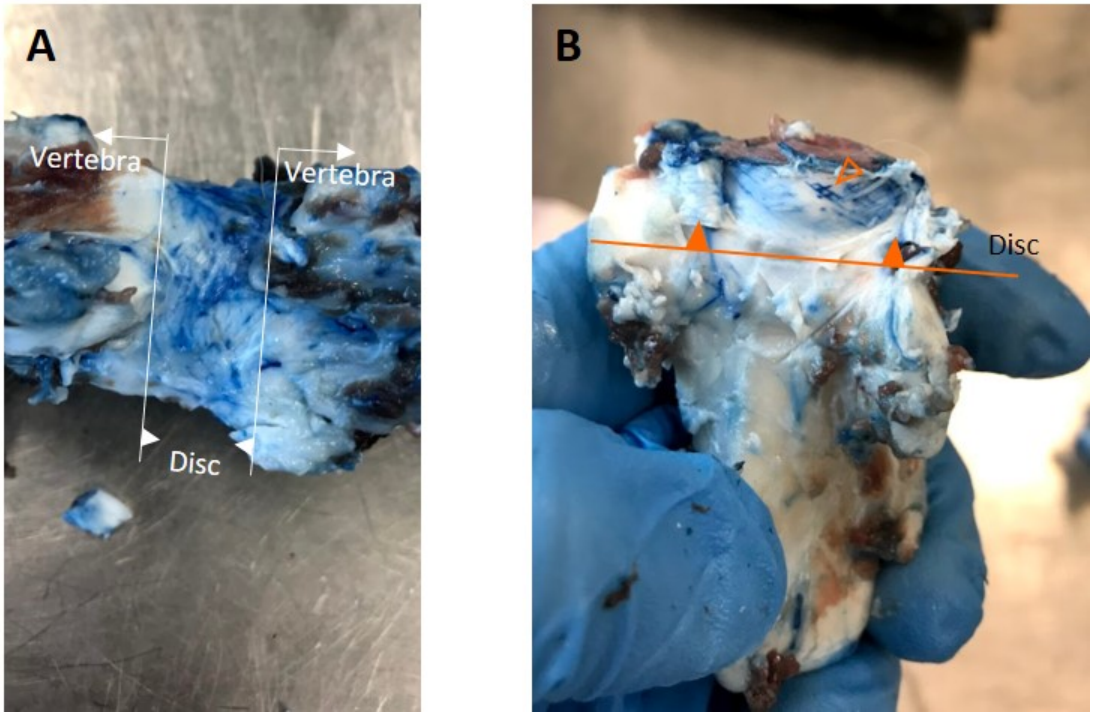

Figure 5.29: *Photograph of A) Motion segment with the musculature removed. Disc is central with a vertebra either side. Blue indicates perfused vasculature of the soft tissue around the disc. B) Motion segment excised at the disc with soft tissue removed. Unfilled arrow head indicates where the Evans Blue has entered the annulus.*

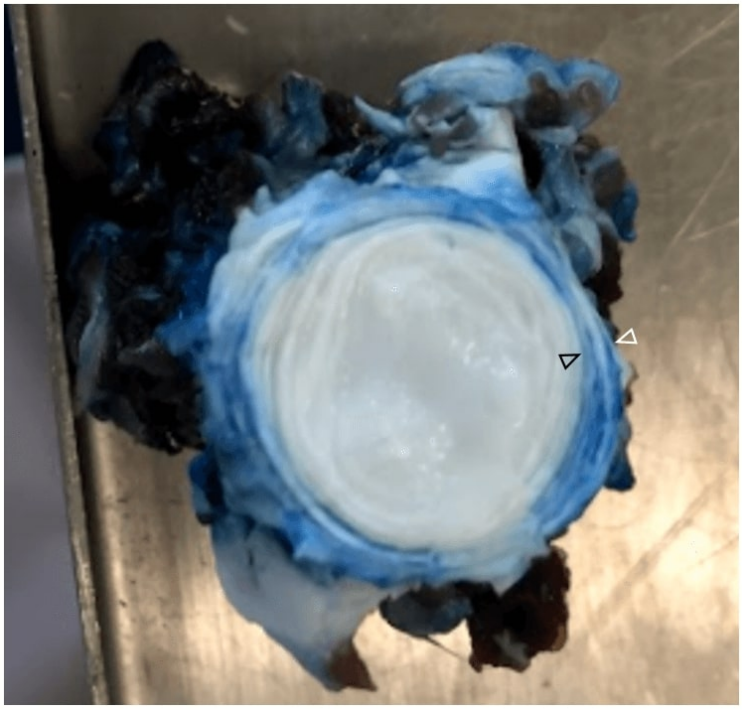

Figure 5.30: *Photograph of A) Motion segment excised at the disc with soft tissue removed. Unfilled arrow head indicates where the Evans Blue has entered the outer annulus.*

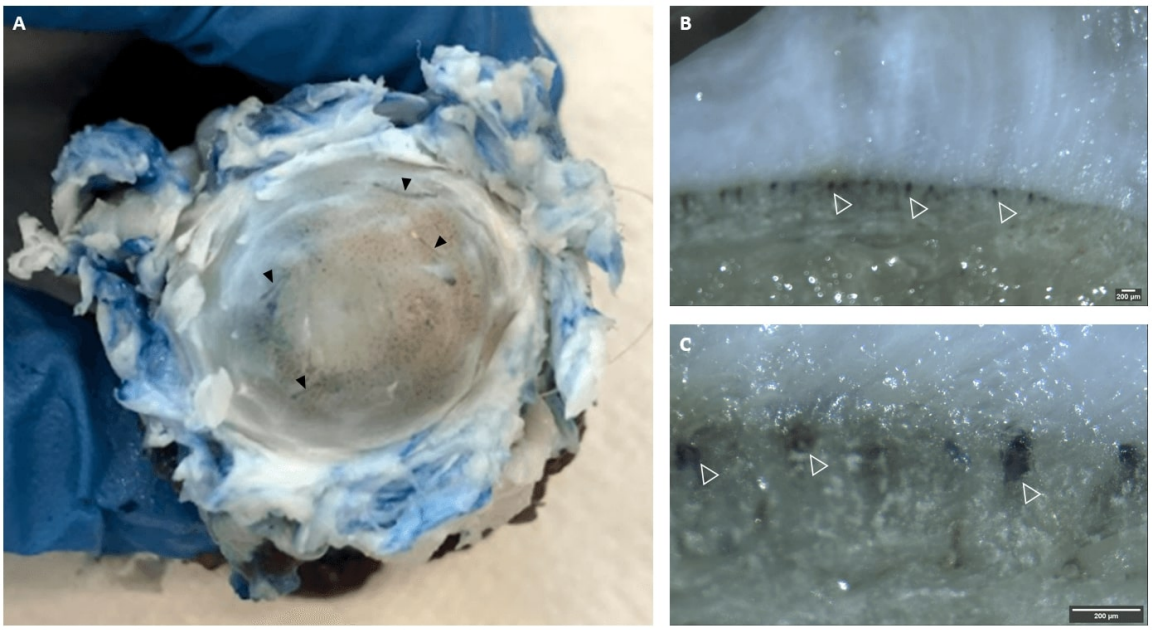

Figure 5.31: *A) Photograph of the exposed cartilage endplate with dye filled buds present. Filled arrow heads indicate where dye has filled a cut made by the scalpel blade. B and C) Dissection Microscope image (16 x and 80 x magnification respectively) of a sagital slice showing the dye filled buds. Buds indicated with a white unfilled arrowhead.*

To investigate the nutritional route through the endplate, the disc was removed to expose the cartilagenous surface below. Whilst cutting, small spots of blue dye became visible (Fig. 5.31 A), the further cut into the cartilage the more became obvious. Additionally when the scalpel penetrated the surface, damaged areas were quickly filled with dye. Whilst on superficial examination it appeared that there was a greater number of filled spots in the outer region, this was actually due to the cartilage being thicker centrally obscuring the tracer. When the samples were cut sagitally so as to image the endplate perfusion, again the spots were obvious (Fig.5.31 B and C). However, the route of filling was not obvious. There were no detectable vessels directly leading to the endplate at all. Fig. 5.32 shows the only vessel that was seen clearly in any of the samples (indicated by the filled arrow heads). Even under multiphoton excitation, Evans Blue was not visible (5.33).

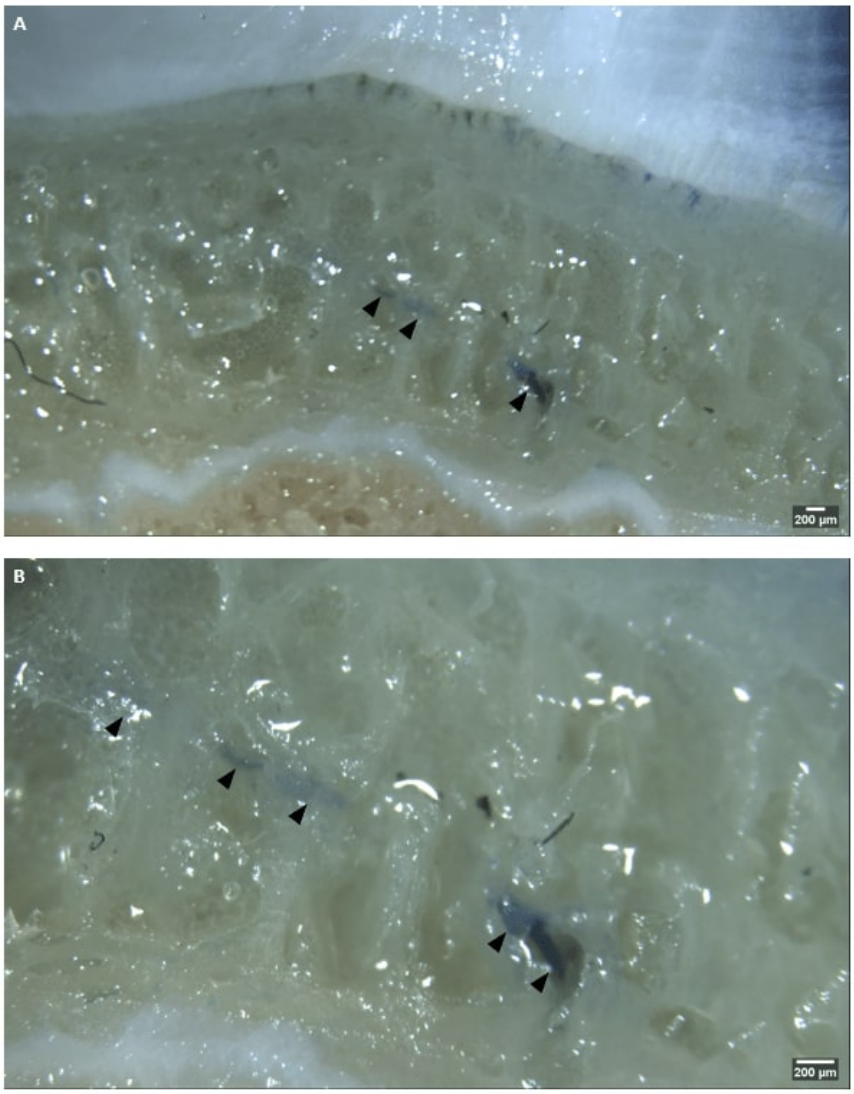

Figure 5.32: *A and B) Dissection Microscope image (12.5 x and 25 x magnification respectively) of a sagital slice showing a dye filled vessel. Vessel path tracked by filled arrowheads.*

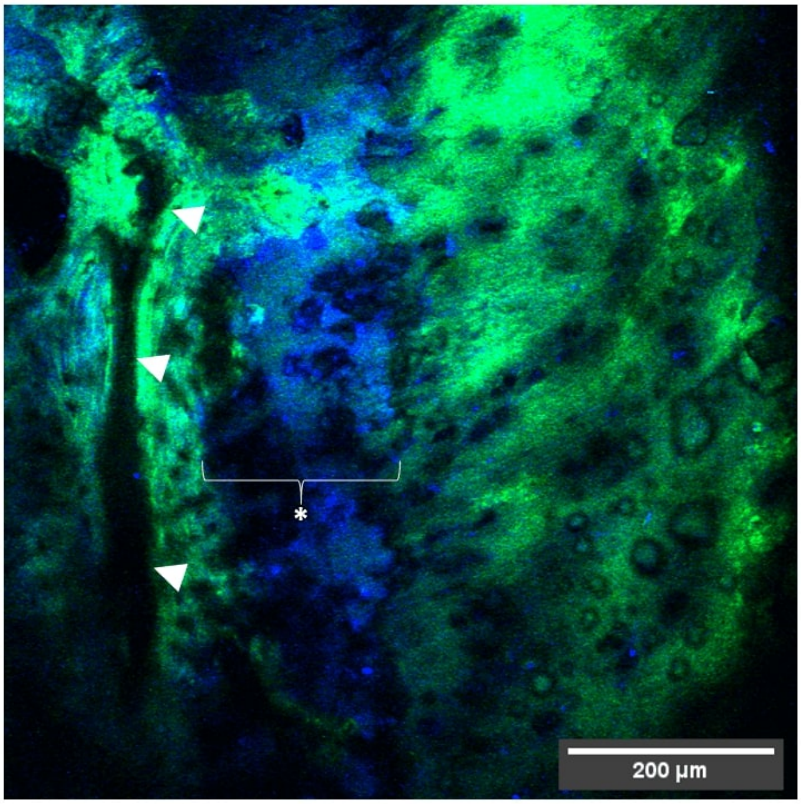

Figure 5.33: *Composite multiphoton image of SHG (green) and TPF (blue) of an Evans Blue perfused tail. Arrow heads indicate a channel and asterisk indicates a region high in TPF signal.*

5.4 Discussion

This study focused on the role of the endplate as a nutritional path for the intervertebral disc. First the vessels will be discussed and their role in nutritional transport. Secondly the diffusion of molecules will be examined followed by the perfusion of the bovine tail.

5.4.1 The Vessels of the Endplate

Fig. 5.9 shows a vessel visible within the MC matrix. It sits close to the tidemark between the mineralised and non-MC. The highly aligned fibres of the annulus are clearly shown on the left hand side of the image; however, the fibres are anchored in the cartilage layer as there is evidence of sub-bundling (see split arrow in 5.9A) which as discussed previously in chapter 4, occurs in the non-MC. It is important to note that the vessel does not cross the tide mark and yet is still in close proximity to the anchored annulus fibres of the intervertebral disc (70 μm). In fact all vessels seen (apart from 5.10) 'ended' prior to the tidemark, insinuating that the vessels do not penetrate into the non-MC. Vessels were shown with differential interference contrast microscopy (DIC) in chapter 4, where they did not cross the tidemark (Fig. 5.34), this is similar to research in articular cartilage where 'bony-specules' containing blood vessels remain behind the tidemark.[260] The images from the current study were ascertained at a much higher magnification than those taken with DIC, and do not show the tidemark following such a tight line around the vessel ends. This is most likely as the DIC is showing a larger branch of the vessel network then seen with the multiphoton (Fig. 5.34).

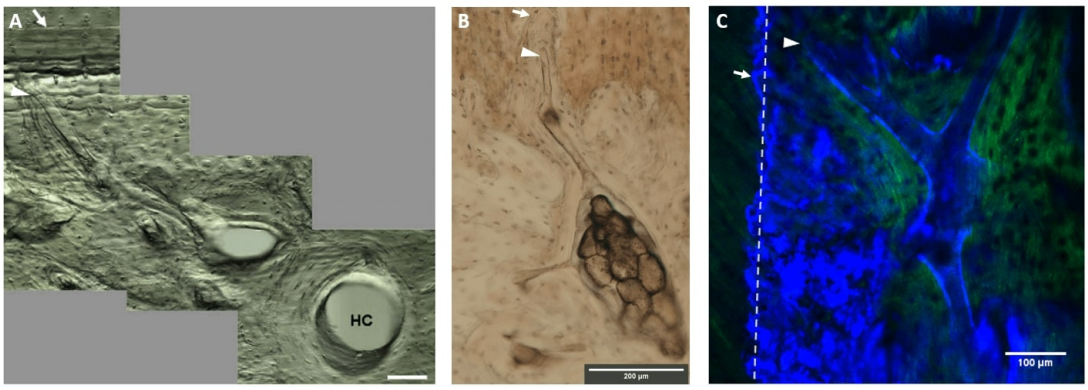

Figure 5.34: *A) Image taken from Thambyah and Broom[260] showing a 'bony-specule' (arrowhead) originating in a Haversian like cannal and extending towards the cartilage. The tide mark, indicated with the arrow, always remain ahead of the specule. B) Image from Chapter 4 (REF) of a similar structure seen in the endplate of mature ovine. Specule (arrowhead) and tidemark (arrow) are labelled. C) Fig., 5.9 illustrating the ending of a capillary seen with the multiphoton. Specule (arrowhead) and tidemark (arrow) are labelled.*

Ayotte et al.,[78] suggested that vessels 'peep' through the calcified endplate as a way to explain pores in the non-MC surface. The wording that they use suggests that the vessels actually pass through the MC layer, into the non-MC (Fig. 5.35 A). This was suggested from their images of fluorescent tracers, however, the diffusion of tracers out of a vessel is not indicative of the vessel path. The 'peeping' suggested was not obvious from any of the imaged vessels in the current study, nor in other literature on the tide mark.[260] What is more likely, especially given the presence of small transverse vessels is that they run close to the surface of the tidemark, without actually crossing it as shown in Fig. 5.35 B. This theory was not directly imaged in this study, however, it provides the best explanation for pores in the mineralised endplate without the vessels penetrating the non-MC.

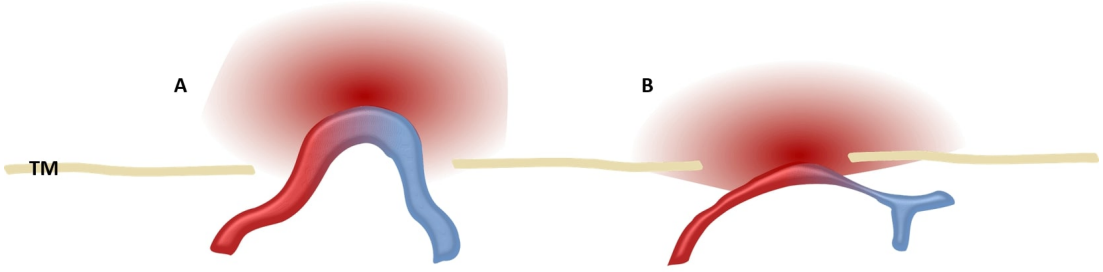

Figure 5.35: *Proposed structure vessels in relation to pores in the MC endplate. A) Proposal based on Ayotte et al.,[78] that vessels 'peep' through the pores. B) Proposal of transverse vessels that does not cross the tidemark (TM) based on images of vessels in this study*

No coiled structures such as those described by Crock and Goldwasser 1984 and Oki et al., 1994 reported were visible within the images attained in this study.[111,115] In terms of the size of vessels the images presented in the study above agree with Oki et al., however, neither the 'loops' at the end of capillaries, the extensive vessel network, nor the 'flat buds' from Crock and Goldwasser were seen.[111,115] In the majority of images showing longitudinal vessel sections, the diameter was relatively uniform (~ 12 μm, Fig. 5.12). However, transverse vessels measured as small as 5 μm in diameter (i.e a true capillary as red blood cells are 6 - 8 μm[261]). These transverse vessels appeared more frequently closer to the endplate. Distinguishing the 5 μm vessel was difficult, due to the blurring of the TPF, meaning some smaller vessels may have been missed. The asterisks in Fig. 5.10 illustrate how an area can become saturated in the TPF signal. This may be a particular problem at the edges of the tidemark which have high levels of TPF due to the hypermineralisation, which interfere with visualising smaller capillaries. Additionally, beacuse a number of tissue give a TPF signal, cell lacunae could be confused for transverse cut vessels. A vessel specific dye may help in this regard.

The closest images attained to the loops referred to above were seen in Fig. 5.15 A/B and 5.16 E and D. However in comparison to those reported in Oki et al.,[112] these loops are too big to be considered vascular buds. Buds were previously reported to measure a maximum of 50 μm where as the 'loops' presented in Fig. 5.15 were closer to 100 μm in diameter. The differences in animal model could be playing a role in the differences. Oki et al.,[112] were utilising a rabbit model, a much smaller animal than either the ovine or bovine model used in this study. A paper investigating the glomeruli of the kindey (another complex capillary loop) suggested that cappilary radius can be assumed as 2% of the diameter of the renal capsule, which actually results in very little difference between rabbit, sheep and cow (3 μm, 4 μm and 5 μm respectively).[262] The smallest vessel measured in this study was 5 μm making it comparable to those repoted by Rytand 1938[262] as well as those reported in Oki et al.,[112] suggesting that capillary size is not a factor. Scmidt-Nielson and Pennicuik[263] reported of the variations in capillary density within the muscles of varying sizes of mammals. They found a relationships between body mass and density, yet there was no significant difference shown between that of the rabbit (232 - 316 cap/mm^2) and sheep (270 - 408 cap/mm^2). Thus, there has been little reported difference in capillary size and density between these animal models, suggesting that the same size and spacing of capillary buds should expected in the ovine and bovine model, as seen in the rabbit. Given this, it is surprising that loops were not visualised with the multiphoton microscope using any of the methods above. However,

given the complexity, 'coiled' structure and previously discussed difficulty with TPF saturation, another method is required to asses the detail of this region.

Some of the of the larger vessels have been imaged as 'dead-ends'. Fig. 5.9 especially shows a rounded end to the vessel rather than just losing focus as the larger trunk does. This suggests that for some vessels, there is actually no loop present. However, by its nature, a vascular network needs to loop for the deoxygenated blood to return to the heart and lungs.[264] Even though historical literature has included references to 'end arterioles',[265] a dead end such as the one imaged would cause the blood to clot, blocking, rather than creating, a nutritional pathway to the disc. In structures such as the eye, these supposed 'end-arterioles' have later proven to have connectivity through higher powered imaging technologies, however, multiphoton microscopy should provide sufficient resolution. An explanation for these 'dead-ends' could be angiogenesis, the growth of new capillaries from pre-existing blood vessels. Angiogenesis usually only occurs during certain physiological situations for example in the placenta during pregnancy, during wound healing or tumour growth. In fact a paper by Hunter et al., reported capillary sprout tips within epiphyseal growth plates. These were characterised by plastic casting and histology, showing abrupt capillary ends containing blood stasis (slowing or pooling). Below these sprout tips, a network of laterally projecting vessels 'serves as capillary loops for the venous return'. Their study was carried out in pre-pubescent rats which raises the question of whether these sprouts continue throughout maturation, and would therefore still be present in mature endplates. Evidence of angiogenesis has been seen in excised herniated discs, and its presence linked with increased pain post-operatively.[266] Rather than image vessels, David et al., detected vascular endothelial growth factor (VEGF, an indicator of angiogenesis) using imunohistochemical techniques on samples from patients undergoing surgery for disc herniations. Though their work does not directly solve the question raised by this study of the 'dead-end' vessels, as angiogenesis in this case is most likely due to the trauma of herniation, it does suggest a route for further investigation of the capillaries.

Another explination could be lymph vessels as they can have dead ends. In their role of 'mopping up' debris, waste material and water from cellular activity they act alongside the vasculature. The presence of lymph vessels in relation to the disc is not well established, and as previously discussed (2.5) the two main articles contradict each other on the presence of lymph in human discs up to the age of 20 years.[120,121] Anatomically, a lymph vessel could play a vital role in the waste removal of the disc as large amounts of water are lost from the disc each day, and little is understood about how this is removed. Comparing this region to others in the body proves difficult because of the

complex combination of tissues. For example, lymphatics are reportedly not present in bone, neither cancellous nor trabecular at any age.[267] However, in the knee joints of mice, lymphatic capillaries and mature vessels are present in various soft tissues around articular spaces.[268] Thus it is difficult to ascertain whether the presence of lymphatics would be expected in the disc-endplate-bone junction. Additionally, the lymphatic vessels are usually closely intertwined with the vasculature, suggesting that both vessel types could have been imaged in this study, but failing to distinguish between the two.

In contrast to these 'dead end' vessels, Fig. 5.10 poses an all together different conundrum. The figure proposes a vessel that appears to open completely to the disc anchoring (Fig. 5.13). Again, anatomically blood requires a circulatory route, and if it followed this vessel, would pool in the disc matrix. Due to the size of this channel, (>20 μm) it could be argued that this is not actually a vessel itself, but rather a canal of the marrow network that would contain vessels. The proximity to a larger trabecular-like hole (also outlined in blue like the vessel) as well as the proximity of multiple smaller vessels (indicated with white arrows) could support this stance. Additionally, a channel of this kind, opening through the tidemark would create pores in the MC such as Ayotte et al.,[78] suggested. What is unclear is how a vessel would operate within a channel such as this, as there is no visual indication of the vessels themselves. The size of this channel could allow a two way traffic system with a loop at the top. There is a possibility that in lysing these samples to remove the clotted blood, some vessels were damaged and removed, meaning that the 'flow' we visualise in Fig. 5.11 was in fact an artefact of the sample preparation rather than anatomy.

Conclusions on the vasculature, especially in relation to the capillaries closest to the disc and therefore involved in nutrient exchange, are difficult to make. All of the work presented appears to raise more questions than it answers. All vessels imaged have appeared to not pass the tidemark, however, their 'endings' require further investigation. This raises the necessity for further work, focused specifically on the tide mark and non-MC as to whether capillary loops are visible, and what the 'openings' from the MC endplate lead to.

5.4.2 The Role of Vessels in Disc Nutrition

Although the centre of the nucleus has the lowest cell density of the IVD, it also has the lowest concentrations of oxygen and glucose, whilst having the highest concentrations of lactic acid.[156] This is primarily due to the distance from the blood supply, as much as

7 - 8 mm for cells at the most central point. Considering that even small molecules have shown low diffusivity in the cartilage endplate (Fig. 5.22), such a distance could appear limiting. However, distances as small as 37 μm between the visible end of a vessel and anchored disc fibres have also been shown (Fig. 5.17).

Further, these vessels form part of the wider structural network within the endplate and bone. Fig. 5.23 and 5.13 illustrate the inter-connectivity of these channels, much like Thambyah and Broom[260] reported in articular cartilage. Cao et al., reportedly imaged this network of marrow canals, and found a few canals with diameter as small has 10 μm, though many more were ~ 25 μm.[257] Images such as Fig. 5.12 show vessels 12 μm as well as slightly larger ones ~ 20-26 μm. In their paper, Cao et al's.[257] method was unable to differentiate blood vessels within the canal network and as such they were only detecting the empty spaces rather than the tissue structures creating them. Multiphoton microscopy is advantageous in this as it allows the visualisation of soft and hard tissues simultaneously.

The 'marrow channels' are shown to contain large cellular structures as made visible by the pooling of fluorescein around the cells in Fig. 5.23. Gruber et al.,[258] also reported on the canal network, however, they stained for blood cells, showing them to be present along with the fatty marrow. This is unsurprising as capillaries are commonly shown in bone marrow.[269–271] Fig. 5.36 (B) shows a 3D reconstruction of capillaries imaged in the marrow spaces of the human illiac crest compared to the cell outlines visible in Fig. 5.23.[271] Although the fluorescein in the marrow spaces show similarities to the capillary reconstruction, it shows a more uniform arrangement, suggesting that this is not visualising the capillaries in the marrow, rather the tracer is just pooling around the fat calls. Additionally, very little variance is seen in the diameter and distribution of the fluorescein path, again suggesting that these are not capillaries. These results do not rule out the existence of vessels in this region, they merely suggest that other methods may be more appropriate to view them. For example Steiniger at al., utilised an endothelial specific stain which was specific to the microvessel walls.[271] Combining a vessel specific stain with the multiphoton capabilities could prove useful.

5.4.3 Molecular Diffusion

Quantifying the diffusion of molecules through the endplate proves difficult due to the heterogeneity of the tissue structures. Roberts et al.,[64] demonstrated with a range of molecular sizes that with an increase in weight of the molecule there was a decrease in

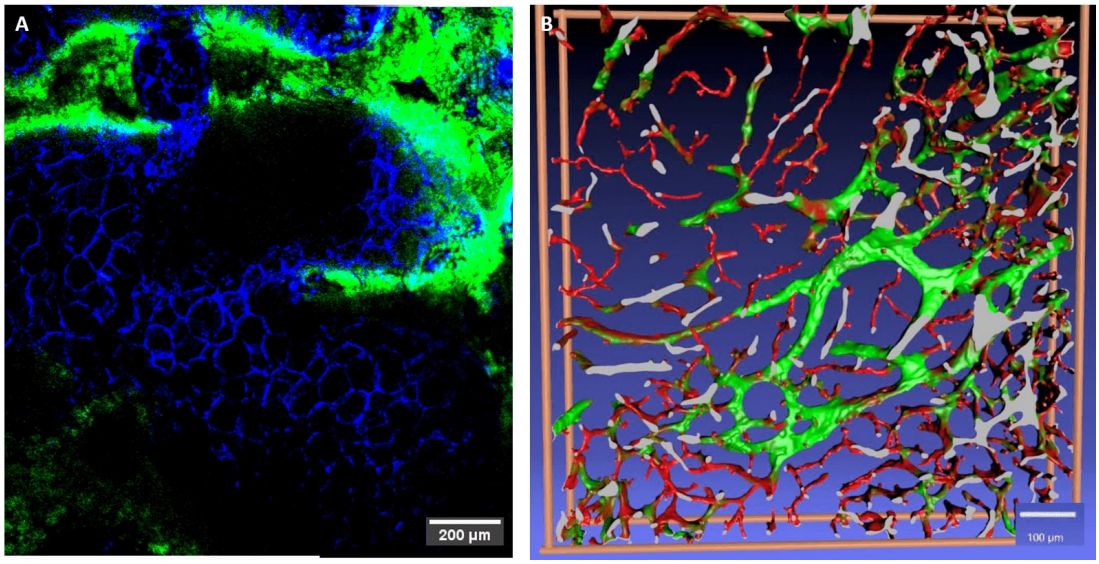

Figure 5.36: *A) Section of Fig. 5.23 showing the fluorescein in the marrow channels. B) 3D reconstruction of capillaries within bone marrow taken from Seiniger et al.*[271]

the distance traveled. This was certainly true in this study comparing the labelled albumin to the free fluorescein. The fluorescein had a >20x higher diffusion coefficient than the albumin, resulting in a greater distance travelled in less time. Some literature has suggested that larger molecules such as labelled albumin are aided in their movement through the disc by mechanical loading.[272] This would also rely upon the mechanics of the endplate as well as the diffusion of molecules and warrants further investigation.

What was unclear from the previous research, was the route of travel of the solutes through the tissue. This work demonstrated preferred pathways and barriers. Fig. 5.18 shows us than initially the dye is held up by the tide mark, and then small pores in the MC endplate become filled (Fig. 5.19 and 5.20). Arkhill and Winlove utilised a similar investigation of diffusion through the articular cartilage of a horse metocarpalphalangeal joint.[273] They too struggled with tissue heterogeneity and related this specifically to regional differences at the level of subchondral microcirculation. The advantage their study had over the present was their ability to section samples to 20 μm which allowed for use of a microscope that could filter for the tracer and gain a true intensity map in relation to distance from the tidemark. Using the same cryotome as Arkill and Winlove, this study was unable to produce mineralised sections without breaking either the sample or blade due to the bone of the vertebral body. However, had the samples had been demineralised, they would not have been indicative of the physiological environment. Additionally, it should be noted that the vertebral endplate and articular cartilage have different tissue mechanics. Despite these drawbacks, an interaction of the fluorescein

dye with some vessels was seen. The interaction varied, Fig. 5.16 shows a number of these images. Some images (A, D and H) showed the fluorescein contained by vessels, whereas others (B, E and I) indicated that some had diffused out from these vessels into the surrounding matrix. This suggests that although the vessels offer an express route out of the disc, solutes also diffuse through the tissue. The proximity of the vessels to the disc is relatively close, meaning minimal necessity of diffusion through the MC which is reported as five-fold lower than in non-MC regions.[137]

5.4.4 Tail Perfusion Experiments

Perfusion studies have proven useful in previous literature to bring light to the vasculature of the complex endplate region.[102,111,274] In this study Evans blue was utilised not only due to its visibility in transmitted light, but also because it is more strongly detected by its fluorescence. The perfusion of the tail was shown to be successful as the capillaries of the skin were visible once it had been removed (Fig. 5.28). Additionally, the muscle had taken on a purple hue, and there was diffusion visible at the outer annulus (Fig. 5.29 B and 5.30). The diffusion visible from the outer annulus was greater than had been expected as literature has indicated that this is a minor transport route for the disc nutrition.[109,275] Within the current experiment, exact time of perfusion could not be measured due to the uncontrollable wash-in period and freezing time. Additionally, some of the capillaries related to this region were removed when cutting to the disc itself. Future work should be aware of this lack of data in this region.

In relation to the endplate, Fig. 5.31 shows that the Evans blue has reached the endplate and appears in 'buds' (concentrated regions of dye) as previous literature has reported.[115] The density of the 'buds' was not able to be measured due to the obscuring cartilage layer, and the flow of tracer when the cartilage was penetrated (Fig. 5.31). Multiple sections of perfused disc were imaged, however, Fig. 5.32 shows the only vessel visible. This was disappointing, and counter-intuitive as the bone is a highly vascularised region. It is unlikely that there is blood clotted in vessels that are not visible as the bone would appear more pink, and other regions show the penetration of the Evans blue suggesting there may be another reason for this lack of vessel visibility. Further, sectioning the Evans blue perfused tail and imaging under the multiphoton proved equally disappointing (Fig. 5.33). No vessels were made evident by the dye and even the 'buds' seen with the dissection microscope were difficult to locate. This suggests that the concentration of dye was potentially too low, increasing the concentration may remedy this issue.

5.5 Conclusions

This chapter focused on the endplates role as a nutritional pathway to the intervertebral disc. Two main avenues were investigated, first the vasculature and second the diffusion through the endplate tissues. The main findings are summarised in Fig. 5.37.

Vessels within the endplate were imaged within close proximity to anchored disc fibres (< 70 μm), which is beneficial considering the low diffusivity of small solutes in the endplate (Fig. 5.37 C). The vessels, which stemmed from the marrow contact channels, were not shown to cross the tidemark (Fig. 5.37 A and B). However, the ends of vessels were not always visible. This work raised questions about the 'dead ends' of the vessels seen both in this study and in the literature, suggesting they may be due to capillary sprouting, or lymph vessels (Fig. 5.37 D). Further work is required in this area to better understand the vessels in the endplate.

Although perfusion of the bovine tail was disappointing, it still showed a small amount of diffusion at the edge of the annulus. Under the disc, the number of buds/vessel endings was observed to increase towards the centre of the disc (Fig. 5.37 E). However, this finding was qualitative and a further quantitative analysis of this would be beneficial to the literature. In terms of diffusion, it was unclear from previous research the route that solutes follow through the tissue. Through the use of real-time imaging of a fluorescent tracer, this study showed barriers- initially the dye is held up by the tide mark- and preferred pathways- the small pores in the mineralised cartilage. The fluorescent tracer confirmed the diffusion from the disc into vessels in the endplate, however, solutes were not restricted to their path. This confirmed the importance of the endplate vasculature within solute transport.

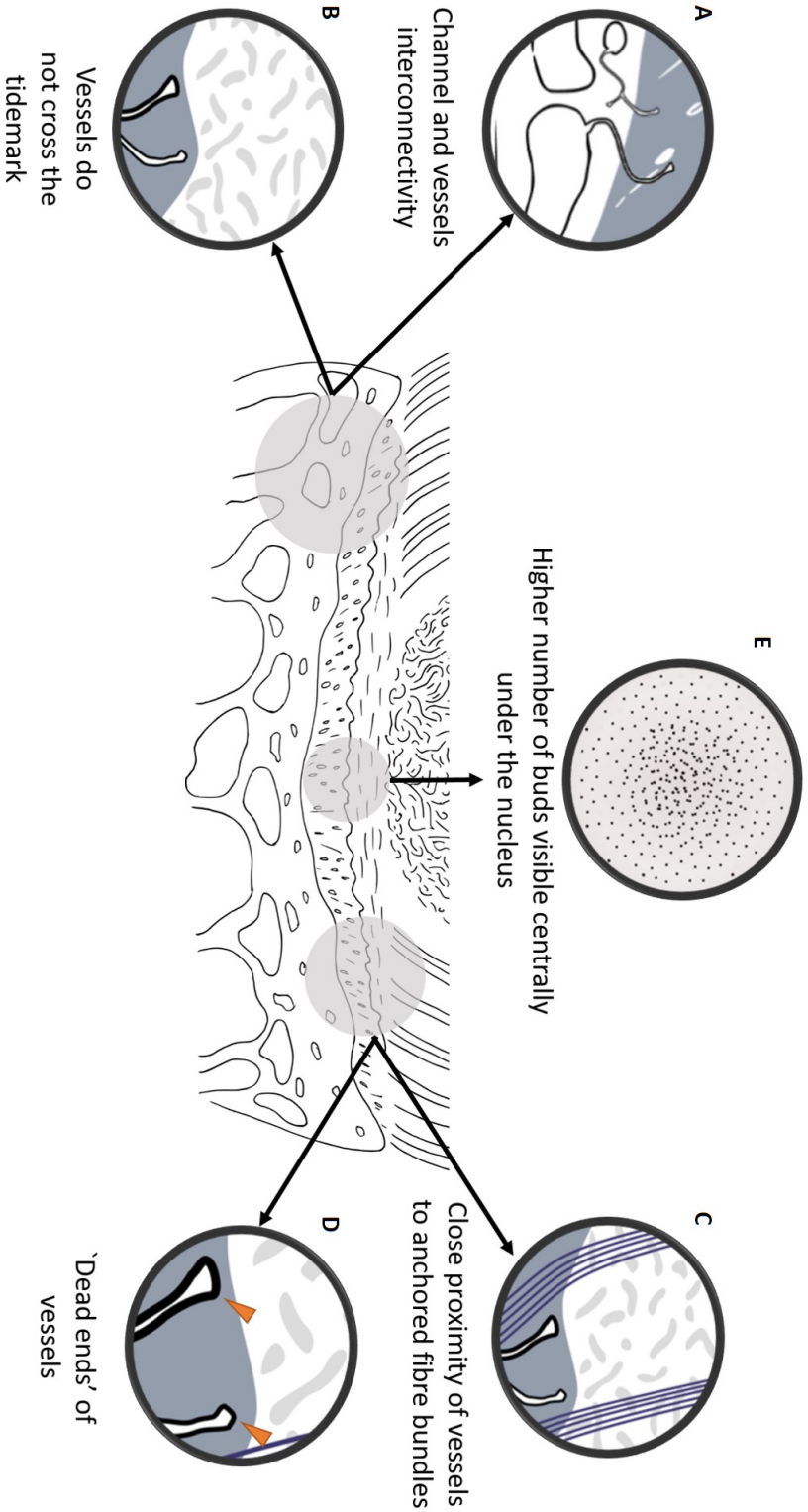

Figure 5.37: *Schematic representing the main findings from chapter five.*

6 Micro-Mechanics of the Cartilage Endplate

6.1 Introduction

This chapter proposes a novel method of loading the endplate while simultaneously imaging, which allows for understanding of the micromechanics of the endplate.

The structure of the endplate and interactions with the disc play an important role in the mechanics of the motion segment and thus the spine. All aspects of the spinal unit contribute to the deformation and recovery during loading and unloading cycles of every day events such as standing (~ 1000 N) or light manual work (~ 1500-2000 N).[276] Segment response to this compressive loading is non-linear due to the diverse material properties and complex structure of the segment.[83,84] The structure of the intervertebral disc, with the nucleus and surrounding annulus fibrosis contribute largely to the mechanics of the endplate.[85] Load acting on the vertebrae is usually axial compression from one endplate to the next, however, it also incurs flexion, extension and torsion (see Fig. 2.6). When the disc is compressed, the annulus bulges outwards,[85] and the endplate bulges into the vertebral body.[87] As a result, uniaxial loading of the motion segment results in biaxial loading of the endplate, which could lead to higher occurance of damage than estimated with uniaxial loading.[27] The role of the endplate in compression has been discussed and investigated using a variety of methods, but due to the difficulty of direct measurement, it is still unclear. Additionally, a wide variety of methods has made consensus difficult.

A whole specimen in vitro method was suggested by Hulme et al., using fiducial markers on the superior and inferior endplates of an intact motion segment.[277] Unsurprisingly, they reported that the higher the load, the greater the deformation of the endplate. Their study was unable to identify the separate regions of the endplate (non-mineralised, mineralised and bony), and thus is limited in exploring the individual contributions of the regions.

Some studies have attempted to address the regional variations of endplate mechanics using indentation techniques.[88,89,278–280] These studies have utilised a standard method

of 'cleaning' the endplate through the removal of disc and cartilage using a scalpel,[281] suggesting their focus on the BEP, though this was not always explicitly stated. Following soft tissue removal the surface of the endplates are then indented following a uniform grid system which allows for comparison of regional mechanics. Using this method Ash et al., showed that failure forces correlated with the thickness of the BEP[280] and Bailey et al., showed that the anterior endplate was stronger than the posterior (strength dictated by the failure load).[278] These methods require exposure of the BEP possibly causing damage to the BEP surface, as well as removing the possibility of relating its mechanics to the surrounding structures.

Very little work has been produced on the mechanics of the non-MC of the endplate. Fields et al., stamped dog-bone shaped sections of cadaver non-MC and subjected them to tensile loading.[282] They showed an average tensile modulus of 5.8 ± 5.7 MPa and that the tensile modulus was associated with the collagen/GAG ratio. Although their study sheds light on the mechanics of the non-MC which is under represented in the literature, its methods are still highly destructive, lacking physiological relevance and still cannot answer questions of the tissues mechanical association with the disc and MC.

A recurring issue in the research on the endplate is the inability to investigate local micromechanics with regards to the surrounding tissues. The whole segment approach utilised by Hulme et al., does keep the tissues intact, however, the CT they employed cannot detect soft tissues, and had a limiting resolution of 82 μm.[277] A method that can measure the micromechanics of the endplate in relation to the disc and bone is required.

Within the department of Bio-medical Physics, Exeter, a number of studies have utilised real-time imaging of biological materials with the multiphoton microscope set up. Investigations into lamella disc strain[51,283] and articular cartilage[284] have shed light on the micromechanics of these regions using custom rigs. The ability of the multiphoton system to image mineralised and non-mineralised tissues with minimal sample processing means that cross-sections of tissue containing disc, non-MC, MC and bone can be utilised. This not only allows for investigation of the specific regions of the endplate, but also how they interact with the neighbouring tissues. The aim of this study was to develop a method of real-time imaging of the endplate under axial loading.

6.2 Methods

6.2.1 Loading Rig

Two rigs for applying mechanical loads to tissue samples under the multiphoton microscope were available for adaptation. A rig with automated displacement control had been designed for investigating the mechanics of the annulus of the disc,[51,283] and another had been designed for articular cartilage compression testing.

The automated rig, shown in Fig. 6.1 A, is driven by a motor that moves both sides of the rig simultaneously, loading symmetrically by displacement control, which maintains a central focal point position. This rig can be programmed to follow a loading protocol of static or cyclic compression or tension. The limitation of this rig becomes apparent when the region of interest (ROI) of a sample is not central. As Fig. 6.2 illustrates, symmetrical loading will shift a non-central ROI out of the focal point as the load is progressively applied. Due to the endplates being situated either side of a central disc, imaging them under load within this rig would be very difficult. Additionally, the positioning of the rig within the microscope set-up physically limits the movement of the objective (the rig machinery blocks its path), restricting the ability to correct for the movement of the ROI through the adjustment of the focal point. Therefore this rig is not feasible for use in investigating the endplate mechanics at this stage.

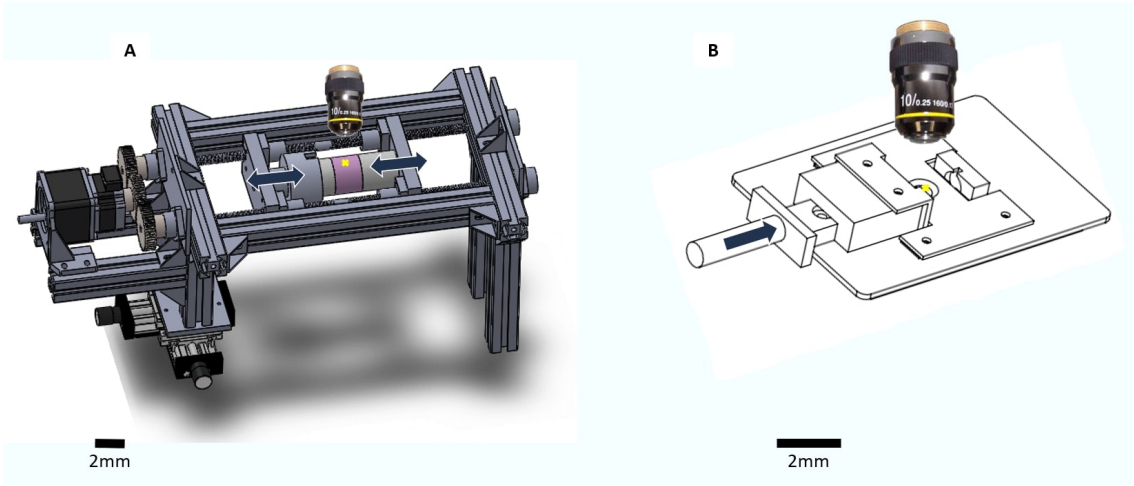

Figure 6.1: *Schematics of the two rigs created for use within the multiphoton system. A) An automated rig designed for intervertebral disc mechanics. B) Manual compression rig designed to compress strips of cartilage.*

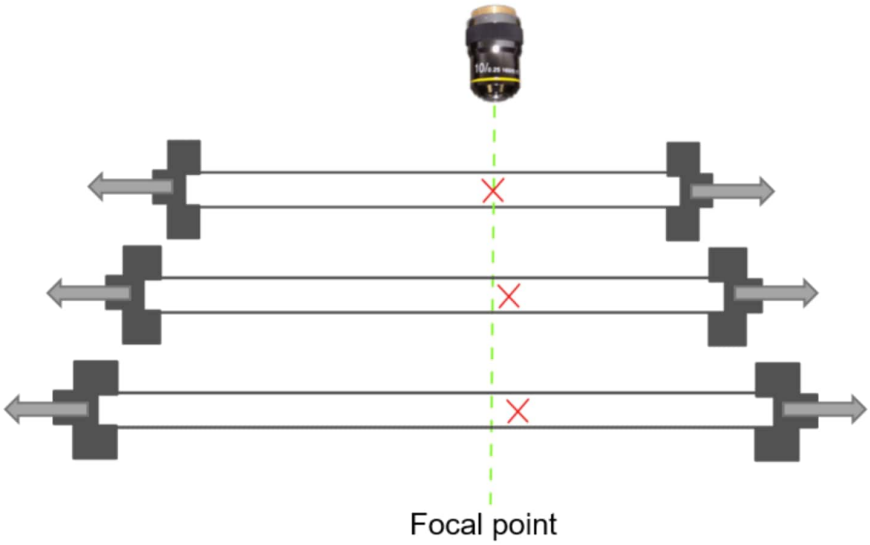

Figure 6.2: *Schematics illustrating the symmetrical loading of a sample, with an off centre region of interest (red X). Note how as the sample is stretched, the ROI moves out of the focal point (denoted with dotted green line).*

The manual compression rig, shown in Fig. 6.1 B was originally designed for the compression of thin articular cartilage strips. One end of the sample is positioned against a load cell which is fixed to the device. The opposing side of the rig holds a micrometer which guides a plate in order to apply compression the the sample (Fig. 6.3). This rig is primarily designed for static loading due to the manual use of the micrometer to apply a displacement. An advantage of this system is that it has an inbuilt cover slip, meaning that the rig can be utilised with an immersion objective. The device is limited in that it requires thin samples. The PVC spacers (see Fig. 6.3) which hold the sample in place allow for samples up to 1.5 mm thick which means that the samples have to be sliced and ground before they can fit in the rig. Despite this, the manual rig offered the best chance of real-time imaging the micromechanics of the cartilage endplate. Therefore this rig was employed in this study.

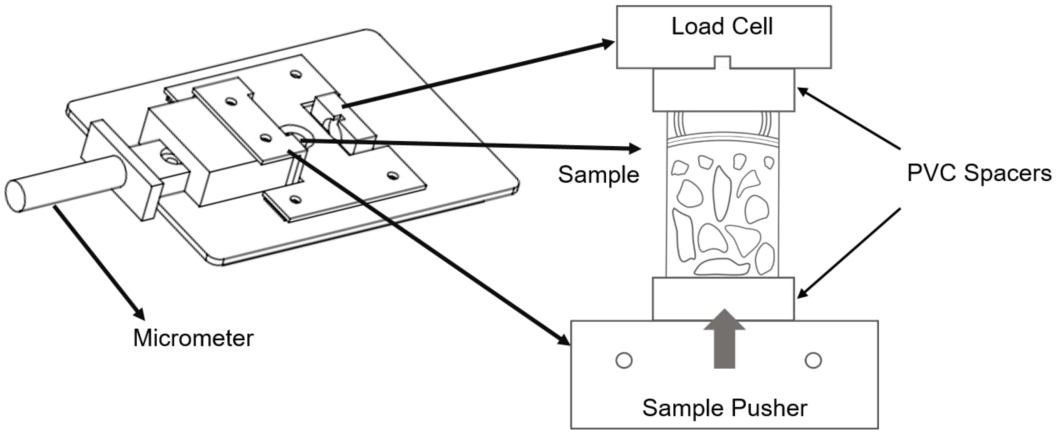

Figure 6.3: *Labelled schematic of the manual compression rig. Not drawn to scale*

6.2.2 Sample Preparation

Bovine tail samples were were prepared by standard preparation procedures described in chapter 3.3.3. However, samples were thinned until they were < 1.5 mm and then cut using a scalpel into rectangles from the annular region, roughly 15 mm by 5 mm in size. Samples were then matched to spacers of the same height, (spacers differed in thickness by 0.2 mm and ranged from 0.1 to 1.5 mm) and were then loaded into the rig with the spacers as shown in Fig. 6.4. The samples were loaded so that the applied load would mimic physiological axial compression. The cover slip was attached to the 'top plate' using vacuum grease to create a seal so the immersion medium was kept beneath the objective.

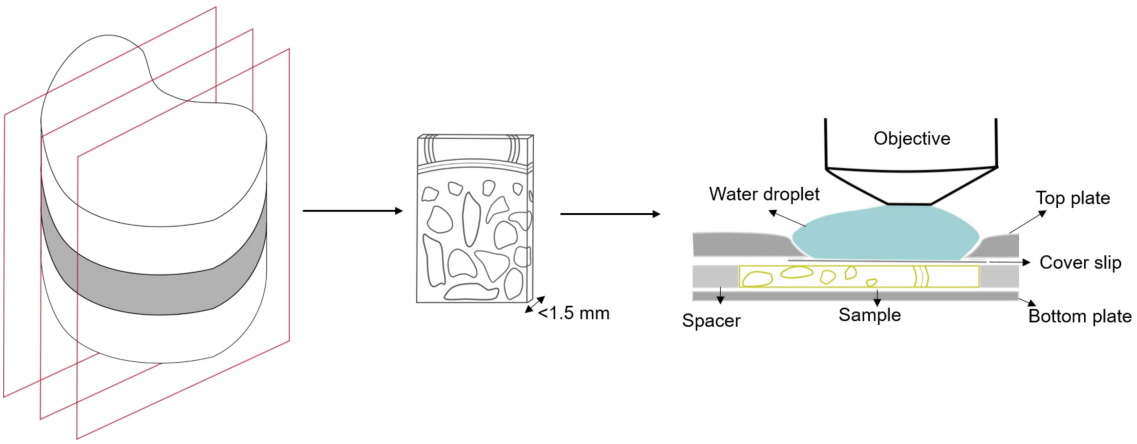

Figure 6.4: *Schematic representation of the sample preparation and the sample loaded in the rig. Not to scale.*

6.2.3 Loading Protocol

Once the sample was set-up in the rig, the sample pusher was positioned so that there was no space between the sample pusher, and sample, without applying compression. The rig was then transferred to the multiphoton stage. A series of images from the edge of the disc to the bone were then taken whilst unloaded (purple * in Fig. 6.5). This was used to give an initial estimate of the compressible area which would was used as the 'original length' and so an estimate of the applied strain could be calculated (change in length/original length = strain). The micrometer was then adjusted until a force was registered by the load cell. An initial relaxation period of ~ 30 mins was given between the application of the load and the image being taken to reduce creep during imaging. At each step, a displacement of 15 μm was applied,which equated to a ~ 2 % strain. As Fig. 6.5 shows, after a period of relaxation (~ 20 to 30 mins) an image map was taken from the disc to the bone, and then the process repeated with the next applied displacement of 15 μm. This was continued until the sample was no longer visible within the focal plane of the objective. This was a result of sample moving, bulging or dehydrating.

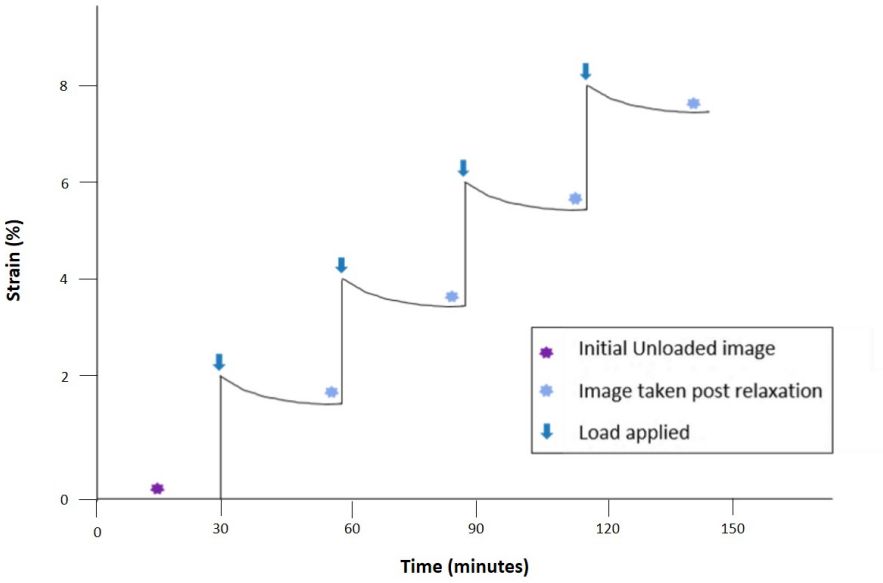

Figure 6.5: *Schematic representation of the loading protocol.*

6.2.4 Data Analysis

In order to build the maps acquired at each applied displacement, SHG images were separated from the TPF and built into a continuous map in GNU Image Manipula-

tion Program (GIMP, 2.8.18). After a map was constructed for each load, they were assembled into a stack and aligned using the FIJI version of ImageJ®(Fiji is just ImageJ http://fiji.sc/) plugin for linear alignment (translation only) with the 'scale invariant features' transform.[285]

Tissue Tracking Software

'Yet Another Tissue Tracking Software' (YATTS), was utilised to obtain a displacement map from each stack (one stack per experiment) and calculate microscopic strains. YATTS is a custom software written in Matlab 2014b (The MathWorks, Inc., Natick MA) by Dr. Claudio Vergari for the purpose of calculating microscopic strains in annular bundles.[283] On the first image of a stack, a grid was drawn to divide the image into square elements which were automatically tracked in the following images by digital image correlation. The tracking of elements can be checked for reliability using the reliability map. The reliability of the tracking can be affected by the size of the elements as well as the image contrast and smoothing applied. To increase the likelihood of reliable tracking, the images were enhanced through histogram equalization and displacement smoothing was applied to the tracking. Additionally, care must be taken over the area covered by the grid as large holes such as trabeculae will not track well. The elements should ideally be as small as possible while still allowing for reliable correlation.

Using the structural information of the SHG image the elements were assigned to regions of: BEP (15 elements), MC (12 elements), non-MC (5 elements) and disc (7 elements). At the boundaries between tissues, some elements contained more than one tissue type. In these instances, the element was assigned to the predominant tissue group. This helped in distinguishing the disc and non-MC as it was easier to identify a predominant tissue than the exact boundary between the two. Elements within a region were averaged and their standard deviations calculated for analysis.

Macro Analysis

As YATTS has never been used in a combination tissue (i.e. bone and cartilage) macro measurements of the changes in lengths measured from the start, to end of a region as shown by the green and blue lines in Fig. 6.6. In FIJI, images were scaled and the length of the compressible region (disc and non-MC), and the MC was measured at each applied load. There was high variability in the measurements taken from the disc region. As Fig. 6.6 A shows, when the disc is uncompressed, both the edge of the disc and the

tidemark are uneven, giving variability in the compressible length. Additionally, when compressed (B), the change in length is not proportional due to the loss of the uneven disc edge. This results in a high standard deviation of the macro strain measures.

The non-MC was not measured separately from the disc, as the boundary line between the two was difficult to distinguish as mentioned above. The total applied strain was calculated by measuring the length of the unloaded compressible region (disc and non-MC) and the applied displacement. The strain of disc and MC was calculated from change in length, divided by the original length of each region respectively.

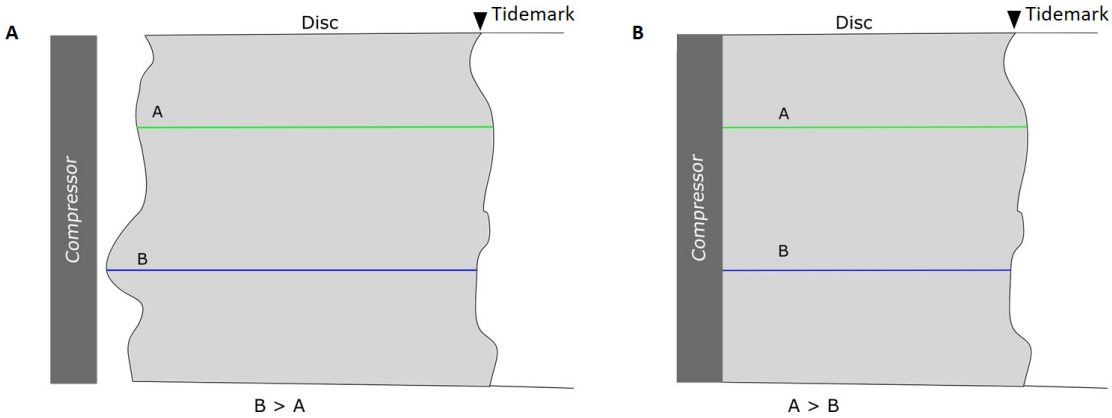

Figure 6.6: *Schematic representation of the loading protocol.*

Directionality

To parametise the change in organisation of the collagen fibres, a region of interest only containing the compressible region (disc and non-MC) was created and the directionality plugin in FIJI was applied as described in chapter 4.6.2.

6.3 Results

Utilising the rig shown in Fig. 6.3, samples (n = 8) were loaded following the aforementioned protocol. Due to the issues that arose, which will be discussed later in the chapter, only one sample provided a usable image stack and therefore the results discussed will be a case study of this sample. The issues will be discussed and the reasons they arose.

A 60 x 60 pixel grid was formed on the initial image of the stack shown in Fig. 6.7. This gave an uncertainty of 2.5 %, however, increasing the element size did not decrease the uncertainty of the tracking. The strain was calculated for each individual element, recorded and presented in a colour map as shown in Fig. 6.7. Fig 6.7 shows maps generated by YATTS for strain in the direction of loading (axial compression), and Fig 6.8 displays the average strain for each of the tissue types with the corresponding force detected by the load cell.

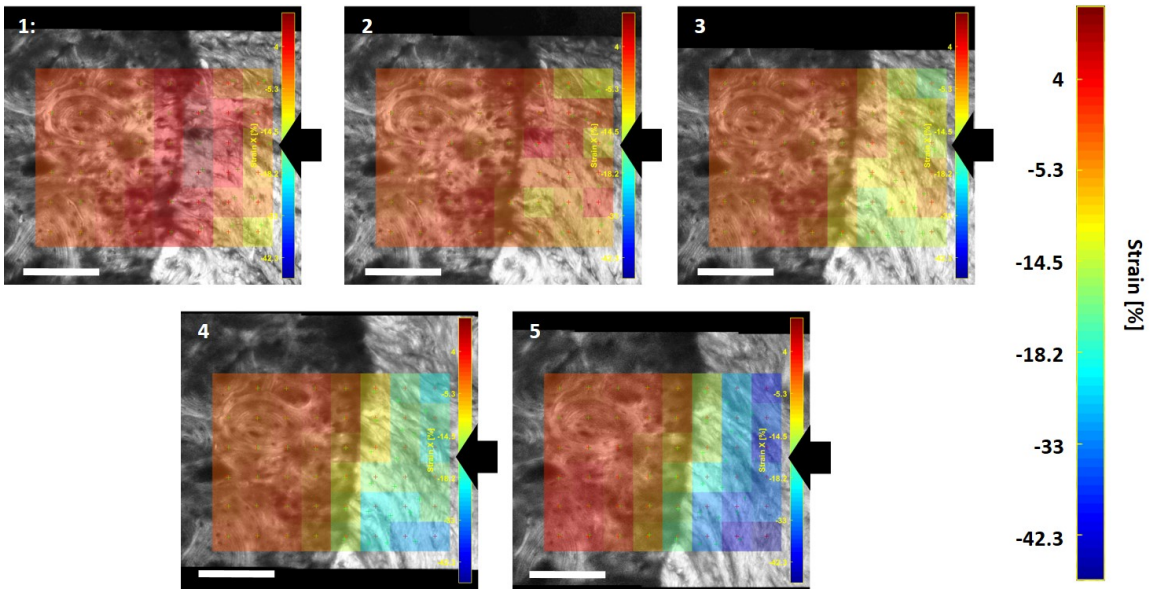

Figure 6.7: *Micromechanics of the bovine endplate under the annulus. 1-5) Colour maps of strain in the direction of loading (indicated by black arrows) as produced by YATTS. White scale bar on images = 200 µm. Colour scale on right hand side.*

The positive strain at the first applied load of 3.586 N is surprising, and does not fit the pattern of the rest of the results. It is clear that the disc is very compressible and takes the majority of the initial strain, however, the non-MC also begins to compress, though not to the same extent as the disc. The MC shows some compression in the loads above 8 N, and shows an average strain of -3.8 % at the last applied load of 18.8 N, however, it also displays high standard deviation. The BEP varies very little in strain (-1.69 to +0.80 %) throughout the experiment.

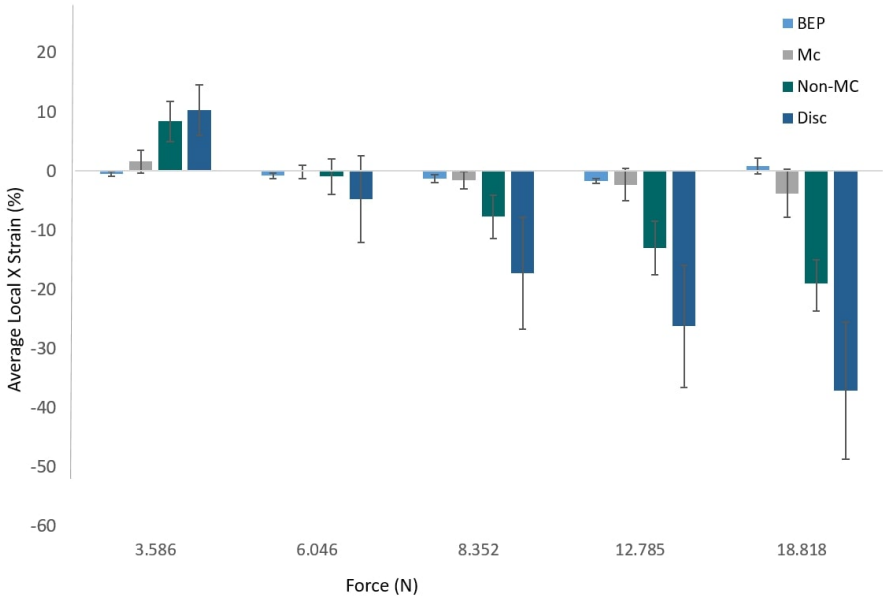

Figure 6.8: *Graph displays the average strain in the direction of loading (axial) for the BEP, MC, non-MC and the disc. Force was obtained from the load cell.*

Macroscopic measurements of the change in length of the disc and MC were utilised to calculate the regional strains. These macroscopic calculated strains are compared to the average microscopic strains calculated in YATTS in Fig. 6.9 A. However, as mentioned previously and shown in Fig. 6.9 B, the macroscopic measurements gave high standard deviations due to tissue heterogeneity. The strain applied has a relatively linear relationship with the load detected at the load cell (N). Unlike the applied strain, the macroscopic calculation of the disc and MC strain do not show a linear relationship with the load, neither do they reflect the patterns of strain seen in their corresponding average microscopic strain from YATTS. The microscopic strain in the disc is shown to be much higher when measured microscopically, with the opposite being true of the MC. The standard deviation is shown to be much higher in the macroscopic measurements of the MC compared to YATTS, however, these are large compared to the strain magnitudes.

A

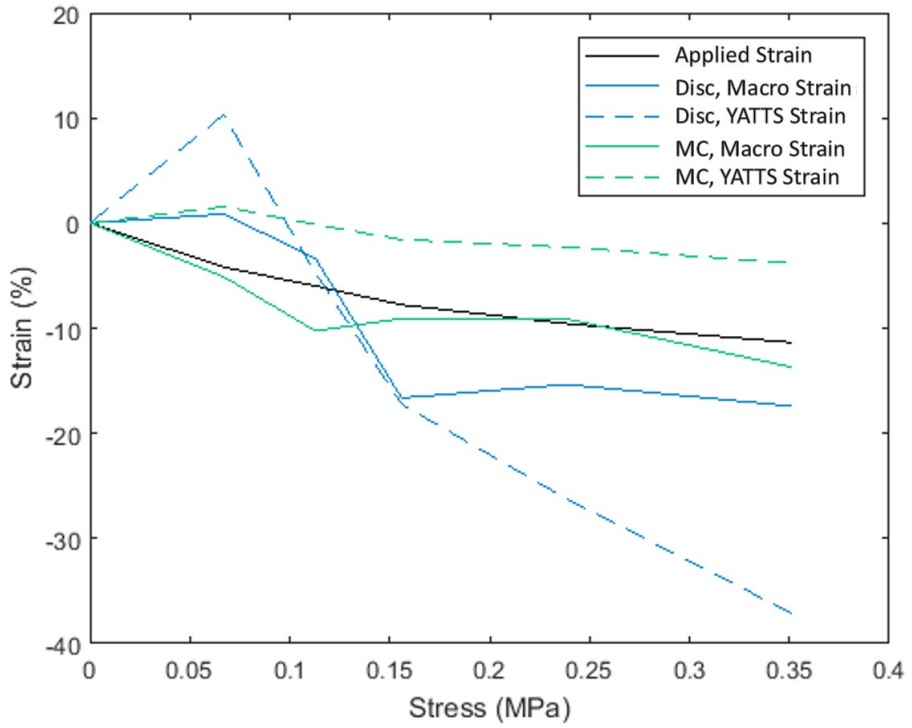

B

Force (N)	Standard Deviation (Strain %)				
	Total	Disc		MC	
	Applied	Macro	YATTS	Macro	YATTS
3.5	± 0.39	± 8.35	± 4.24	± 1.57	± 1.93
6.0	± 0.56	± 5.31	± 7.27	± 26.34	± 1.17
8.4	± 0.73	± 18.34	± 9.46	± 26.72	± 1.47
12.8	± 0.89	± 11.25	± 10.33	± 25.76	± 2.72
18.8	± 1.06	± 11.72	± 11.57	± 21.132	± 4.06

Figure 6.9: *A) Relationship between the force (N) and the macroscopic calculated strain (solid lines) and the YATTS calculated strain (dashed lines). The applied strain (black line) was calculated from the unloaded length (disc and cartilage) and the applied displacement. B) Table of the standard deviations of the regional averages and standard deviations.*

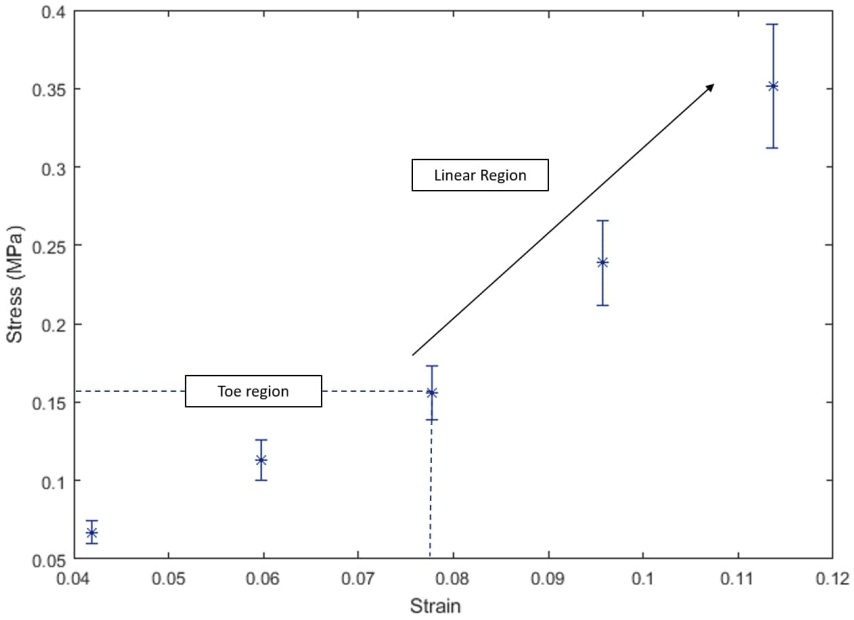

Figure 6.10: *Stress strain curve of the applied strain. The third data point indicates the transition from the toe to linear region. Note that the sample was not loaded to failure.*

Elastic modulus was estimated to average at 0.22 ± 0.06 MPa, however, Fig. 6.10 shows that with an increase in strain, the standard deviation in stress increases. The initial three points suggest a toe region, and show an increase in stress of 0.09 MPa. The next points suggest the start of a linear region, though as the sample was not loaded to failure, this cannot be said for certain. However, the change in stress from the mid to last point is 0.20 MPa, more than double the change in the first three points.

6.3.1 Fibre Angle

Images were analysed for the directionality of the disc fibres. Fig. 6.11 shows a trend that suggests with an increase in load, the fibres become more organised and decrease their angle relative to the endplate. The highest load (royal blue, 18.8 N), shows the highest and narrowest peak, suggesting that at this load the fibres are highly ordered and have a peak angle of 122 °, compared to unloaded (black line) which shows a broad peak with a peak angle of ~ 140 °. Acute fibre bending at the tidemark was observed in the images, and indicates regions of high stress concentrations at the site of insertion (see circled region in Fig. 6.12). As seen in Fig. 6.11 and noted from the YATTS data, load 1 (light grey, 3.6 N) is the outlier to the observed trend.

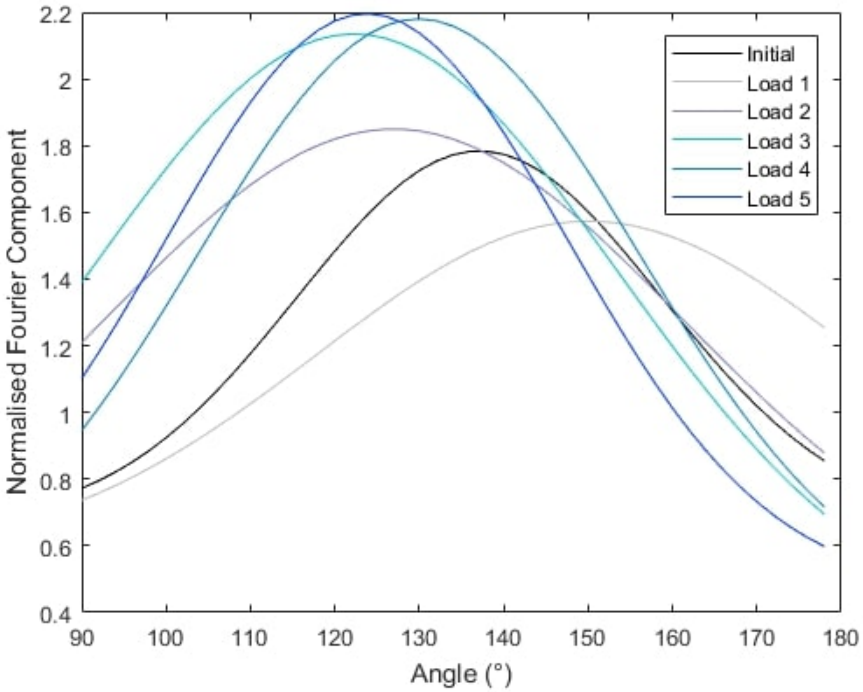

Figure 6.11: *Normalised Fourier components of the directionality of fibres in the disc region of the sample. Taken from no load (initial), to the fifth applied displacement.*

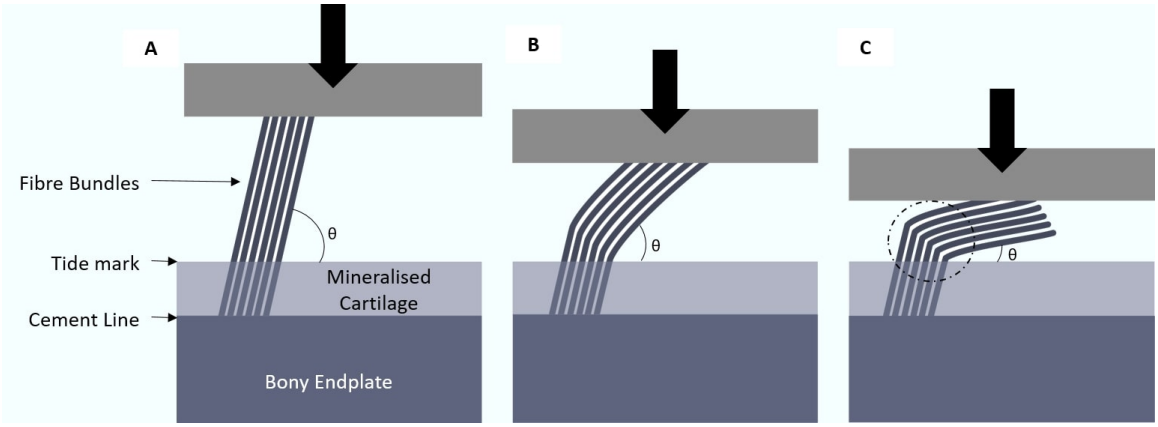

Figure 6.12: *Illustration of the decrease in angle (θ) of the fibre bundles relative to the endplate as they are progressively compressed. Note the bending of the fibres occurs above the tidemark. Circled area indicates region of high stress.*

6.3.2 Technical issues

The aim of this study was to image the effects axially loading the disc has on the endplate as demonstrated by Fig. 6.13 A and B. The expectation was that the samples would compress the non-MC and disc, whilst the MC, BEP and bone remained uncompressed. However, a number of issues arose during testing. These are represented schematically in Fig. 6.13 C-E.

A, demonstrates the unloaded samples and B, shows the applied displacement compressing the disc and cartilage as was shown in Fig. 6.7 when the sample loads correctly. C, shows the disc curling in on itself and bulging. This was caused by the disc fibres getting caught under the spacer, and then pushed underneath as the force was progressively applied. This issue still produced images, but did affect the measurements taken. D, is an exaggeration of the issue of C. The cover-slip and top plate prevented some raising of the sample, however, in one case the cover-slip was cracked by the pressure of the sample pressing up against it.

Lastly, as shown in Fig. 6.13 E, high loads generated movement orthogonally. This issue occurred for samples which did not have flat loading surfaces. This happened frequently as even when cutting the bone with a scalpel or razor blade, an uneven surface was often produced due to the bone fragmenting.

These issues not only affected the force detected by the load cell, but also image acquisition. This study protocol relies on the same region being imaged at each step, however, when the sample bulged or shifted, the focal point changed too. This led to some sample losing focus completely, whilst others shifted so a different region of the sample was imaged. This made the tracking of elements not possible.

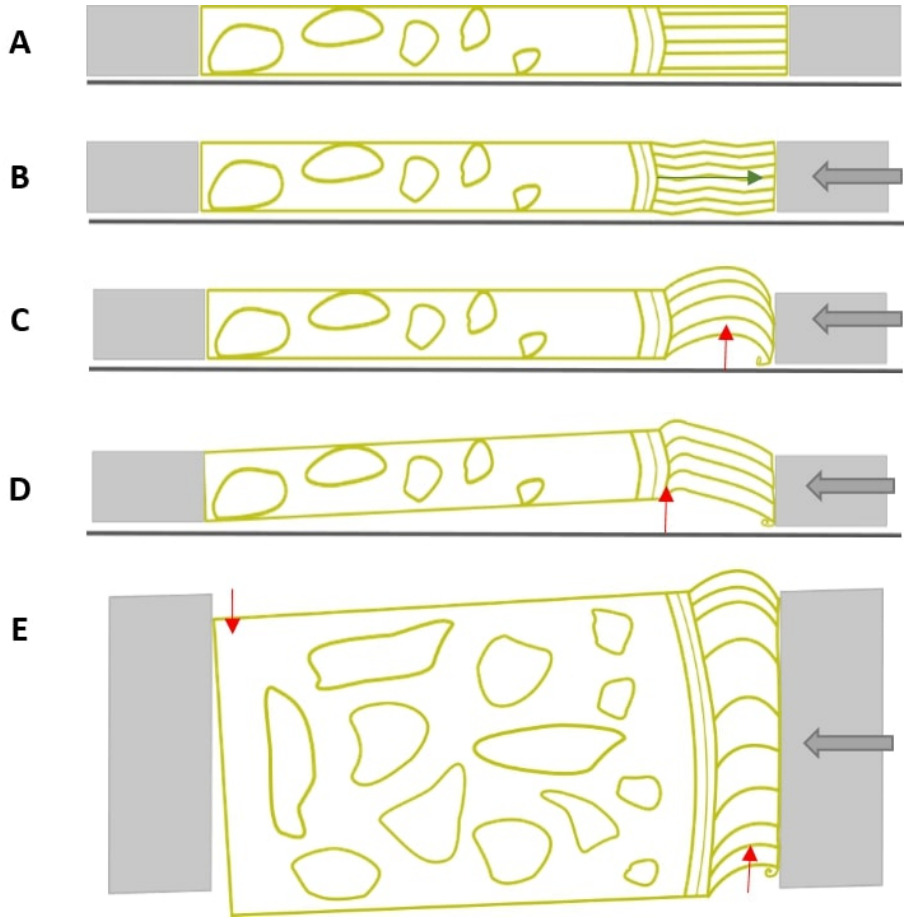

Figure 6.13: *Illustration of sample loading issues. A-C) Sagittal views of sample loaded in the compression rig. A) Sample uncompressed. B) Sample compressing correctly, green arrow indicates axial compression. C) Disc section of the sample curls in on itself, causing a bulge indicated by the red arrow. D) Sample hinges at the soft/hard tissue junction, indicated by the red arrow. E) Transverse view of sample in the rig, showing orthogonal shifting of the sample as it is compressed. Red arrows indicate the unwanted movement.*

6.4 Discussion

6.4.1 Compression of the Endplate

This chapter has explored imaging of the micromechanics of the cartilage endplate under compression with the multiphoton microscope. Difficulties were encountered in measuring strain at small stress and this may in part be due to the difficulty in determining the initial point of contact between the push plate and the sample.

Elastic modulus for the whole sample was shown to be 0.22 ± 0.6 MPa on average, which when compared to whole disc measurements from the literature is very low (between 1.4 and 2.2 MPa[286]), however, when compared with studies which also sectioned the disc, the modulus was much more comparable, though still lower (between 0.4 - 0.6 MPa[287,288]). It should be noted that this study focused on the annular region for the sake of uniformity, however, the mechanics of the region under the nucleus would be notably different due to the differences in structure between the nucleus and annulus.[85]

The stress-strain curve in Fig. 6.10 showed a 'toe region' which could be attributed to the straightening of the collagen fibres as they bend at the tidemark.[289] It is unlikely that these fibres would fully straighten at ~ 10 % applied strain, as a previous study has shown crimp still visible in the annulus at strains of 28 %.[283] Alternatively, the toe region could relate to the realignment of the fibre bundles at the inter-lamella interface[51] which would explain the sharp re-ordering of fibres within the the first three applied loads, which occur at relatively low strain (Fig. 6.11). Following the toe region, the the non-MC and MC show increases in strain in the direction of the load (Fig. 6.8). This suggests that the modulus in the linear region is dependent upon the combination of the disc and both cartilage components of the endplate. Previous research has shown instantaneous displacement of the endplate during axial compression, however, compared to this study, the loads have been higher (up to 1600 N) and applied more rapidly.[80,290] This work additionally disagrees with the suggestion that at low loads the role of the endplate is limited, and that the compliance of the functional spinal unit is primarily through the bulging of the IVD. This work has shown that even at low loads in comparison to physiological loads (peak force ~ 18 N verses ~ 200 N at rest[291]), the cartilagenous components of the endplate still showed strain in the direction of the load. It is important to note that in vivo, the annulus fibres would also be required to resist the bulging of the nucleus outwards during compression,[292] and therefore loading would be more complex than illustrated here. Additionally, care should be taken in directly

relating this or to many mechanical studies on the disc, as this study includes a combination of tissue, not just disc material.[287,288]

Previous discussions of the mechanical properties of the endplate have not differentiated between the MC from the 'mineralised endplate' (a grouping term for BEP and MC of the endplate) or the cartilage endplate (a grouping term for the non and MC). Additionally, in this study the calculation of the applied strain (Fig. 6.11) utilised the compressible region which was classed as the disc and non-MC, the MC along with the BEP were not included due to their high stiffness. This was based on previous work which has shown high Young modulus in similar tissues (subchondral bone: 5.7 ± 1.9 GPa and calcified cartilage: 0.32 ± 0.25 GPa), as no Young's modulus of the endplate regions are currently available in the literature. This study has shown a small amount of local strain in the MC region. The MC strain reached a maximum of ~ - 8 %, however the average was much lower and the standard deviation is larger than the strain magnitude (- 3.8 ± 4.1 %). This highlights the issues of sample hetrogeneity when assesing the micromechanics of the endpalte. Even within the same sample, variation is high. Due to this, the role of the MC in the endplate requires further investigation, and the method described in this study offers exciting potential. Gupta et al., was able to plot indentation modulus as a function of local calcium weight percentage of articular cartilage at transitions between the cartilage and zone of calcified cartilage, and zone of calcified cartilage and bone.[293] They showed a clear relationship between the mineral content, and indentation modulus, which also clearly distinguished the MC and bone.[293] Taking this idea, combining the spectroscopy techniques from chapter 4 and the loading protocol described in the above study could shed light on the variability and role of the MC within the endplate mechanics.

One of the striking observations was the realignment of the collagen fibres of the disc illustrated in Fig. 6.11. The bending at the site of insertion indicates a potential for high stress concentrations at the tidemark, though the purely compressive load applied was not representative of the complexity of physiological loading. Rodrigues suggested a similar region of high stress due to laterally directed forces as a result of disc bulging, though it was suggested that the stress was attenuated by the supporting matrix as illustrated in Fig. 6.14.[34] In the current study, the disc fibre bundles were not able to be resolved within the MC matrix, therefore the suggestion of attenuated stress could not be measured. As shown in chapter 4, anchored fibre bundles have been resolved with the multiphoton at higher magnifications, thus, future work could focus on the disc and non-MC boundary to further understand the strain relationship.

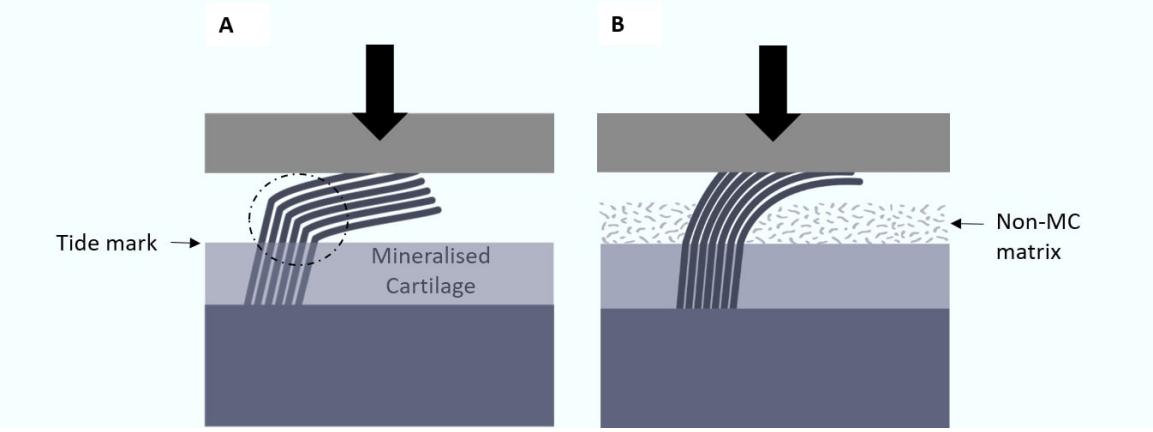

Figure 6.14: *Illustration of A) the disc fibre bundles, circled area indicates region of high stress and B) Attenuation of the high stress by the supporting matrix of the non-MC, suggested by Rodrigues 2015.*[34]

6.4.2 Critique of Experimental Methods

An advantage of real-time imaging the compression of the endplate, as previously discussed, is the ability to visualise the disc, non-MC, MC and BEP simultaneously while load is applied. Similar real-time imaging of tensile loading has been carried out in the annulus to detect inter-lamella bundle strain[51,283] however, this appears to be the first study that has applied such a techniques across cartilage and bone. The endplate is complicated to analyse as it combines soft and hard tissues.

The benefit of utilising a tracking software such as YATTS is the reduction of human error. As Fig. 6.9 B showed at 18.8 N, the MC had a standard deviation that was 154% of the average strain calculated. Such high deviations are due to a combination of tissue heterogeneity, and the change in shape of the disc as it is compressed (as illustrated in Fig. 6.6). The standard deviation of the YATTS strain was much lower compared to the macroscopic measurements. It was still high in places though this was most likely due to the initial uncertainty of 2.5 %. It has been suggested that an uncertainty of below 0.5 % is optimum for correct tracking,[283] however, the quality of the image did not allow for such precision. This raises a disadvantage of the YATTS software, the images have to be of consistently high quality in order to correctly track as it relies on the native tissue structure rather than applied markers.[277,283] This can be difficult with combination tissues, as it can be difficult to focus across a boundary, especially when aiming to maintain the focal point for mapping.

As shown with the technical issues illustrated in Fig 6.13, the combination of soft and hard tissues poses issues to the loading technique, as well as the strain measurements.

Essentially in B-D the sample hinges at the tidemark. Adaptations to the methods need to address movement out of the imaging plane.

For future work the suggested adaptations are as follows.

- Shorter Samples

  If the sample is thought of as two beans connected at a hinge (the tidemark), in order to maintain the compressive force applied during the loading protocol, but reduce the possibility of bending the sample at the tidemark, the distance between the applied force the and hinge should be reduced (Fig. 6.15. This should allow a greater force to be applied before the sample bends.

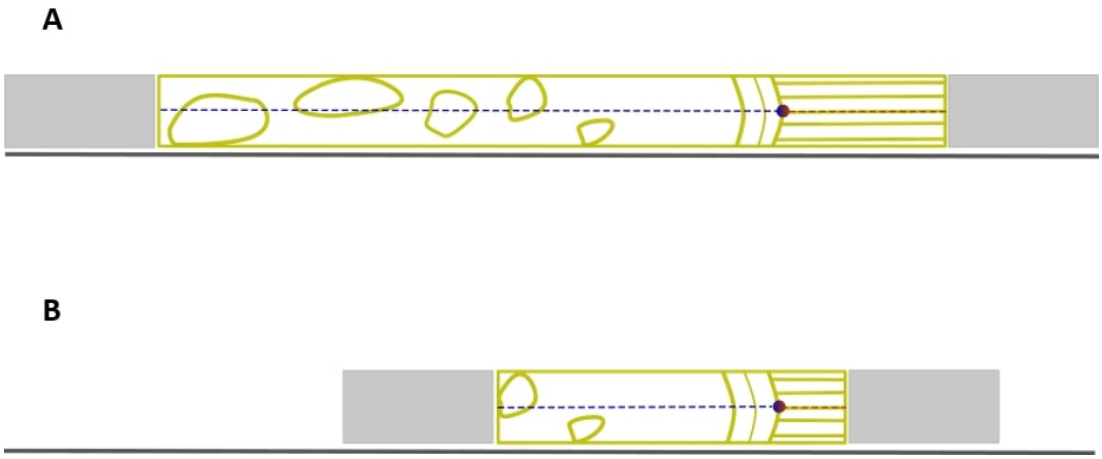

Figure 6.15: *Illustration of A) Original sample length used in this study. Circle indicates the 'hinge' at the tidemark. B) Reduced sample length. Not both sides of the sample have been reduced, as either side could produce a moment.*

- Thicker and Wider Samples

  If the sample is thought of as a fixed beam, sample thickening and widening could be useful.[294] In order to reduce central deflection (ω_0) without altering the load, the second moment of area (I) needs to be increased. I is dependent upon the thickness cubed (a^3) and width (b), therefore increasing sample thickness and width could help reduce bending. Due to the design of the rig, during this study the sample could not be thicker than 2mm, however, if the thickness of the sample pusher was increased, and spacers created to lift the top plate (so not to compress the sample with the cover slip), it would be possible to increase the sample thickness, which could reduce bending at the tidemark. Additionally, the sample width can be increased up to the width of the push-plate connected to the micrometer (4 cm). The width of the sample was kept small in this study to ensure sole focus

on the annulus. Using full width cross-sections would allow for greater sample width, however, the annular and nuclear regions will have different mechanics, and combination samples could complicate the results.

- Thicker Cover-slip

  Utilising a thicker cover slip would reduce the potential of the glass to be broken by the pressure of the sample against the glass as happened in one of the experiments in this study. However, the cover slip should not be applying a compression to the sample.

6.5 Conclusion

This chapter explored imaging of the micro-mechanics of the cartilage endplate under compression with the multiphoton microscope. The main findings are summarised in Fig. 6.16.

The method utilised in this study offers novel insight into the micromechanics of the distinct regions of the endplate under axial loading. The study showed a very low elastic modulus though this was most likely due to the sectioned disc, and low applied loads. It is clear that the disc acts initially, with high strain likely being due to the realignment of the fibre bundles. Conversely to what previous research has suggested, the cartilage components of the endplate were shown to strain even at low applied force. It is suggested that the cartilage endplate matrix plays a role in the attenuation of stress at the anchoring of the annular fibres. This method could now be applied to understand regional differences in micromechanics under the nucleus and annulus, as well as how this changes with degeneration.

The use of YATTS software in order to track the movement of regional elements appeared advantageous over macroscopic measurements of strain due to the complexity of the disc under compression. It offers a viable method for regional investigation into the micromechanics of the vertebral endplate, however, increased image quality is required. Some adaptations to the methods have been discussed, with these, this study offers a method of gaining invaluable regional information on the role of the endplate in axial loading of the disc.

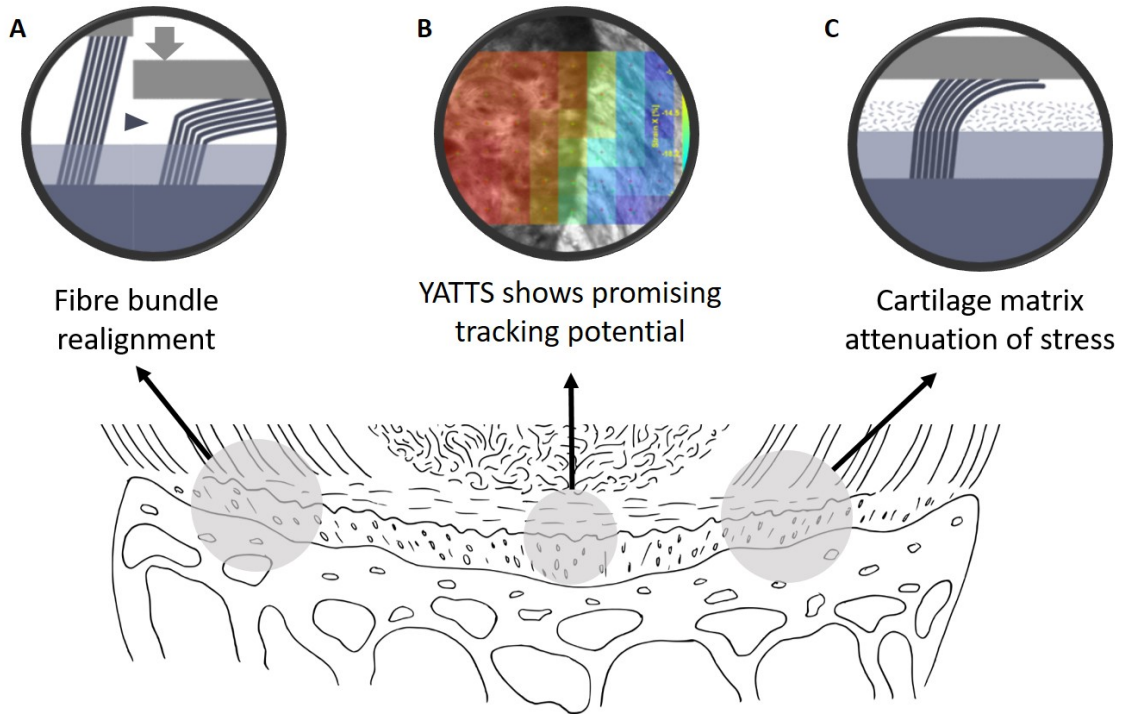

Figure 6.16: *Schematic representing the main findings from chapter six.*

7 Summary & Conclusions

The preceding three chapters described experimental studies which aimed to investigate the vertebral endplate in terms of its structure and function, in relation to the intervertebral disc. In each of the chapters, the methods utilised and results obtained were presented, along with a discussion of those results.

Although each chapter focused on a specific aspect of the structure and function of the endplate, these aspects will influence one another. This will be explored now.

The findings on the changes in the BEP with aging (reduction of osteons and increase in trabeculae) will effect the nutritional routs of the endplate due to changes in vasculature. Previous work has talked about the reduction of blood vessels with aging,[258] and trabecularisation of the BEP is a viable explanation for this. The decrease in the number of osteons and change in structure of the BEP may also influence the distance between vessel ends and anchored disc fibres. Due to the low diffusivity of small molecules through the endplate, any increase in the distance between the vessel and disc has a negative effect of the nutrient density of the nucleus.[110]

Similarly the structure will have an effect on the mechanics, both in terms of the anchoring of the disc- whether remodelling of the bone will effect the integration of the disc with osteon fibrils- as well as with the redistribution of forces applied to the disc. Chapter six of this thesis proposed a method for investigating the mechanics and interactions of the three regions of the endplate, it showed that even at low loads the CEP played a role. The role of the CEP in the disc mechanics will be influenced by the collagen fibre orientation (as discussed in 4.8.4 but also the elastin content 4.8.4 and alignment as the coexistence of these fibre networks influence the mechanical properties of a tissue.[231]

Additionally, the mechanics of the endplate is thought to have an effect on nutrient transport, especially that of large molecules. As shown in chapter 5, large molecules such as albumin have a very low diffusion rate compared with small molecules. It is suggested that the daily loading and unloading of the disc and endplate could contribute to the diffusion of molecules, aiding their movement.[272]

7.1 Future Work

At various points throughout the thesis, necessity for future work has been indicated.

In this thesis the majority of the work has been carried out within animal models, and therefore continuing this work in human samples, and relating to clinical conditions is paramount. Clinically, the endplates are poorly understood in regards to pathologies. Modic changes are often described in clinical literature as endplate changes,[75,132,134] however, these can effect as much as 75 % of the vertebral body, suggesting these are not endplate specific issues. Additionally as Fig. 7.1 illustrates, even under optimum conditions (high resolution, small scan area and long scan duration) the detail of the endplate is hard to distinguish in MRI scans.

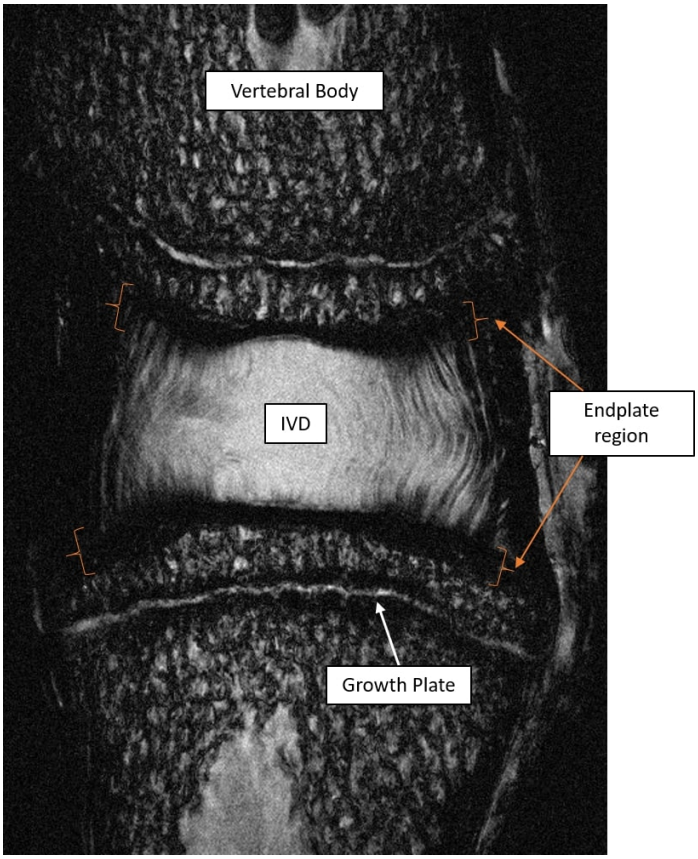

Figure 7.1: *MRI of bovine tail using a 23 mm Microscopy coil in 1.5-T unit (Philips). Thickness 0.3 mm/spacing 0.05 mm. Scan duration 6 h 45 mins*

This thesis had originally aimed to investigate the relationships between the results from the animal studies and clinical measures in patients with symptomatic degenerative disc disease. However, due to issues with ethics and material transfer agreements the first samples were only collected in the last month of the project. The aim had been to

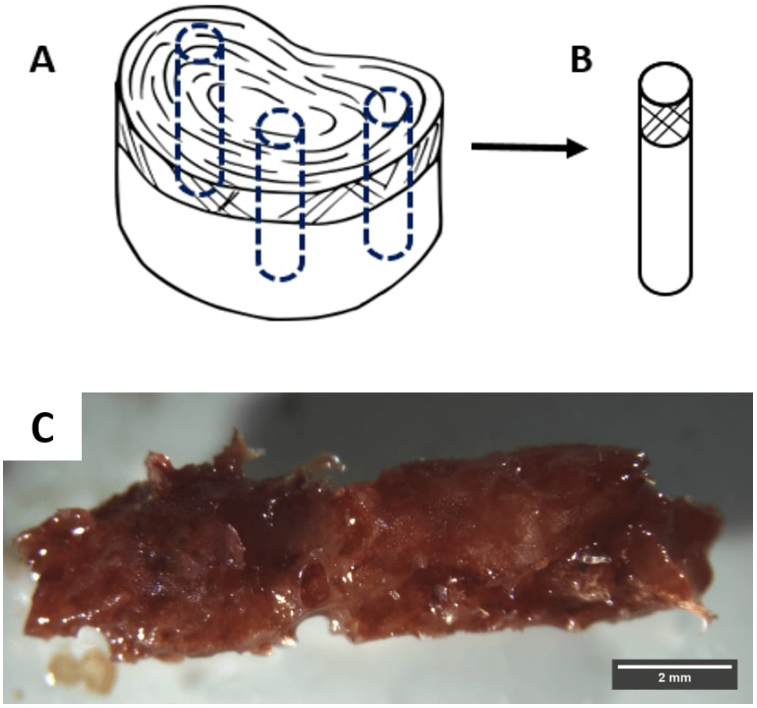

Figure 7.2: *Human Samples A) Samples taken from sites of inter-body cage screws. B) samples should result in a core containing disc, endplate and bone. C) Received samples only contained blood clotted bone.*

utilise samples removed with a trephine from the sites where inter-body cages would be attached to the bone (Fig. 7.2 A). The resulting sample would contain disc, endplate and bone (Fig. 7.2 B), allowing for cross-sectional investigation as was utilised repeatedly thought this thesis. However, the first samples collected only contained severely blood-clotted bone.

Though useless for the intended analysis, these samples highlight the disparity between clinical practice and experimental literature. Surgeons routinely remove the endplate cartilage along with the disc during fusion surgeries to instigate blood supply,[295] however, literature reports that stability of implants is improved through the retention of endplates.[200,295] This highlights the necessity for further work on the mechanics and blood supply of the endplate. Additionally, much work is being produced in relation to regenerative therapies and biological implants.[17–19] Answering the questions raised in this study in regards to the vasculature and regional mechanics would increase long term viability of such implants.

7.2 Conclusion

The vertebral endplate has been previously underappreciated in its role within the functional spinal unit. In relation to the aims of thesis research, this thesis has established a structural understanding of the endplate, that it is formed of three distinct tissues which are intimately linked with the intervertebral disc through collagen fibre integration. It has shed light on the complexities of the endplate vasculature, as well as displaying the vital role the endplate plays in the supply of water and solutes, and removal of waste. Lastly this thesis has presented a viable method for investigating mechanical relationship between the bone, endplate and disc, as well as showing that the endplate attenuates stress of the disc as it bends at the tidemark when axially loaded.

Bibliography

[1] R. A. Deyo, D. Cherkin, D. Conrad, E. Volinn, "Cost, Controversy, Crisis: Low Back Pain and the Health of the Public", in *Annual Review of Public Health* **1991**, *12*, 141–156, DOI 10.1146/annurev.pu.12.050191.001041, (cit. on p. 1).

[2] C. E. Dionne, K. M. Dunn, P. R. Croft, "Does back pain prevalence really decrease with increasing age? A systematic review", in *Age and Ageing* **2006**, *35*, 229–234, DOI 10.1093/ageing/afj055, (cit. on p. 1).

[3] J. Rapoport, P. Jacobs, N. Bell, S. Klarenbach, "Refining the measurment of economic burden of chronic diseases in Canada", in *Chronic Disease Canada* **2004**, *25*, 13–21, (cit. on p. 1).

[4] P. R. Croft, A. C. Papageorgiou, E. Thomas, G. J. Macfarlane, A. J. Silman, "Short-term physical risk factors for new episodes of low back pain. Prospective evidence from the South Manchester Back Pain Study", in *Spine* **1999**, *24*, 1556, DOI 10.1097/00007632-199908010-00009, (cit. on p. 1).

[5] D. Hoy, P. Brooks, F. Blyth, R. Buchbinder, "The Epidemiology of low back pain", in *Best Practice and Research: Clinical Rheumatology* **2010**, *24*, 769–781, DOI 10.1016/j.berh.2010.10.002, (cit. on p. 1).

[6] B. F. Walker, R. Muller, W. D. Grant, "Low back pain in australian adults. Prevalence and associated disability", in *Journal of Manipulative and Physiological Therapeutics* **2004**, *27*, 238–244, DOI 10.1016/j.jmpt.2004.02.002, (cit. on p. 1).

[7] M. L. Walsh, E. W. Banister, "The influence of inspired oxygen on the oxygen uptake response to ramp exercise", in *European Journal of Applied Physiology and Occupational Physiology* **1995**, *72*, 71–75, DOI 10.1007/BF00964117, (cit. on p. 1).

[8] S. Taimela, U. Kujala, J. Salminen, T. Viljanen, "The prevalence of low back pain among children and adolescents. A nationwide, cohort-based questionnaire survey in Finland", in *Spine* **1997**, *22*, 1132–1136, DOI 10.1097/00007632-199705150-00013, (cit. on p. 1).

[9] L. Hestbaek, C. Leboeuf-Yde, M. Engberg, T. Lauritzen, N. H. Bruun, C. Manniche, "The course of low back pain in a general population. Results from a 5-year prospective study", in *Journal of Manipulative and Physiological Therapeutics* **2003**, *26*, 213–219, DOI 10.1016/S0161-4754(03)00006-X, (cit. on p. 1).

[10] B. R. Whatley, X. Wen, "Intervertebral disc (IVD): Structure, degeneration, repair and regeneration", in *Materials Science and Engineering C* **2012**, *32*, 61–77, DOI 10.1016/j.msec.2011.10.011, (cit. on p. 1).

[11] M. A. Adams, P. J. Roughley, "What is intervertebral disc degeneration, and what causes it?", in **2006**, *31*, 2151–2161, DOI 10.1097/01.brs.0000231761.73859.2c, (cit. on pp. 1, 10).

[12] A. Endean, K. T. Palmer, D. Coggon, "Potential of Magnetic Resonance Imaging Findings to Refine Case Definition for Mechanical Low Back Pain in Epidemiological Studies", in *Spine* **2011**, *36*, 160–169, DOI 10.1097/BRS.0b013e3181cd9adb, (cit. on p. 1).

[13] National Spinal Taskforce, "Commissioning Spinal Services – Getting the Service Back on Track", in **2013**, 1–193, (cit. on pp. 1, 2).

[14] M. C. Battié, Á. Lazáry, J. Fairbank, S. Eisenstein, C. Heywood, M. Brayda-Bruno, P. P. Varga, I. McCall, "Disc degeneration-related clinical phenotypes", in *European Spine Journal* **2014**, *23*, DOI 10.1007/s00586-013-2903-5, (cit. on p. 1).

[15] T. R. Oxland, J. P. Grant, M. F. Dvorak, C. G. Fisher, "Effects of endplate removal on the structural properties of the lower lumbar vertebral bodies.", in *Spine* **2003**, *28*, 771–777, DOI 10.1097/01.BRS.0000060259.94427.11, (cit. on pp. 2, 95).

[16] Y. Hou, W. Yuan, J. Kang, Y. Liu, "Influences of endplate removal and bone mineral density on the biomechanical properties of lumbar spine", in *PLoS ONE* **2013**, *8*, DOI 10.1371/journal.pone.0076843, (cit. on p. 2).

[17] J. T. Martin, A. H. Milby, J. A. Chiaro, D. H. Kim, N. M. Hebela, L. J. Smith, D. M. Elliott, R. L. Mauck, "Translation of an engineered nanofibrous disc-like angle-ply structure for intervertebral disc replacement in a small animal model", in *Acta Biomaterialia* **2014**, *10*, 2473–2481, DOI 10.1016/j.actbio.2014.02.024, (cit. on pp. 2, 172).

[18] S. Reitmaier, A. Shirazi-Adl, M. Bashkuev, H.-J. J. Wilke, A. Gloria, H. Schmidt, "In vitro and in silico investigations of disc nucleus replacement.", in *Journal of the Royal Society Interface / the Royal Society* **2012**, *9*, 1869–1879, DOI 10.1098/rsif.2012.0016, (cit. on pp. 2, 172).

[19] M. C. Dahl, A. M. Ellingson, H. P. Mehta, J. H. Huelman, D. J. Nuckley, "The biomechanics of a multilevel lumbar spine hybrid using nucleus replacement in conjunction with fusion", in *Spine Journal* **2013**, *13*, 175–183, DOI 10.1016/j.spinee.2012.11.045, (cit. on pp. 2, 172).

[20] H. Gray in *Gray's Anatomy*, (Eds.: W. R. PL, Williams), Edinburgh: Longman, **1973**, pp. 200–385 (cit. on pp. 5, 7, 41).

[21] M. A. Adams, P. Dolan, "Spine biomechanics", in *Journal of Biomechanics* **2005**, *38*, 1972–1983, DOI 10.1016/j.jbiomech.2005.03.028, (cit. on p. 5).

[22] G. Love, M. Walsh, "Intraspinal Protrusion of Intervertebral Disks", in *Archves of Surgery* **1940**, 454–484, DOI 10.1001/archsurg.1940.04080020083007, (cit. on p. 5).

[23] C. Weiler, M. Schietzsch, T. Kirchner, A. G. Nerlich, N. Boos, K. Wuertz, "Age-related changes in human cervical, thoracal and lumbar intervertebral disc exhibit a strong intra-individual correlation", in *European Spine Journal* **2012**, *21*, 810–818, DOI 10.1007/s00586-011-1922-3, (cit. on p. 5).

[24] G. J. Tortora, B. Derrickson, *Principles of Anatomy and Physiology, Vol. 9406*, **2014**, p. 1127 (cit. on p. 5).

[25] N. Bogduk, Clinical Anatomy of the Lumbar Spine & Sacrum (4th Ed.) **2005** (cit. on pp. 5, 16).

[26] H. Haberl, P. A. Cripton, T. E. Orr, T. Beutler, H. Frei, W. R. Lanksch, L. P. Nolte, "Kinematic response of lumbar functional spinal units to axial torsion with and without superimposed compression and flexion/extension", in *European Spine Journal* **2004**, *13*, 560–566, DOI 10.1007/s00586-004-0720-6, (cit. on p. 5).

[27] A. J. Fields, G. L. Lee, T. M. Keaveny, "Mechanisms of initial endplate failure in the human vertebral body", in *Journal of Biomechanics* **2010**, *43*, 3126–3131, DOI 10.1016/j.jbiomech.2010.08.002, (cit. on pp. 7, 12, 149).

[28] R. J. Moore, "The vertebral end-plate: what do we know?", in *European Spine Journal* **2000**, *9*, 92–96, DOI 10.1007/s005860050217, (cit. on pp. 7, 15, 20).

[29] M. Alini, S. M. Eisenstein, K. Ito, C. Little, A. A. Kettler, K. Masuda, J. Melrose, J. Ralphs, I. Stokes, H. J. Wilke, "Are animal models useful for studying human disc disorders/degeneration?", in *European Spine Journal* **2008**, *17*, 2–19, DOI 10.1007/s00586-007-0414-y, (cit. on pp. 7, 27–29, 35).

[30] M. B. Coventry, R. K. Ghormley, J. W. Kernohan, "The intervertebral disc: its anatomy and pathology. Part I. anatomy, development and physiology", in *The Journal of Bone & Joint Surgery* **1945**, *27*, 105–112, (cit. on pp. 7, 8, 12, 35, 41, 89).

[31] R. Hanson, "On the development of spinal vertebrae, as seen on skiagrams, from late foetal life to the age of fourteen", in *Acta Radiologica* **1926**, *5*, 112–126, DOI 10.3109/00016922609133311, (cit. on pp. 7, 35).

[32] E. M. Bick, J. W. Copel, "Longitudinal growth of the human vertebra; a contribution to human osteogeny.", in *The Journal of bone and joint surgery. American volume* **1950**, *32 A*, 803–14, (cit. on pp. 7, 35).

[33] H. Madry, C. N. van Dijk, M. Mueller-Gerbl, "The basic science of the subchondral bone", in *Knee Surgery Sports Traumatology Arthroscopy* **2010**, *18*, 419–433, DOI 10.1007/s00167-010-1054-z, (cit. on p. 7).

[34] S. A. Rodrigues, PhD thesis, The University of Auckland, **2015**, pp. 9–55 (cit. on pp. 7, 12, 64, 165, 166).

[35] H. Hashizume, "Three-dimensional architecture and development of lumber intervertebral discs.", in *Acta medica Okayama* **1980**, *34*, 301–14, (cit. on pp. 8, 41).

[36] L. Kazarian, "Injuries to the Human Spinal Column: Biomechanics and Injury Classification", in *Exercise and Sport Science Reviews* **1981**, *9*, 297–352, (cit. on pp. 8, 13).

[37] D. Eyre, H. Muir, "Biochemistry of the Intervertebral Disc", in *International Review of Connective Tissue Research* **1979**, *8*, 227–291, (cit. on pp. 8, 9).

[38] J. P. G. Urban, S. Roberts, J. R. Ralphs, "The Nucleus of the Intervertebral Disc from Development to Degeneration", in *American Zoologist* **2000**, *40*, 53–61, DOI 10.1093/icb/40.1.53, (cit. on pp. 8, 30).

[39] H. A. L. Guerin, D. M. Elliott, "Degeneration affects the fiber reorientation of human annulus fibrosus under tensile load", in *Journal of Biomechanics* **2006**, *39*, 1410–1418, DOI 10.1016/j.jbiomech.2005.04.007, (cit. on p. 8).

[40] F. Happey, A. G. Johnson, A. Naylor, R. L. Turner, "Preliminary observations concerning the fine structure of the intervertebral disc", in *Journal of Bone and Joint Surgery - Series B* **1964**, *46B*, 563–567, (cit. on p. 8).

[41] H. Inoue, T. Takeda, "Three-dimensional observation of collagen framework of lumbar intervertebral discs.", in *Acta orthopaedica Scandinavica* **1975**, *46*, 949–956, DOI 10.3109/17453677508989283, (cit. on pp. 8, 9).

[42] M. D. Humzah, R. W. Soames, "Human intervertebral disc: Structure and function", in *The Anatomical Record* **1988**, *220*, 337–356, DOI 10.1002/ar.1092200402, (cit. on pp. 8, 9).

[43] H. Inoue, Three-dimensional architecture of lumbar intervertebral discs. **1978** (cit. on p. 8).

[44] K. R. Wade, P. A. Robertson, N. D. Broom, "A fresh look at the nucleus-endplate region: New evidence for significant structural integration", in *European Spine Journal* **2011**, *20*, 1225–1232, DOI 10.1007/s00586-011-1704-y, (cit. on p. 8).

[45] C. C. Yu, D. J. Hao, D. G. Huang, L. X. Qian, H. Feng, H. K. Li, S. C. Zhao, "Biomechanical analysis of a novel prosthesis based on the physiological curvature of endplate for cervical disc replacement", in *PLoS ONE* **2016**, *11*, 1–12, DOI 10.1371/journal.pone.0158234, (cit. on p. 8).

[46] J. J. Cassidy, A. Hiltner, E. Baer, "Hierarchical structure of the intervertebral disc.", in *Connective tissue research* **1989**, *23*, 75–88, DOI 10.3109/03008208909103905, (cit. on p. 9).

[47] S. Roberts, "Disc morphology in health and disease", in *Biochemical Society transactions* **2002**, *30*, 864–869, DOI 10.1042/[doi], (cit. on p. 9).

[48] F. Marchand, A. M. Ahmed, "Investigation of the laminate structure of lumbar disc anulus fibrosus.", in *Spine* **1990**, *15*, 402–410, DOI 10.1097/00007632-199005000-00011, (cit. on p. 9).

[49] M. Tanaka, S. Nakahara, "A Pathologic study of discs in the elderly. Separation between the cartilaginous endplate and the vertebral body", in *Spine* **1993**, *18*, 1456–1462, (cit. on p. 9).

[50] J. Yu, "Elastic tissues of the intervertebral disc", in *Biochemical Society Transactions* **2002**, *30*, 848–852, (cit. on pp. 9, 10, 91).

[51] C. Vergari, D. Chan, A. Clarke, J. C. Mansfield, J. R. Meakin, P. C. Winlove, "Bovine and degenerated human annulus fibrosus: a microstructural and micromechanical comparison", in *Biomechanics and Modeling in Mechanobiology* **2017**, *16*, 1–10, DOI 10.1007/s10237-017-0900-z, (cit. on pp. 9, 23, 39, 150, 151, 164, 166).

[52] G. Lyons, S. M. Eisenstein, M. B. E. Sweet, "Biochemical changes in intervertebral disc degeneration", in *BBA - General Subjects* **1981**, *673*, 443–453, DOI 10.1016/0304-4165(81)90476-1, (cit. on p. 9).

[53] W. E. Gower, V. Pedrini, "Age-related variations in proteinpolysaccharides from human nucleus pulposus, annulus fibrosus, and costal cartilage.", in *The Journal of bone and joint surgery. American volume* **1969**, *51*, 1154–1162, DOI 10.2106/00004623-196951060-00011, (cit. on p. 9).

[54] D. R. Eyre, H. Muir, "Quantitative analysis of types I and II collagens in human intervertebral discs at various ages", in *BBA - Protein Structure* **1977**, *492*, 29–42, DOI 10.1016/0005-2795(77)90211-2, (cit. on p. 9).

[55] R. J. Moore, The Origin and Fate of Herniated Lumbar Intervertebral Disc Tissue. **1996** (cit. on p. 9).

[56] B. Vernon-Roberts, R. J. Moore, R. D. Fraser, "The natural history of age-related disc degeneration: the pathology and sequelae of tears.", in *Spine* **2007**, *32*, 2797–804, DOI 10.1097/BRS.0b013e31815b64d2, (cit. on pp. 9, 93).

[57] M. a. Adams, T. P. Green, P. Dolan, "The strength in anterior bending of lumbar intervertebral discs.", in *Spine* **1994**, *19*, 2197–2203, DOI http://dx.doi.org/10.1097/00007632-199410000-00014, (cit. on pp. 9, 10).

[58] S. P. Veres, P. a. Robertson, N. D. Broom, "ISSLS Prize Winner: Microstructure and Mechanical Disruption of the Lumbar Disc Annulus", in *Spine* **2008**, *33*, 2711–2720, DOI 10.1097/BRS.0b013e31817bb906, (cit. on p. 9).

[59] C. A. Pezowicz, H. Schechtman, P. A. Robertson, N. D. Broom, “Mechanisms of Anular Failure Resulting From Excessive Intradiscal Pressure”, in *Spine* **2006**, *31*, 2891–2903, DOI 10.1097/01.brs.0000248412.82700.8b, (cit. on p. 10).

[60] S. Brown, S. Rodrigues, C. Sharp, K. Wade, N. Broom, I. W. McCall, S. Roberts, “Staying connected: structural integration at the intervertebral disc–vertebra interface of human lumbar spines”, in *European Spine Journal* **2017**, *26*, 248–258, DOI 10.1007/s00586-016-4560-y, (cit. on pp. 10, 41).

[61] C. Balkovec, M. A. Adams, P. Dolan, S. M. McGill, “Annulus Fibrosus Can Strip Hyaline Cartilage End Plate from Subchondral Bone: A Study of the Intervertebral Disk in Tension”, in *Global Spine Journal* **2015**, *5*, 360–365, DOI 10.1055/s-0035-1546956, (cit. on pp. 10, 12, 41, 94).

[62] R. J. Moore, “The vertebral endplate: Disc degeneration, disc regeneration”, in *European Spine Journal* **2006**, *15*, 333–337, DOI 10.1007/s00586-006-0170-4, (cit. on pp. 10, 41, 95).

[63] P. Lama, U. Zehra, C. Balkovec, H. A. Claireaux, L. Flower, I. J. Harding, P. Dolan, M. A. Adams, “Significance of cartilage endplate within herniated disc tissue”, in *European spine journal : official publication of the European Spine Society the European Spinal Deformity Society and the European Section of the Cervical Spine Research Society* **2014**, *23*, 1869–1877, DOI 10.1007/s00586-014-3399-3, (cit. on pp. 10, 13, 41, 93).

[64] S. Roberts, J. P. Urban, H. Evans, S. M. Eisenstein, Transport properties of the human cartilage endplate in relation to its composition and calcification. **1996** (cit. on pp. 10, 16, 41, 100, 105, 144).

[65] C. F. P. S. Herrero, S. B. Garcia, L. V. Garcia, H. L. Aparecido Defino, “Endplates changes related to age and vertebral segment”, in *BioMed Research International* **2014**, *2014*, DOI 10.1155/2014/545017, (cit. on pp. 10, 41).

[66] R. C. Paietta, E. L. Burger, V. L. Ferguson, “Mineralization and collagen orientation throughout aging at the vertebral endplate in the human lumbar spine”, in *Journal of Structural Biology* **2013**, *184*, 310–320, DOI 10.1016/j.jsb.2013.08.011, (cit. on pp. 10, 13, 26, 41).

[67] R. C. Hilton, J. Ball, “Vertebral rim lesions in the dorsolumbar spine”, in *Annals of the Rheumatic Diseases* **1984**, *43*, 302–307, DOI 10.1136/ard.43.2.302, (cit. on pp. 10, 41).

[68] M. A. Adams, P. Lama, U. Zehra, P. Dolan, “Why do some intervertebral discs degenerate, when others (in the same spine) do not?”, in *Clinical Anatomy* **2015**, *28*, 195–204, DOI 10.1002/ca.22404, (cit. on pp. 10, 41).

[69] D. C. Ayotte, K. Ito, S. M. Perren, S. Tepic, “Direction-dependent constriction flow in a poroelastic solid: the intervertebral disc valve.”, in *Journal of biomechanical engineering* **2000**, *122*, 587–593, DOI 10.1115/1.1319658, (cit. on pp. 10, 41).

[70] P. Dolan, J. Luo, P. Pollintine, P. R. Landham, M. Stefanakis, M. A. Adams, "Intervertebral Disc Decompression Following Endplate Damage", in *Spine* **2013**, *38*, 1473–1481, DOI 10.1097/BRS.0b013e318290f3cc, (cit. on pp. 10, 41).

[71] A. Malandrino, J. A. Planell, D. Lacroix, "Statistical factorial analysis on the poroelastic material properties sensitivity of the lumbar intervertebral disc under compression, flexion and axial rotation", in *Journal of Biomechanics* **2009**, *42*, 2780–2788, DOI 10.1016/j.jbiomech.2009.07.039, (cit. on pp. 10, 31, 41).

[72] J. M. Buckley, "Sensitivity of Vertebral Compressive Strength to Endplate Loading Distribution", in *Journal of Biomechanical Engineering* **2006**, *128*, 641, DOI 10.1115/1.2241637, (cit. on pp. 10, 41).

[73] S. P. Hughes, A. L. Wallace, I. D. McCarthy, R. H. Fleming, B. C. Wyatt, "Measurement of blood flow to the vertebral bone and disc", in *European Spine Journal* **1993**, *2*, 96–98, DOI 10.1007/BF00302710, (cit. on p. 10).

[74] S. Rajasekaran, N. Bajaj, V. Tubaki, R. M. Kanna, A. P. Shetty, "Lumbar Vertebral Endplate Lesions", in *Spine* **2013**, *38*, 1491–1500, DOI 10.1097/BRS.0b013e31829a6fa6, (cit. on p. 10).

[75] R. M. Kanna, R. Shanmuganathan, V. R. Rajagopalan, S. Natesan, R. Muthuraja, K. M. C. Cheung, D. Chan, P. Y. P. Kao, A. Yee, A. P. Shetty, "Prevalence, patterns, and genetic association analysis of modic vertebral endplate changes", in *Asian Spine Journal* **2017**, *11*, 594–600, DOI 10.4184/asj.2017.11.4.594, (cit. on pp. 10, 21, 41, 171).

[76] W. E. I. N. P. J. D, E. Werkmeister, N. De Isla, P. Netter, J. F. Stoltz, D. Dumas, W. E. I. N. P. J. D, "Collagenous extracellular matrix of cartilage submitted to mechanical forcesstudied by second harmonic generation microscopy.", in *Photochemistry and Photobiology* **2010**, *86*, 302–310, DOI 10.1111/j.1751-1097.2009.00648.x, (cit. on p. 10).

[77] J. Y. Rho, L. Kuhn-Spearing, P. Zioupos, "Mechanical properties and the hierarchical structure of bone", in *Medical Engineering and Physics* **1998**, *20*, 92–102, DOI 10.1016/S1350-4533(98)00007-1, (cit. on p. 11).

[78] D. C. Ayotte, K. Ito, S. Tepic, "Direction-dependent resistance to flow in the endplate of the intervertebral disc: An ex vivo study", in *Journal of Orthopaedic Research* **2001**, *19*, 1073–1077, DOI 10.1016/S0736-0266(01)00038-9, (cit. on pp. 11, 15, 102, 105, 140, 143).

[79] L. M. Benneker, P. F. Heini, M. Alini, S. E. Anderson, K. Ito, "2004 Young investigator award winner: Vertebral endplate marrow contact channel occlusions and intervertebral disc degeneration", in *Spine* **2005**, *30*, 167–173, DOI 10.1097/01.brs.0000150833.93248.09, (cit. on p. 11).

[80] A. J. van der Veen, M. G. Mullender, I. Kingma, J. H. Van, T. H. Smit, "Contribution of verftebral bodies, endplates, and intervertebral discs to the compression creep of spinal motion segments", in *Journal of Biomechanics* **2008**, *41*, 1260–1268, DOI 10.1016/j.jbiomech.2008.01.010, (cit. on pp. 12, 164).

[81] S. A. Rodrigues, A. Thambyah, N. D. Broom, "A multiscale structural investigation of the annulus-endplate anchorage system and its mechanisms of failure", in *Spine Journal* **2015**, *15*, 405–416, DOI 10.1016/j.spinee.2014.12.144, (cit. on pp. 12, 13, 41, 94).

[82] T. P. Green, M. A. Adams, P. Dolan, "Tensile properties of the annulus fibrosus II. Ultimate tensile strength and fatigue life.", in *European spine journal : official publication of the European Spine Society the European Spinal Deformity Society and the European Section of the Cervical Spine Research Society* **1993**, *2*, 209–214, DOI 10.1007/BF00299447, (cit. on p. 12).

[83] A. M. Kaigle, S. H. Holm, T. H. Hansson, 1997 Volvo Award winner in biomechanical studies. Kinematic behavior of the porcine lumbar spine: a chronic lesion model, **1997** (cit. on pp. 12, 149).

[84] M. M. Panjabi, T. R. Oxland, I. Yamamoto, J. J. Crisco, "Mechanical behavior of the human lumbar and lumbosacral spine as shown by three-dimensional load-displacement curves", in *Journal of Bone and Joint Surgery - Series A* **1994**, *76*, 413–424, DOI 10.2106/00004623-199403000-00012, (cit. on pp. 12, 149).

[85] D. C. Keyes, E. L. Compere, "The normal and pathological physiology of the nucleus pulposus of the intervertebral disc", in *J Bone Joint Surg Am* **1932**, *14*, 897–938, (cit. on pp. 12, 149, 164).

[86] P. Brinckmann, W. Frobin, E. Hierholzer, M. Horst, "Deformation of the vertebral endplate under axial loading of the spine", in *Spine* **1983**, *8*, 851–856, DOI 10.1097/00007632-198311000-00007, (cit. on p. 12).

[87] M. Reuber, a. Schultz, F. Denis, D. Spencer, "Bulging of lumbar intervertebral disks.", in *Journal of biomechanical engineering* **1982**, *104*, 187–192, DOI 10.1115/1.3138347, (cit. on pp. 12, 149).

[88] J. P. Grant, T. R. Oxland, M. F. Dvorak, "Mapping the structural properties of the lumbosacral vertebral endplates.", in *Spine* **2001**, *26*, 889–896, DOI 10.1097/00007632-200104150-00012, (cit. on pp. 13, 149).

[89] R. S. Ochia, A. F. Tencer, R. P. Ching, "Effect of loading rate on endplate and vertebral body strength in human lumbar vertebrae", in *Journal of Biomechanics* **2003**, *36*, 1875–1881, DOI 10.1016/S0021-9290(03)00211-2, (cit. on pp. 13, 149).

[90] J. H. van Dieën, I. Kingma, R. Meijer, L. Hänsel, R. Huiskes, "Stress distribution changes in bovine vertebrae just below the endplate after sustained loading.", in *Clinical biomechanics (Bristol Avon)* **2001**, *16 Suppl 1*, S135–42, DOI 10.1016/S0268-0033(00)00105-4, (cit. on p. 13).

[91] D. Hickey, D. Hukins, Relation between the structure of the Annulus Fibrosus and the function and failure of the Intervertebral Disc, **1980** (cit. on p. 13).

[92] H. Inoue, "Three-dimensional architecture of lumbar intervertebrai discs", in *Spine* **1981**, *6*, 139–146, DOI 10.1097/00007632-198103000-00006, (cit. on pp. 13, 41).

[93] R. J. Francois, A. Dhem, "Microradiographic study of the normal human vertebral body", in *Acta Anat (Basel)* **1974**, *89*, 251–265, (cit. on pp. 13, 41).

[94] S. A. Rodrigues, K. R. Wade, A. Thambyah, N. D. Broom, "Micromechanics of annulus-end plate integration in the intervertebral disc", in *Spine Journal* **2012**, *12*, 143–150, DOI 10.1016/j.spinee.2012.01.003, (cit. on pp. 13, 41, 64, 92, 93).

[95] N. H. Sapiee, A. Thambyah, P. A. Robertson, N. D. Broom, "New evidence for structural integration across the cartilage-vertebral endplate junction and its relation to herniation", in *Spine Journal* **2019**, *19*, 532–544, DOI 10.1016/j.spinee.2018.08.013, (cit. on pp. 13, 14, 41, 93, 98).

[96] J. J. Costi, T. C. Hearn, N. L. Fazzalari, "The effect of hydration on the stiffness of intervertebral discs in an ovine model", in *Clinical Biomechanics* **2002**, *17*, 446–455, DOI 10.1016/S0268-0033(02)00035-9, (cit. on p. 14).

[97] D. S. Pflaster, M. H. Krag, C. C. Johnson, L. D. Haugh, M. H. Pope, "Effect of test environment on intervertebral disc hydration", in *Spine* **1997**, *22*, 133–139, DOI 10.1097/00007632-199701150-00003, (cit. on p. 14).

[98] A. Race, N. D. Broom, P. Robertson, Effect of loading rate and hydration on the mechanical properties of the disc. **2000** (cit. on p. 14).

[99] A. G. Rodriguez, A. E. Rodriguez-Soto, A. J. Burghardt, S. Berven, S. Majumdar, J. C. Lotz, "Morphology of the human vertebral endplate", in *Journal of Orthopaedic Research* **2012**, *30*, 280–287, DOI 10.1002/jor.21513, (cit. on pp. 14, 20, 89).

[100] U. Zehra, K. Robson-Brown, M. A. Adams, P. Dolan, "Porosity and Thickness of the Vertebral Endplate Depend on Local Mechanical Loading.", in *Spine* **2015**, *40*, 1173–1180, DOI 10.1097/BRS.0000000000000925, (cit. on p. 14).

[101] A. Nachemson, T. Lewin, A. Maroudas, M. A. Freeman, "In vitro diffusion of DYE through the end-plates and the annulus fibrosus of human lumbar inter-vertebral discs", in *Acta Orthopaedica* **1970**, *41*, 589–607, DOI 10.3109/17453677008991550, (cit. on pp. 15, 100).

[102] M. Van Der Werf, P. Lezuo, O. Maissen, C. C. Van Donkelaar, K. Ito, "Inhibition of vertebral endplate perfusion results in decreased intervertebral disc intranuclear diffusive transport", in *Journal of Anatomy* **2007**, *211*, 769–774, DOI 10.1111/j.1469-7580.2007.00816.x, (cit. on pp. 15, 102, 146).

[103] J. P. Urban, S. Holm, A. Maroudas, "Diffusion of small solutes into the intervertebral disc: An in vivo study", in *Biorheology* **1978**, *15*, 203–223, DOI 10.3233/BIR-1978-153-409, (cit. on p. 15).

[104] D. B. Das, A. Welling, J. P. Urban, O. A. Boubriak, "Solute transport in intervertebral disc: Experiments and finite element modeling", in *Annals of the New York Academy of Sciences* **2009**, *1161*, 44–61, (cit. on p. 15).

[105] A. Shirazi-Adl, M. Taheri, J. P. G. Urban, "Analysis of cell viability in intervertebral disc: Effect of endplate permeability on cell population", in *Journal of Biomechanics* **2010**, *43*, 1330–1336, DOI 10.1016/j.jbiomech.2010.01.023, (cit. on p. 15).

[106] H. Brodin, "Paths of nutrition in articular cartilage and intervertebral discs", in *Acta Orthopaedica* **1954**, *24*, 177–183, DOI 10.3109/17453675408988561, (cit. on pp. 15, 100).

[107] S. Holm, A. Maroudas, J. P. Urban, G. Selstam, A. Nachemson, "Nutrition of the intervertebral disc: solute transport and metabolism", in *Connect Tissue Res* **1981**, *8*, 101–119, DOI 10.3109/03008208109152130, (cit. on pp. 15, 28, 100).

[108] S. K. Mirza, A. A. White, "Anatomy of intervertebral disc and pathophysiology of herniated disc disease", in *J Clin Laser Med Surg* **1995**, *13*, 131–142, DOI 10.1089/clm.1995.13.131, (cit. on p. 15).

[109] O. Hassler, "The Human Intervertebral Disc: A Micro-Angiographical Study on its Vascular Supply at Various Ages", in *Acta Orthopaedica Scandinavia* **1970**, *40*, 765–772, (cit. on pp. 15, 146).

[110] M. Bendtsen, C. Bunger, P. Colombier, C. Le Visage, S. Roberts, D. Sakai, J. P. Urban, "Biological challenges for regeneration of the degenerated disc using cellular therapies", in *Acta Orthopaedica* **2016**, *87*, 39–46, DOI 10.1080/17453674.2017.1297916, (cit. on pp. 15, 170).

[111] S. Oki, Y. Matsuda, T. Itoh, T. Shibata, H. Okumura, J. Desaki, "Scanning electron microscopic observations of the vascular structure of vertebral end-plates in rabbits", in *Journal of Orthopaedic Research* **1994**, *12*, 447–449, DOI 10.1002/jor.1100120318, (cit. on pp. 16, 102–104, 141, 146).

[112] S. Oki, Y. Matsuda, T. Shibata, H. Okumura, J. Desaki, "Morphologic differences of the vascular buds in the vertebral endplate: Scanning electron microscopic study", in *Spine* **1996**, *21*, 174–177, DOI 10.1097/00007632-199601150-00003, (cit. on pp. 16, 141).

[113] H. V. Crock, H. Yoshizawa, "The blood supply of the lumbar vertebral column", in *Clinical orthopaedics and related research* **1976**, *115*, 6–21, (cit. on p. 16).

[114] H. Crock, M. Goldwasser, H. Yoshizawa, "Vascular anatomy related to the intervertebral disc", in *Biology of the intervertebral disc* **1988**, 109–133, (cit. on p. 16).

[115] H. V. Crock, M. Goldwasser, Anatomic Studies of the Circulation in the Region of the Vertebral End-Plate in Adult Greyhound Dogs, **2006** (cit. on pp. 16, 17, 20, 103, 104, 141, 146).

[116] H. V. Crock, H. Yoshizawa, S. K. Kame, "Observations on the Venous Drainage of the Human Vertebral Body", in *The Journal of Bone and Joint Surgery. British volume* **2018**, *55-B*, 528–533, DOI 10.1302/0301-620x.55b3.528, (cit. on pp. 16, 17).

[117] F. Paneni, "The ESC Textbook of Vascular Biology", in *European Heart Journal* **2017**, *38*, 2868–2868, DOI 10.1093/eurheartj/ehx574, (cit. on p. 17).

[118] M. G. Butler, S. Isogai, B. M. Weinstein, Lymphatic development, **2009** (cit. on p. 17).

[119] P. S. Puligandla, J. M. Laberge in *Pediatric Surgery: Sixth Edition, Vol. 1-2*, **2006**, pp. 1001–1037 (cit. on pp. 17, 19).

[120] M. Rudert, B. Tillmann, "Lymph and blood supply of the human intervertebral disc: Cadaver study of correlations to discitis", in *Acta Orthopaedica* **1993**, *64*, 37–40, DOI 10.3109/17453679308994524, (cit. on pp. 17, 20, 89, 142).

[121] T. G. Kashima, A. Dongre, N. A. Athanasou, "Lymphatic involvement in vertebral and disc pathology", in *Spine* **2011**, *36*, 899–904, DOI 10.1097/BRS.0b013e3182050284, (cit. on pp. 17, 142).

[122] M. C. Hsu, M. Itkin, Lymphatic Anatomy, **2016** (cit. on p. 18).

[123] L. M. Benneker, P. F. Heini, S. E. Anderson, M. Alini, K. Ito, "Correlation of radiographic and MRI parameters to morphological and biochemical assessment of intervertebral disc degeneration", in *European Spine Journal* **2005**, *14*, 27–35, DOI 10.1007/s00586-004-0759-4, (cit. on pp. 20, 102).

[124] Adams MA., "Biomechanics of back pain", in *Acupuncture in Medicine* **2004**, *22*, 178–188, DOI 10.1136/aim.22.4.178, (cit. on p. 20).

[125] Y. Wang, M. C. Battié, S. K. Boyd, T. Videman, "The osseous endplates in lumbar vertebrae: Thickness, bone mineral density and their associations with age and disk degeneration", in *Bone* **2011**, *48*, 804–809, DOI 10.1016/j.bone.2010.12.005, (cit. on p. 20).

[126] A. B. Fagan, R. Moore, B. V. Roberts, P. Blumbergs, R. Fraser, "ISSLS Prize Winner: The Innervation of the Intervertebral Disc: A Quantitative Analysis", in *Spine* **2003**, *28*, 2570–2576, DOI 10.1097/01.BRS.0000096942.29660.B1, (cit. on p. 20).

[127] R. B. Duthie, "The Human Spine in Health and Disease", in *The Journal of Bone and Joint Surgery. British volume* **2018**, *55-B*, 889–889, DOI 10.1302/0301-620x.55b4.889, (cit. on p. 21).

[128] Y. Wang, M. C. Battie, T. Videman, "A morphological study of lumbar vertebral endplates: Radiographic, visual and digital measurements", in *European Spine Journal* **2012**, *21*, 2316–2323, DOI 10.1007/s00586-012-2415-8, (cit. on pp. 21, 35, 36).

[129] B. Vernon-Roberts, C. J. Pirie, "Degenerative changes in the intervertebral discs of the lumbar spine and their squeletae", in *Rheumatology and rehabilitation* **1977**, *16*, 13–21, (cit. on p. 21).

[130] O. Perey, "Fracture of the Vertebral End-Plate in the Lumbar Spine: An Experimental Biomechanical Investigation", in *Acta Orthopaedica Scandinavica* **2014**, *28*, 1–101, DOI 10.3109/ort.1957.28.suppl-25.01, (cit. on p. 21).

[131] S. Roberts, J. Menage, S. M. Eisenstein, "The cartilage end-plate and intervertebral disc in scoliosis: Calcification and other sequelae", in *Journal of Orthopaedic Research* **1993**, *11*, 747–757, DOI 10.1002/jor.1100110517, (cit. on p. 21).

[132] M. Kuisma, J. Karppinen, J. Niinimäki, M. Kurunlahti, M. Haapea, H. Vanharanta, O. Tervonen, "A three-year follow-up of lumbar spine endplate (Modic) changes.", in *Spine* **2006**, *31*, 1714–1718, DOI 10.1097/01.brs.0000224167.18483.14, (cit. on pp. 21, 41, 171).

[133] O. L. Osti, S. Zahari, J. T. C. Ooi, L. Truong, E. Perilli, N. L. Fazzalari, "Microstructure and Remodelling in Modic Changes", in *Spine Journal Meeting Abstracts* **2010**, 13, (cit. on p. 21).

[134] T. S. Jensen, T. Bendix, J. S. Sorensen, C. Manniche, L. Korsholm, P. Kjaer, "Characteristics and natural course of vertebral endplate signal (Modic) changes in the Danish general population", in *BMC Musculoskeletal Disorders* **2009**, *10*, DOI 10.1186/1471-2474-10-81, (cit. on pp. 21, 41, 171).

[135] E. Perilli, I. H. Parkinson, L. H. Truong, K. C. Chong, N. L. Fazzalari, O. L. Osti, "Modic (endplate) changes in the lumbar spine: bone micro-architecture and remodelling", in *European Spine Journal* **2015**, *24*, 1926–1934, DOI 10.1007/s00586-014-3455-z, (cit. on p. 21).

[136] J. C. Mansfield, C. Peter Winlove, "A multi-modal multiphoton investigation of microstructure in the deep zone and calcified cartilage", in *Journal of Anatomy* **2012**, *220*, 405–416, DOI 10.1111/j.1469-7580.2012.01479.x, (cit. on pp. 23, 27, 48, 90, 93).

[137] K. P. Arkill, J. Moger, C. P. Winlove, "The structure and mechanical properties of collecting lymphatic vessels: An investigation using multimodal nonlinear microscopy", in *Journal of Anatomy* **2010**, *216*, 547–555, DOI 10.1111/j.1469-7580.2010.01215.x, (cit. on pp. 23, 146).

[138] A. Diaspro, P. Bianchini, G. Vicidomini, M. Faretta, P. Ramoino, C. Usai, "Multi-photon excitation microscopy", in *BioMedical Engineering OnLine* **2006**, *5*, 36, DOI 10.1186/1475-925X-5-36, (cit. on p. 24).

[139] J. B. Pawley, "Confocal and two-photon microscopy: Foundations, applications and advances", in *Microscopy Research and Technique* **2002**, *59*, 148–149, DOI 10.1002/jemt.10188, (cit. on p. 24).

[140] P. T. C. So, C. Y. Dong, B. R. Masters, K. M. Berland, "Two-photon excitation fluorescence microscopy", in *Annual Review of Biomedical Engineering* **2000**, *2*, 399–429, (cit. on p. 24).

[141] W. R. Zipfel, R. M. Williams, W. W. Webb, "Nonlinear magic: multiphoton microscopy in the biosciences.", in *Nature biotechnology* **2003**, *21*, 1369–1377, DOI 10.1038/nbt899, (cit. on p. 25).

[142] J. Mansfield, PhD thesis, University of Exeter, **2008** (cit. on pp. 25, 60, 90, 91).

[143] P. Stoller, K. M. Reiser, P. M. Celliers, A. M. Rubenchik, "Polarization-modulated second harmonic generation in collagen", in *Biophysical Journal* **2002**, *82*, 3330–3342, DOI 10.1016/S0006-3495(02)75673-7, (cit. on p. 26).

[144] G. Cox, E. Kable, A. Jones, I. Fraser, F. Manconi, M. D. Gorrell, "3-Dimensional imaging of collagen using second harmonic generation", in *Journal of Structural Biology* **2003**, *141*, 53–62, DOI 10.1016/S1047-8477(02)00576-2, (cit. on p. 26).

[145] S. Roth, I. Freund, "Optical second-harmonic scattering in rat-tail tendon", in *Biopolymers* **1981**, *20*, 1271–1290, DOI 10.1002/bip.1981.360200613, (cit. on p. 26).

[146] P. J. Campagnola, A. C. Millard, M. Terasaki, P. E. Hoppe, C. J. Malone, W. A. Mohler, "Imaging of Endogenous Structural Proteins in Biological Tissues", in *Biophysical Journal* **2002**, *82*, 493–508, DOI 10.1016/S0006-3495(02)75414-3, (cit. on p. 26).

[147] D. A. Dombeck, K. A. Kasischke, H. D. Vishwasrao, M. Ingelsson, B. T. Hyman, W. W. Webb, "Uniform polarity microtubule assemblies imaged in native brain tissue by second-harmonic generation microscopy", in *Proceedings of the National Academy of Sciences* **2003**, *100*, 7081–7086, DOI 10.1073/pnas.0731953100, (cit. on p. 26).

[148] S. W. Chu, S. Y. Chen, G. W. Chern, T. H. Tsai, Y. C. Chen, B. L. Lin, C. K. Sun, "Studies of $\chi(2)/\chi(3)$tensors in submicron-scaled bio-tissues by polarization harmonics optical microscopy", in *Biophysical Journal* **2004**, *86*, 3914–3922, DOI 10.1529/biophysj.103.034595, (cit. on p. 26).

[149] S. V. Plotnikov, A. C. Millard, P. J. Campagnola, W. A. Mohler, "Characterization of the myosin-based source for second-harmonic generation from muscle sarcomeres", in *Biophysical Journal* **2006**, *90*, 693–703, DOI 10.1529/biophysj.105.071555, (cit. on pp. 26, 88).

[150] T. Yasui, Y. Tohno, T. Araki, "Determination of collagen fiber orientation in human tissue by use of polarization measurement of molecular second-harmonic-generation light", in *Applied Optics* **2004**, *43*, 2861, DOI 10.1364/ao.43.002861, (cit. on pp. 26, 88).

[151] P. Stoller, B.-M. Kim, A. M. Rubenchik, K. M. Reiser, L. B. Da Silva, "Polarization-dependent optical second-harmonic imaging of a rat-tail tendon", in *Journal of Biomedical Optics* **2002**, *7*, 205, DOI 10.1117/1.1431967, (cit. on p. 26).

[152] P. Stoller, P. M. Celliers, K. M. Reiser, A. M. Rubenchik, "Quantitative second-harmonic generation microscopy in collagen", in *Applied Optics* **2003**, *42*, 5209, DOI 10.1364/ao.42.005209, (cit. on pp. 26, 88).

[153] J. C. Lotz, Animal models of intervertebral disc degeneration: Lessons learned, **2004** (cit. on p. 27).

[154] C. Daly, P. Ghosh, G. Jenkin, D. Oehme, T. Goldschlager, A Review of Animal Models of Intervertebral Disc Degeneration: Pathophysiology, Regeneration, and Translation to the Clinic, **2016** (cit. on pp. 27–29, 31).

[155] G. D. O'Connell, E. J. Vresilovic, D. M. Elliott, "Comparison of animals used in disc research to human lumbar disc geometry", in *Spine* **2007**, *32*, 328–333, DOI 10.1097/01.brs.0000253961.40910.c1, (cit. on pp. 28, 30–32).

[156] J. P. Urban, S. Smith, J. C. Fairbank, Nutrition of the intervertebral disc, **2004** (cit. on pp. 28, 143).

[157] K. D. Luk, D. K. Ruan, D. H. Chow, J. C. Leong in Clinical Orthopaedics and Related Research, **1997**, pp. 13–26 (cit. on p. 28).

[158] C. W. GOFF, W. LANDMESSER, "Bipedal rats and mice; laboratory animals for orthopaedic research.", in *The Journal of bone and joint surgery. American volume* **1957**, *39 A*, 616–622, DOI 10.2106/00004623-195739030-00014, (cit. on p. 28).

[159] H. J. Wilke, A. Rohlmann, S. Neller, F. Graichen, L. Claes, G. Bergmannt, "ISSLS Prize Winner: A Novel Approach to Determine Trunk Muscle Forces during Flexion and Extension: A Comparison of Data from an in Vitro Experiment and in Vivo Measurements", in *Spine* **2003**, *28*, 2585–2593, DOI 10.1097/01.BRS.0000096673.16363.C7, (cit. on p. 28).

[160] K. W. Kim, K. Y. Ha, J. B. Park, Y. K. Woo, H. N. Chung, H. S. An, "Expressions of membrane-type I matrix metalloproteinase, Ki-67 protein, and type II collagen by chondrocytes migrating from cartilage endplate into nucleus pulposus in rat intervertebral discs: A cartilage endplate-fracture model using an intervertebral d", in *Spine* **2005**, *30*, 1373–1378, DOI 10.1097/01.brs.0000166155.48168.0e, (cit. on p. 29).

[161] K. W. Kim, T. H. Lim, J. G. Kim, S. T. Jeong, K. Masuda, H. S. An in Spine, *Vol. 28*, **2003**, pp. 982–990 (cit. on p. 29).

[162] D. J. Aguiar, S. L. Johnson, T. R. Oegema, "Notochordal cells interact with nucleus pulposus cells: Regulation of proteoglycan synthesis", in *Experimental Cell Research* **1999**, *246*, 129–137, DOI 10.1006/excr.1998.4287, (cit. on p. 29).

[163] T. R. Oegema, S. L. Johnson, D. J. Aguiar, J. W. Ogilvie, "Fibronectin and its fragments increase with degeneration in the human intervertebral disc", in *Spine* **2000**, *25*, 2742–2747, DOI 10.1097/00007632-200011010-00005, (cit. on p. 29).

[164] J. W. Stevens, G. L. Kurriger, A. S. Carter, J. A. Maynard, "CD44 expression in the developing and growing rat intervertebral disc", in *Developmental Dynamics* **2000**, *219*, 381–390, DOI 10.1002/1097-0177(2000)9999:9999<::AID-DVDY1060>3.0.CO;2-P, (cit. on p. 29).

[165] C. J. Hunter, J. R. Matyas, N. A. Duncan, "Cytomorphology of notochordal and chondrocytic cells from the nucleus pulposus: A species comparison", in *Journal of Anatomy* **2004**, *205*, 357–362, DOI 10.1111/j.0021-8782.2004.00352.x, (cit. on p. 29).

[166] N. Bergknut, L. A. Smolders, G. C. Grinwis, R. Hagman, A. S. Lagerstedt, H. A. Hazewinkel, M. A. Tryfonidou, B. P. Meij, Intervertebral disc degeneration in the dog. Part 1: Anatomy and physiology of the intervertebral disc and characteristics of intervertebral disc degeneration, **2013** (cit. on p. 29).

[167] S. Sobajima, J. F. Kompel, J. S. Kim, C. J. Wallach, D. D. Robertson, M. T. Vogt, J. D. Kang, L. G. Gilbertson, "A slowly progressive and reproducible animal model of intervertebral disc degeneration characterized by MRI, X-ray, and histology", in *Spine* **2005**, *30*, 15–24, DOI 10.1097/01.brs.0000148048.15348.9b, (cit. on p. 29).

[168] J. C. Lotz, J. R. Chin, "Intervertebral disc cell death is dependent on the magnitude and duration of spinal loading", in *Spine* **2000**, *25*, 1477–1483, DOI 10.1097/00007632-200006150-00005, (cit. on p. 29).

[169] H. E. Gruber, E. N. Hanley, "Analysis of aging and degeneration of the human intervertebral disc: Comparison of surgical specimens with normal controls", in *Spine* **1998**, *23*, 751–757, DOI 10.1097/00007632-199804010-00001, (cit. on p. 29).

[170] J. Antoniou, T. Steffen, F. Nelson, N. Winterbottom, A. P. Hollander, R. A. Poole, M. Aebi, M. Alini, "The human lumbar intervertebral disc: Evidence for changes in the biosynthesis and denaturation of the extracellular matrix with growth, maturation, ageing, and degeneration", in *Journal of Clinical Investigation* **1996**, *98*, 996–1003, DOI 10.1172/JCI118884, (cit. on pp. 29, 30).

[171] C. N. Demers, J. Antoniou, F. Mwale, "Value and limitations of using the bovine tail as a model for the human lumbar spine.", in *Spine* **2004**, *29*, 2793–2799, DOI 10.1097/01.brs.0000147744.74215.b0, (cit. on pp. 29, 31, 32).

[172] J. Melrose, S. Roberts, S. Smith, J. Menage, P. Ghosh in Spine, *Vol. 27*, **2002**, pp. 1278–1285 (cit. on pp. 29, 32).

[173] C. Hunter, J. Matyas, N. Duncan, "The Notochordal Cell in the Nucleus Pulposus: A Review in the Context of Tissue Engineering", in *Tissue Engineering* **08/2003**, *9*, 667–677, DOI 10.1089/107632703768247368, (cit. on pp. 30, 31).

[174] N. A. Scott, P. F. Harris, K. M. Bagnall, "A morphological and histological study of the postnatal development of intervertebral discs in the lumbar spine of the rabbit.", in *Journal of anatomy* **1980**, *130*, 75–81, (cit. on p. 30).

[175] P. Ghosh, T. K. Taylor, K. G. Braund, "Variation of the glycosaminoglycans of the intervertebral disc with ageing: Ii. non-chondrodystrophoid breed", in *Gerontology* **1977**, *23*, 99–109, DOI 10.1159/000212178, (cit. on pp. 30, 31).

[176] N. Hirano, H. Tsuji, H. Ohshima, S. Kitano, A. Sano, "Analysis of rabbit intervertebral disc physiology based on water metabolism: I. Factors influencing metabolism of the normal intervertebral discs", in *Spine* **1988**, *13*, 1291–1296, DOI 10.1097/00007632-198811000-00015, (cit. on p. 30).

[177] E. Kääpä, S. Holm, X. Han, T. Takala, V. Kovanen, H. Vanharanta, "Collagens in the injured porcine intervertebral disc", in *Journal of Orthopaedic Research* **1994**, *12*, 93–102, DOI 10.1002/jor.1100120112, (cit. on pp. 30, 31).

[178] H. Ohshima, H. Tsuji, N. Hirano, H. Ishihara, Y. Katoh, H. Yamada, "Water diffusion pathway, swelling pressure, and biomechanical properties of the intervertebral disc during compression load", in *Spine* **1989**, *14*, 1234–1244, DOI 10.1097/00007632-198911000-00017, (cit. on p. 31).

[179] P. Ghosh, T. K. Taylor, K. G. Braund, L. H. Larsen, "The collagenous and non-collagenous protein of the canine intervertebral disc and their variation with age, spinal level and breed", in *Gerontology* **1976**, *22*, 124–134, DOI 10.1159/000212129, (cit. on p. 31).

[180] H.-J. Hansen, "A Pathologic-Anatomical Study on Disc Degeneration in Dog: With Special Reference to the So-Called Enchondrosis Intervertebralis", in *Acta Orthopaedica Scandinavica* **1952**, *23*, 1–130, DOI 10.3109/ort.1952.23.suppl-11.01, (cit. on p. 31).

[181] E. W. Carlier, "Fate of the Notochord and Development of the Intervertebral Disc in the Sheep, with Observations on the Structure of the Adult Disc in these Animals.", in *Journal of Anatomy and Physiology* **1890**, *24*, 573, (cit. on p. 31).

[182] Y. Sun, M. Hurtig, R. M. Pilliar, M. Grynpas, R. A. Kandel, "Characterization of nucleus pulposus-like tissue formed in vitro", in *Journal of Orthopaedic Research* **2001**, *19*, 1078–1084, DOI 10.1016/S0736-0266(01)00056-0, (cit. on p. 32).

[183] I. Busscher, J. J. Ploegmakers, G. J. Verkerke, A. G. Veldhuizen, "Comparative anatomical dimensions of the complete human and porcine spine", in *European Spine Journal* **2010**, *19*, 1104–1114, DOI 10.1007/s00586-010-1326-9, (cit. on pp. 33, 34).

[184] L. A. Monaco, S. J. Dewitte-Orr, D. E. Gregory, "A comparison between porcine, ovine, and bovine intervertebral disc anatomy and single lamella annulus fibrosus tensile properties", in *Journal of Morphology* **2016**, *277*, 244–251, DOI 10.1002/jmor.20492, (cit. on pp. 33, 34).

[185] V. R. Yingling, J. P. Callaghan, S. M. McGill, "The porcine cervical spine as a model of the human lumbar spine: An anatomical, geometric, and functional comparison", in *Journal of Spinal Disorders* **1999**, *12*, 415–423, DOI 10.1097/00002517-199912050-00012, (cit. on p. 33).

[186] M. Egermann, J. Goldhahn, E. Schneider in Osteoporosis International, *Vol. 16*, **2005** (cit. on p. 33).

[187] L. Mosekilde, "Sex differences in age-related loss of vertebral trabecular bone mass and structure-biomechanical consequences", in *Bone* **1989**, *10*, 425–432, DOI 10.1016/8756-3282(89)90074-4, (cit. on p. 34).

[188] J. Aerssens, S. Boonen, G. Lowet, J. Dequeker, "Interspecies differences in bone composition, density, and quality: Potential implications for in vivo bone research", in *Endocrinology* **1998**, *139*, 663–670, DOI 10.1210/endo.139.2.5751, (cit. on p. 34).

[189] S. R. Sheng, H. Z. Xu, Y. L. Wang, Q. A. Zhu, F. M. Mao, Y. Lin, X. Y. Wang, "Comparison of cervical spine anatomy in calves, pigs and humans", in *PLoS ONE* **2016**, *11*, DOI 10.1371/journal.pone.0148610, (cit. on p. 34).

[190] H. J. Wilke, A. Kettler, K. H. Wenger, L. E. Claes, "Anatomy of the sheep spine and its comparison to the human spine", in *Anatomical Record* **1997**, *247*, 542–555, DOI 10.1002/(SICI)1097-0185(199704)247:4<542::AID-AR13>3.0.CO;2-P, (cit. on pp. 34, 36).

[191] N. Kumar, S. Kukreti, M. Ishaque, R. Mulholland, "Anatomy of deer spine and its comparison to the human spine", in *Anatomical Record* **2000**, *260*, 189–203, DOI 10.1002/1097-0185(20001001)260:2<189::AID-AR80>3.0.CO;2-N, (cit. on p. 34).

[192] G. Dar, Y. Masharawi, S. Peleg, N. Steinberg, H. May, B. Medlej, N. Peled, I. Hershkovitz, "The Epiphyseal Ring", in *Spine* **2011**, *36*, 850–856, DOI 10.1097/brs.0b013e3181e9b19d, (cit. on pp. 35, 88).

[193] M. J. Silva, C. Wang, T. M. Keaveny, W. C. Hayes, "Direct and computed tomography thickness measurements of the human, lumbar vertebral shell and endplate", in *Bone* **1994**, *15*, 409–414, DOI 10.1016/8756-3282(94)90817-6, (cit. on p. 36).

[194] H. Ritzel, M. Amling, M. Pösl, M. Hahn, G. Delling, "The thickness of human vertebral cortical bone and its changes in aging and osteoporosis: a histomorphometric analysis of the complete spinal column from thirty-seven autopsy specimens.", in *Journal of bone and mineral research : the official journal of the American Society for Bone and Mineral Research* **1997**, *12*, 89–95, DOI 10.1359/jbmr.1997.12.1.89, (cit. on p. 36).

[195] E. B. Van Der Houwen, P. Baron, A. G. Veldhuizen, J. G. M. Burgerhof, P. M. A. Van Ooijen, G. J. Verkerke, "Geometry of the intervertebral volume and vertebral endplates of the human spine", in *Annals of Biomedical Engineering* **2010**, *38*, 33–40, DOI 10.1007/s10439-009-9827-6, (cit. on pp. 36, 92).

[196] Y. Wang, T. Videman, M. C. Battié, "ISSLS prize winner: Lumbar vertebral endplate lesions: Associations with disc degeneration and back pain history", in *Spine* **2012**, *37*, 1490–1496, DOI 10.1097/BRS.0b013e3182608ac4, (cit. on p. 36).

[197] S. Roberts, J. Menage, J. P. G. Urban, "Biochemical and structural properties of the cartilage end-plate and its relation to the intervertebral disc", in *Spine* **1989**, *14*, 166–174, DOI 10.1097/00007632-198902000-00005, (cit. on p. 41).

[198] Y. S. Nosikova, J. P. Santerre, M. Grynpas, G. Gibson, R. A. Kandel, "Characterization of the annulus fibrosus-vertebral body interface: Identification of new structural features", in *Journal of Anatomy* **2012**, *221*, 577–589, DOI 10.1111/j.1469-7580.2012.01537.x, (cit. on pp. 41, 92).

[199] S. A. Rodrigues, A. Thambyah, N. D. Broom, "How maturity influences annulus-endplate integration in the ovine intervertebral disc: a micro- and ultra-structural study", in *Journal of Anatomy* **2017**, *230*, 152–164, DOI 10.1111/joa.12536, (cit. on p. 41).

[200] A. Polikeit, S. J. Ferguson, L. P. Nolte, T. E. Orr, "The importance of the endplate for interbody cages in the lumbar spine", in *European Spine Journal* **2003**, *12*, 556–561, DOI 10.1007/s00586-003-0556-5, (cit. on pp. 41, 172).

[201] N. S. J. Lim, Z. Hamed, C. H. Yeow, C. Chan, Z. Huang, "Early detection of biomolecular changes in disrupted porcine cartilage using polarized Raman spectroscopy", in *Journal of Biomedical Optics* **2011**, *16*, 017003, DOI 10.1117/1.3528006, (cit. on pp. 44, 74, 96).

[202] P. H. C. Eilers, H. F. M. Boelens, "Baseline Correction with Asymmetric Least Squares Smoothing", in *Life Sciences* **2005**, 1–26, DOI 10.1021/ac034173t, (cit. on p. 44).

[203] C. G. Jones, "Scanning electron microscopy: Preparation and imaging for SEM", in *Methods in Molecular Biology* **2012**, *915*, 1–20, DOI 10.1007/978-1-61779-977-8_1, (cit. on p. 46).

[204] J. J. Bozzola, "Conventional specimen preparation techniques for scanning electron microscopy of biological specimens", in *Methods in Molecular Biology* **2014**, *1117*, 133–150, DOI 10.1007/978-1-62703-776-1_7, (cit. on p. 46).

[205] M. Pluta, ""Nomarski's DIC microscopy: a review", Proc. SPIE 1846, Phase Contrast and Differential Interference Contrast Imaging Techniques and Applications", in *International Society for Optics and Photonics*. **1994**, 10–25, DOI 10.1117/12.171873, (cit. on p. 46).

[206] D. Way, "Principles and Applications of Differential Interference Contrast Light Microscopy", in *Microscopy and Analysis; Light Microscopy Supplement* **2006**, *20*, 9–11, (cit. on p. 46).

[207] J. Tinevez, Directionality Fiji Image J, **2010** (cit. on p. 48).

[208] K. A. Esmonde-White, F. W. L. Esmonde-White, M. D. Morris, B. J. Roessler, "Fiber-optic Raman spectroscopy of joint tissues", in *The Analyst* **2011**, *136*, 1675, DOI 10.1039/c0an00824a, (cit. on pp. 74, 94).

[209] B. G. Frushour, J. L. Koenig, "Raman scattering of collagen, gelatin, and elastin", in *Biopolymers* **1975**, *14*, 379–391, DOI 10.1002/bip.1975.360140211, (cit. on p. 74).

[210] A. Bonifacio, C. Beleites, F. Vittur, E. Marsich, S. Semeraro, S. Paoletti, V. Sergo, "Chemical imaging of articular cartilage sections with Raman mapping, employing uni- and multi-variate methods for data analysis", in *The Analyst* **2010**, *135*, 3193, DOI 10.1039/c0an00459f, (cit. on p. 74).

[211] J. J. Cárcamo, A. E. Aliaga, E. Clavijo, M. Brañes, M. M. Campos-Vallette, "Raman and surface-enhanced Raman scattering in the study of human rotator cuff tissues after shock wave treatment", in *Journal of Raman Spectroscopy* **2012**, *43*, 248–254, DOI 10.1002/jrs.3019, (cit. on p. 74).

[212] M. D. Morris, G. S. Mandair in Clinical Orthopaedics and Related Research, *Vol. 469*, **2011**, pp. 2160–2169 (cit. on pp. 75, 76, 94).

[213] B. Wopenka, A. Kent, J. D. Pasteris, Y. Yoon, S. Thomopoulos, "The tendon-to-bone transition of the rotator cuff: A preliminary Raman spectroscopic study documenting the gradual mineralization across the insertion in rat tissue samples", in *Applied Spectroscopy* **2008**, *62*, 1285–1294, DOI 10.1366/000370208786822179, (cit. on p. 75).

[214] G. S. Mandair, T. A. Bateman, M. D. Morris in Optics in Bone Biology and Diagnostics, *Vol. 7166*, **2009**, p. 716607 (cit. on p. 75).

[215] G. S. Mandair, F. W. L. Esmonde-White, M. P. Akhter, A. M. Swift, J. Kreider, S. A. Goldstein, R. R. Recker, M. D. Morris in Photonic Therapeutics and Diagnostics VI, *Vol. 7548*, **2010**, p. 754846 (cit. on p. 75).

[216] H. Isaksson, M. J. Turunen, L. Rieppo, S. Saarakkala, I. S. Tamminen, J. Rieppo, H. Kröger, J. S. Jurvelin, "Infrared spectroscopy indicates altered bone turnover and remodeling activity in renal osteodystrophy", in *Journal of Bone and Mineral Research* **2010**, *25*, 1360–1366, DOI 10.1002/jbmr.10, (cit. on pp. 75, 77).

[217] D. H. Kohn, N. D. Sahar, J. M. Wallace, K. Golcuk, M. D. Morris in Cells Tissues Organs, *Vol. 189*, **2008**, pp. 33–37 (cit. on p. 76).

[218] A. Carden, M. D. Morris, "Application of vibrational spectroscopy to the study of mineralized tissues (review)", in *Journal of Biomedical Optics* **2000**, *5*, 259–268, DOI Doi10.1117/1.429994, (cit. on p. 76).

[219] S. Goh, C. Tan, R. I. Price, S. J. Edmondston, S. Song, S. Davis, K. P. Singer, "Influence of age and gender on thoracic vertebral body shape and disc degeneration: An MR investigation of 169 cases", in *Journal of Anatomy* **2000**, *197*, 647–657, DOI 10.1017/S0021878299007049, (cit. on p. 88).

[220] L. R. Hedlund, J. C. Gallagher, C. Meeger, S. Stoner, "Change in vertebral shape in spinal osteoporosis", in *Calcified Tissue International* **1989**, *44*, 168–172, DOI 10.1007/BF02556559, (cit. on p. 88).

[221] R. B. Martin, Porosity and Specific Surface of Bone, **1984** (cit. on p. 89).

[222] H. Brockstedt, M. Kassem, E. F. Eriksen, L. Mosekilde, F. Melsen, "Age- and sex-related changes in iliac cortical bone mass and remodeling", in *Bone* **1993**, *14*, 681–691, DOI 10.1016/8756-3282(93)90092-O, (cit. on p. 89).

[223] Y. N. Yeni, C. U. Brown, Z. Wang, T. L. Norman, "The influence of bone morphology on fracture toughness of the human femur and tibia", in *Bone* **1997**, *21*, 453–459, DOI 10.1016/S8756-3282(97)00173-7, (cit. on p. 89).

[224] K. L. Bell, N. Loveridge, G. R. Jordan, J. Power, C. R. Constant, J. Reeve, "A novel mechanism for induction of increased cortical porosity in cases of intracapsular hip fracture", in *Bone* **2000**, *27*, 297–304, DOI 10.1016/S8756-3282(00)00318-5, (cit. on p. 89).

[225] R. Zebaze, E. Seeman, Cortical bone: A challenging geography, **2015** (cit. on p. 89).

[226] K. Schrödter, G. Bettermann, T. Staffel, F. Wahl, T. Klein, T. Hofmann in *Ullmann's Encyclopedia of Industrial Chemistry*, **2008** (cit. on p. 89).

[227] N. Kourkoumelis, I. Balatsoukas, M. Tzaphlidou, "Ca/P concentration ratio at different sites of normal and osteoporotic rabbit bones evaluated by Auger and energy dispersive X-ray spectroscopy", in *Journal of Biological Physics* **2012**, *38*, 279–291, DOI 10.1007/s10867-011-9247-3, (cit. on p. 89).

[228] G. Fountos, S. Yasumura, D. Glaros, "The skeletal calcium/phosphorus ratio: A new in vivo method of determination", in *Medical Physics* **1997**, *24*, 1303–1310, DOI 10.1118/1.598152, (cit. on p. 90).

[229] H. H. Bolotin, H. Sievänen, "Inaccuracies Inherent in Dual-Energy X-Ray Absorptiometry In Vivo Bone Mineral Density Can Seriously Mislead Diagnostic/Prognostic Interpretations of Patient-Specific Bone Fragility", in *Journal of Bone and Mineral Research* **2001**, *16*, 799–805, DOI 10.1359/jbmr.2001.16.5.799, (cit. on p. 90).

[230] J. Mansfield, J. Yu, D. Attenburrow, J. Moger, U. Tirlapur, J. Urban, Z. Cui, P. Winlove, "The elastin network: Its relationship with collagen and cells in articular cartilage as visualized by multiphoton microscopy", in *Journal of Anatomy* **2009**, *215*, 682–691, DOI 10.1111/j.1469-7580.2009.01149.x, (cit. on p. 91).

[231] E. M. Green, J. C. Mansfield, J. S. Bell, C. P. Winlove, The structure and micromechanics of elastic tissue, **2014** (cit. on pp. 91, 170).

[232] A. Kazarine, A. A. Gopal, P. W. Wiseman, "Nonlinear microscopy of common histological stains reveals third harmonic generation harmonophores", in *Analyst* **2019**, *144*, 3239–3249, DOI 10.1039/c9an00267g, (cit. on p. 91).

[233] A. O. Ortiz, R. Bordia, "Injury to the vertebral endplate-disk complex associated with osteoporotic vertebral compression fractures", in *American Journal of Neuroradiology* **2011**, *32*, 115–120, DOI 10.3174/ajnr.A2223, (cit. on pp. 92, 97).

[234] L. Junhui, M. Zhengfeng, S. Zhi, M. Mamuti, H. Lu, F. Shunwu, Z. Fengdong, "Anchorage of annulus fibrosus within the vertebral endplate with reference to disc herniation", in *Microscopy Research and Technique* **2015**, *78*, 754–760, DOI 10.1002/jemt.22536, (cit. on pp. 92, 93, 96, 97).

[235] B. Berg-Johansen, A. J. Fields, E. C. Liebenberg, A. Li, J. C. Lotz, "Structure-function relationships at the human spinal disc-vertebra interface", in *Journal of Orthopaedic Research* **2017**, 192–201, DOI 10.1002/jor.23627, (cit. on p. 93).

[236] K. A. Dehring, N. J. Crane, A. R. Smukler, J. B. McHugh, B. J. Roessler, M. D. Morris, "Identifying chemical changes in subchondral bone taken from murine knee joints using raman spectroscopy", in *Applied Spectroscopy* **2006**, *60*, 1134–1141, DOI 10.1366/000370206778664743, (cit. on pp. 94, 96).

[237] M. Kazanci, P. Roschger, E. P. Paschalis, K. Klaushofer, P. Fratzl, "Bone osteonal tissues by Raman spectral mapping: Orientation-composition", in *Journal of Structural Biology* **2006**, *156*, 489–496, DOI 10.1016/j.jsb.2006.06.011, (cit. on pp. 94, 96).

[238] G. Penel, C. Delfosse, M. Descamps, G. Leroy, "Composition of bone and apatitic biomaterials as revealed by intravital Raman microspectroscopy", in *Bone* **2005**, *36*, 893–901, DOI 10.1016/j.bone.2005.02.012, (cit. on pp. 94, 96).

[239] B. R. McCreadie, M. D. Morris, T. ching Chen, D. Sudhaker Rao, W. F. Finney, E. Widjaja, S. A. Goldstein, "Bone tissue compositional differences in women with and without osteoporotic fracture", in *Bone* **2006**, *39*, 1190–1195, DOI 10.1016/j.bone.2006.06.008, (cit. on p. 94).

[240] M. D. Shoulders, R. T. Raines, "Collagen Structure and Stability", in *Annual Review of Biochemistry* **2009**, *78*, 929–958, DOI 10.1146/annurev.biochem.77.032207.120833, (cit. on p. 94).

[241] A. Awonusi, M. D. Morris, M. M. Tecklenburg, "Carbonate assignment and calibration in the Raman spectrum of apatite", in *Calcified Tissue International* **2007**, *81*, 46–52, DOI 10.1007/s00223-007-9034-0, (cit. on p. 94).

[242] M. Müller-Gerbl, S. Weißer, U. Linsenmeier, "The distribution of mineral density in the cervical vertebral endplates", in *European Spine Journal* **2008**, *17*, 432–438, DOI 10.1007/s00586-008-0601-5, (cit. on p. 95).

[243] H. W. Deng, F. H. Xu, K. M. Davies, R. Heaney, R. R. Recker, "Differences in bone mineral density, bone mineral content, and bone areal size in fracturing and non-fracturing women, and their interrelationships at the spine and hip", in *Journal of Bone and Mineral Metabolism* **2002**, *20*, 358–366, DOI 10.1007/s007740200052, (cit. on p. 95).

[244] J. Kaluzny, P. Purta, Z. Poskin, J. D. Rogers, A. A. Fawzi, "Ex vivo confocal spectroscopy of autofluorescence in age-related macular degeneration", in *PLoS ONE* **2016**, *11*, DOI 10.1371/journal.pone.0162869, (cit. on p. 95).

[245] R. Meerwaldt, H. L. Lutgers, T. P. Links, R. Graaff, J. W. Baynes, R. O. Gans, A. J. Smit, "Skin autofluorescence is a strong predictor of cardiac mortality in diabetes", in *Diabetes Care* **2007**, *30*, 107–112, DOI 10.2337/dc06-1391, (cit. on p. 95).

[246] S. Khandelwal, R. K. Saxena, "Erratum to: Age-dependent increase in green autofluorescence of blood erythrocytes", in *Journal of Biosciences* **2007**, *32*, 1345–1345, DOI 10.1007/s12038-007-0144-7, (cit. on p. 95).

[247] W. Denk, D. W. Piston, W. W. Webb in *Handbook Of Biological Confocal Microscopy*, (Ed.: J. B. Pawley), Springer US, Boston, MA, **2006**, pp. 535–549 (cit. on p. 95).

[248] N. Ignatieva, O. Zakharkina, G. Leroy, E. Sobol, N. Vorobieva, S. Mordon, "Molecular processes and structural alterations in laser reshaping of cartilage", in *Laser Physics Letters* **2007**, *4*, 749–753, DOI 10.1002/lapl.200710042, (cit. on p. 96).

[249] H. W.C., M. H., L. J., E. W.A., Y. S.T., M. A., A. T., T. K., "The Effect of Blocking a Nutritional Pathway to the Intervertebral Disc in the Dog Model", in *Journal of Spinal Disorders and Techniques* **2004**, *17*, 53–63, DOI 10.1097/00024720-200402000-00011, (cit. on p. 100).

[250] K. A. Tomaszewski, D. Adamek, T. Konopka, R. Tomaszewska, J. A. Walocha, "Endplate calcification and cervical intervertebral disc degeneration: The role of endplate marrow contact channel occlusion", in *Folia Morphologica (Poland)* **2015**, *74*, 84–92, DOI 10.5603/FM.2015.0014, (cit. on p. 100).

[251] N. Rahamimov, H. Mulla, A. Shani, S. Freiman, "Percutaneous augmented instrumentation of unstable thoracolumbar burst fractures", in *European Spine Journal* **2012**, *21*, 850–854, DOI 10.1007/s00586-011-2106-x, (cit. on p. 100).

[252] Z. Feng, L. Chen, X. Hu, G. Yang, Z. Chen, Y. Wang, "Vertebral Augmentation can Induce Early Signs of Degeneration in the Adjacent Intervertebral Disc: Evidence from a Rabbit Model", in *Spine* **2018**, *43*, E1195–E1203, DOI 10.1097/BRS.0000000000002666, (cit. on p. 100).

[253] R. Kang, H. Li, S. Ringgaard, K. Rickers, H. Sun, M. Chen, L. Xie, C. Bünger, "Interference in the endplate nutritional pathway causes intervertebral disc degeneration in an immature porcine model", in *International Orthopaedics* **2014**, *38*, 1011–1017, DOI 10.1007/s00264-014-2319-9, (cit. on p. 100).

[254] J. Krebs, S. J. Ferguson, B. G. Goss, E. Stauffer, L. Ettinger, N. Aebli, "Effect of vertebral cement augmentation with polymethylmethacrylate on intervertebral disc and bone tissue", in *Journal of Biomedical Materials Research - Part B Applied Biomaterials* **2012**, *100 B*, 660–667, DOI 10.1002/jbm.b.31990, (cit. on p. 101).

[255] H. Fernández-Susavila, J. P. Pardo-Seco, R. Iglesias-Rey, T. Sobrino, F. Campos, M. A. Díez-Ulloa, "Model of Disc Degeneration in Rat Tail Induced Through a Vascular Isolation of Vertebral Endplates", in *Journal of Investigative Surgery* **2018**, *31*, 265–274, DOI 10.1080/08941939.2017.1317373, (cit. on p. 101).

[256] J. M. Laffosse, F. Accadbled, F. Molinier, N. Bonnevialle, J. S. De Gauzy, P. Swider, "Correlations between effective permeability and marrow contact channels surface of vertebral endplates", in *Journal of Orthopaedic Research* **2010**, *28*, 1229–1234, DOI 10.1002/jor.21137, (cit. on pp. 101, 102).

[257] Y. Cao, S. Liao, H. Zeng, S. Ni, F. Tintani, Y. Hao, L. Wang, T. Wu, H. Lu, C. Duan, J. Hu, "3D characterization of morphological changes in the intervertebral disc and endplate during aging: A propagation phase contrast synchrotron micro-tomography study", in *Scientific Reports* **2017**, *7*, DOI 10.1038/srep43094, (cit. on pp. 102, 103, 144).

[258] H. E. Gruber, N. Ashraf, J. Kilburn, C. Williams, H. J. Norton, B. E. Gordon, E. N. Hanley, "Vertebral endplate architecture and vascularization: Application of micro-computerized tomography, a vascular tracer, and immunocytochemistry in analyses of disc degeneration in the aging sand rat", in *Spine* **2005**, *30*, 2593–2600, DOI 10.1097/01.brs.0000187877.30149.83, (cit. on pp. 102, 144, 170).

[259] S. J. Ferguson, K. Ito, L. P. Nolte, "Fluid flow and convective transport of solutes within the intervertebral disc", in *Journal of Biomechanics* **2004**, *37*, 213–221, DOI 10.1016/S0021-9290(03)00250-1, (cit. on p. 105).

[260] A. Thambyah, N. Broom, "On new bone formation in the pre-osteoarthritic joint", in *Osteoarthritis and Cartilage* **2009**, *17*, 456–463, DOI 10.1016/j.joca.2008.09.005, (cit. on pp. 139, 140, 144).

[261] G. Lim H. W., M. Wortis, R. Mukhopadhyay in *Soft Matter, Vol. 4*, **2009**, pp. 83–139 (cit. on p. 141).

[262] D. A. Rytand, "The number and size of mammalian glomeruli as related to kidney and to body weight, with methods for their enumeration and measurement", in *Developmental Dynamics* **1938**, *62*, 507–520, DOI https://doi.org/10.1002/aja.1000620406, (cit. on p. 141).

[263] K. Schmidt-Nielsen, P. Pennycuik, "Capillary density in mammals in relation to body size and oxygen consumption", in *American Journal of Physiology-Legacy Content* **1961**, *200*, 746–750, DOI 10.1152/ajplegacy.1961.200.4.746, (cit. on p. 141).

[264] H. Gray, *The classic collector's edition grays anatomy*, **1901**, pp. 1–1257 (cit. on p. 142).

[265] E. Eriksson, G. Germann, A. Mathur, Microcirculation in muscle, **1986** (cit. on p. 142).

[266] G. David, A. V. Ciurea, S. M. Iencean, A. Mohan, "Angiogenesis in the degeneration of the lumbar intervertebral disc.", in *Journal of medicine and life* **2010**, *3*, 154–61, (cit. on p. 142).

[267] J. R. Edwards, K. Williams, L. G. Kindblom, J. M. Meis-Kindblom, P. C. Hogendoorn, D. Hughes, R. G. Forsyth, D. Jackson, N. A. Athanasou, "Lymphatics and bone", in *Human Pathology* **2008**, *39*, 49–55, DOI 10.1016/j.humpath.2007.04.022, (cit. on p. 143).

[268] J. Shi, Q. Liang, M. Zuscik, J. Shen, D. Chen, H. Xu, Y. J. Wang, Y. Chen, R. W. Wood, J. Li, B. F. Boyce, L. Xing, "Distribution and alteration of lymphatic vessels in knee joints of normal and osteoarthritic mice", in *Arthritis and Rheumatology* **2014**, *66*, 657–666, DOI 10.1002/art.38278, (cit. on p. 143).

[269] S. C. Miller, W. S. Jee, "The microvascular bed of fatty bone marrow in the adult beagle", in *Metabolic Bone Disease and Related Research* **1980**, *2*, 239–246, DOI 10.1016/0221-8747(80)90013-2, (cit. on p. 144).

[270] K. Vandoorne et al., "Imaging the Vascular Bone Marrow Niche During Inflammatory Stress", in *Circulation research* **2018**, *123*, 415–427, DOI 10.1161/CIRCRESAHA.118.313302, (cit. on p. 144).

[271] B. S. Steiniger, V. Stachniss, V. Wilhelmi, A. Seiler, K. Lampp, A. Neff, M. Guthe, O. Lobachev, "Three-dimensional arrangement of human bone marrow microvessels revealed by immunohistology in undecalcified sections", in *PLoS ONE* **2016**, *11*, DOI 10.1371/journal.pone.0168173, (cit. on pp. 144, 145).

[272] A. R. Jackson, T. Y. Yuan, C. Y. C. Huang, F. Travascio, W. Yong Gu, "Effect of compression and anisotropy on the diffusion of glucose in annulus fibrosus", in *Spine* **2008**, *33*, 1–7, DOI 10.1097/BRS.0b013e31815e4136, (cit. on pp. 145, 170).

[273] K. P. Arkill, C. P. Winlove, "Solute transport in the deep and calcified zones of articular cartilage", in *Osteoarthritis and Cartilage* **2008**, *16*, 708–714, DOI 10.1016/j.joca.2007.10.001, (cit. on p. 145).

[274] Y. J. Liu, G. S. Huang, C. J. Juan, M. S. Yao, W. P. Ho, W. P. Chan, "Intervertebral disk degeneration related to reduced vertebral marrow perfusion at dynamic contrast-enhanced MRI", in *American Journal of Roentgenology* **2009**, *192*, 974–979, DOI 10.2214/AJR.08.1597, (cit. on p. 146).

[275] N. Boos, S. Weissbach, H. Rohrbach, C. Weiler, K. F. Spratt, A. G. Nerlich, "Classification of Age-Related Changes in Lumbar Intervertebral Discs", in *Spine* **2002**, *27*, 2631–2644, DOI 10.1097/00007632-200212010-00002, (cit. on p. 146).

[276] A. J. van der Veen, J. H. van Dieën, A. Nadort, B. Stam, T. H. Smit, A. J. van der Veen, T. H. Smit, J. H. van Dieën, "Intervertebral disc recovery after dynamic or static loading in vitro: Is there a role for the endplate?", in *Journal of Biomechanics* **2007**, *40*, 2230–2235, DOI 10.1016/j.jbiomech.2006.10.018, (cit. on p. 149).

[277] P. A. Hulme, S. J. Ferguson, S. K. Boyd, "Determination of vertebral endplate deformation under load using micro-computed tomography", in *Journal of Biomechanics* **2008**, *41*, 78–85, DOI 10.1016/j.jbiomech.2007.07.018, (cit. on pp. 149, 150, 166).

[278] C. S. Bailey, S. G. Sjovold, M. F. Dvorak, C. G. Fisher, T. R. Oxland, "The strength profile of the thoracolumbar endplate reflects the sagittal contours of the spine", in *Spine* **2011**, *36*, 124–128, DOI 10.1097/BRS.0b013e3181cc8a32, (cit. on pp. 149, 150).

[279] S. Xavier, C. Habura, C. Maglaras, R. Garafalo, K. Vaz, A. Valdevit, A. Ritter, "The Response of the Vertebral Endplate to Indentation Fatigue", in *The Spine Journal* **2010**, *10*, S60, DOI 10.1016/j.spinee.2010.07.163, (cit. on p. 149).

[280] J. H. Ash, J. R. Kerrigan, C. Arregui-Dalmases, E. Del Pozo, J. Crandall, "Endplate indentation of the fourth lumbar vertebra", in *Biomedical Sciences Instrumentation* **2010**, *46*, (cit. on pp. 149, 150).

[281] J. P. Grant, T. R. Oxland, M. F. Dvorak, C. G. Fisher, "The effects of bone density and disc degeneration on the structural property distributions in the lower lumbar vertebral endplates", in *Journal of Orthopaedic Research* **2002**, *20*, 1115–1120, DOI 10.1016/S0736-0266(02)00039-6, (cit. on p. 150).

[282] A. J. Fields, D. Rodriguez, K. N. Gary, E. C. Liebenberg, J. C. Lotz, "Influence of biochemical composition on endplate cartilage tensile properties in the human lumbar spine", in *Journal of Orthopaedic Research* **2014**, *32*, 245–252, DOI 10.1002/jor.22516, (cit. on p. 150).

[283] C. Vergari, J. Mansfield, J. R. Meakin, P. C. Winlove, "Lamellar and fibre bundle mechanics of the annulus fibrosus in bovine intervertebral disc", in *Acta Biomaterialia* **2016**, *37*, 14–20, (cit. on pp. 150, 151, 155, 164, 166).

[284] J. S. Bell, J. Christmas, J. C. Mansfield, R. M. Everson, C. P. Winlove, "Micromechanical response of articular cartilage to tensile load measured using nonlinear microscopy", in *Acta Biomaterialia* **2014**, *10*, 2574–2581, DOI 10.1016/j.actbio.2014.02.008, (cit. on p. 150).

[285] T. G. Lowe, S. Hashim, L. a. Wilson, M. F. O'Brien, D. a. B. Smith, M. J. Diekmann, J. Trommeter, "A biomechanical study of regional endplate strength and cage morphology as it relates to structural interbody support.", in *Spine* **2004**, *29*, 2389–2394, DOI 10.1097/01.brs.0000143623.18098.e5, (cit. on p. 155).

[286] Y. Chotar-Vasseur, C. Halimi, T. Cachon, C. Carozzo, G. Sudre, L. David, E. Viguier, "Mechanical properties of porcine spinal segments after intervertebral disc fenestration: an in vitro preliminary study", in *Computer Methods in Biomechanics and Biomedical Engineering* **2015**, 1–2, DOI 10.1080/10255842.2015.1069630, (cit. on p. 164).

[287] Y. Fujita, D. R. Wagner, A. A. Biviji, N. A. Duncan, J. C. Lotz, "Anisotropic shear behavior of the annulus fibrosus: Effect of harvest site and tissue prestrain", in *Medical Engineering and Physics* **2000**, *22*, 349–357, DOI 10.1016/S1350-4533(00)00053-9, (cit. on pp. 164, 165).

[288] N. T. Jacobs, L. J. Smith, W. M. Han, J. Morelli, J. H. Yoder, D. M. Elliott, "Effect of orientation and targeted extracellular matrix degradation on the shear mechanical properties of the annulus fibrosus", in *Journal of the Mechanical Behavior of Biomedical Materials* **2011**, *4*, 1611–1619, DOI 10.1016/j.jmbbm.2011.03.016, (cit. on pp. 164, 165).

[289] T. T. Tower, M. R. Neidert, R. T. Tranquillo, "Fiber alignment imaging during mechanical testing of soft tissues", in *Annals of Biomedical Engineering* **2002**, *30*, 1221–1233, DOI 10.1114/1.1527047, (cit. on p. 164).

[290] A. D. Holmes, D. W. Hukins, A. J. Freemont, "End-plate displacement during compression of lumbar vertebra-disc-vertebra segments and the mechanism of failure", in *Spine* **1993**, *18*, 128–135, DOI 10.1097/00007632-199301000-00019, (cit. on p. 164).

[291] M. L. Villarraga, A. J. Bellezza, T. P. Harrigan, P. A. Cripton, S. M. Kurtz, A. A. Edidin, "The biomechanical effects of kyphoplasty on treated and adjacent nontreated vertebral bodies", in *Journal of Spinal Disorders and Techniques* **2005**, *18*, 84–91, DOI 10.1097/01.bsd.0000138694.56012.ce, (cit. on p. 164).

[292] K. B. Broberg, "On the mechanical behaviour of intervertebral discs", in *Spine* **1983**, *8*, 151–165, DOI 10.1097/00007632-198303000-00006, (cit. on p. 164).

[293] H. S. Gupta, S. Schratter, W. Tesch, P. Roschger, A. Berzlanovich, T. Schoeberl, K. Klaushofer, P. Fratzl, "Two different correlations between nanoindentation modulus and mineral content in the bone-cartilage interface", in *Journal of Structural Biology* **2005**, *149*, 138–148, DOI 10.1016/j.jsb.2004.10.010, (cit. on p. 165).

[294] Cambridge University Engineering Department, The Three Point Bend - Beam theory, **2015** (cit. on p. 167).

[295] C. H. Flamme, N. Von Der Heide, C. Heymann, C. Hurschler, "Primary stability of anterior lumbar stabilization: Interdependence of implant type and endplate retention or removal", in *European Spine Journal* **2006**, *15*, 807–818, DOI 10.1007/s00586-005-0993-4, (cit. on p. 172).

So it is with you. Unless you speak intelligible words with your tongue, how will anyone know what you are saying?

You will just be speaking into the air.

1 Corinthians 14:9